

DOCTORAL THESIS

Development of a Transferable Microfluidic Droplet Generator

Rauno Jõemaa

TALLINN UNIVERSITY OF TECHNOLOGY
DOCTORAL THESIS
46/2024

Development of a Transferable Microfluidic Droplet Generator

RAUNO JÕEMAA



TALLINN UNIVERSITY OF TECHNOLOGY

School of Information Technologies

Thomas Johann Seebeck Department of Electronics

This dissertation was accepted for the defence of the degree 22/08/2024

Supervisor: Senior Researcher, Dr. Tamás Pardy
Thomas Johann Seebeck Department of Electronics
Tallinn University of Technology
Tallinn, Estonia

Co-supervisor: Tenured Associate Professor, Dr. Ott Scheler
Department of Chemistry and Biotechnology
Tallinn University of Technology
Tallinn, Estonia

Opponents: Professor, Dr. András Poppe
Department of Electron Devices
Budapest University of Technology and Economics
Budapest, Hungary

Professor, Dr. Ørjan Grøttem Martinsen
Department of Physics
University of Oslo
Oslo, Norway

Defence of the thesis: 09/09/2024, Tallinn

Declaration:

Hereby I declare that this doctoral thesis, my original investigation and achievement, submitted for the doctoral degree at Tallinn University of Technology has not been submitted for doctoral or equivalent academic degree.

Rauno Jõemaa



European Union
European Regional
Development Fund



Investing
in your future

signature

Copyright: Rauno Jõemaa, 2024

ISSN 2585-6898 (publication)

ISBN 978-9916-80-190-1 (publication)

ISSN 2585-6901 (PDF)

ISBN 978-9916-80-191-8 (PDF)

DOI <https://doi.org/10.23658/taltech.46/2024>

Printed by Koopia Niini & Rauam

Citation: Jõemaa, R. (2024). *Development of a Transferable Microfluidic Droplet Generator* [TalTech Press]. <https://doi.org/10.23658/taltech.46/2024>

TALLINNA TEHNIKAÜLIKOOL
DOKTORITÖÖ
46/2024

Ülekantava mikrovedelik-tilkade generaatori arendus

RAUNO JÕEMAA



Contents

List of Publications	7
Author’s Contribution to the Publications	8
Abbreviations	9
Symbols	12
1 Introduction	13
1.1 Context	13
1.2 Background and Trends	16
1.3 Challenges.....	18
1.4 Problem Statement and Research Questions.....	19
1.5 Contributions of the Thesis.....	20
1.6 Thesis Organization	22
2 Transferable Flow Regulation for Water-in-Oil Droplet Generation.....	25
2.1 Background	25
2.2 Design Considerations	27
2.2.1 Fluidics.....	27
2.2.2 Actuators.....	27
2.2.3 Sensors	28
2.2.4 Controller	29
2.2.5 Device Exterior and Fluidic Joints.....	30
2.2.6 User Interface.....	31
2.2.7 Design Overview and Connections.....	31
2.3 Performance Evaluation	32
2.3.1 Methodology.....	32
2.3.2 Results	34
2.4 Case study of Transferability	36
2.4.1 Context	36
2.4.2 Results	37
2.5 Chapter Summary.....	37
2.5.1 Discussion.....	37
2.5.2 Device Specifications.....	38
2.5.3 Considerations for the Next Stage	38
3 Transferable Droplet Generation Platform Design and Automation	40
3.1 Chapter Overview.....	40
3.1.1 Background	40
3.1.2 Design Criteria	42
3.2 Design Considerations	43
3.2.1 Layout and Fluidic Circuitry.....	43
3.2.2 Integration of the LED-PD Droplet Detector	48
3.2.3 Integration of the Developed Flow Regulation Device	53
3.2.4 System Controller.....	53
3.2.5 Droplet Size and Generation Rate Control Algorithms	57
3.3 Platform Evaluation Methodology	59
3.3.1 Computational Performance.....	59
3.3.2 Module Calibration	60
3.3.3 Parametric Control of Droplet Generation.....	61

3.4 Performance Evaluation Results.....	62
3.4.1 Computational Performance.....	62
3.4.2 Module Calibration	64
3.4.3 Parametric Control of Droplet Generation.....	65
3.5 Chapter Summary.....	67
3.5.1 Discussion.....	67
3.5.2 Platform Specifications	68
3.5.3 Considerations	69
4 Explorative Platform Modifications to Extend the Utility of PZT Diaphragm Micropumps in Droplet Generation.....	71
4.1 Chapter Overview.....	71
4.1.1 Motivation.....	71
4.1.2 Background of Piezoelectrically Produced Pulsations for Droplet Manipulation.....	74
4.1.3 Design Criteria.....	76
4.2 Design Components.....	79
4.2.1 Upgrading Pressure Sensors in Flow Regulation Module.....	79
4.2.2 Developing Piezoelectric Micropump Drivers for Flow Regulation Module.....	80
4.2.3 Facilitative Modifications Accompanying the Changes in Flow Regulation Module.....	84
4.2.4 Modified Droplet Detection	86
4.3 Custom PPD Performance Evaluation.....	88
4.3.1 Context.....	88
4.3.2 Results	88
4.4 Modified CogniFlow-Drop Platform Performance Evaluation.....	92
4.4.1 Context.....	92
4.4.2 Results	93
4.5 Chapter Summary.....	95
4.5.1 Discussion.....	95
4.5.2 Updated Platform Specifications.....	97
4.5.3 Open Challenges	98
5 Conclusion.....	99
6 Future Perspectives.....	101
6.1 Addressing Limitations	101
6.2 Created Research Interests.....	101
List of Figures	103
List of Tables	106
References	107
Abstract.....	117
Lühikokkuvõte.....	119
Appendix 1	121
Appendix 2	131
Appendix 3	137
Curriculum vitae.....	164
Elulookirjeldus.....	165

List of Publications

The list of author's publications, based on which the thesis has been prepared:

- I **R. Jõemaa**, M. Grosberg, T. Rang, T. Pardy, "Low-cost, portable dual-channel pressure pump for droplet microfluidics," 2022 45th Jubilee International Convention on Information Communication and Electronic Technology (MIPRO), IEEE, 2022.
- II N. Prabatama, **R. Jõemaa**, K. Hegedus, T. Pardy, "Low-cost open-source flow velocity sensor for droplet generators," 2022 18th Biennial Baltic Electronic Conference (BEC), IEEE, 2022.
- III **R. Jõemaa**, N. Gyimah, K. Ashraf, K. Pärnamets, A. Zaft, O. Scheler, T. Rang, T. Pardy, "CogniFlow-Drop: Integrated modular system for automated generation of droplets in microfluidic applications," IEEE Access, IEEE, 2023.
- IV Forthcoming publication: **R. Jõemaa**, T. Pardy. "Modular, dual-tone piezoelectric micropump driver for low cost, portable droplet generation," 2024 19th Biennial Baltic Electronic Conference (BEC), IEEE, 2024.

Other related publications:

- V M. Grosberg, **R. Jõemaa**, T. Rang, T. Pardy, "Wireless microfluidic dual-channel pressure pump," patent application. Priority number P202200009, Estonia, 2022.
- VI K. Pärnamets, K. Ashraf, N. Gyimah, **R. Jõemaa**, T. Pardy, "Integrated modular system for automated generation of droplets in microfluidic applications and method thereto," patent application. Priority number P202300024, Estonia. 2023.
- VII N. Gyimah, **R. Jõemaa**, K. Pärnamets, O. Scheler, T. Rang, T. Pardy, "PID controller tuning optimization using genetic algorithm for droplet size control in microfluidics," 2022 18th Biennial Baltic Electronic Conference (BEC), IEEE, 2022.
- VIII **R. Jõemaa**, T. Pardy, "Integrated modular multi-tone piezoelectric element driver and method of driving modular multi-tone piezoelectric element driver for pressure generation," patent application. Priority number P202400014, Estonia, 2024.

Author's Contribution to the Publications

Contribution to the papers in this thesis are:

- I For paper I, I carried out the benchmarking and evaluation experiments, prepared the bulk of the figures, experimental results, and wrote the draft.
- II As a co-author in paper II, I had a co-supervisory role in the design and experimental methodology. More specifically, in the implementation of the device from paper I, and methods of how to produce droplets/bubbles and how to approach their measurement and interpretation. At the end I reviewed and edited the paper.
- III As the first author in paper III, I wrote the control algorithms, designed the fluidics and automation related experimental methodology, and carried out the related experiments, result analysis and visualization. I wrote the drafts for sections: II/B/2,3,5; II/C/2; II/D/2; III/A/2,3,4; III/B/1,2; IV/A/2,3,4; IV/B/1,2; V/A; V/B. At the end I reviewed and aligned the contributions from all authors to the style of the paper.
- IV For paper IV, I proposed a novel design for a piezoelectric micropump driver and a method to use a secondary tone in the piezoelectric element driving signal as an additional interface with droplet generation. I updated the design of the system presented in paper III to use as the experimental setup for the proposed driver. I prepared the figures, carried out the evaluation experiments, result analysis, visualization and wrote the draft.

Abbreviations

A/D	Analog/Digital
AADS	Absorbance-Activated Droplet Sorting
AC	Alternating Current
ADC	Analog to Digital Converter
API	Application Programming Interface
ASWCH	Analog Switch
BC	Boost Converter
BC-O	Boost Converter Output (pin)
BC-OFB	Boost Converter Output Feedback
BC-OFB-B	Boost Converter Output Feedback Buffer
BC-OVL	Boost Converter Over Voltage Limiter
BC-SCC	Boost Converter Short Circuit Control (pin)
BC-SCC-SWCH	Boost Converter Short Circuit Control SWITCH
BC-SWCH	Boost Converter Switch
BC-SWCH-GD	Boost Converter Switch Gate Driver
BC-SWCH-GD-CPD	Boost Converter Switch Gate Driver Charge Pump Driver
BJT	Bipolar Junction Transistor
BOM	Bill of Materials
BPF	Band Pass Filter
CMOS	Complementary Metal-Oxide-Semiconductor
CMP	Comparator
COTS	Commercial Off-the-Shelf
CPU	Central Processing Unit
CS	Chip Select (signal)
CV	Coefficient of Variability
DAC	Digital to Analog Converter
DC	Direct Current
DIP18	Dual In-line Package (18-pins)
DIW	Deionized Water
DoF	Degrees of Freedom
DP	Digital Potentiometer
DPS*	Droplets Per Second
DSSP	Droplet Sensor Signal Processing
DSSP-B	Droplet Sensor Signal Processing Board
eCAL	Enhanced Communication Abstraction Layer
EOC	End of Conversion
FADS	Fluorescence-Activated Droplet Sorting
FFD	Flow Focusing Device
FO	Fluorinated Oil

FRC-B	Flow Regulation Control Board
FTSAW	Focused Traveling Surface Acoustic Waves
GPIO	General Purpose Input Output
GUI	Graphical User Interface
HPF	High Pass Filter
HW	Hardware
I/O	Input/Output
I2C	Inter-Integrated Circuit (communication protocol)
ID	Inner Diameter
IPA	Isopropyl Alcohol
IR	InfraRed
L1	Layer 1
L2	Layer 2
L3	Layer 3
LED	Light Emitting Diode
LED-PD	Light Emitting Diode-Photodiode (sensor)
LOC	Lab-on-a-Chip
LPF	Low Pass Filter
MCU	Microcontroller Unit
MISO	Master In Slave Out (signal)
MO	Mineral Oil
MOSI	Master Out Slave In (signal)
MP	Midpoint
NC	No Connection
N-MOS	N-type Metal-Oxide-Semiconductor Field-Effect-Transistor
OA	Operational Amplifier
OD	Outer Diameter
OOC	Organ-on-a-Chip
OS	Operating System
PC	Personal Computer
PCB	Printed Circuit Board
PD	Photodiode
PD-TIA	Photodiode-Transimpedance Amplifier (circuit)
PDMS	Polydimethylsiloxane
PET	Piezoelectric Transducer
PID	Proportional-Integral-Differential (controller)
P-MOS	P-type Metal-Oxide-Semiconductor Field-Effect-Transistor
POC	Point-of-Care
PPD	Piezo Pump Driver
PS-B	Pressure Sensor Board
PZT	Lead Zirconate Titanate – Pb(ZrTi), piezoelectric ceramic material
PTFE	Polytetrafluoroethylene (Teflon™)

PWM	Pulse-Width Modulation
QOA	Quad Operational Amplifier
R&D	Research and Development
ROI	Region of Interest
RPI	Raspberry Pi
SBC	Single-Board Computer
SCLK	Serial Clock (signal)
SMD	Surface Mount Device
SPI	Serial Peripheral Interface (communication protocol)
SW	Software
TIA	Transimpedance Amplifier
USB	Universal Serial Bus
VCA	Voltage Controlled Amplifier

Symbols

Ca	Capillary number
Re	Reynolds number
R _{DS}	(MOSFET) Drain-Source Resistance
V _{DS}	(MOSFET) Drain-Source Voltage
V _{HP}	Highest Peak Voltage
V _{LP}	Lowest Peak Voltage
V _{PP}	Peak-to-Peak Voltage
w/w	Weight in weight

1 Introduction

1.1 Context

Microfluidics is a field of research, which handles liquids at scales where one of the flow-path cross-sectional dimensions is shorter than a millimeter [1]–[3]. A peculiar fluid dynamic is reached when the flowing liquid volume and mass become small enough that forces independent of mass such as viscosity, surface tension and channel wettability become the dominant forces in flow behavior [2]. Thus, when inertial forces have been made insignificant in comparison [4], [5], liquid can be made to flow in a predictable, layered form, without turbulence – a phenomenon referred to as laminar flow [6], [7], where flow lines do not break. The most notable advantage gained from this, besides higher process accuracy and resolution, is the drive to design tools and methods to managing and thereby requiring smaller and smaller sample sizes [2], [8]. In efforts to highlight these benefits, since the 1990s, microfluidic research has been seeking ways to shrink biochemical process volumes in laboratories [2], [8]–[12] for the purposes of efficient use of resources [13]–[16], single-cell precision [17], [18], and automation [5], [11], [13], [19], [20].

In early 2000s [12], a method was developed to try and isolate cells and bacteria from a larger liquid body (i.e., blood sample) into compartments or droplets to behave as individual, easily separable units in following tests [21]. This separation gave the ability to monitor each cell individually and to analyze the content of a biological liquid sample at a cellular resolution [6], [21]. The production of microscopic droplets and cellular encapsulation into them is finding increasing implementation in biochemical, medical, and pharmaceutical research [16], [21]–[23]. This technology has been used to develop novel applications in a variety of areas [1], [6], [26], [27], [12], [15], [16], [20]–[22], [24], [25]: flow-cytometry, polymerase chain reaction (PCR), drug development, drug delivery, cosmetics, nano-material synthesis, etc.

After generating and collecting droplets containing organic material, similarly to petri dishes, the droplets are often transported to incubators [28], [29] to enable biological processes to continue separately within each droplet [30]. The transportability of droplets is a matter of efficiency for applications observing cellular metabolism, multiplication, and/or survival. To preserve the experiment's viability over time, it's essential that the droplets maintain their integrity [8]. After hours or days of incubation, droplets are transferred onto imaging slides (typically by pipetting) or into a microfluidic funnel chip where droplets are serialized for optical analysis of their content [29] or further sorting [31]. Tools and appliances for droplet transportation and off-chip incubation are normally not of microfluidic scale [19], [31]–[33], which allow for the significance of gravitational and inertial forces to re-emerge, increasing the potential failure of droplet integrity.

Droplet volume determines the environmental parameters around the encapsulated cell(s), thereby making the droplet's size of critical importance for the experiments [29]. To keep the experiments comparable, it is necessary to generate droplets with high monodispersity. As such, it has become a core objective to control the droplet size during formation. For most biochemical experiments to succeed, a size variance lower than 5% is expected [15], [34], 1% is considered excellent [4]. Such droplets are typically formed of aqueous liquid where cells and proteins can retain their viability [29]. However,

to achieve highly uniform droplet formation, deterministic flows of two immiscible liquids (e.g., oil and water) are made to interact [24] to force a repetitive dispersion of one. In microfluidic two-phase flows (e.g., continuous phase – oil, dispersed phase – water), there are known channel geometries that are efficient in monodisperse droplet formation (**Fig. 1**).

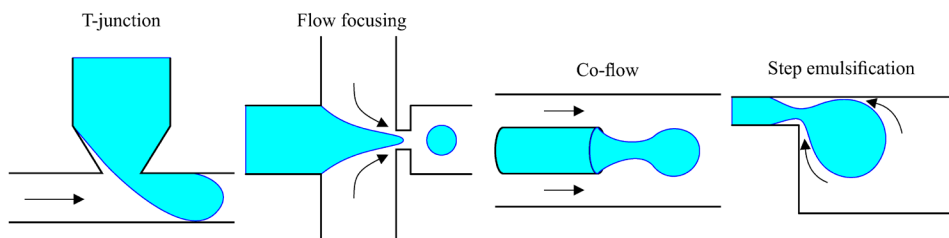


Figure 1. A selection of widely used microfluidic droplet generation channel geometries. Reproduced from [35].

Whether the dispersion of droplets becomes predictably repetitive, depends on the flow regime (dripping¹, squeezing², jetting³, threading⁴) of the dispersed phase liquid [4], [36]. While this is largely influenced by the fixed properties of the liquids at specified individual flow rates, described by capillary (Ca) and Reynolds numbers (Re), movement between the regimes can take place by changing the flow rate ratio between the two liquids [4]. Amongst the proposed geometries (**Fig. 1**), the symmetry in co-flow and flow-focusing designs provides better control within the regimes [4]. This in turn extends the size range of droplets generated with one fixed set of channel dimensions – extending the versatility of a settled chip design. While both have become widely used, the flow-focusing design gains an additional advantage over co-flow by being more easily fabricable due to its planar design [37], [38], lowering the cost and time spent in setup development.

After the formation of a droplet, a typical microfluidic droplet generation setup directs the droplet into a non-microfluidic container for collection and transportation. The immiscibility and difference in fluid densities in such containers allows the collected droplets to pool together and subsequently coalesce. As prevention, a method of droplet coating has been used [8], [10], [22], [27], [28], [39]–[41]. This coating has also been used to alter droplet formation and increase the process repeatability [22]. The coating substance is known as a surface-active agent or surfactant, consisting of an asymmetric elongated molecule with one of its ends being polarized while the other being apolar [42]. The polarized end is attracted to polarized media such as water and thereby called hydrophilic [42]. Surfactant can be mixed into either phase in droplet generation. However, to reduce the chance of encapsulating surfactant molecules

¹ *Dripping regime* develops droplets which are smaller than the channel they form in.

² *Squeezing regime* develops plug-like droplets with dimensions large enough to become limited by the channel they form in.

³ *Jetting regime* forms a jet which extends beyond the vicinity of the droplet formation junction. In case the droplet-forming channel is long enough for the jet to become unstable, chaotic droplet formation can occur.

⁴ *Threading regime* is a form of jetting in which a stable jet extends beyond the microfluidic chip and does not result in droplets.

together with cells, the surfactant is preferably mixed into the continuous phase. When water encounters oil at the interface junction (**Fig. 1**), the droplet can quickly become coated by the surfactant particles (**Fig. 2**).

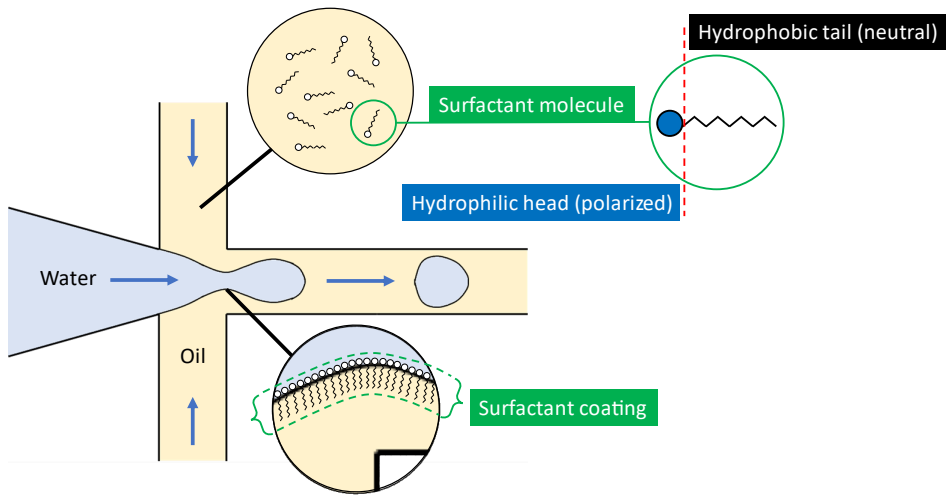


Figure 2. Illustration of a flow-focusing type droplet generation geometry, forming droplets from oil and water. The oil contains premixed surfactant molecules with a neutral hydrophobic tail and a polarized hydrophilic head. Polarized ends of the surfactant are attracted by the polarizable water, forming a coating layer at the oil-water interface. Surfactant coating aids in droplet formation and mitigates coalescing when coming in contact with other droplets.

Because microfluidic droplet generation is so reliant on laminar flows, it is important to consider that the introduction of microparticles (more so for cells and markers than surfactant) can impact droplet formation and encapsulation predictability [22]. Typically, cells and other particulates in the dispersed phase flow are spaced irregularly due to being sourced from a dynamically changing body of liquid into which the particulates were initially mixed. With this irregularity, the success of their encapsulation into droplets has been found to follow a statistical Poisson distribution [8], [17], [43]. Illustratively, if the percentage of cells sparsely floating in 1 ml of water, compared to the number of droplets obtainable from it, is 10%, then about 9% of the produced droplets contain one cell, about 0.5% contain more than one and the remaining ~90.5% of droplets are generated empty. The passive encapsulation process is largely dependent on the number of cells used per volume of liquid media to be split into droplets [43]. A high initial cell percentage can significantly decrease the number of empty droplets, however, this comes at the cost of an increasing number of droplets housing multiple cells [43]. This phenomenon detracts from the intrinsic efficiency gained from microfluidics. A number of solutions have been devised to counter this setback [17], [43]–[45]: increased throughput of droplets by method refinement, geometrically induced uniformity in particle spacing, active encapsulation, etc.

1.2 Background and Trends

Along with fluidics related mechanical solutions, the interdisciplinary foundation of microfluidics has greatly benefited from the developments in electronics and computing [46]. Much support has been found from continuously improving accessibility to electronic components, and single-board computers (SBC). Peculiarly, the technology of microfluidic (liquified tin) droplet generation has become linked to the shrinking cost and scale of microchip circuits through extreme ultraviolet (EUV) lithography [47]–[49]. Increased accessibility to electronics allows research labs in various fields around the world to quickly explore new actuation, sensing, and feedback methods for microfluidic setups. Increases in computing power can be seen as experimental microfluidic models are replicated in virtual environments using finite element modeling and computational fluid dynamics [50]. Even so, the implementation of multidisciplinary methods requires extensive know-how. To reduce the integratory barriers of cost and expertise, more attention is continually sought in simplification, modularization, commercialization, and automation of microfluidic setups [6], [21], [51], [52].

Visualized, the amount of yearly scientific publications in areas of microfluidics, microfluidic droplet generation and related automation reveals considerable growth of the fields and continued interest in them over the recent decades (**Fig. 3**). A control query “1* OR a*” in **Fig. 3** (covering approximately all publications on the Scopus database) shows notably a similar growth trend in overall publications. However, the differences among the steepness of each line points to a rising interest in microfluidics and droplet generation as fields. In contrast, droplet generation and related automation (query: microfluidic* AND “droplet generation” AND automation) have yet to break the norm.

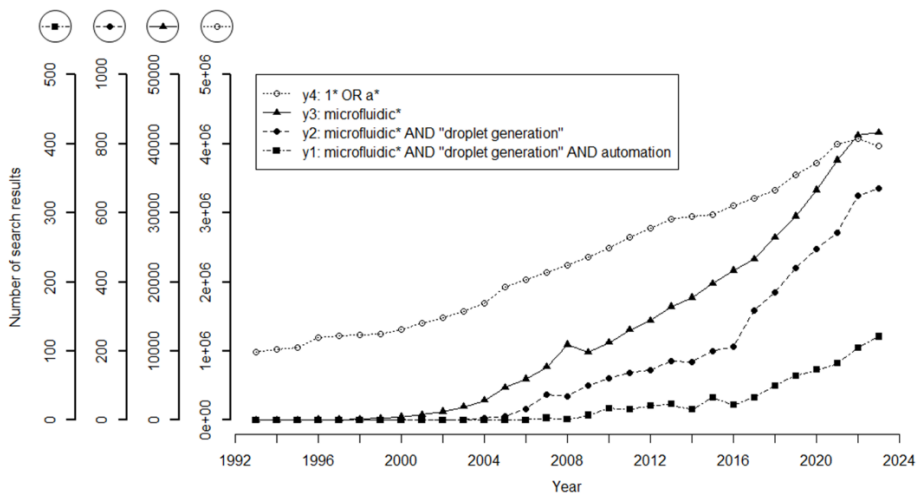


Figure 3. Scientific database (Scopus) “ALL” fields search result counts over the past 30 years (1993 - 2023). Each queried keyword combination (1* OR a*; microfluidic*; microfluidic* AND “droplet generation”; microfluidic* AND “droplet generation” AND automation) has been plotted on a separate y-axis. Search was conducted in January of 2024.

While the number of new droplet generation solutions keeps increasing, the absence of harmonization and standardization [11], [52] keeps the implementation of the methods difficult at the application level. As the adoption rate of a technology is largely tied to the success of its applications, this absence is also hampering much of the commercial

development in droplet-based technologies. In microfluidics, slow adoption of novel methods is apparent and notably linked to the extensive secondary integration steps required for the experimental setups consisting of many complex and non-portable components [53], [54]. Yet, the primary focus continues to lie in maximizing specific performance parameters instead:

- **Throughput (monodisperse droplet generation rate)** – since 2021, generation rate of bubbles, sized between 2.5 μm and 20 μm , reached 10^6 units per second [55]; generation rate of droplets reached over 10^5 units per second in 2023 [56]; two-phase droplet generation rate has been above 10^4 units per second since 2006 [57] and with the help of parallelization above 10^6 units per second since 2015 [58], [59].
- **Droplet size coefficient of variability (CV%)** – since 2023, the lowest droplet size CV% was recorded at 0.036%, using pressure sources, generating droplets in diameters of $\sim 220 \mu\text{m}$ at a rate of $\sim 32.4 \text{ Hz}$, and utilizing closed-loop control with feedback from detecting droplets with integrated electrodes [60].
- **Range of dynamically adjustable size of generated droplets** – since 2021, the broadest microfluidic droplet diameter control achieved was recorded to range from 6.77 μm to 661 μm , with droplet generation rates at up to 5000 Hz and a CV% below 4% [61].
- **Encapsulation rate (controlled deviation from Poisson distribution)** – in 2020, selective encapsulation at a droplet formation rate of 125 Hz was demonstrated with a pico-injection method using traveling surface acoustic waves (TSAW) [62], [63]; in 2022, encapsulation was improved by passive hydrodynamic pre-focusing and ordering of cells prior to droplet formation, achieving up to 86% of single bead encapsulation at a droplet generation rate around 10 kHz [64] – limited by being critically dependent on the geometry of the microfluidic channels.
- **Sorting rate (managing throughput losses from Poisson distribution)** – in 2014, nearly 100% sorting rate (at $\sim 29 \text{ kHz}$) was reached with fluorescence-activated droplet sorting (FADS) using a dielectrophoretic separation force combined with a gap divider in front of diverging sorting channels [65]; in 2019, nearly 100% sorting rate (at $\sim 833 \text{ Hz}$) was reached with FADS using focused traveling surface acoustic waves (FTSAW) [66]; in 2023, 100% sorting rate at 1 kHz was achieved with absorbance-activated droplet sorting (AADS) using dielectrophoretic force [67].

Introducing automation into the droplet generation process has an inherent potential to compensate for the temporal losses caused by droplet throughput (e.g., accepting lower throughput to improve the CV%) and regular encapsulation rates (e.g., when robustness and simplicity of the setup is of higher importance). Additionally, using droplet size as feedback for automation could enable optimization between the variance and dynamic range of droplet sizes. Commercially prevalent methods can already offer some automation using computer vision with image analysis AI [68], whereas scientific efforts lean towards the potential of less complex solutions such as a light intensity sensors [69], [70] or integrated electrodes with PID control [60]. Further details on the state-of-the-art setups utilizing droplet size as feedback can be found in paper III (see full

text in **Appendix 3**), and in the first sections of each body chapter (see chapter layout in Section 1.6). Following the metrics of interest in droplet generation, a general-purpose automated platform, applicable for various applications, ought to cover requirements complementing flexibility, and portability (**Table 1**).

Table 1. Microfluidic droplet generation platform requirements to be on par with the state-of-the-art.

Specification	Property/Range
Compatible media	Liquid (aqueous and non-aqueous) [29]
Droplet media	Aqueous [29]
Nominal adjustable droplet diameter	< ~1241 μm (1 mm^3 ; 1 μL) [29], [71]–[74]
Nominal adjustable droplet throughput rate	> 1 kHz (derived from SOTA of AADS) [67]
Droplet diameter coefficient of variability (CV)	< 5% [4], [15], [22], [34], [71], [75]
Dimensions (full setup)	< 55 x 36 x 23 cm (most carry-on luggage) [76]
Power consumption	< 10 W
Cost ⁵	< 1000 €

1.3 Challenges

Based on the background and trends in Section 1.2, I was able to identify the following challenges:

1. With an expectation for aqueous droplet size CV to remain below 5% for droplet generation rates at least above 1 kHz, a challenge was found in the lack of examples of droplet generation platforms using transferable flow regulation and droplet detection modules. In the context of this work, transferability implies portability and affordability, while also encompassing a simple, replicable methodology and accessibility to all its components. A flow regulation module aimed for flexibility of use (including automation), primarily limited by cost and size, is required to prioritize responsiveness – dynamic stability over static stability.
2. Publications of transferable droplet generation which focus on performance metrics such as throughput, but even monodispersity, neglect the importance of cost-effective scalability and verifiability of the entire output (every droplet produced). The challenge lies in cataloguing all generated droplets on a high throughput platform using low-cost droplet detection and control loop hardware.
3. Microfluidic droplet generation is still missing easily adoptable, yet flexible setups. There are numerous novel methods presented in literature (**Appendix 3**), however being repeatedly hampered by different research groups focusing narrowly on specific performance metrics or designs individualized by subjectively familiar infrastructure. As there are many potential applications behind the barrier of expertise and expensive infrastructure, the challenge lies in expanding

⁵ Cost of the platform, limited to cover the cost of structural materials and low volume prices of COTS electronic and mechanical components; bill of materials.

the use of droplet microfluidics by finding a design for a transferable automated platform. Automation which includes a focus on real-time adjustable droplet generation output values (droplet size and generation rate) with lightweight PID controllers.

1.4 Problem Statement and Research Questions

The primary problem this thesis focuses on is the development of a transferable automated droplet generation platform for research experiments that could facilitate novel applications which are otherwise inefficient⁶ to pursue. In addition to the specifications in **Table 1**, the platform should be accompanied by high repeatability⁷ that can speed up droplet generation experiments by reducing the time taken in finding the droplet generation settings when there are otherwise critical changes introduced to the test setup such as:

- Method of droplet generation (microfluidic channel dimensions, shapes)
- Fluidics (channel surface roughness, hydrophobicity, liquids, additives)
- Encapsulated sample (content ratio, content type)

An automated droplet generation platform designed to reduce time in setup adaptation will reduce switching time between encapsulation processes of different samples. This kind of rapid adaptive system would have open-ended use-cases in a variety of fields.

- Biochemistry (e.g., water/soil content sampling)
- Medicine (e.g., drug development, personalized medicine)
- Multidisciplinary microfluidic technology (e.g., sensors, organ-on-a-chip (OOC), neuromorphic computing, etc.)

To make a system flexible for a variety of research fields, portability and cost are considered critical development goals. The platform ought to allow for easy transfer from lab to lab while maintaining repeatability, which could be achieved by transfer of the design or by transportation of the device. Fast technology transfer is not only beneficial during development of a multidisciplinary platform, not only efficient by bringing the lab closer to the source, but crucial for flexibility in generation, incubation, and analysis methods, where experimental parameters are uncommon.

To increase the appeal of such a platform for research, additional focus was put on development goals regarding stability, accuracy, accessibility, and modularity. High stability and accuracy ensure comparability of produced droplets. Whereas accuracy provides credibility for results, accessibility provides credibility for accuracy. The system ought to have easy access to all available sensory data to be able to assess the accuracy and improve repeatability. On top of this, a modular system would ensure fast and affordable upgradability. Moreover, it would allow for modifications to both generation and detection methods to better keep up with the state-of-the-art.

⁶ In this context, *inefficient* refers to ideas and methods which result in misallocation of resources.

⁷ In this context, *high repeatability* implies for a platform to have the functionality to produce an output with closely matching properties (e.g., droplets of specific size), with or without limited modifications to the platform, by relying on criteria with higher level abstraction from inputs such as flow parameters – desired outputs achievable more easily across deviations in methodology.

Final objectives for the platform were efficiency and a high degree of control. In efficiency, the emphasis is put on power consumption and waste reduction to complement the advantages of microfluidics and the design for portability. In high degree of control, which complements efficiency, the system is to provide rapid launch and stabilization of droplet generation regardless of variations in flow characteristics.

Based on the background, motivation, and challenges of this doctoral dissertation, it is possible to formulate the following **hypothesis**:

By feedback control of pressure and droplet size in a compact, modular, transferable droplet generation platform, it is possible to meet performance metrics of state-of-the-art droplet microfluidic setups while providing a higher standard of automation focused on responsiveness, sensitivity, and replicability.

Sub-hypothesis:

Combined closed-loop PID controllers for pressure, droplet size and generation rate feedback in a modular, transferable droplet generation platform with pulsatile flow characteristics, can pass below the minimum acceptable droplet generation stability of 5% CV.

The work was built upon the following research questions:

RQ1: What is a highly responsive, transferable microfluidic flow regulation method, which allows for droplet generation with precise and accurate control, as well as flexible configuration for different application use cases?

RQ2: Can microfluidic droplet parameters be estimated from low-cost brightfield light intensity measurements well enough for droplet generation control?

RQ3: How to automate droplet generation while maintaining repeatability and flexibility with piezoelectric micropump actuators, pressure-based flow sensors and PD-LED droplet sensor for varying droplet generation parameters, FFD cross-junctions, and reagents?

RQ4: How can the performance of piezoelectric micropumps in droplet generation be improved through their driving signal and what effect does it have on control stability in droplet generation with pulsatile flows?

1.5 Contributions of the Thesis

This thesis is written to cover the primary components, the design process, and results in constructing and automating a transferable droplet generation platform. My parts in it define its flow regulation, droplet identification methodology, droplet size and generation rate control methodology, system design integration process and addressing the design limitations.

This PhD thesis makes the following contributions:

- I Contributions relating to **RQ1**, in publication 1, I focused on enhancing the Proportional-Integral-Derivative (PID) pressure control system and refining its algorithm. This involved further development of the existing pump communication interface. I devised an experimental methodology to evaluate the device's performance in terms of flow stabilization speed and droplet uniformity.

This included collecting initial data on PID control, assessing feedback sensor feasibility, and examining the effects of the micropump's pulsatile operation on flow dynamics. Following, alongside analyzing the results, I prepared the result-oriented figures and drafted the manuscript. My additional contributions include the evaluation of the device's battery-powered performance, micropump characteristics for droplet generation and the pump and its driver responsiveness for automation.

Claim no. 1: A novel, portable, low-cost microfluidic flow regulation device, using piezoelectric micropumps with audible frequency range pulsations, was presented and evaluated as feasible (< 2% CV) for water-in-oil droplet generation.

- II Contributions relating to **RQ1**, with publication 2, I was able to evaluate the transferability of the flow regulation device developed in the first publication. The device was transferred abroad as a design to which I provided consultation regarding its flow regulation. I provided further consultation in optical and pressure sensorics which was used for the development of a droplet flow velocity sensor. Lastly, I reviewed the resulting manuscript.

Claim no. 2: The design transfer and application of a portable, low-cost microfluidic flow regulation device, using piezoelectric micropumps with audible frequency range pulsations, in optical flow rate sensor as air-water segment generator proved its transferability and flexibility as a module.

- III Contributions relating to **RQ2** and **RQ3**, in publication 3, building upon an enhanced design and PID control from publication 1, I merged the tested droplet generation method with a droplet monitoring method, developed by Kaiser Pärnamets et al. [77], into a prototype droplet generator platform. The methods were joined by designing purpose-built fluidic pathways and writing the droplet feedback algorithm on the primary system controller. A unique feature I added to the sensing method was a tiltable microfluidic chip mount, enabling optical droplet measurement from varying angles. I developed the control software on the system controller specifically for this platform; focusing on automating droplet generation rate and size control; incorporating features like calibration and dual-PID algorithms. To estimate the droplet size, interpretable from the droplet sensor, I designed a custom image intensity visualization program allowing the use of arbitrary pinholes to scan over droplet images, imitating droplet movement over the sensor. In regard to platform evaluation, I conducted the droplet generation experiments and their subsequent analysis. I was responsible for preparing corresponding visual data, analyzing the results, and contributing to the manuscript on these aspects. The design in this work addressed themes such as cost-effectiveness, energy efficiency, portability, flexibility, stability, accuracy, modularity, repeatability, comprehensive control, and responsiveness. Additional contributions extended to designing, programming, and assembling the electronic components for droplet signal processing and fluidic control.

Claim no. 3: To have sufficient sensitivity and resolution over the low-cost brightfield LED-PD light intensity measurements, a band-pass filter, a multi-stage amplifier and a digitizing A/D converter are required to obtain sufficient data for droplet size and generation rate control.

Claim no. 4: A state-of-the-art, PID-controlled, two-phase droplet generation platform CogniFlow-Drop was developed, using a low-cost pressure-based flow regulation and an optical PD-LED droplet detector.

Claim no. 5: Using the CogniFlow-Drop platform, a comparison between 90° and 38.33° flow-focusing cross-junction angle showed higher degree of generated water-in-oil droplet parameter control for 90° cross-junction angle.

Claim no. 6: A two-stage calibration algorithm was devised and used on CogniFlow-Drop platform to characterize the specifics of the used fluidics, including chip geometry and reagents to be able to keep track of repeatability issues.

Claim no. 7: Using the CogniFlow-Drop platform with an FFD, droplets can be generated from mineral and fluorocarbon oil, with and without surfactants, in various sizes and generation rates.

- IV Contributions relating to **RQ4**, in publication 4 (forthcoming), I developed a piezoelectric micropump driver that surpasses similarly sized and priced commercial alternatives in terms of capabilities and features. I designed the driver to be easily interchangeable with the commercial drivers I used in publication 3, for which I made necessitated supporting updates to the platform's electronics, fluidics, and sensory components. I conducted the evaluation experiments with the custom driver on the modified droplet generation platform. To enhance the piezoelectric micropump's performance in droplet generation, I designed the driver with a focus on control over the driving waveform's amplitude and frequency. I achieved this by using two analog waveform sources in Wien Bridge configuration with adjustable frequency, whose outputs could be controlled by voltage-controlled amplifiers (VCA). Additional key features of the driver included an optional external waveform input, compatibility with the commercial driver used previously, a multi-level modular design, full control over the boost-converter, and an analog waveform summer. In this publication my writing responsibilities included the preparation of the methodology and figures, description, and analysis of conducted experiments, and writing the manuscript.

Claim no. 8: A novel, small footprint, low-cost, driver with dual pure tone oscillators was developed for dual chamber series piezoelectric micropumps.

Claim no. 9: Modified CogniFlow-Drop platform can generate droplets in adjustable sizes and generation rates with CVs for both below 1%.

1.6 Thesis Organization

The thesis is split into six chapters, including an introduction, three body chapters, a conclusion, and a separate chapter for future perspectives. The combined focus from challenges and research questions posed in the introduction connects to each of the respective publications marked with green boxes in the body chapter columns on **Fig. 4**. Each body chapter is based on the results of a first-authored publication, which are strongly dependent on each other. The main timeline is illustrated by continuous orange arrows, whereas a supportive publication is connected through a dashed arrow (**Fig. 4**).

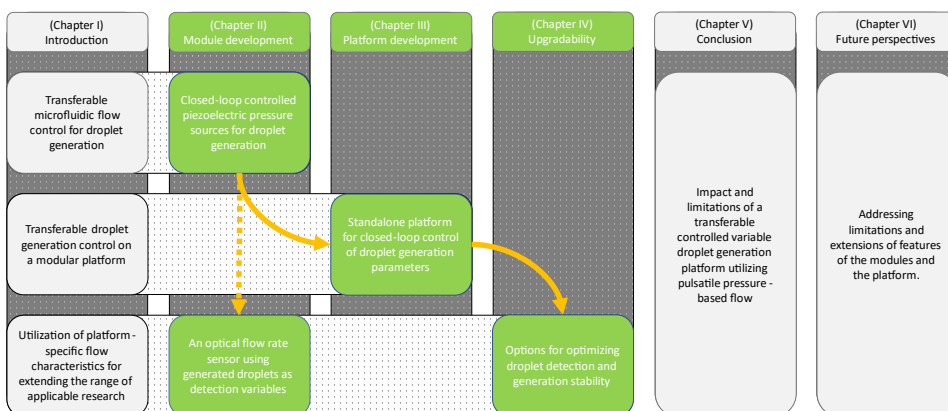


Figure 4. Illustrative thesis layout showing how the supporting publications tie back to the challenges and research questions, and how they connect to each other in this thesis.

Table 2. Overview of alignment of chapters, research questions and contributions in the thesis.

Chapter	Topic	Research question	Contribution
I	Introduction: topicality, appeal, motivation, aims, contributions, approach etc.	-	-
II	Module development: microfluidic flow control	RQ1	I, II
III	Platform development: droplet generation control	RQ2, RQ3	III
IV	Upgradability: pulsatile flow utilization, droplet generation control improvements	RQ4	IV
V	Conclusion: thesis summary, resolutions to research questions	-	-
VI	Future perspectives: limitations, possible solutions, research interests	-	-

- Chapter I – Introduction

- The introduction into the thesis is split into six sub-sections (topicality, appeal, motivation, aims, contributions, approach) used to help the reader see the link between the prominent phrasings (such as microfluidic, droplet, droplet generation, automation, responsiveness, etc.) most often mentioned in the thesis. And be able to build a perspective and an expectation of the outcomes.

Body chapters II, III and IV start with a brief introduction into a chapter-specific context and conclude with a chapter overview with observations of open challenges.

- Chapter II – Module development

- The first body chapter starts with the design description and methodology of a transferable, standalone droplet generation device which is aimed to become the flow regulation module on an automated droplet generation platform.

2 Transferable Flow Regulation for Water-in-Oil Droplet Generation

This chapter presents a highly responsive, portable, and affordable microfluidic pumping device specifically aimed at droplet generation. The named characteristics are acquired to use the described device as part of a transferable automated droplet generation platform. Implying both portability and flexibility, transferability of the developed device is required for streamlining its implementation as a module, enabling transferability for the following stages, and having sufficient control and operability with variations in fluidic inputs and outputs.

The chapter summarizes the evaluation of the performance and transferability of the developed flow regulation device as a response to **RQ1**, relying on the following publications:

Appendix 1: R. Jõemaa, M. Grosberg, T. Rang, T. Pardy, “Low-cost, portable dual-channel pressure pump for droplet microfluidics,” 2022 45th Jubilee International Convention on Information Communication and Electronic Technology (MIPRO), IEEE, 2022.

Appendix 2: N. Prabatama, R. Jõemaa, K. Hegedus, T. Pardy, “Low-cost open-source flow velocity sensor for droplet generators,” 2022 18th Biennial Baltic Electronic Conference (BEC), IEEE, 2022.

Other related publications: M. Grosberg, R. Jõemaa, T. Rang, T. Pardy, “Wireless microfluidic dual-channel pressure pump,” patent application. Priority number P202200009, Estonia, 2022.

2.1 Background

As microfluidic droplets are relatively fragile in non-microfluidic environments; to reduce the risks involved in their transportation between labs, a portable droplet generator design can be considered as mitigation. Such a generator can be furthered in transferability by keeping its design compact, affordable and its parts easily replaceable. To achieve a coefficient of variability (CV) of generated droplets below 5%, additional attention ought to be placed on flow regulation.

Microfluidic flow regulation leans on two primary tasks: flow actuation and sensing. In microfluidic droplet generation, external vibrations, in-line flow disruptors, and fouling of the fluidics can decrease the monodispersity of the generated droplets. Sensing the flow either by flow rate or by pressure can help to mitigate the effect of undesired flow behavior through feedback, prompting an appropriate compensative response from the pumps. Such mitigation favors responsiveness from both the sensors and pumps. Most commonly used microfluidic pumps, such as syringe pumps, peristaltic pumps, and compressed-air systems [78], differ in responsiveness due to their operation mechanism. Each pumping mechanism carries a nuanced flow characteristic [79]. Positive pressure flow characteristics are categorized as either pulsatile or continuous [79] (**Fig. 5**), often depending on relative comparison.

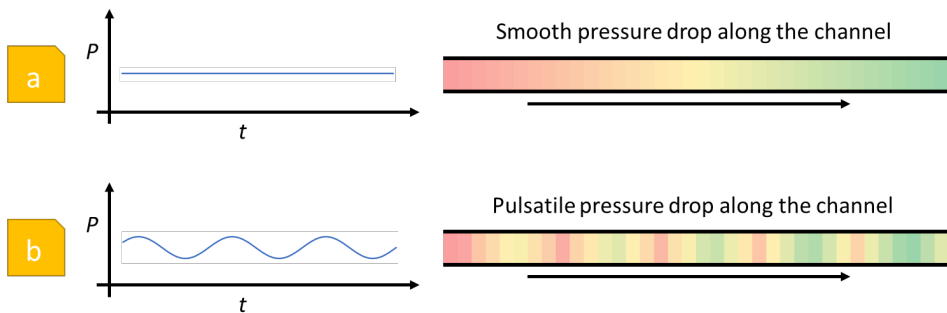


Figure 5. Illustrative distinction between continuous (a) and pulsatile (b) flow characteristics as pressure over time and as a gradient through a microfluidic channel.

Among the popular pumping methods, the valve-regulated compressed-air systems and syringe pump are considered stable when compared to a peristaltic pump. However, compared to valve-regulated pressure tanks, even syringe pumps are considered pulsatile [78]. Syringe pumps coupled with motorized actuators are widely used for their calibration-dependent flow-rate feedback and simplicity in connecting to a microfluidic circuit [7], [78]. Peristaltic pumps, preferred in microfluidic cell culturing for their ability to operate in a closed fluidic circuit, are advantageous for tasks like dialysis [80] and cell culture perfusion [79], [81]. Valve-regulated compressed-air systems offer the best performance in flow regulation from their inherent source stability [60] but are costly [82], [83] and together with the pressure tank also less portable. For a portable, compact microfluidic device, the aforementioned pumps are in a disadvantageous position compared to micropumps [7], [84]. Specific micropumps which use inverse piezoelectric effect for actuation, have the required design focus [85]. However, due to their diaphragm-based mechanism, their flow characteristic is pulsatile.

Where uniformity of produced droplets is of high priority, the choice of a pumping method with pulsatile characteristics, particularly a diaphragm type micropump, is unconventional. However, there are several examples to demonstrate piezoelectric pumps to be sufficiently stable for the monodisperse droplet generation [86]–[88]. The inherent responsiveness of a piezoelectric element [89] makes them highly favorable in flow control where relevant timescales range from several milliseconds down to microseconds (droplet formation time). Unlike valve-regulated compressed air, which offers stability and arguably enough responsiveness, but falling short in terms of cost and size, a piezoelectric solution can provide the needed balance between performance and accessibility.

Pulsatile flow have their place in biomimetic microfluidics [90], [91] but due to the increased flow complexity are generally avoided in two-phase fluidics where an interface between different media is forced at the cross-junction. However, what makes the pulsatile flow generated with piezoelectric micropumps more manageable is their low pumping volume, and the directly proportional relationship between the actuation voltage across the piezo element and the following physical motion [92]. Despite the inherent complications, using pulsatile flow has been shown to be feasible and even taken advantage of in droplet formation [56], [61], [93].

2.2 Design Considerations

2.2.1 Fluidics

To facilitate a highly controllable, high-throughput droplet generation [24], [27], a microfluidic polydimethylsiloxane (PDMS)-glass chip with a flow-focusing geometry was used (**Fig. 6**). Channels formed of PDMS can be advantageous for its low fabrication price, low curing temperature, optical transparency, and biocompatibility [15], [24]. In principle, a flow-focusing device (FFD) uses a passive fluidic pinching point where at a specific flow rate the “continuous” oil flow will pinch and disperse the water flow into droplets with a consequential interval as the shearing force overcomes the interfacial tension [16]. Obtained droplet size is determined primarily by shear stress (viscosity), channel characteristic size and flow rates [11], [16], [22], [24], [39].

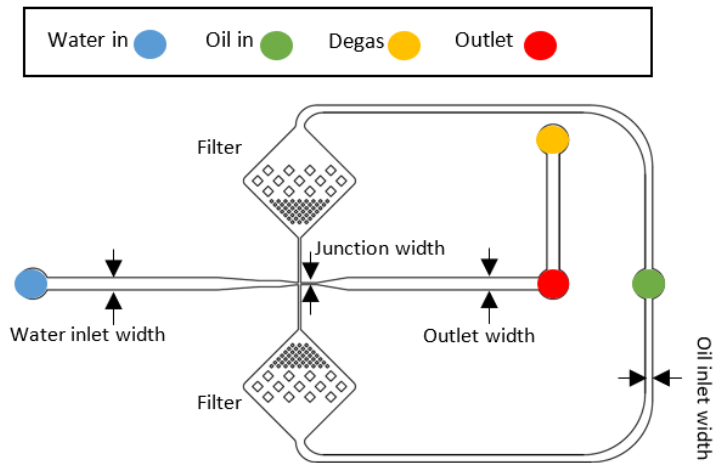


Figure 6. Flow-focusing device channel design used for droplet generation. Junction dimensions are $125 \mu\text{m} \times 100 \mu\text{m}$ (width \times height), **Appendix 3** [94].

In this chapter, the droplets were generated from deionized water (DIW); separated using mineral oil (MO) mixed with Span[®] 80 surfactant (widely used; adds comparability) with a mixing ratio of 2% w/w. Actuators and sensors were fluidically connected to the chip through 0.5 mm internal diameter (ID) Polytetrafluoroethylene (PTFE, Teflon[®]) tubing.

2.2.2 Actuators

Considering the requirement for the device components to be commercially available, numerous producers of microfluidic devices such as Bartels [95], Takasago [96], NITTO KOHKI [97], and TTP Ventus (acquired by The Lee Company in 2022 [98]) [99] were found to offer a range of piezoelectric micropumps. Most of the available micropumps, priced at around 100 EUR consist of a single-diaphragm actuator. To determine the direction of the flow through a diaphragm pump, the pumps incorporate check valves [100]. Piezo-electric micropumps are known to diverge into single (SCP) and multi chamber pumps (MCP) [85]. With a comparatively small, low-cost design, Bartels Mikrotechnik offers a multi chamber series pump (MCSP) allowing for higher backflow pressure at smaller size (**Fig. 7**). Moreover, the smaller diameter piezoelectric discs and pumping chambers in Bartels' design translate into reduced pulsation amplitudes in pressure generation.

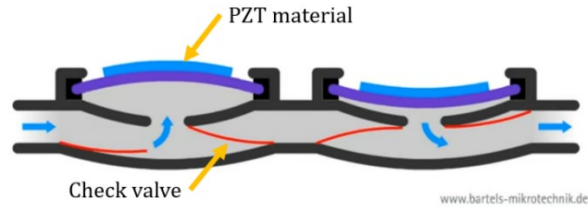


Figure 7. Flow generation diagram in a Bartels' dual diaphragm micropump design. Reproduced from [101].

In a piezoelectric micropump, applying a changing voltage difference across the opposing faces of a thin disc of piezoelectric material, acting as the diaphragm, deforms and alternates the deformation direction of the disc [100]. Depending on the direction of disc deformation, an increase or decrease in pressure can be generated in the diaphragm housing. In Bartels' design, two series diaphragms are operated in antiphase with alternating signals in the audible frequency range, enabling to produce an output pressure of up to 50 kPa. With the antiphase operation of the two diaphragms, a rocking effect is inadvertently caused across the pump. Such vibrational forces lost to the pump's exterior can diminish the output pressure and its stability, which in droplet generation can reduce the droplet uniformity. Hence, the pumps ought to be fixed in place with contact surfaces ideally padded with sound dampening material like foam or rubber.

The Bartels piezoelectric pumps require high voltages to operate at their maximum capability, up to several hundred volts, alternating with a repetitive waveform pattern – for which a specialized electronic circuit is required. As manufacturers of piezoelectric micropumps often patent their pump designs [102]–[104], unique driving methods become implied. Because of this, manufacturers tend to develop their own dedicated drivers. Typically, these drivers come minimally equipped with frequency and amplitude control capabilities, allowing users to access the full output pressure range of their pumps. Some drivers also provide limited control over the waveform shape among options like sinusoidal, trapezoidal, and square wave. It is common for the waveforms to be generated digitally, formed of voltage steps following an equation or a precalculated lookup table stored in memory. In this work, digital mp-Highdrivers from Bartels were selected to accompany the mp6-liq micropumps from Bartels. These drivers can operate at frequencies ranging from 50 – 800 Hz and amplitudes from 10 – 250 V (0 V when turned OFF). The frequency step resolution varies with the frequency range, and the operational amplitude is divided into 32 levels with a size of about 8 V at the expected capacitive load of the mp6-liq piezoelectric element.

2.2.3 Sensors

For a two-phase microfluidic process, two separate liquid flows need to be monitored. This sets the minimum requirement of pressure sensors at two. A third pressure sensor was introduced to decouple the pressure control response from any fluctuations and accumulating deviations at the end of the setup's output (e.g., when the output tube, settled at the bottom of the droplet collector container, sees a rising output pressure due to an increasing column of liquid on top of it). A three-sensor configuration allows for the droplets to continue flowing into other mechanisms such as active sorting, mixing or multi-layered encapsulation which is the main to limiter of open-loop droplet generation.

To measure pressure quickly and accurately, we can use resistive or capacitive pressure sensors. Commercial electronic pressure sensors are nowadays primarily piezoresistive and designed with a digital output – meaning that the pressure sensor, after detecting and measuring the voltage produced by a pressure acting on a piezoelectric diaphragm, will use an integrated A/D converter (ADC) to convert it further into a binary message. For a proof-of-concept design, the choice of the pressure sensor is made based on price-to-feature performance and its compatibility with different liquid media. For the functionality and evaluation tests, low-cost pressure sensors with food-grade silicone coating were used (further detailed in **Table 3**).

Table 3. Revision 1, droplet generation device, pressure sensor specifications.

Component name	MPRLF0006KG0000SC	Output resolution	14-24 bits
Sensor type	Gage	Typical polling frequency	~204 Hz
Pressure range	0 - 6 kPa (max. -2 - 8 kPa)	Typical power usage	10 mW
Communication protocol	SPI	Liquid compatibility	+
Unit Price (Q1 2024)	14.10 € (VAT excl., Mouser)	C° compensated	+

To optimize the sensor communication for responsiveness, the least significant byte was discarded, leaving 16-bits of data to work with. This was permitted on the basis that the ever-present ripple produced by the piezoelectric pumping (typ. $\gg 0.1$ Pa) was significantly greater than the sacrificed finer decimals of the measurement (< 0.1 Pa). As there were three pressure points of interest, this optimization allowed to poll and process the data from all three sensors after every ~ 5.3 ms (~ 189 Hz). Aside from detecting the pump’s flow characteristics and possible artifacts introduced by the droplet formation process, the sensor responsiveness was important for updating the pressure level produced by the pumps. Moreover, the pressure data can be a valuable indicator for the device’s evaluation.

2.2.4 Controller

For data extraction/interpretation from the pressure sensors and controlling the pumps through their drivers by using the pressure data as feedback, a microcontroller development board ESP32 DevKitC-32U was used. Additionally, this development board provided options for all necessary communication protocols (SPI, I2C, serial, Wi-Fi). The ESP32 was used to communicate with the sensors using SPI, with the pump drivers using I2C and with the user via USB or Wi-Fi. The advantage of the ESP32 DevKitC over other low-cost, low-power microcontroller boards is its two independent processing cores with a relatively high clock rate of 240 MHz. A dual-core processor enables one core to focus solely on handling the hardware behavior and leaves the other available to focus on responding to user controls. In this way, one does not interrupt the other, which is critical in ensuring stable droplet generation.

In combination with the chosen pumps, chip geometry, liquids, sensors, and their positions, the full fluidic setup can be illustrated (**Fig. 8**).

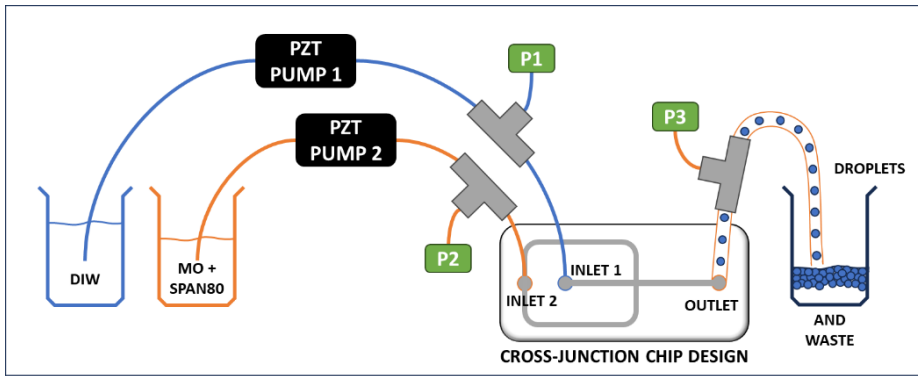


Figure 8. Illustration of the droplet generation setup – including three inline pressure sensors (P1, P2, P3), an FFD, DIW as the disperse phase, MO with Span® 80 as the continuous phase, droplet/waste collector, and two inline PZT pumps.

To control the pumps for oil and water flows, pressure feedback was measured from three points (Fig. 8 – P1, P2, P3), with pressure differences calculated cyclically on the first core of the ESP32 for either pump. To control the oil pump, a corresponding pressure difference was calculated from the FFD’s outlet pressure (Fig. 8 – P3) being subtracted from the pressure measured between the oil pump and the FFD’s oil inlet (Fig. 8 – P2). Analogously for the water pump, the outlet pressure (Fig. 8 – P3) was subtracted from the pressure between the water pump and the FFD’s water inlet (Fig. 8 – P1). These continually updated differential pressures were used as inputs for calculating the errors from the individual pressure setpoints specified for the water and oil Proportional-Integral-Derivative (PID) control loops. Using a PID algorithm meant that the respective coefficients (K-values: Kp, Ki, Kd) and an update cycle duration also needed to be found. To acquire the cycle duration, a cyclically resetting timer was added into the code managing the pressure data acquisition and pump control. This provided a dynamic cycle duration for every PID calculation. For PID coefficients, the K-values were explored heuristically. However, to not be left with an excessively sensitive pump control, one more coefficient was necessary for the PID error calculation. Namely, the binary sensing data read by the ESP32 was translated into pressure units (Pascals), yet the generation of pressure was controlled through voltage, applied over the piezoelectric actuators. Hence, the measured pressure needed to also be mapped into voltage. From the datasheet of Bartels micropumps, the relationship between the pumped pressure and the change in amplitude of the driving waveform showed a predominantly linear, positive correlation. Followingly, the maximum output pressure of the pump was measured with a pressure sensor in a blocked fluidic circuit. By blocking off the flow, the pressure at the sensor was allowed to build up as high as the pump could produce. The pressure-to-voltage coefficient could then be found by dividing the used voltage by the measured pressure. This process was performed separately for oil and water due to the pump’s performance being linked to the pumped media [95].

2.2.5 Device Exterior and Fluidic Joints

Using a 3D filament printer, Original Prusa i3 MK3, housings for the controller, pumps, and sensors were printed from Polylactic Acid (PLA) [105]. Using a 3D resin printer, Anycubic Mono X, microfluidic T-junctions were printed from Anycubic Standard clear resin [106].

2.2.6 User Interface

To operate the droplet generation device at a component level without a complex physical interface, using wireless communication enabled by the ESP32 DevKitC, a graphical user interface (GUI), loaded onto the ESP32, was transferred to a connecting computer. Using ESPAsyncWebServer library [107], an ESP32 could be made to operate as a local server, to which a nearby smart phone or laptop could directly connect to via Wi-Fi. The GUI could then be loaded using a web browser by connecting to a set IP address.

The GUI was designed to allow numeric access to variables such as PID K-values, target pressure levels for each pump, operation timer, sensor polling loop delay and lastly the mp-Highdriver settings, including driving waveform amplitude, frequency, and shape.

2.2.7 Design Overview and Connections

Inter-component links inside the device and with the user can be seen on Fig. 9. The design choice summary is explained in Table 4.

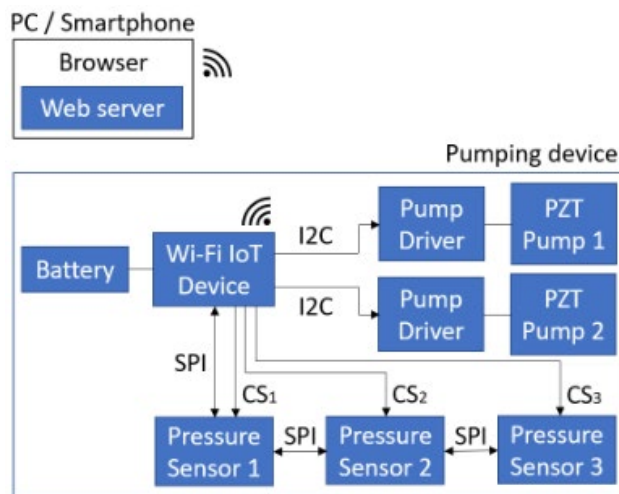


Figure 9. Block diagram of the device components and communication methods, **Appendix 1** [108].

Table 4. Dual-channel, portable pressure pump design criteria.

Category	Field-specific needs (based on section 2.1-2.2)	Explanation
Nr. of pumps	2	To control both oil and water independently.
Pump type	Piezoelectric; water and oil compatible	Compact, low-power, highly responsive.
Nr. of sensors	3	To monitor both pumping pressures involved in droplet generation.
Sensor type	Pressure; non-reactive, liquid compatible coating	Easier to correlate to pressure-based pumping.

Table 4 continued on the next page

Table 4 continued from previous page

Category	Field-specific needs (based on section 2.1-2.2)	Explanation
Closed-loop feedback	Yes	For translating pumping pressure target to voltage. For flow stabilization.
Control type	PID	Fast and lightweight
Commercial availability of components	All	To ensure design transferability.
Target CV%	< 5%	[4], [15], [22], [34], [71], [75]
Portable	Yes	[109]
Wireless communication	Yes	[110]
Battery life	> 10 h	[111]
Cost ⁸	< 500 €	[109]–[112]

2.3 Performance Evaluation

The following section presents the methodology leading to and the outcomes gained from publication I, focusing on the performance of aspects such as battery-powered operation, pumping with PZT micropumps, droplet generation with pulsatile flows and feedback control in a setup example on **Fig. 10.a**.

2.3.1 Methodology

Following aspects were tested for the evaluation of this proof-of-concept droplet generation device (ambient temperature was measured at 25 °C for all tests):

- I. Duration of operations on battery support at nominal power use.
 In consideration of portability, for battery selection, the nominal device power consumption was calculated using documented nominal rates for its active components.
 As for defining conditions for the nominal power use, both pumps were set to operate with a switching frequency of 100 Hz with the maximum peak-to-peak pumping voltage of 250 V_{pp}. Both pumps were connected in separate closed-loop flow paths, to continuously circulate DIW. To monitor proper device operation, the device controller was connected to a laptop over Wi-Fi, with cyclic updates of pressure sensor data at a rate of 1 Hz.
- II. Observations of the impact on the pumping pressure caused by pump's operation frequency.
 With pulsatile characteristics expected from reciprocating diaphragm micropumps, an open-ended flow path with two in-series pressure sensors was connected after one of the PZT micropumps. The flow path included three parts of 0.5 mm ID PTFE tubing, each with a length of 200 mm, separated with a T-junction for every sensor.

⁸ Cost of the pumping device, limited to cover the cost of structural materials and low volume prices of COTS electronic and mechanical components.

The pump was operated with a sinusoidal waveform with an amplitude of $\sim 111 V_{PP}$ ($250/255 * 113$) to hold the pressure within the sensor's compensated pressure range of 0 - 6 kPa. Pumped pressure data was collected over 1 minute at each frequency (50 Hz, 100 Hz, 200 Hz and 400 Hz) and compared after a stabilization period of 40 seconds.

III. Testing droplet generation feasibility without pressure feedback control.

A fixed pumping frequency of 200 Hz and 50 Hz for water and oil respectively together with driving voltages set to 100 V_{PP} and 90 V_{PP} for water and oil respectively, were used to generate droplets in a setup illustrated in **Fig. 9**.

The FFD was positioned between a high-speed camera (acA640-750uc, Basler) and a brightfield LED to record images of generated droplets while still flowing inside the FFD. A 20x microscope lens was connected to the camera to limit the area of interest. Using ImageJ software and the known channel width of 125 μm as a reference point, the recorded area of 640 by 480 pixels was estimated to cover 1250.0 by 937.5 μm of the microfluidic chip. After stabilization of about a minute after droplets began forming, a series of images were captured from the flow-focusing junction at 750 frames per second (FPS) over 100 ms. Obtained frames were used to estimate the droplet generation rate by counting frames from the formation of one droplet to the formation of another.

To get the first overview of the uniformity of the generated droplets, the camera was moved to capture the 625 μm wide portion of the outlet channel to record as many droplets per frame as possible from inside the chip. This was deemed necessary as the used surfactant and its amount in the oil did not prevent the droplets from merging when exiting the FFD. Followingly, a 25 second video was recorded of generated droplets. From the video, frames were extracted at various timestamps. The frames taken were separated with enough time in-between to prevent taking frames containing the same droplets. The extracted frames were analyzed using ImageJ. Droplets could be separated, and their cross-sectional areas measured by pixel translation to physical dimensions (tied to the known channel dimensions on the images) and counting.

IV. Gauging flow regulation responsiveness heuristically with an unoptimized PID control.

In the device firmware, the PID was enabled for both pumps with matching conservative K-values for oil and water of 0.5, 0 and 0.1 for K_p , K_i and K_d , respectively. The pumping device was connected to a laptop through a USB connection to log the pressure data and to eliminate any possible effects the Wi-Fi routine could have on the expected feedback loop durations and noise from the wireless communication could have on the sensors. During USB connection, the battery was disconnected and the power for device operation was received from the laptop. Reliable pressure data collection was necessary to compare the effects of differing rates of responsiveness (minimum achieved ~ 5.3 ms; +5 ms; +50 ms) have on the pressure stabilization in two-phase microfluidics. For the artificially slowed responsiveness (+5 ms; +50 ms) each with 3 repetitions, the time taken to reach stable pressure levels was measured. For these tests, the pressure targets were set to 4.30 kPa for water and 5.95 kPa for oil. To keep both the stabilized and the initial overshoot pressure levels within

the compensated sensing range, for nominal feedback delay of ~5.3 ms, water and oil pressure targets were set at 3.80 kPa and 4.80 kPa, respectively.

2.3.2 Results

For the tested points, following results were obtained:

I. Duration of operations on battery support at nominal power use.

With an estimated continuous power requirement of 1.33 W, a 14.8 Wh Li-Po battery (LP805080, Cellevia Batteries) was used to reach the specified battery duration. The device became inoperable after ~11 hours of nominal continuous use when the wireless connection with the laptop and the pumping stopped.

II. Observations of the impact on the pumping pressure caused by pump's operation frequency.

The tests showed relatively slow periodic pulsations with varying rates between 1 to 20 Hz (**Fig. 10.b**). From the in-series dual-diaphragm design of the micropump, pumping frequency transfer to the pump's exterior and translation into a slower resonant rocking motion was hypothesized to be propagating along the tubes. As there were two points at which pressure was monitored, the up- and downstream pressures were following the expected pressure drop, leaving all downstream pressure values below their upstream counterparts. However, the average pressure levels compared among pumping frequencies came with unexpected deviations – as the maximum pressure level was obtained with pumping water with 200 Hz driving frequency (**Fig. 10.b**), the pressure levels were expected to drop as the frequency became more distant from it; however, 50 Hz driving signal produced a slightly larger pressure than the 100 Hz driving signal (**Fig. 10.b**).

From analogous tests with mineral oil, the pressure level generated decreased with the increase in pumping frequency. As for following evaluation tests, the water pumping frequency was set to 200 Hz, oil pumping frequency was left at 50 Hz – the minimum frequency available for the mp-Highdriver.

III. Testing droplet generation feasibility without pressure feedback control.

With the fixed driver settings, pressures of 5.82 kPa and 6.87 kPa were produced across the FFD for water and oil, respectively. Empty water droplets, measured with average cross-sections of $28\,517\ \mu\text{m}^2$ (**Fig. 10.c**) were generated into mineral oil at an estimated continuous rate of ~30 Hz. From a prolonged droplet generation video, a randomized sampling of 85 unique droplets yielded a coefficient of variation (CV) of less than 2%, including outliers deviating from average by -4.58% to +4.74%.

IV. Gauging flow regulation responsiveness heuristically with an unoptimized PID control.

With a +50 ms added feedback delay, the PID controller managed to stabilize the pressure levels at 4.07 kPa and 5.74 kPa for water and oil respectively, after ~25 seconds. In contrast, the pressures stabilized within ~8 seconds when the total feedback delay was reduced to ~10.3 ms. At nominal feedback delay of ~5.3 ms, the pressure levels stabilized at 3.86 kPa and 4.61 kPa for water and oil

respectively, in ~ 7 seconds (**Fig. 10.d**). Considering the decrease in targeted pressure levels, the gain in responsiveness was marginal.

With an increasing pressure sampling rate, the pump control noise started to emerge (**Fig. 10.e**). This was attributed to the pump's driving signal's amplitude step size of $\sim 7.5V$ – trying to stabilize at a pressure level optimally generated with amplitudes between limited available steps.

The repeated stabilization of pressure levels at a distance from the setpoints was attributed to the PID controller not utilizing the accumulation of such deviations by having had the K_i value as zero.

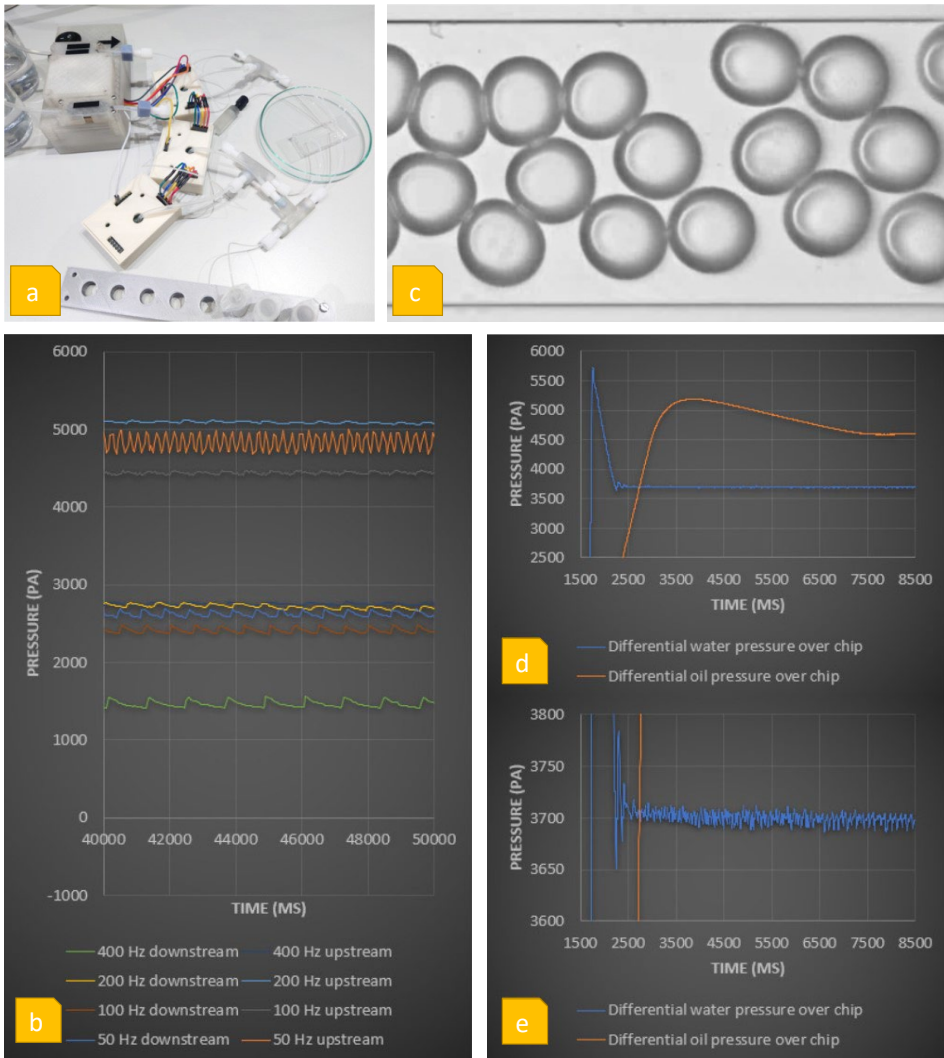


Figure 10. a) Piezoelectrically regulated microfluidic droplet generation setup, connected to an FFD; b) Graphed water pressure readings during pump operation characterization at varying pumping frequencies; c) Sample image from a high-speed camera of water droplets flowing in mineral oil in a $625 \mu\text{m}$ wide channel. d) Graphed oil and water pressure readings of feedback-controlled pressure stabilization; e) Closeup of water pressure readings from nominal feedback control delay of ~ 5.3 ms, **Appendix 1** [108].

2.4 Case study of Transferability

The following section focuses on the inputs and outcomes of the transfer and flexibility of the piezoelectric droplet generation device.

2.4.1 Context

To demonstrate transferability, the device designs and firmware were given to a student unfamiliar with the device. The student's work was aimed at developing an open-source flow velocity (mm/s) sensor for microfluidics which contained a flow of intermittent media such as droplets or bubbles distinguishable through differences in spectral absorption.

The sensor was non-invasive and could be positioned around a translucent tubing at any point with an OD smaller than 3.6 mm. With a known tubing cross-sectional area, from flow velocity, flow rate could be calculated. To devise a setup to benchmark the developed flow velocity sensor, the portable pumping device played the role of generating a segmented flow of water and air (Fig. 11).

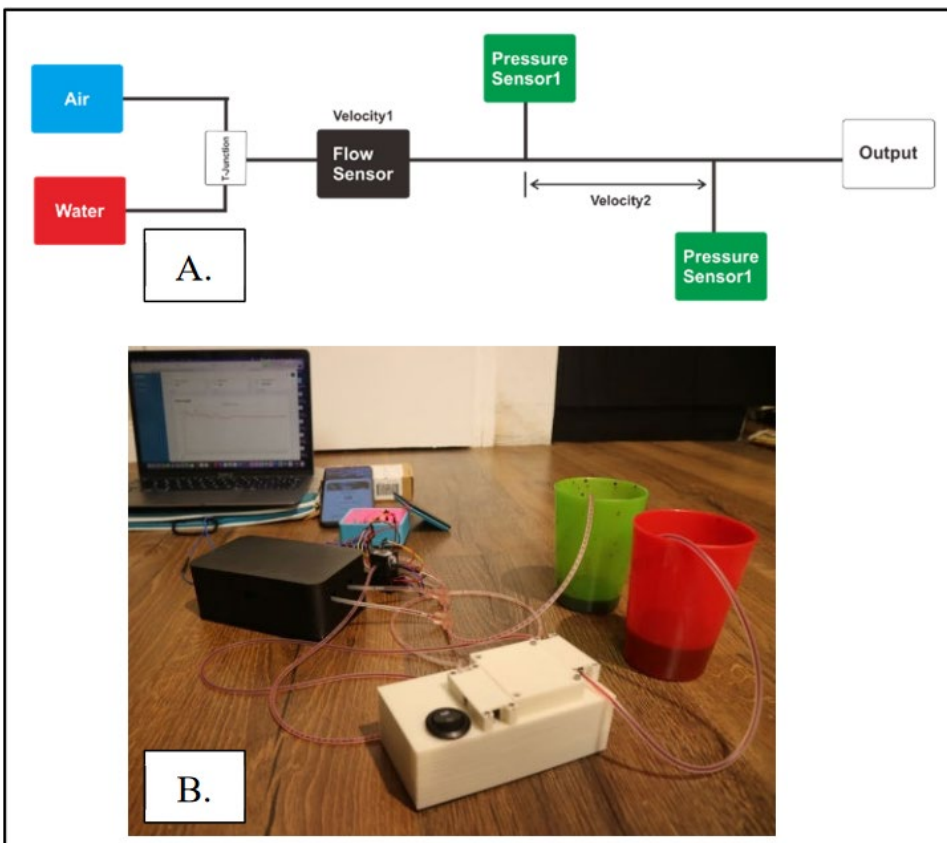


Figure 11. Flow velocity sensor benchmarking setup using the dual-channel droplet generator to pump air and colored water into a 3D printed T-junction to produce a segmented flow of air and water, distinguishable by the developed flow velocity sensor, **Appendix 2** [113].

The developed sensor type was optical, an amalgamation of previously reported methods (**Appendix 2**), using two phototransistor (spectral range above 90% relative sensitivity: 820 – 950 nm, 860 nm peak, SFH309, OSRAM) and infrared (IR) emitter (890 nm, OP298A, TT Electronics) pairs placed perpendicularly to the observed translucent food-grade silicone tubing (1 mm ID, 3 mm OD) and to each other, spaced 3 mm apart along the tube. To measure flow velocity from a segmented air-water flow, the length of both the droplet and the bubble could not be as small as to fit multiple of each between the 3 mm sensor gap as it would cause the two optical detection points to decouple. For this reason, the segmentation could be simplified for the testing phase, using a 3D printed T-junction to join the water and air flows together.

For benchmarking the developed optical sensor, consultation was provided for the student to utilize fast commercial calibrated pressure sensors to mathematically calculate the flow velocity over a known tubing volume (**Fig. 11. A**).

The student developed their own interface for the sensor and the portable pumping device and joined their communication over Wi-Fi, making the pump controller an integral part of the setup. The pumps were operated in open-loop control without the designed pressure sensors, controlled only by commands directly affecting the pump drivers. The commands covered the driving waveform shape, frequency, and voltage.

2.4.2 Results

With comparable flow velocity measurements obtained from the developed sensor and an alternative measurement method using commercial, calibrated pressure sensors, the pumping device was deemed sufficient for the experiment as seen from the graphed results in **Fig. 7 of Appendix 2** [113].

To drive the mp6-liq (Bartels) piezoelectric pump to generate pressure for air input, the effective driving frequencies needed to reach closer to 400 Hz and above. With the mp-Highdriver (Bartels) pump driver, enabling driving waveform frequencies up to 800 Hz, the necessary pumping capability was available, demonstrating the suitability of the pumping device for applications utilizing both gaseous and liquid phases.

The inclusion of Paper II in this thesis serves to support the flexibility of the pumping device for different experimental setups. Successful design adaptation underscores the primary prerequisite for the envisioned automated droplet generation platform.

2.5 Chapter Summary

2.5.1 Discussion

In this chapter, the design criteria and the methodology of component selection were laid out for the construction of a portable, comparatively affordable, and highly responsive droplet generation device. The pumping device included a closed-loop PID pressure controller, enabling uniform droplet generation in pulsating flow conditions.

The device was evaluated feasible for stable droplet generation with preliminary monodispersity measurements at less than 2% CV. Additionally, the device shows sufficient responsiveness for automation with two-phased flow stabilization speeds reaching below 10 s. Moreover, with the ability to function through both battery-powered wireless connection and direct USB connection, the device design is flexible enough for use as a module on a larger system. Lastly, the affordable, simple design and wide availability of its components proved successful for the device transferability to a different lab and application.

2.5.2 Device Specifications

Table 5. Standalone, transferable pumping device specifications.

Category	Value
Number of independent pumps	2
Pump description	Bartels, mp6-liq, PZT, dual diaphragm,
Number of pump drivers	2
Driver description	Bartels, mp-Highdriver, 10-250 V _{PP} , 50-800 Hz
PZT pumping frequency (water)	~200 Hz
PZT pumping frequency (oil)	~50 Hz (limited by driver)
Number of sensors	3
Sensor description	Honeywell, MPRLF0006KG0000SC, pressure-based, max. range (-2 kPa to 8 kPa)
Controller	ESP32 DevKitC-32U
Feedback rate	~189 Hz
Battery performance	>10 h @ Wi-Fi update rate of 1 Hz; pump operation settings: 100 Hz, 250 V _{PP}
Estimated max. power consumption	1.33 W
Device dimensions (excl. sensors)	120x60x30 mm
BOM Cost (Q1 2023)	~250 €

2.5.3 Considerations for the Next Stage

When transferring the designed pressure-based flow regulation device onto an automatable droplet generation platform, there are several aspects that need to be considered.

- I. The ESP32 DevKitC controller will not be able to manage droplet generation automation due to insufficient cores, memory, and I/Os. Thereby, with the assumption of another controller for the automated system, the pump controller does not benefit from the use of its Wi-Fi routine, as the proximity to the higher-level controller allows for direct USB connection. In which case, as the pumping device's main PCB was designed to be operational by both battery and USB connection, the device-specific battery can be excluded from the transfer. To operate this pumping device through an intermediary control module over USB, on top of increased communication reliability other benefits can be gained: with the Wi-Fi module on the ESP32 in sleep mode, power consumption is reduced; with Wi-Fi non-operational, the EMI is reduced; with reduced EMI the pressure sensors can be brought closer to the ESP32 – further compacting the pumping device.
- II. To utilize the full potential of the piezoelectric micropumps, the sensor's pressure range ought to be above but in proximity of the maximum pumping pressure (~50 kPa), to get the most resolution out of the sensor's integrated ADC. The 6 kPa rated pressure sensors are not sufficient to cover the full range of the pumping pressure available with Bartels micropumps.

- III. By testing the pumps inherent vibrational mode transfer into the flow at different liquid pumping frequencies. Higher pulsation amplitudes in the measured pressure feedback were considerably more prevalent in the denser water as opposed to the thinner, mineral oil, when tested separately. When tested together, it was observed that the oil absorbed some of the vibrations carried by water.
- IV. For a specific liquid density and viscosity there is an optimal pumping frequency for the piezo elements. This implies a possibility that the effect can apply for liquids altered by particles such as surfactants and particles to be encapsulated.
- V. The pumps are audible and considerably more-so when driven by a square-wave.
- VI. As droplets generated in mineral oil with 2% w/w Span 80 surfactant were observed to not preserve initial separation after exiting the FFD, another more stable type of oil and surfactant ought to be tested.

3 Transferable Droplet Generation Platform Design and Automation

This chapter proposes a modular design for a microfluidic droplet generation platform and a method to attain its process automation. For automation, the developed platform relies on the integration of highly responsive and robust, yet easily accessible and inexpensive actuation and sensing modules. In addition to organizing the platform design around a compact, portable form, the transferability of the developed platform is demonstrated and further evaluated through its operability with different input liquids, fluidic setup configurations, and a range of user-specified droplet generation parameters.

The chapter details the functionality and the integration process of the modules, and the overall performance of the automated droplet generation platform as a response to **RQ2** and **RQ3**, relying on the following publications:

Appendix 3: R. Jõemaa, N. Gyimah, K. Ashraf, K. Pärnamets, A. Zaft, O. Scheler, T. Rang, T. Pardy, “CogniFlow-Drop: Integrated modular system for automated generation of droplets in microfluidic applications,” *IEEE Access*, IEEE, 2023.

Other related publications: K. Pärnamets, K. Ashraf, N. Gyimah, R. Jõemaa, T. Pardy, “Integrated modular system for automated generation of droplets in microfluidic applications and method thereto,” patent application. Priority number P202300024, Estonia. 2023.

3.1 Chapter Overview

3.1.1 Background

For a droplet generation platform, automation comes in the form of being able to initiate, hold and recover consistent droplet generation against sudden or periodic disruptions, and gradual changes in the setup – i.e., sudden pressure shocks from downstream valves; periodic pressure waves from pulsatile flow generators; gradual degradation and fouling of the fluidics. Against the disruptions, automated stabilization enables generating uniform droplets over extended periods, adding to replicability and throughput. To automate and attain the subsequent benefits, knowledge of the following is implied:

- A target parametric point at which droplets ought to be produced, by their size and/or generation frequency.
- A model, representative of platform fluidics, which links flow parameters together with the resulting droplets.
- Latest droplet generation parameter(s) (droplet size; generation frequency) during the generation process.

In principle, when a desired stabilization point is given, the platform ought to know at least roughly, how to get there. Moreover, it needs a way to verify that it is indeed approaching the objective and how well it is doing so. If any distance remains from the stabilization point, the platform ought to know in which direction and to what degree to reconfigure its flow generators. To have an idea how to respond to dynamic changes in generation parameters, static properties of the platform can provide the initial reference through a model. By varying the inputs, the outputs change characteristically how the static fluidic properties act on the dynamic properties. This relationship can range from a simple best fit line equation obtained through empirical testing [114] to a set of neural

network weights obtained through training on recorded [115], [116] or simulated data [117]. While a pretrained neural network may not impose considerably more on the available computational resources on the platform, the training process itself becomes the bottleneck if anything changes in the static properties. Additionally, with the fouling of the fluidics inherent to microfluidic processes, unless there is a fouling model, active error correction can be realized by monitoring the droplet generation parameters. There are many active error correction methods to choose from, such as PID control, fuzzy logic control, a neural network with backpropagation and others. However, with the focus on transferability, the available computational resources are expectedly limited. Therefore, methods leaning towards simplicity and computation speed ought to be chosen.

When using an FFD for droplet generation, it ought to be taken into account that the range of stable generation points is not just limited by flow rate ratio, but also by the intercept angle between the continuous and disperse phases [118], [119]. Approaching the limits of the available stable droplet formation range, results in droplets with ever increasing parametric variance. The impact from variance to re-stabilization is worsened at higher throughput. As a solution, together with flow control, the feedback ought to be oriented towards responsiveness, to extend the range of experiments without needing to redesign the static components of the system. In consideration of the requirements of transferability, modularity, and responsiveness, an optical in-flow⁹ droplet detection and quantification method was used. An optical sensor allows it to keep a distance from the fluidics, preserving the option for using different microfluidic chips. For the sensor to 'understand' what can be classified as a droplet, it needs to distinguish between flow-phases. An optical method can do so either by detecting the differences between spectral absorption of the different liquid media, or by changes in captured light intensity, produced by refraction that occurs at the curved phase-transition interface surrounding the droplet. In state-of-the-art optical examples phase-differentiation characteristics are created either with an infrared (IR) laser [55], whose wavelengths are known to be absorbed well by water, or with a light emitting diode (LED) in the visible spectra [70], used to create droplet 'shadows' through refraction. To register these optical characteristics, the most prevalent detection options include a high-speed camera [70], a phototransistor [120] or a photodiode (PD) [55], [70], [121]. A complementary metal-oxide-semiconductor (CMOS) camera sensor consists of an array of photodiodes and is thereby in principle always less responsive than a single photodiode. Even so, the acquisition and polling speeds of a high-speed, compact CMOS camera can easily exceed the aimed droplet throughput. However, a significant temporal drag occurs during image processing, more so on a limited computational budget.

To be defined as a platform for droplet generation, the design needs to demonstrate performance parameters and features to be applicable for a wide range of droplet related applications. This implies flexibility, extended periods of continuous operability, and high degree of control over droplet generation parameters. With control over both the droplet size and generation rate, the platform allows for fast empirical characterization of the fluidics. A platform capable of self-characterization can improve the replicability and standardization that is prevalent in droplet generation.

A detailed overview of state-of-the-art platforms comparable to the one proposed in this chapter is shown in paper III (**Appendix 3**).

⁹ In this context, *in-flow* refers to droplets detected in the droplet generation stream, in proximity of the droplet formation point.

3.1.2 Design Criteria

With the context behind the available design choices in mind:

- The transferability of the platform can be improved by focusing on simple, widely available, and cost-effective hardware; by using a system-descriptive model that can be produced on the platform.
- Modularity of the platform can be maintained by choosing a droplet sensor type that can operate without making contact with the fluidics.
- Responsiveness of the platform can be ensured by using a droplet sensor which outputs a minimum number of variables per measurement; by using a feedback control method that balances simplicity, speed, and adaptiveness.

Table 6. Transferable, modular, droplet generation platform design criteria.

Category	Value	Additional details
Module: Flow regulation	Dual-channel, pressure-based pumping device (from Chapter 2).	Has built-in closed-loop pressure feedback. Uses pulsatile piezoelectric pumps. Controllable via USB.
Module: Microfluidics	Flow-focusing type chip, PDMS-glass 75x25 mm	In-house master mold available with different cross-junction channel widths and intercept angles.
Module: Droplet sensor	Optical, Brightfield LED-PD	An LED-PD droplet sensor, capable of detection rates $\gg 1$ kHz, was developed and rigorously tested by K. Pärnamets et al. [77].
Module: System controller	Raspberry Pi 4B	Popular, low-cost, high-performance multi-core single-board-computer (SBC) with Wi-Fi.
Closed-loop feedback	Yes	For translating droplet generation parameter targets (droplet size and generation rate) to pressure values for the flow regulation module. For droplet generation stabilization.
<i>Table 6 continued on the next page</i>		

<i>Table 6 continued from previous page</i>		
Category	Value	Additional details
Control parameters	Droplet size. Generation rate.	Droplet size control allows for monodisperse droplet generation. Droplet generation rate control allows for synchronization with the pulsatile flow generation.
System modelling method	Best fit line. Common regression models.	Fast and simple. Requires minimal computational resources for re-calibration.
Commercial availability of components	All	To ensure design transferability.
Target CV% (size)	< 5%	[4], [15], [22], [34], [71], [75]
Portable	Yes	See Table 1
Wireless communication	Yes	No examples exist for this particular application.
Cost ¹⁰	< 1000 €	See Table 1

3.2 Design Considerations

3.2.1 Layout and Fluidic Circuitry

As previously established, the flow circuitry required for droplet generation includes pumps, flow-descriptive sensors, a controller, and a microfluidic chip with a droplet generation specific channel geometry. By defining automation for droplet generation as a system capable of self-configuring its actuators to generate droplets at specified sizes with specific intervals, droplet generation parameters would need to be observed. An actuator module, capable of multiscale droplet generation, was put together in Chapter 2. A droplet sensing setup, focused on responsiveness and simplicity, was devised in parallel by K. Pärnamets et al. [77], which needs to be embedded onto the planned platform as a module. To coordinate the required modules a unifying control module is required. To structure the platform categorically, a first revision design (**Fig. 12**) included a droplet sensor column to primarily accommodate the brightfield LED-PD detector setup; an electronics column to accommodate both the flow controller and the system controller. The fluidics module, including the pressure pumps, the pressure sensors, the microfluidic chip, the connective T-junctions, and the tubing were spread over the platform for better accessibility for the pump controller and the droplet sensor. Due to the intrinsic vibrational nature of the micropumps, the pumps and the droplet sensor were placed with the greatest distance available on the platform. The proof-of-concept platform was assembled on top of a wooden baseplate for its rigidity and workability for modifications.

¹⁰ Cost of the platform, limited to cover the cost of structural materials and low volume prices of COTS electronic and mechanical components; bill of materials.

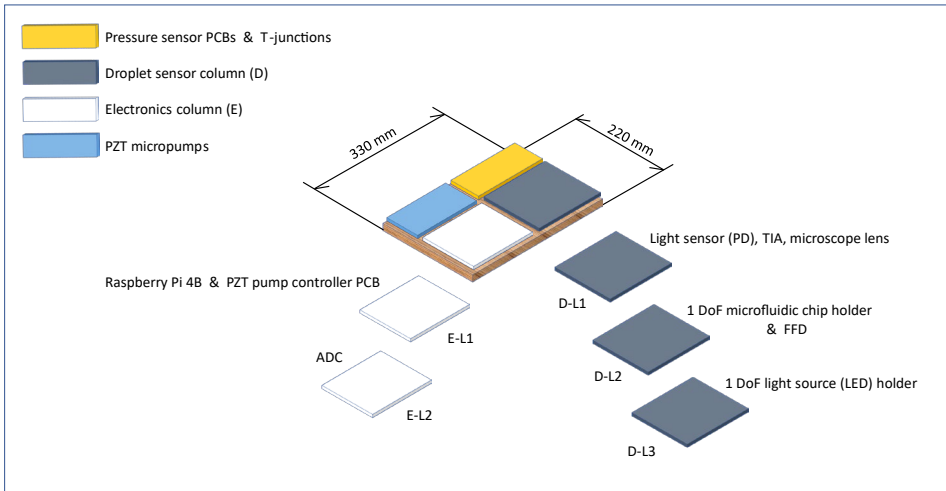


Figure 12. Revision 1 – placement of droplet generation modules on 330 x 220 mm base platform. (“Lx” – Layer x)

Preliminary testing on the first revision of the platform covered the functionality of its modules. Namely, the system controller was given commands to produce fixed oil and water pressures at levels known prior to producing droplets. The system controller would then need to transfer these commands to the pump controller. To verify the production of droplets the droplet sensor was connected to both an analog-digital-converter (ADC) (Fig. 12 E-L2) communicating with the system controller and an oscilloscope, to get an understanding of how a passing droplet would represent itself in voltage. In the aftermath, the first design revealed notable problems with both the droplet sensor and the pressure sensors. The pressure sensor placement on the platform required extending the power and communication wires, which with the added length started to accumulate more of the surrounding electromagnetic interference (EMI) and cause noticeable noise to be measured by an ADC inside the pressure sensor. The droplet sensor column, however, showed significant difficulty in the process which required the PD, the LED, and the microscopic cross-junction in the microfluidic chip all to be brought in alignment, for any change in voltage to be detected. However, even with a satisfactory alignment the PD signal reached slightly above the noise level. Whilst a poor signal-to-noise ratio (SNR) was largely attributable to the low signal intensity from the PD, the relatively high noise level was attributed to relying on power sent to both the pumps and the droplet sensor through the system controller which was bound to add its own EMI to the mix.

A second revision was devised, shown on Fig. 13. To address the SNR from the signal side of the droplet sensor, additional processing was added in front of the signal digitizing ADC (further detailed in Subsection 3.2.2.1). Addressing the noise side of the sensor, the electronics column was raised to fit two switch-mode power supplies (ECS45US05, XP Power) with a pair of 5V outputs on E-L1 (Fig. 13). Having two allowed powering the system and pump controller separately from the LED-PD sensor and the PD signal processing board. The power lines were joined over a single grounding wire between the system controller and the PD signal processing board, acting as a star connection to minimize ground noise transfer. Having a 5V output, the power supply units (PSU) could be simply replaced with widely available battery banks for further noise mitigation.

To address the noisy pressure sensor wiring, the pump controller and the sensor PCBs were modified to be able to join with board-to-board connectors. This enabled both to be positioned on E-L2 (**Fig. 13**) which contributed to the shortening of the fluidic circuitry (further detailed in Subsection 3.2.3.1).

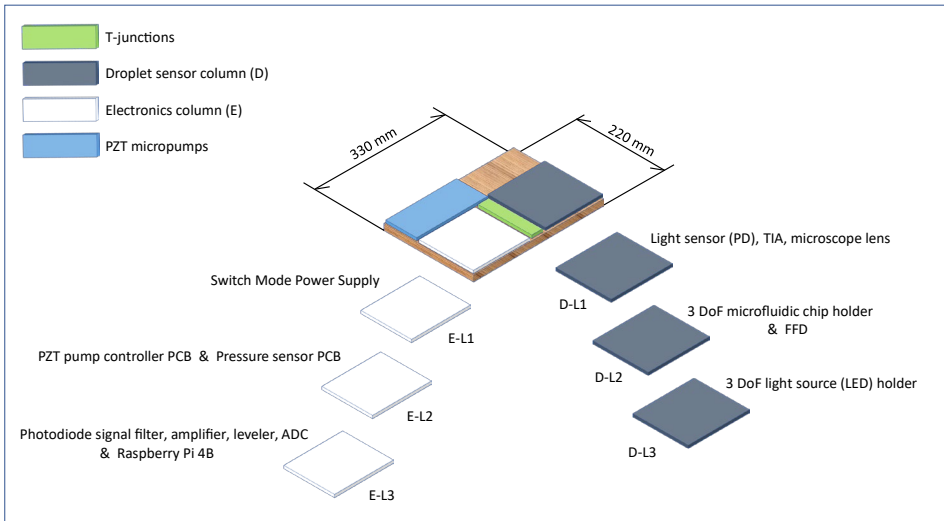


Figure 13. Revision 2 – placement of droplet generation modules on 330 x 220 mm base platform. (“Lx” – Layer x)

Lastly, a mechanical, mitigative, solution was found for the droplet detector alignment problem. The droplet sensor column was reworked to have its 2nd and 3rd layers tiltable with custom removable holders with 3 degrees of freedom (DoF; height, roll, pitch) for both the FFD and the LED PCB. While the cross-junction on the FFD still required most of the alignment with the fixed PD to be done by eye, the fine errors could now be corrected using the added dimensional freedom. Likewise, the directional light from the LED could more easily be directed at the cross-junction. From the work of K. Pärnamets [77] a thin metal plate with a micro-drilled pinhole was added between the FFD holder and the FFD. This both minimized the background noise around a passing droplet and redirected the LED light along its alignment instead.

The final design in CAD view can be seen on **Fig. 14**.

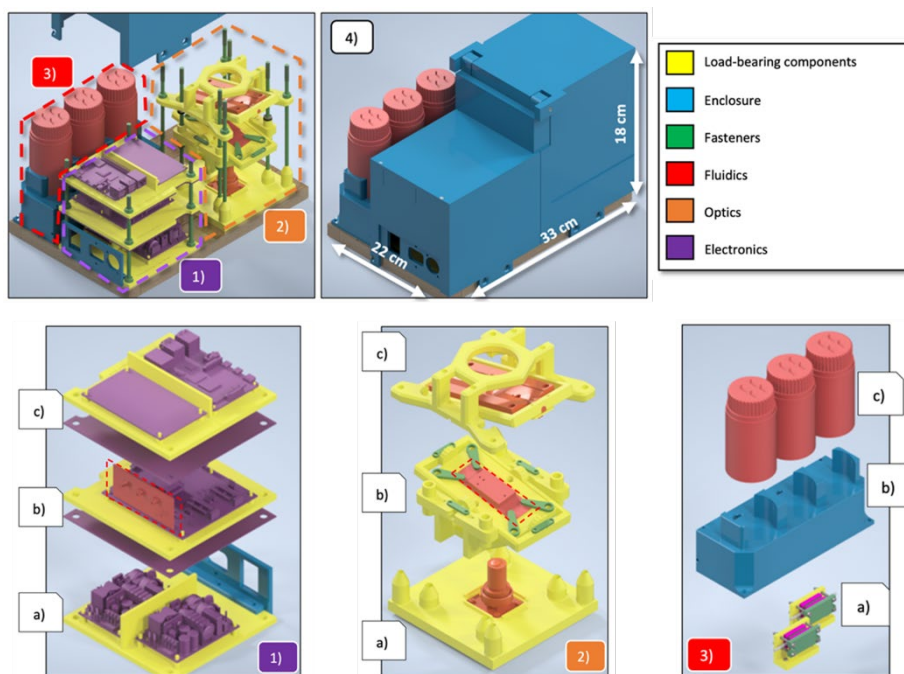


Figure 14. Revision 2 – platform CAD model. An exploded view of the setup, **Appendix 3** [94].

The fluidics of the platform ended up consisting of three regions, whose placement aimed to keep the lengths of the tubing and wiring to a minimum. The piezoelectric micropumps were separated from each other (3)a) on **Fig. 14**), mainly due to their intrinsic vibrational and switching noise which typically did not match in frequency. To reduce the transfer of their vibrational noise to other parts of the platform, they were attached to the baseplate via L-shaped 3D printed mounts. Additionally, the pumps were enclosed with a 3D-printed box (3)b) on **Fig. 14**), with its walls padded with vibration dampening rubber. The box had small holes for the incoming and outgoing tubing, and the wiring for the pumps. Additionally, the box preserved space on the baseplate, as three liquid containers (water, oil, waste) could be placed on top of it (3)c) on **Fig. 14**). The liquid containers were 100 ml GL-45 type glass lab bottles. The caps of these bottles were replaced with custom 3D-printed variants which had barbed ports designed for the attachment of silicone tubing. A ~12 cm length of silicone tubing was connected to the inside of the cap, leaving the loose end of the tube to lie at the bottom of the bottle. Another ~20 cm piece of tubing was attached to the outside of the cap, which for the case of water, headed into the pump enclosure box, attaching directly to the inlet of the piezoelectric pump dedicated for pumping water. From the outlet of the pump, another ~20 cm silicone tube headed back out of the box into the second fluidic region – the T-junctions (placement marked on **Fig. 13**). The T-junctions were clamped into a custom 3D-printed “wall” which directed one of its ports towards the pressure sensors in the electronics column (1)b) on **Fig. 14**). Out of 3 ports on the T-junction, 2 male barbed variants connected the pumps and the pressure sensors with silicone tubing, 1 female HPLC variant lead the flow through a Teflon™ tube to the third fluidic region – microfluidic chip (2)b) on **Fig. 14**). The microfluidic FFD was first clamped into the removable chip holder, aligning its region of interest (ROI) with the centers of the pinhole

and the holder. The holder was then placed into its mount in the droplet sensor column, where the tubes from T-junctions were connected to the inlets and outlet of the FFD, completing the fluidic circuitry.

The electronics column was made of three layers, the first of which housed the power supplies, powering everything on the platform (1)a on **Fig. 14**). The second layer housed the flow regulation module PCBs. The pressure sensor PCB was attachable to the pump controller PCB vertically, allowing its inlets to face the pressure sensors directly at the T-junctions, further reducing fluidic dead volume between them. The topmost layer in the electronics column housed the system controlling Raspberry Pi (RPI) and the droplet sensor signal processing (DSSP) PCB (1)c on **Fig. 14**). Power for the RPI and DSSP was provided by 5V supply wires from the first layer. The flow regulation PCBs were powered from a USB connecting with the RPI. The DSSP was connected to the RPI's general purpose input-output (GPIO) header with separate wires to receive a regulated 3.3V supply for the ADC and to send over the processed readings from the droplet sensor.

The droplet sensor column was also made of three layers. Every layer beside the lowest were height adjustable with vertical threaded rods reaching ~20cm off the baseplate. The stages were 3D printed to enable easy design modifications to the tilting mechanism for the microfluidic chip. The current-to-voltage converting transimpedance amplifier (TIA) circuit for the PD, provided by Kaiser Pärnamets et al. [77], was fixed to the lowest level in the column (2)a on **Fig. 14**), with the PD centrally aligned, facing up. A C-mount with a C-mount to RMS connector ring was attached to the PD-TIA PCB. A 20x microscope lens was attached to it with an RMS connection. The second stage in the droplet detector column was the 3 DoF (vertical, pitch, roll) microfluidic chip mount. The chip mount included a detachable chip holder, with clamps at each corner for fastening and loosening of the microfluidic chip and a 2x2mm hole at the center for the monitorable microfluidic channel to be transparent for the optical sensor and to allow for a range of unobstructed visibility when tilting. The chip's ROI was reduced further with a thin sheet metal (~200 μm thickness) placed to the bottom of the microfluidic chip before being clamped to the chip holder. The sheet metal had a ~150 μm diameter pinhole drilled into it which was aligned with the FFD's channel region where newly forming droplets could be seen passing over individually. The topmost stage in the detector column held the light source – LED (2)c on **Fig. 14**). To simplify the design process, but to also allow for configurable light source alignment to the centers of the previous stages, the light source was mounted to an analogous 3 DoF tilt-bed as was the microfluidic chip. The light source was an LED PCB, obtained from the thesis work of K. Pärnamets [77], which included a cold-white LED with a fixed current supply circuit using an LED controller. Both the PD and the LED PCBs were powered by the 5V supply from the electronics column.

3.2.2 Integration of the LED-PD Droplet Detector

A design of a microfluidic droplet detector shown on **Fig. 15**, acquired from the work of K. Pärnamets et. al [77] showed promise in fulfilling the platform requirements in terms of throughput, simplicity, and cost.

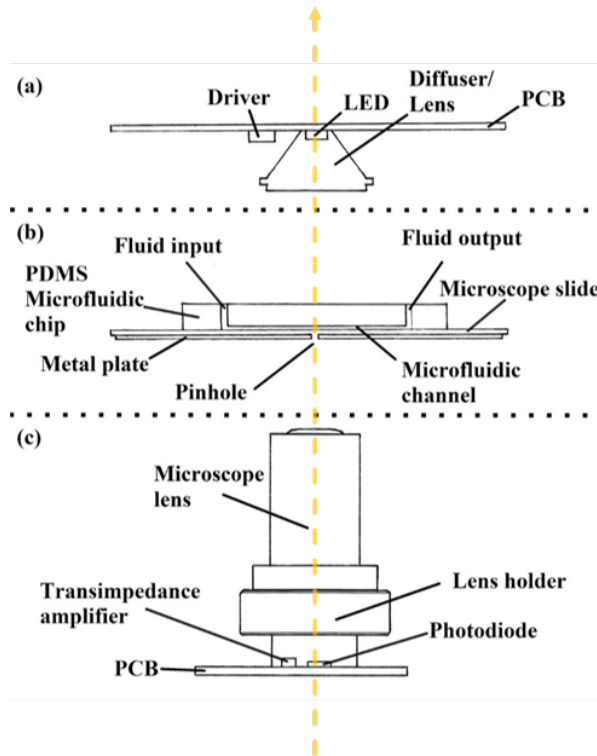


Figure 15. Cross-section of the aligned microfluidic droplet detector setup, **Appendix 3** [94].

The design required a microfluidic chip to be sandwiched between an illumination and sensor stage. To boost the potential droplet detection rates, while prioritizing simplicity, a fast-acting non-imaging type sensor was used – a photodiode. The illumination and the sensor stages (a, c, respectively – **Fig. 15**) were fabricated by K. Pärnamets in conjunction with the development of the droplet detector column design. The sensor circuit was compacted onto a small PCB, that had an input for a 5 VDC supply and an output for a voltage level, dependent on the light intensity collected by the PD. Likewise, the illumination circuit was compacted onto a PCB in the same dimensions as a generic microfluidic chip in order to fit into the same holder as was used for the microfluidic chip. As the light source was a low-cost 1 W wide-beam LED, to concentrate more light on the ROI, a focusing lens was added over the LED.

The following sub-sections will cover:

- 1) How does the detector work?
- 2) How is the detector signal processed?
- 3) How is the droplet found from the signal?

3.2.2.1 Operation Principle

In order to 'see' with a photodiode type sensor, there needs to be a source of illumination. The source could be the ambient Sun light or a ceiling lamp, however, to preserve continuity between experiments, the source must be able to precisely hold its illumination strength. With a dedicated LED and a current limiting driver, the light source was known, fixed, and mountable to the platform, maintaining its transferability.

While a non-imaging sensor, a photodiode, offers just a single pixel resolution of what is seen, its sensitivity is not binary. A photodiode produces a measurable current depending on the captured light intensity, in principle, with a resolution of a photon. Even though there is just one pixel to work with, a photodiode can still be used to characterize the morphology of a droplet from its 'shadow'. As explained before, the 'shadow' of a droplet in a brightfield setting is produced by the refraction of light at its edges, particularly those which are close to being or parallel to the light rays. To limit the number of 'shadows' on the photodiode to 1, a pinhole was placed underneath the microfluidic chip's ROI. In this way, a passing droplet's morphology will be characterizable by its 'shadow' as it passes through the photodiode viewport and etches a waveform of current values into a temporal plot. To estimate the possible waveforms produced with a pinhole, a simple pixel color summation application was made. Within the application, a rectangular pinhole could be adjusted around an imaged droplet flowing inside a microfluidic channel. The defined pinhole area is then moved across the image horizontally to imitate a moving droplet and map an estimated waveform that the measured droplet could produce (Fig. 16).

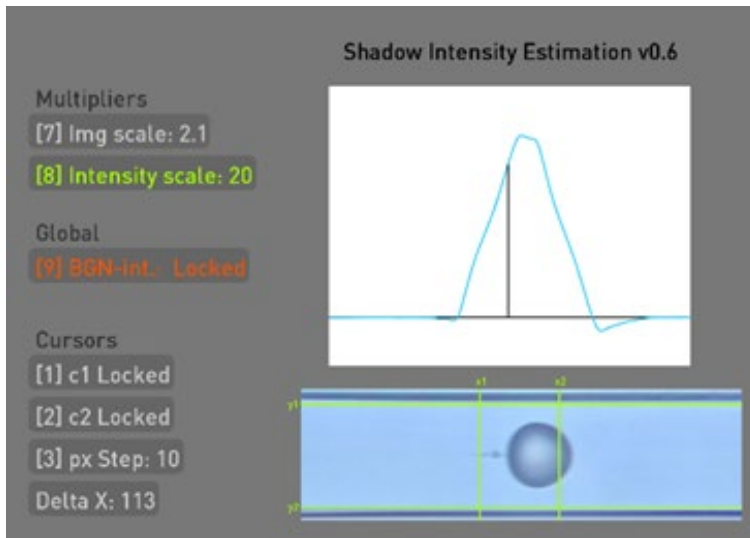


Figure 16. Pixel color summation application measuring the possible light intensity differences produced by a droplet passing through a photodiode viewport, narrowed with an arbitrary pinhole, **Appendix 3** [94].

To characterize a droplet's morphology with a single PD, the droplet needs to be in a stable continuous motion. As the droplet is moving in the view of the PD, the PD develops a change in its current output, which is converted to voltage with the help of a TIA.

3.2.2.2 Signal Processing

A TIA with an amplification of 10^6 , the produced signal is prone to carry considerable noise which may be insignificant at first. To separate as much of the original signal from the noise as possible, the signal from the TIA was led into a filter circuit. As most of the EMI originated from the high-frequency (~ 50 kHz) SMPS, with estimated droplet generation rates much lower, a steep 2nd order Sallen-Key low pass filter (LPF) was used to limit frequencies higher than ~ 7.26 kHz. Following that, a first-order capacitor-resistor (CR) high pass filter (HPF), with a cutoff frequency at ~ 67.7 Hz was used. With the expected droplet generation to typically exceed 100 Hz, the HPF did not impose on the platform expected functionality but helped to mitigate the detection of low frequency vibrations from the PZT pumps if any were to reach the detector column.

Because the default current level from the PD was dependent on the light collected from the LED, with an adjustable distance and alignment, that amount was not constant. If the available light was not enough to saturate the PD, the default level floated between the available 0 to 5 V window enabled by the TIA. To eliminate this unknown, the AC coupling capacitor from the CR HPF removed the DC component from the signal. However, to maximize the signal in various detector configurations and to detect droplets of differing sizes, another coupling capacitor was needed as additional amplification was required. The band-pass filter (BPF) was followed by an operational amplifier (OPA) in an inverted configuration allowing to produce an actively stabilized DC bias of ~ 2.5 V. At the end of the droplet sensing circuit, the signal is led to the ADC (ADS8681, Texas Instruments) which results in a digitized value, made understandable for the system controller. The detection and processing method are depicted in **Fig. 17**.

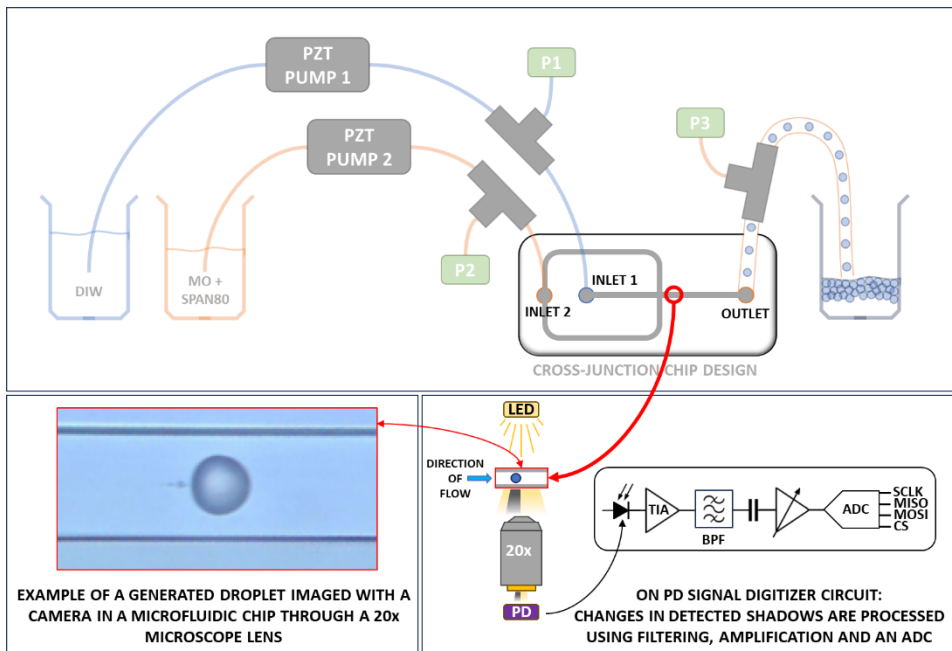


Figure 17. Illustrated acquisition of droplet's 'shadow' from a LED-PD detector with its signal processing circuit diagram.

3.2.2.3 Signal Interpretation

While droplet 'size' alone could provide one updating pressure target, there is a valid option to fix the other and allow the system to adjust the droplet size produced within a limited pressure range away from the fixed one. However, the broad variability of setup inputs (liquids, microfluidic chip designs, size targets, etc.), among possible research experiments, lessens the likelihood of producing any droplets, let alone reaching the target droplet size. To improve the odds of finding a combination of pressures for successful generation, both flows ought to be adjustable. To better visualize the relationship between flows inside an FFD, in case we have a fixed water stream, an increase in oil flow will pinch the water stream with more force causing the water stream to split more often – increasing the droplet generation rate at the cost of droplet size. Alternatively, if the oil flow were to be fixed, increasing the water flow would push more water into a forming droplet before being pinched off – increasing droplet size at the cost of droplet generation rate. However, if the flow pressures are too low or too high for a specific chip geometry, the water flow stays in the threading or jetting regime causing droplets to either not form at all (parallel flow) or form with no stability in either size or frequency (jet termination due to flow instability) [122], [123]. Followingly, to produce pressure targets for both liquids, two droplet parameters are required to form respective relationships for proper droplet generation control. The simplest two parameters are droplet size and droplet generation rate. Both of which could be derived from optical sensor data, observing every possible moment of a passing droplet, identifying the key moments and signal extremes.

The data received from the ADC was a voltage value between 0 and 5 volts, describing the light intensity absorbed by the PD and light intensity lost to a passing droplet. Having used a level shifting OPA in an inverting configuration, caused the droplet 'shadows' to be interpretable as voltage spikes instead of troughs – instead of light intensity, the change in voltage was positively correlated with the size of the shadow. Because of the inversion, a voltage increase detected above the hardware-defined offset or midpoint¹¹ (MP) of 2.5 V and a margin for hysteresis specified in software, +0.1 V (2.6 V), ought to be set as the condition to raise a flag in the system controller to indicate a possible appearance of a droplet. As long as the flag remains raised, following ADC measurements ought to be collected into a temporary buffer, each attributable to that specific droplet. The next relevant event ought to be registered after the measured voltage falls below the MP and a chosen margin for hysteresis, -0.1 V (2.4 V). Between these two MP-crossings, the highest peak (V_{HP}) is expected to represent the moment when the droplet, in its entirety, reaches visibility over the PD. However, because the PD signal is actively being level-shifted, it can be misleading to assume that the amplitude, between the MP and V_{HP} , reflects the real size of the 'shadow', at least for every droplet besides the first. As the droplet waveform is rapidly averaging around the MP, the attainable peak voltage is always going to end up with an offset closer to the MP. Trying to predict this offset would not be advantageous due to its dependence on frequency. As the frequency of droplet generation was not expected to be fixed, the required prediction process would have made the interpretation unnecessarily complex. Moreover, this process could not afford preventable losses in responsiveness. Instead, through active balancing, it could be expected that the droplet waveform would start

¹¹ Midpoint refers to a voltage level around which the photodiode signal was re-coupled to in the electronic circuit using the inverting level shifter.

oscillating around the MP. To resolve the issues with an arbitrary V_{HP} , the measurement ought to continue until the oscillation returns the waveform a third time through the MP. As with the first detection point, the event would be detected 0.1 V above the MP, during which, the lowest peak (V_{LP}) could be found.

With the highest and lowest peaks captured, a droplet interpretation algorithm could calculate a more accurate representation of the size of the droplet. Additionally, from the timings of the first and third MP-crossing events (incorporating the hysteresis margins specified in software), the algorithm could infer the droplet generation frequency, as the implication of a second upward MP-crossing is expected to indicate the detection of the next droplet. The process could be visualized as shown on **Fig. 18**.

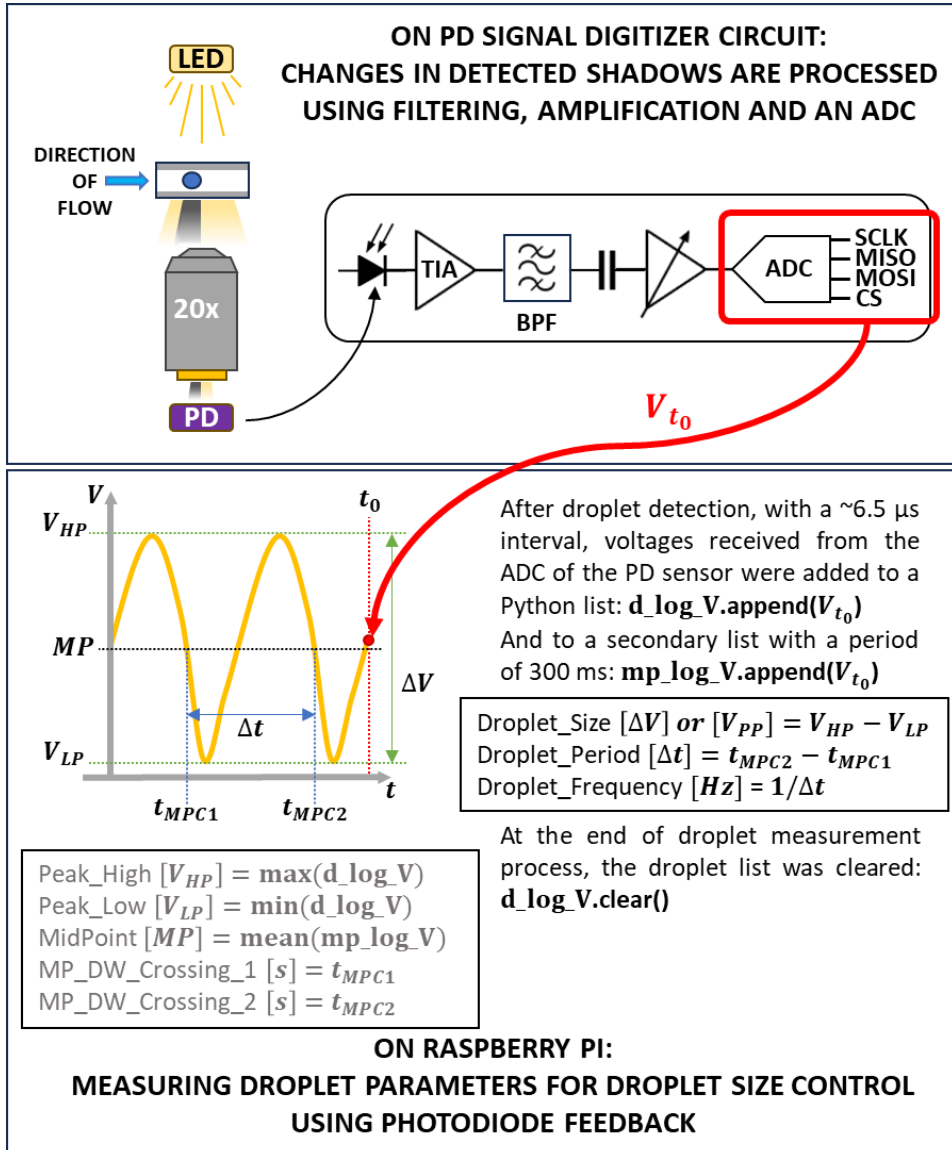


Figure 18. Illustration showing how the PD signal could be captured and measured over time, resulting in quantifiable parameters of droplet size and generation frequency.

3.2.3 Integration of the Developed Flow Regulation Device

The transfer of the pumping device was relatively straight forward. To address the concerns brought up in Chapter 2 and Subsection 3.2.1, following design modifications were made:

- The pressure sensors were upgraded to a higher-pressure range (0 to ~103 kPa, MPRLS0015PG0000SA, Honeywell) to exceed the pressure output of the PZT micropump. The upper limit was large enough to accommodate two pumps in series for further upgradability. The cost of the PCB was minimal as the new sensors had the same footprint and pin layout as the previous.
- Because the pumping device would now rely on commands and power coming from the system controller, the Wi-Fi code was omitted from the firmware on the pump controller (ESP32 DevKitC) and the battery could be omitted from transfer. The pump controller connected to the system controller with a USB cable.
- To mitigate noise and improve signal integrity on the communication lines between the pump controller and the pressure sensor PCBs, the three sensors were brought onto a single, more compact PCB and together with the pump controller PCB, were modified to be able to connect with board-to-board pin headers and connectors.
- The pressure feedback PID controllers (K-values) received the needed optimization, firstly by computational means (**Appendix 3 – Fig. 13**) using genetic algorithm (GA) tuning [124], and later heuristically adjusted for the setup. For water pump drivers, the PID K-values were 10.5, 17.5, and $5.81e-5$, respectively and 40.0, 18.0, $4.78e-4$ for oil pump driver [94]. The approach and stabilization of pressures at given targets was significantly improved, enabling droplet formation from cold start in ~10 seconds.

3.2.4 System Controller

To accommodate the conversion of optically obtained droplet parameters into pressure targets for the pump drivers, a control layer above the pumping module was required. The system control consists of two functions: managing communication with the user and communication between the droplet detection and flow regulation modules. With an increased computational demand, an SBC was chosen as the system control board instead of a microcontroller. With a good price to performance ratio, a Raspberry Pi 4B ended up as the final option. Its quad-core CPU allowed for multiple tasks to be split up into separate cores for operational speed improvement, as some tasks, such as droplet sensing, needed to be much more responsive than others.

A Linux-based operating system (OS) was installed on the Raspberry Pi (RPI) – Ubuntu Desktop version 21.10. The automation program was written in Python 3.9. The RPI interfaced with the actuator module via USB, with its speed limited on the pump controller end (ESP32 DevKitC, UART-to-USB converter – 3 Mbps max.). It interfaced with the ADC on the DSSP PCB via 4-wired SPI. The RPI was communicable with a remote user via eCAL network API.

The operational tasks of the system controller could be categorized into four components, split onto separate CPU cores using Python’s multiprocessing library (Fig. 19):

- 1) (CPU core 1) Communication with the user
- 2) (CPU core 2) Communication with the pump controller
- 3) (CPU core 3) Communication with the droplet detection ADC
- 4) (CPU core 4) Managing tasks and controlling droplet generation parameters.

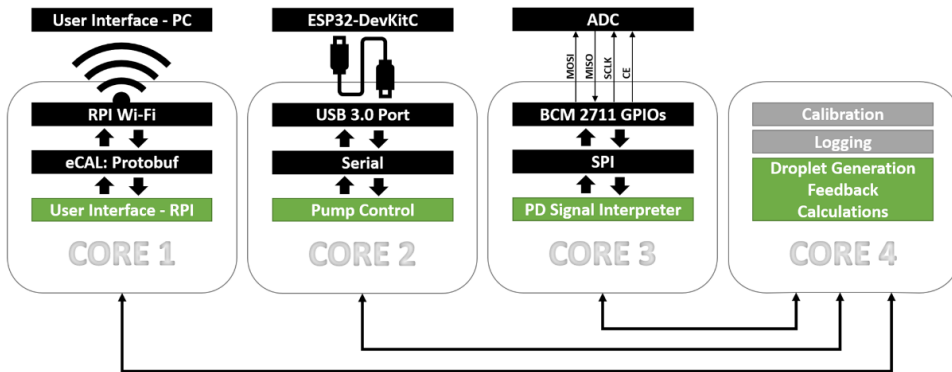


Figure 19. System controller diagram of its connective links and operational tasks split among its CPU cores, **Appendix 3** [94].

3.2.4.1 Task 1

The RPI communicated with the user over a Wi-Fi connection, which was sourced from a mobile hotspot. Communication took place on an open-source cross-platform enhanced communication abstraction layer (eCAL, v5.9.5) [125]. The middleware was addressable from the RPI’s Python code through dedicated eCAL libraries.

eCAL operates on a subscriber-publisher model, but to manage operational and droplet data logs wirelessly, a bidirectional approach was necessitated, requiring devices to function as both publishers and subscribers simultaneously. During regular operation, with minimal data being shared, communication with the user was not expected to be frequent, a 0.1 s artificial delay was added to the task’s loop duration with the priority on reducing CPU load. The messages were encoded with a Google Protobuf serialization structure, which could be extended without much effort. The Protobuf message included a unique device name, microfluidic chip name, generation rate, droplet size, transmission/reception status, flag for different process activation, and message ID. To catch any broadcast data, both communication participants required cyclical polling of eCAL subscriber’s listening function.

As the 4th task/core played the role of the middleman between all tasks, simpler user commands, such as start and stop of droplet generation, were passed from task 1 to 4 through an inter-core argument passing multiprocessing “queue” – a communication pathway between two tasks in the main code.

3.2.4.2 Task 2

Pump controller task managed the data exchange between the pump controller board and the RPI over serial protocol. The message structures had slight variances on either end. The structure from the pump controller board included readings of PZT driver

voltages, water and oil pressures, and a binary indicator if the flow-regulation PIDs were enabled. The structure from the RPI, however, included targets for PZT driver voltages, water, and oil pressures, and an 8-bit message containing PZT pump driving waveform shapes, frequencies, driver start and stop command flags, and flow-regulation PID enabling flag. In principle, the data coming from the ESP32 DevKitC was mostly used for setup characterization or as extra data points of the droplet generation process. The data being sent originated from the 4th task/core, which calculated new pressure targets based on the droplet generation parameters.

3.2.4.3 Task 3

The droplet identification and measurement algorithm operated semi-independently on the 3rd task/core on the RPI. This task had to continuously poll for a 16-bit resolution ADC reading of the PD-TIA signal, interpret it and update the main task about each measured droplet. It had to have a high degree of independence to minimize reliance on slower, more dependent processes which could cripple the stabilization of any automated process. Because this task had to prioritize responsiveness above all else, the SPI messaging between the RPI and the ADC was written into a C-module – a separate custom function, written in C programming language, to be called from within the main Python code. The C-module, using the RPI's low-level Broadcom GPIO library, was coded to poll the ADC data, achieving an average update speed of ~2.3 microseconds. The polling rate was bottlenecked by a limited clocking rate of 24 MHz, beyond which the SPI communication became unstable.

A typical sequence of rapid updates from the ADC revealed a sinusoidal waveform, to represent a series of droplets. As explained in Subsection 3.2.2.3, three MP crossing points would be enough to detect a droplet from such a sinewave. The algorithm, however, could not avoid becoming more complicated as during preliminary testing, it was noticed that generated droplets were not fully opaque at all sizes. When the produced droplet diameter exceeded the height of the microfluidic channel, the droplet was flattened against the top and bottom of the channel. As most of the 'shadow' of a water droplet, in brightfield lighting, is not caused by absorption but by refraction along its curved oil-water interface, the more flattened surfaces, parallel with the photodiode created a pathway for light to pass through with minor deviations. In some scenarios, the droplet even behaved analogously to a magnifying lens. This meant that such droplets, when fully aligned with the PD, would produce a valley in the 'shadow' intensity at an expected peak (**Appendix 3 – Fig. 16 (c)**). A significant exacerbation of the effect was observed when fluorinated oil was used instead of mineral oil (**Appendix 3 – Fig. 18**). To the detriment of the amplitude of the measurable voltage, water droplets formed in oil, ~50% denser than water, had noticeably thinner phase-transition regions as the flow-aligned faces of the droplet would perceive comparatively more pressure. Because of the increased relative pressure on the flow-aligned faces, the droplet was forced to increase the area of its interface with the channel walls, increasing the region of transparency and thereby the observed valley in the waveform. In extreme cases, a passing droplet in fluorinated oil would not produce just one sinusoidal wave but imitate two. This meant that in order to not miss droplets consisting of two pulses, the droplet identification algorithm had to be extended to monitor five MP-crossing events at a time.

Having five MP-crossings, the algorithm observed 5 timestamps and 4 peaks in between (V_{HP} and $V_{LP} - 2$ of each). Since the possible valley in 'shadow' intensity, caused by the transparent region of the droplet, will appear in the middle of two darker regions

at the beginning and end of the droplet, it becomes expected to appear between the second and third crossing. In theory, the algorithm could ignore the lowest peak measured there, and the next highest peak measured afterwards, however, a further complication needs to be considered. Namely, variation in droplet sizes caused by stabilization fluctuations in flow parameters and/or the gradual increase in droplet sizes at the start and gradual decrease at the end of droplet generation, it became plausible that a smaller pulse between two larger ones does not necessarily indicate a transparent region in the droplet. It could simply be a change in the droplet generation process. The distinction between these scenarios was aided through another complication noticed during observation of generated droplets over a camera. Rapidly flowing droplets were deforming into bullet-like shapes, aimed in the direction of the flow. This bullet-like shape caused a recognizable change in how the shadow was represented in the waveform. As the front of the droplet was elongated, the phase-transition region extended with it. The resulting voltage slope, of a droplet entering the view of the photodiode, was thereby slower. This extra averaging time subsequently lowered the achievable V_{PH} . This created a unique combination between the measured peak-to-peak voltage (V_{PP}) and single-pulse period. For a droplet with an inconsiderable transparent region, without complicating the algorithm, the bullet-like shape was expected to go unnoticed, as there was no separation event of the flow-aligned faces detectable at the MP. This meant that unlike double-pulse droplets, single-pulse types would have a positive correlation between its duration and amplitude. For example, a small single-pulse droplet would produce a short duration pulse with a relatively small amplitude, whereas the first pulse of a double-pulse droplet, with the same amplitude, would have a comparably longer duration. The duration of the first pulse of a double-pulse droplet was generally longer than its second pulse, which had a noticeably larger amplitude. Having considered the observed complications, each of the 4 peaks and 2 periods (time between timestamps 1 and 3, 3 and 5) were compared in the algorithm as soon as they were detected.

Once a droplet was identified and measured, its parameters, such as arbitrary size in voltage and generation frequency, were put into a Python's multiprocessing queue. The queue was read by the droplet size control task whenever possible, and to the benefit of droplet identification task, the queuing function helped to keep the loop schedules uncoupled. The multiprocessing queue function was known to be safe for parallel access for any task by making copies of its buffer for incoming and outgoing data. However, due to this duplication process in combination with the different access speeds of the tasks, the faster droplet identification task would inevitably build up a considerable backlog before being read and cleared. Because of this, the buffer would regularly overflow and cause losses in droplet data. To mitigate this problem, a second queue was added between the 3rd and 4th task. As one queue was being read, the other queue would be accessible for writing. To avoid having to monitor the sizes of the queues, to discern which queue to read, a third separate queue was used to provide an indicative flag. This queue dynamic can be seen illustrated in **Fig. 20**. Using a simple Boolean flag, the droplet identification task knew which queue to write into, expecting the other to be read in the meanwhile. On **Fig. 20**, time t_0 indicates to an arbitrary time when Task 4 sees that the first queue (Q1) has something in it. Until t_1 , a delay (**Fig. 20** - Δt_A) of a maximum of one full cycle of Task 3 takes place before it sees the indicator for queue switching on Q3. As this takes place through the function of multiprocessing queues, while Task 3 has not yet seen the indicator on Q3, both tasks can access the same queue without causing

blocking delays. On **Fig. 20**, Δt_B determines the delay of when Task 3 must switch the queue buffer into which it can push new droplet data. This delay forms from how quickly Task 4 can clear the queue, to which Task 3 previously wrote.

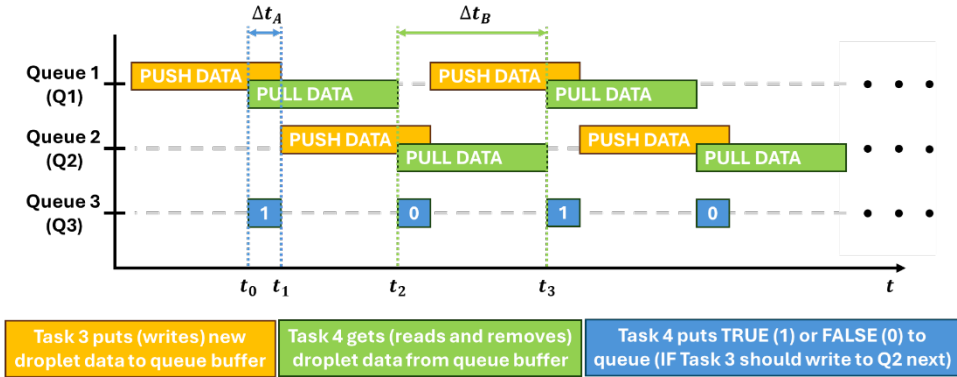


Figure 20. Data exchange queues and their access relationship between Tasks 3 and 4.

3.2.4.4 Task 4

The final task, being the main control task, was used to launch the other three tasks and was in control of shutting them down. After initiating communication with the user through the 1st task, the 4th task started to wait for commands alluding to different operational modes:

- Droplet generation mode “with PIDs disabled.”
- Fluidics characterization/calibration mode.
- Droplet generation mode “with PIDs enabled.”

The primary use-case for droplet generation without feedback was to be able to observe forming droplets on the platform with a camera instead of the PD. Being able to disable the droplet generation PIDs, gave the ability to prime the fluidics, and to characterize the fluidics procedurally with custom pressure patterns. During any mode, the 4th task prioritized looping speed to avoid missing information coming from other tasks, which made it ideal for producing logs populated with every captured droplet. Lastly, the 4th task was in charge of calculating the pressure targets from measured droplet generation parameters using two independent PID controllers.

3.2.5 Droplet Size and Generation Rate Control Algorithms

With an ability to measure both droplet size and generation rate, the acquired data could be combined to characterize the setup considering unique tolerances of each of its components, nuances in behavior with new liquid or gaseous media, unusual phase combinations, surfactants, and particles to be encapsulated. A characterization method, made repeatable and replicable, could support the empirical evaluation of new components and media introduced into the droplet generation setup, making it more flexible for research.

3.2.5.1 Algorithm to Find System-Representative Model Coefficients

As the only control vectors in the system were pressure-driven oil and water pumps, droplet data, reaching the droplet generation control task, could not be used as direct feedback. Unlike PZT pump driver PID control, relying on a linear coefficient,

the relationships between droplet size, generation rate and pressures, were not as straightforward. Moreover, since droplet generation rate and size were generally interdependent, to control them as independently as possible, the coefficients needed to be derived from unique combinations of the available feedback data. To figure out these combinations, a setup characterization algorithm was designed.

The purpose of this algorithm was to run procedurally through water and oil pressure combinations within set ranges and log the obtained droplet generation sizes and rates. The resulting pressure and droplet data log was used to graph multiple 2D combinations to spot surface level relationships. With no signs of linearity, some combinations indicated approximate exponential or logarithmic behavior. Not only for minimizing the droplet generation control loop for operation speed, higher than 3rd order polynomial relationships could not be relied on due to their uncharacteristic behavior at the edge conditions. Final relationships were chosen based on a combination of high coefficient of determination (R-squared) values and the complexity and number of calculation steps, to provide a separate trendline coefficients for droplet size control and droplet generation rate control:

- Droplet size (x) vs. oil-to-water pressure ratio (y) – 3rd order polynomial
- Droplet frequency to droplet size ratio (x) vs. oil pressure (y) – logarithmic regression line

The setup characterization algorithm was run at the start of every modified setup configuration, to incorporate the changes in chip geometry or its positioning in the droplet detector column. Whereas the changes in chip geometry would alter the pressure relationship with the resulting droplet sizes and generation rates directly, its position in the droplet detector column would not only alter the relationship between the droplet's 'shadow' and the amplitude it produced, but also the shape of the resulting waveform. Regardless, the polynomial and logarithmic behaviors remained. At the end of each characterization, the obtained polynomial and logarithmic regression line coefficients were set into their respective equations used to calculate the base reference points for cold starting droplet generation of desired size and generation rate.

3.2.5.2 Algorithm to Control Droplet Generation

After calibration, the main control algorithm on the RPI gains a set of functions that give the first approximate description of the relationships between pressure targets and the resulting droplet sizes and generation rates available for the setup. Before droplet generation correction and stabilization could activate, any droplet reading is required. The first signal could be produced from an initial steady-state pressure combination the results in the formation of droplets with parameters anywhere on the observed detectable range. To determine such an initial steady-state, pressure targets for the pumps are calculated by finding the user defined droplet generation parameters on the calibration curves, respective to each parameter (size and rate). As the pumps stabilize at the initial pressure levels, and the microfluidic chip starts to produce droplets relatively close to the desired size and generation rate, after a few seconds, depending on the target generation frequency, the droplet parametric feedback control becomes operational. The small delay, before becoming operational after the first droplet signal is caused using an initial buffer of 150 droplets, which when collected, can indicate a reasonable stability in droplet formation. Any additional stability is critical in droplet generation control, as sudden changes caused by the PID controllers can throw the

droplet generation out of stability, and each attempt to recover will add another delay and produce more waste in the meanwhile.

Droplet generation parameters were controlled via two separate PID loops – one to control the size of the droplet, the other to control the generation frequency.

3.3 Platform Evaluation Methodology

To test the platform flexibility with different FFD designs, oils, and surfactants, two variations of FFDs (**Table 7**) and two different oil-surfactant mixtures (**Table 8**) were used.

Table 7. Geometric properties of the FFD variants used for the evaluation of the droplet generation platform, Appendix 3 [94].

Chip variant	B	C
Junction width [μm]	125	280
Junction angle of entry [$^\circ$]	90	38.33
Oil inlet width [μm]	380	
Water inlet width [μm]	620	
Outlet width [μm]	620	
Number of filters	2	
Channel height [μm]	100	

Table 8. Liquid properties and combinations used for evaluation of the droplet generation platform, Appendix 3 [94].

Liquid combination	B	C
Disperse phase	Deionized water (DIW)	Deionized water (DIW)
Continuous phase	Sigma-Aldrich 33079 mineral oil + 2% w/w surfactant (Span [®] 80, Sigma, Aldrich)	HFE 7500 fluorocarbon oil (FO) + 2% w/w surfactant (perfluoropolyether (PFPE)-poly(ethylene glycol) (PEG)-PFPE triblock)

- The following descriptions of methodologies and results will use the FFD variant and liquid combination naming schemes from **Tables 7** and **8**.
- By using oils of different densities and viscosities, the oil pumping frequency for mineral oil was kept at 50 Hz, while for fluorocarbon oil (FO), the frequency, showing largest generable pressure levels, was at 320 Hz.
- The droplet generation parameter PID controllers received K-values heuristically, 0.05, 0.05, and 0.0005, respectively for both droplet size and generation rate controllers.

3.3.1 Computational Performance

After all modules were integrated onto the platform, a demo droplet generation was conducted using both chip variants with liquid combination B. Multiple test runs were conducted consisting of droplet generation sets, each with a duration of 90 seconds. After 45 seconds into every test run, a ~ 3 second period of ADC data was logged to be analyzed at higher detail. In the same period a sample image was taken of the generated droplet signal captured with an oscilloscope (DSO5014A, Keysight), with a probe connected to the circuit right before the ADC.

3.3.2 Module Calibration

To initiate the droplet generation control, the setup-specific model required calibration. The calibration algorithm relies on three given parameters:

- 1) Water pressure [kPa] (Range: 3.0 – 12.0 kPa)
- 2) Arbitrary droplet size [V] (Range: 0.2 – 4.8 V)
- 3) Arbitrary droplet generation Rate [kHz] (Range: 0.1 – 1.0 Hz)

A 4th parameter (oil pressure) was derived from parameter 1 with a multiplicative ratio of 'A' (a value reached heuristically from a ratio of 1 and starting to increase oil pressure in relation to water pressure until the emergence of the dripping regime). This calibration included two phases as illustrated on **Fig. 21**.

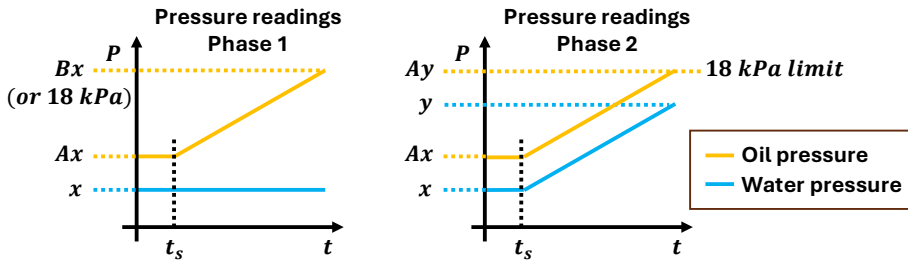


Figure 21. Water and oil pressure characteristics in calibration phases 1 and 2, during which to collect pressure and droplet data to find the 3rd order polynomial and logarithmic relationships, respectively – used for droplet size and generation rate control.

Using the water and oil pressure targets (**Fig. 21** – x and Ax , respectively) given for calibration, the pumps were commanded to reach and stabilize at these levels. In phase 1, once stabilized (**Fig. 21** – t_s), the oil pressure was incrementally updated on every cycle of the pump control task on the RPI. The oil pressure was set to climb until reaching either a pressure level of 18 kPa or a ratio of 'B' (heuristically found to be around 1.7) with water pressure. Both droplet size and generation rate were logged during the process. From the collected pressure ratio and the resulting droplet size relationship, coefficients corresponding to a 3rd order polynomial were calculated. Using the obtained formula, a new pressure coefficient could be found which relates to the 2nd given parameter.

By keeping the water pressure at the initially given value, the oil pressure was returned to oil-to-water pressure ratio 'A'. To start the second phase, the pumps were commanded to reach and stabilize at the set levels (**Fig. 21** – x and Ax). After stabilization (**Fig. 21** – t_s), both oil and water pressures were set to incrementally update on every pump control task cycle, while preserving the ratio. This would last until the oil pressure reached 18 kPa. The pressure limit was set close to the droplet formation limit, which came from the design of the used FFD. After completion, a second formula was calculated from the logarithmic relationship between the oil pressure and the droplet generation frequency.

The calibration concluded by adding the coefficients connecting the oil-to-water pressure ratio with the droplet size and the coefficients connecting the oil pressure level with the droplet generation frequency into the droplet size and generation rate error calculations in their respective PID algorithms. When the system is commanded to generate droplets with given relative size, using the 3rd polynomial model equation and coefficients, the RPI can calculate an oil-to-water pressure ratio which in a specific

pressure range can result in the desired droplet sizes. By including a target for droplet generation rate in the command, using the logarithmic model equation and coefficients, the RPI can calculate a complementary level for oil pressure. With the oil pressure and the oil-to-water pressure ratio, the level for water pressure can also be found.

3.3.3 Parametric Control of Droplet Generation

To evaluate the droplet generation PID controllers on varying FFD designs, both chips B and C were used for the control accuracy and monodispersity tests. In all tests, the liquid combination was B.

To measure the accuracy of reaching set combination of droplet generation parameters, two groups of target series tests (size and generation rate) were done for either of the two chip variants (**Tables 9 – 12**). The test series consisted of multiple 36 second stages where one parameter was held constant. This period was split into two, allocating 15 s to stabilization of droplet generation and the remaining 21 s for error and CV% calculation. As the different chip types were quick to show large differences in feasible droplet generation parametric combinations, each series was limited to combinations which were more likely to produce droplets. Additional longer 75 second (30 s stabilization; 45 s measurement) single-stage tests were done for finding the CV% for larger droplet generation sets.

Table 9. Chip B – Voltage target series over fixed generation frequency targets, **Appendix 3** [94].

	Fixed Generation Rate Target	Voltage Relative to Size Target 1	Voltage Relative to Size Target 2	Voltage Relative to Size Target 3
1	200 Hz	2.0 V	2.8 V	3.6 V
2	400 Hz	2.0 V	2.8 V	3.6 V
3	600 Hz	2.0 V	2.8 V	3.6 V
4	800 Hz	2.0 V	2.8 V	3.6 V

Table 10. Chip B – Frequency target series over fixed voltage (size) targets, **Appendix 3** [94].

	Fixed Voltage Relative to Size Target	Generation Rate Target 1	Generation Rate Target 2	Generation Rate Target 3	Generation Rate Target 4
1	2.0 V	200 Hz	400 Hz	600 Hz	800 Hz
2	2.8 V	200 Hz	400 Hz	600 Hz	800 Hz
3	3.6 V	200 Hz	400 Hz	600 Hz	800 Hz

Table 11. Chip C – Voltage target series over fixed generation frequency targets. Target size and frequency combinations which did not result in stable droplet generation are marked with gray highlights, **Appendix 3** [94].

	Fixed Generation Rate Target	Voltage Relative to Size Target 1	Voltage Relative to Size Target 2	Voltage Relative to Size Target 3	Voltage Relative to Size Target 4
1	200 Hz	3.2 V	3.4 V	3.6 V	*
2	300 Hz	3.2 V	3.4 V	3.6 V	3.8 V
3	400 Hz	3.2 V	* No droplets generated with these parameters.		
4	500 Hz	3.2 V			

Table 12. Chip C – Frequency target series over fixed voltage (size) targets. Target size and frequency combinations which did not result in stable droplet generation are marked with gray highlights, **Appendix 3** [94].

	Fixed Voltage Relative to Size Target	Generation Rate Target 1	Generation Rate Target 2	Generation Rate Target 3	Generation Rate Target 4	Generation Rate Target 5
1	3.2 V	200 Hz	300 Hz	400 Hz	500 Hz	600 Hz
2	3.4 V	200 Hz	300 Hz	400 Hz	500 Hz	600 Hz
3	3.6 V	200 Hz	300 Hz	400 Hz	No droplets generated with these parameters.	
4	3.8 V	200 Hz	300 Hz	400 Hz		

To gain some reference to voltages obtained from the droplet detector, claimed as corresponding to droplet size, real-world measurements were taken of generated droplets under a trinocular microscope (BX61, Olympus). The microscope setup was able to record images with a camera (DP70, Olympus) through a 4x/0.16 microscope lens (UPLSAPO, Olympus). For the measurement setup, the droplets were deposited into a Cell Counting Chamber Slide (Countess™, ThermoFisher) with a channel height of 100 μm. For calculating the imaged droplet cross-sectional diameters, ImageJ software was used. On ImageJ, the droplet outlines were mapped, filled, and measured by pixel summation. The pixels were referenced to the scale bar attached to the image from the microscope image acquisition software.

3.4 Performance Evaluation Results

3.4.1 Computational Performance

A fully assembled platform can be seen on **Fig. 22**.

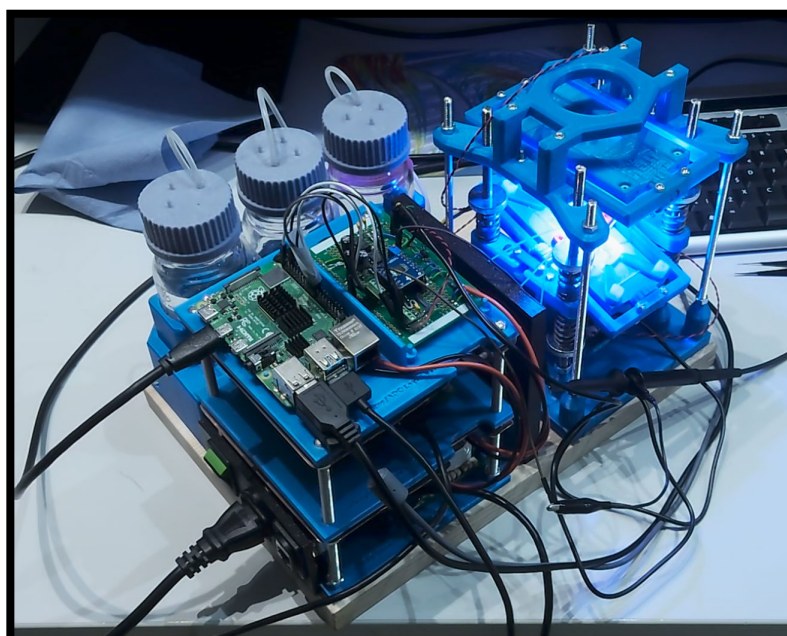


Figure 22. Photo of the assembled droplet generation platform.

From the ADC data collected from a test with chip variant C (**Fig. 23**) generating ~ 500 droplets per second, every other missing peak indicated that the droplet generation parameter calculation and transfer from task 3 to 4 after every 5th MP crossing (**Fig. 23** – arrows indicate every 5th midpoint crossings, where every 5th crossing becomes the 1st for the next droplet), causes $\sim 100 \mu\text{s}$ delay on task 3 which halts the ADC polling. Furthermore, it became apparent that the median voltage between the waveform peaks could shift away from the MP, which could cut off and disregard the real V_{LP} .

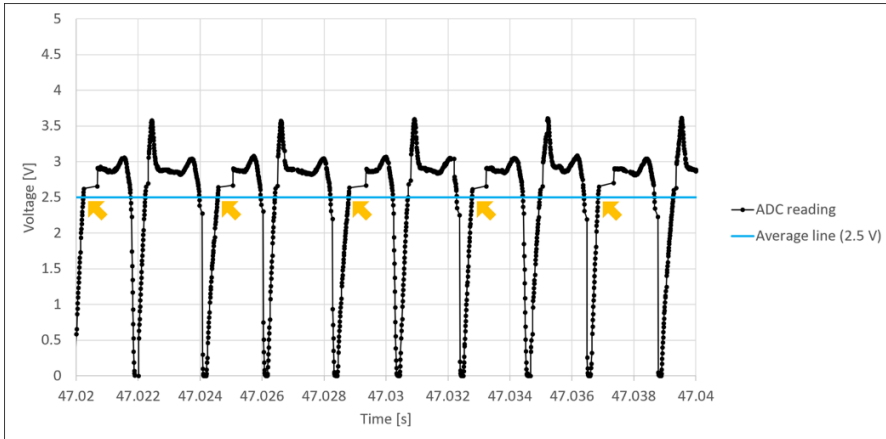


Figure 23. ADC data of droplets generated at 500 Hz with chip variant C and liquid combination B, **Appendix 3** [94].

From the ADC data collected from a test with chip variant B (**Fig. 24**) generating ~ 500 droplets per second, the droplet waveform changed considerably. With less sharp features, the $\sim 100 \mu\text{s}$ measurement and communication delays on task 3 were less impactful in regard to droplet size. However, a long multi ms delay was captured, whose emergence was not traceable to any one function in the code. More of these lengthy delays were noticed in longer ADC datasets. It was noted that they occurred rarely, sporadically, but continuously, which indicated towards hardware-level task management delays possibly caused from using a non-real-time OS.

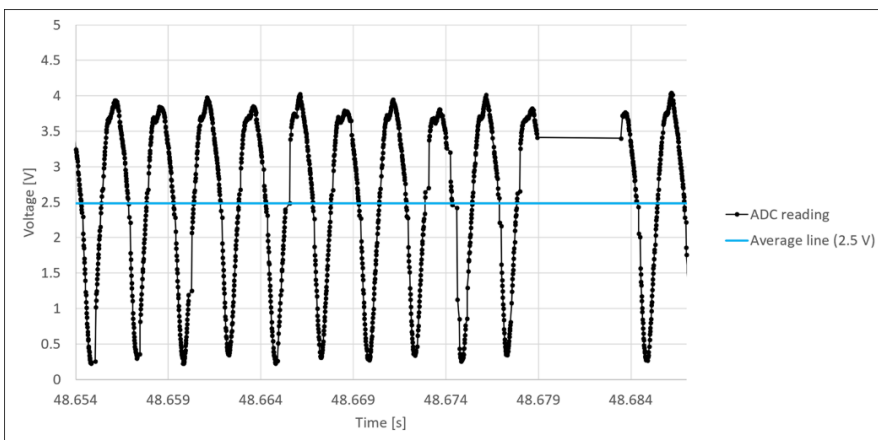


Figure 24. ADC data of droplets generated at 500 Hz with chip variant B and liquid combination B, **Appendix 3** [94].

To not shock the system falsely with an erroneous set of measured parameters in case of an OS latency delay, a moving window averaging sized for 15 values, was added after the PID controller outputs.

By the end of the last 90 second test, the loop duration parameters were collected, as shown in **Table 13**.

Table 13. System control software task loop durations, **Appendix 3** [94].

	Core 1 – User interface coms.	Core 2 – Pumping system coms.	Core 3 – Droplet interpretation	Core 4 – Droplet PID calculations
Maximum [ms]	203.4370	215.0430	20.25914*	21.05400*
Average [ms]	102.0334	18.98948	0.006515	0.169749
Minimum [ms]	100.6310	14.74400	0.002861	0.104000
Loops counted	1005	4 758	14 640 000	530 200
Total [s]	102.54	90.35	95.38	90.00

From the loop durations (**Table 13**) it can be seen how the bottleneck in droplet generation control lies with task 2, controlling the pump, showing the minimum loop duration at ~15 ms. Furthermore, the maximum ADC sampling speed of ~2.3 μs has stretched to an average of ~6.5 μs with the addition of the droplet interpretation algorithm. Additionally, it can be seen how the OS latency has similarly impacted the maximum recorded loop duration in tasks 3 and 4.

3.4.2 Module Calibration

The calibration process took ~5 minutes to complete, resulting in two .csv type logs of captured droplet and pressure data and the coefficient results of both the 3rd order polynomial (**Fig. 25 – Left**) and the logarithmic regression line (**Fig. 25 – Right**).

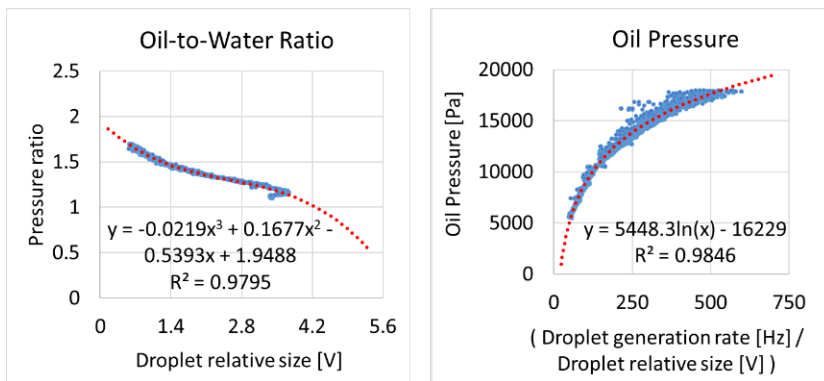


Figure 25. Characteristic 3rd order polynomial (left graph; red dotted line) and logarithmic (right graph; red dotted line) regression lines calculated using droplet relative size, generation rate and pressure data acquired during droplet PID calibration stages.

The resulting regression lines show good matching with the data, with R² value for the 3rd order polynomial 0.9795 and 0.9846 for the logarithmic regression.

3.4.3 Parametric Control of Droplet Generation

For all the test sets from **Tables 9 – 12**, average droplet size error percentages were plotted to **Fig. 26.a**, and average droplet rate error percentages to **Fig. 26.b**. **Fig. 26** is formatted to give a comparative overview of the ranges of CV% values for all configurations used – demonstrating the robustness of the droplet generation control. In comparison to chip C, both the averages and variation ranges of accuracy related droplet size errors were leaning in favor of chip B, indicating that the 90° cross-junction angle manages wider droplet size control better. It is also noticeable that the voltage (V) and frequency (F) series maintain similar spread. In the case of droplet generation rate errors, the variation between chips B and C had shrunk, however, in terms of averages, still favoring chip B.

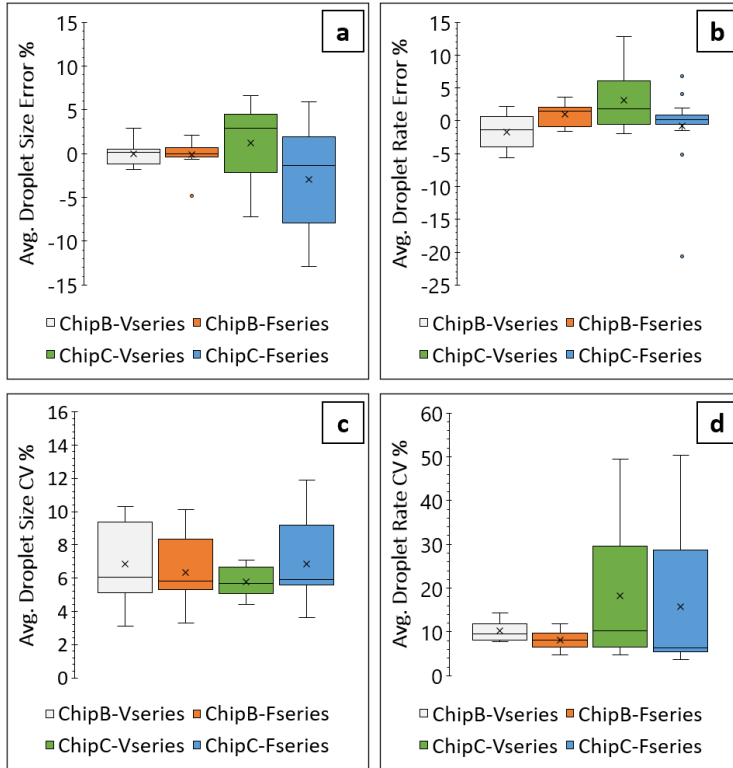
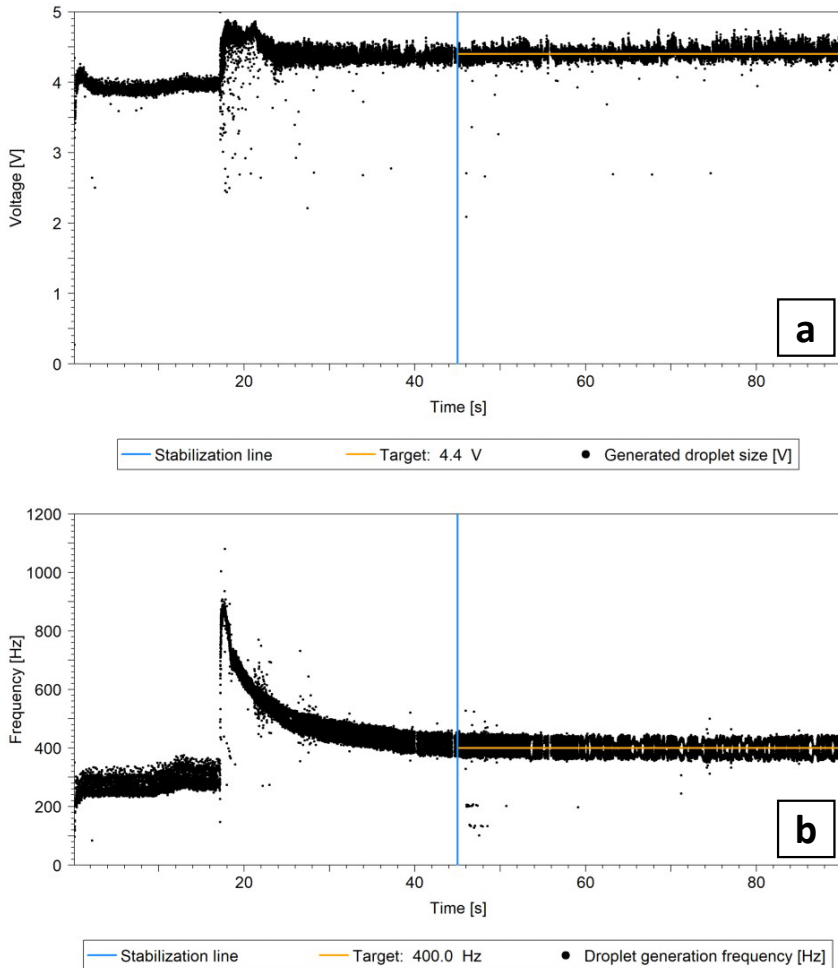


Figure 26. Droplet size and generation rate test series collective average size error graph (a), generation rate error graph (b), droplet size CV% graph (c) and droplet generation rate CV% graph (d) for different FFD cross-junction angles, **Appendix 3** [94].

For all the test sets from **Tables 9 – 12**, average droplet size CV percentages were plotted to **Fig. 26.c** and average droplet generation rate CV percentages to **Fig. 26.d**. While the lowest droplet size CV% values of all test sets reach below 5%, the averages remain above it, moreover, with the highest values reaching slightly over 10%. The CV% variance over the test set combinations is relatively broad, showing the droplet size CV% being less dependent on the cross-junction angle and the junction width. In the case of droplet generation rate CV%, variance by chip type is clear. Since the averages on **Fig. 26.c** and **Fig. 26.d** are from the same data sets, the significant difference gives credence to the notion that through channel geometry, it is possible to decouple the droplet size and the generation rate.

The CV% measurements of prolonged single parameter combinations typically yielded better monodispersity. This improvement can be linked to longer stabilization and larger sample sets. Graphs on **Fig. 27.a** and **Fig. 27.b** depict the droplet size and generation rate control at targets of 4.4 V and 400 Hz, respectively. This combination, contrary to the expectation that 200 Hz generation rate would result in optimal performance as it would synchronize with the water pump, gave the best result for monodispersity (1.77% – droplet size, 6.67% – droplet generation rate).



*Figure 27. Droplet relative size in voltage (a) and generation rate (b) datapoints collected from a target droplet generation parameter combination of [4.4 V; 400 Hz] with chip B. Blue vertical line at the 45 s mark, indicates the point after which the generated droplets were used in the CV% calculation, **Appendix 3** [94].*

Lastly, droplets were generated on the platform with droplet generation control PIDs disabled with multiple combinations of fixed pressure targets, collected, and then measured under a microscope. Using chip B with oil B, the best monodispersity was measured for water and oil pressures set to 9 and 12 kPa, respectively. An oscilloscope measured the generation rate at ~ 1.24 kHz, which posed difficulties for the platform to correctly identify droplets, indicating that the identification process needed a better

solution. Droplets were generated for about ~75 seconds. Estimating with the measured frequency obtained from the oscilloscope, around 90 thousand droplets were generated. A random sample of 6429 droplets were imaged manually and measured. This pressure combination, resulted in droplets with planar diameters of 131.4 μm with a CV of 7.7% when the droplets were slightly flattened in the droplet imaging slide, revealing yet more room for improvement.

3.5 Chapter Summary

3.5.1 Discussion

In this chapter, the design criteria and the methodology of module integration, system unification and droplet generation parametric control were laid out for the construction of a transferable, automated droplet generation platform. In addition to the system controller and PSUs, the platform housed three modules – fluidics, droplet detector, and flow regulator. The flow regulator consisted of the previously developed dual-channel piezoelectric pumping device. The flow regulator was configured to be controllable by the system controller and improved for a more reliable and fitting pressure feedback control. The droplet detector consisted of a separately developed LED-PD non-imaging sensor, which was integrated to the platform as a 3-stage tower. The 2nd and 3rd stage, prepared for the microfluidic chip and the LED, respectively, could be adjusted in 3 DoF. The complex signal obtained from the PD fixed to the 1st stage on the bottom of the tower, was filtered of noise, levelled, and amplified. The cleared signal was digitized before being sent over to the system controller. The fluidics on the platform consisted of water and oil bottles as source containers for the pumps, T-junctions joining together pumps, pressure sensors and the microfluidic droplet generation chip, the chip itself, and the waste bottle as the output container of the setup. Lastly, the system controller was a quad-core SBC whose cores were split among 4 system control tasks. Tasks such as controlling the pumps, interpreting the droplet signal, calculating the droplet generation feedback parameters, and communicating with the user. The droplet generation was controllable both by droplet size and by generation rate. With the ability to specify a target for droplet formation frequency, the available feedback rate, limited to accommodate low-power operation and portability, could be maximized. Moreover, the formation rate could be synchronized with the actuation rate of the piezoelectric micropumps, thereby minimizing the influence of the pressure pulsations on droplet size CV%. During evaluation, this effect was most noticeable instead at the first harmonic of the pumping frequency, reaching the lowest recorded CVs of 1.77% and 6.67% for size and generation rate, respectively.

Overall, the platform satisfied its given CV goals, with droplet sizes reaching below 5% and for generation rates below 10%. While the values were indeed reached, the average CVs collected over multiple droplet size and generation rate combinations were not within those limits, leaving much room for improvement. Additionally, while the generation rates were evaluated up to ~800 Hz, during calibration the system showed its capability in reaching much further beyond.

Having kept the designs simple, low-power, affordable, consisting of widely available commercial components, and easily replicable 3D printed structural parts, the platform maintained the aimed properties of modularity and transferability. How the final platform compares to other controlled droplet generation setups documented in the literature is summarized in paper 3 (**Appendix 3 – Table 1**).

3.5.2 Platform Specifications

Table 14. CogniFlow-Drop (2023) specifications.

Category	Value	
Module 1:	Flow regulation	
	Number of pumps	2
	Pump description	Bartels, mp6-liq, piezoelectric, dual diaphragm
	Number of drivers	2
	Driver description	Bartels, mp-Highdriver, 10-250 V _{PP} , 50-800 Hz
	Pumping frequency (water)	~200 Hz
	Pumping frequency (oil)	~320 Hz (HFE 7500) 50 Hz (Mineral oil) (at mp-Highdriver limit)
	Number of sensors	3
	Sensor description	Honeywell, MPRLS0015PG0000SA pressure-based, typ. range (0 to 103 kPa)
	Controller	ESP32 DevKitC-32U
Feedback rate	~166 Hz	
Module 2:	Droplet sensor	
	Illumination	Cold white, 1 W LED, driven with ~150 mA @ 5V
	Light detector	Osram SFH 2240, photodiode
	Detector signal amplification	x10e ⁶ (1 MV/A) (Transimpedance amplifier circuit)
	ROI focusing zoom	20x (microscope lens)
	Signal filter parameters	~7.26 kHz (generation frequency cutoff), 2 nd order Sallen-Key LPF
	Processed signal properties	Capacitive DC decoupling (~50 Hz HPF), 2.5 V DC offset, inverted, extra 5 - ~46 times adjustable amplification, within 0 – 5 V output range
	ADC	Texas Instruments, ADS8681, 1 MHz max. sampling rate, 16-bit, SPI
Module 3:	System Controller	
	Processing unit	Broadcom BCM2711 (Raspberry Pi 4B)
	OS	Ubuntu desktop, ver. 21.10
	Code	Python 3.9, ~150 KB (main algorithm), C++, ~28 KB (SPI communication module)
	UI	Wi-Fi, Python GUI (eCAL, v5.9.5)
Estimated max. power consumption	~8.0 W	
Platform dimensions (footprint)	330x220 mm	
BOM Cost (Q2 2023)	~650 €	

3.5.3 Considerations

During the evaluation phase, while not impeding operation, several issues crept up which ought to be addressed in any upcoming versions of the platform.

- I. With the feature to tilt the microfluidic chip in the droplet detection column, shifting the droplet slightly out of alignment was made possible. Cutting off some of the visible edges from a passing droplet could still result in a good enough signal. The change in the droplet signal shape allowed for mischaracterization of the oil type that was used.
- II. While some size and generation rate combinations reached below 2% size monodispersity, the typical CV was closer to 10%. This could be tied to the FFD favoring certain combinations by design or how effective the liquid recipes are, but there are more contributors that could be investigated – such as the OS latency on the RPI:
 - a. Impact of the OS latency to the droplet identification task, made significant by high monitoring rates of the writable queue flag, could be reduced by replacing the queue flag with an indicator closer to hardware – an external GPIO connection. One pin on the Raspberry Pi header could be dedicated to the system control task, which would control its digital output value to be HIGH or LOW. A second pin, wired to the first, could be dedicated for the droplet identification task, which when read, could significantly reduce memory overhead and thereby, possibly the OS latency.
 - b. Another option could be to reduce the required loop speed for the task allotted to droplet detection on the RPI. This could be done by transferring the communication with the droplet detection ADC to an external standalone processing unit. With less emphasis on the loop speed, typical inter-task communication delays of $\sim 100 \mu\text{s}$ could seem unnoticeable in comparison.
 - such as the relatively slow pump controller task (avg. $\sim 19 \text{ ms}$):
 - a. The pump controller (ESP32) and system controller (RPI) communication method over USB was already inherently slower than other tasks because of the pressure sensor sampling rate.
 - c. The serial communication algorithm itself on the pump controller task was unoptimized as it had to hold communication with another task, which calculated the new target pressures, in equally high priority.
 - such as the unoptimized droplet size and generation rate PID controllers.
 - such as the large PZT pump driver waveform amplitude step size.
 - such as the unmatched PZT pump driving frequencies.
- III. As droplets were relatively gauged in the units of volts, converting them to units of physical dimensions proved difficult without a general reference point. When the characterization of the fluidic setup was completed, any slight change in the height or orientation of the microfluidic chip, in reference to the aligned sensor, caused the loss of any known links between them. In a dynamic setup as such, a single PD is not enough to identify the droplet's physical measurements without a calibrated reference.

- IV. While the pumps are generally inert to many liquids, with smooth plastic interiors, the danger of clogging the pumps with organic material, such as surfactant or cells, is slim. However, contamination is a more likely scenario. In mitigation, the pumps could be made to instead push a liquid that is both clean and immiscible with the target liquid. This method adds an additional, significant pressure load, which may need multiple PZT micropumps placed in series to overcome.
- V. As the droplet detector was sensitive to mechanical vibrations from the nearby environment, the setup ought to be placed away from known vibration sources. Additionally, preferably, placed on vibration dampening material.
- VI. With a capacitively AC coupled droplet signal balancing over a fixed 2.5 V DC bias in the DSSP circuit, the extreme ends of generable droplet sizes would produce signals with short duration peaks on different sides of the bias level. The recorded waveforms become top or bottom-heavy, leading the median voltage between the signal's maximum and minimum values to shift away from the bias level. If the amplitude of the signal is large enough, in the scenario of a shifted median, one side of the signal will cross the available voltage rails in the 0 to 5 V window, causing droplet readings to become misleading.

With less serious considerations, the platform shows potential in the following aspects:

- I. With an ability to observe droplet generation parameters, the degradation of the fluidics could be gauged also in a pressure-based closed-loop system. This could enable estimating the lifetime of the fluidic device. Furthermore, sudden changes could be used as indicators for possible clogging.
- II. With a tiltable microfluidic chip mount in the droplet detection setup, the angle of the chip also tilts the angle of the channel and thereby the motion of a passing droplet. Since the illumination source is a brightfield LED, the droplet is essentially transparent. Anything encapsulated in the droplet ought to leave its own detectable shadow. By using a microscope lens with a fixed focal distance, the angled motion of a passing droplet allows for the focal distance to 'scan' through the droplet, possibly increasing the signal from the encapsulated particle enough to be detected.
- III. Piezoelectric pumping frequency has already shown hints of having a secondary influence on droplet generation. There is potential in altering the piezoelectric element driving waveform shape and frequency components – possibly altering its interactions with droplet generation or other processes such as passive particle encapsulation rates.
- IV. When characterizing a fluidic setup on this platform, it could be possible to estimate a preferred droplet size and/or generation frequency of the setup. Combinations leading to optimal CV% could be found for various chip designs.

4 Explorative Platform Modifications to Extend the Utility of PZT Diaphragm Micropumps in Droplet Generation

This chapter addresses several of the more impactful issues brought to attention at the end of Chapter 3 regarding the relatively high average CV% of the generated droplets. Among the suggested solutions, a piezoelectric micropump driving methodology is proposed, with features to increase its control resolution and explore possible benefits in the pulsatile characteristics of the pumps.

The chapter describes and evaluates the hardware upgrades made to CogniFlow-Drop to improve its CV% in response to **RQ4**, relying on the following publications:

Forthcoming (Publication IV): R. Jõemaa, T. Pardy. “Modular, dual-tone piezoelectric micropump driver for low cost, portable droplet generation,” 2024 19th Biennial Baltic Electronic Conference (BEC), IEEE, 2024.

Other related publications: R. Jõemaa, T. Pardy, “Integrated modular multi-tone piezoelectric element driver and method of driving modular multi-tone piezoelectric element driver for pressure generation,” patent application. Priority number P202400014, Estonia, 2024.

4.1 Chapter Overview

4.1.1 Motivation

In Chapter 3, a modular, low-cost, actively controlled droplet generation platform was developed. Droplet generation rate and droplet size were regulated using PID controllers running on a Raspberry Pi 4B (RPI) single-board computer (SBC). The 4 cores of the RPI were allocated separately to four tasks. Running in parallel using Python’s multiprocessing library, the tasks were to communicate with a droplet sensor module, a pumping and pressure sensor module, a remote user interface and to update the PID controllers together with inter-process communication task. Droplets generated with this platform were detected and measured from the shadows produced by light refraction at their phase-transition regions. This method introduced an offset between platform-measured and the actual droplet size. This offset adhered largely to the densities of the selected immiscible phases (e.g., oil and water) which determined the size of the phase-transition region and thereby the relationship between the measured shadow and the real cross-sectional area of the droplet. The preliminary results of the CogniFlow-Drop platform did not show the median coefficient of variability (CV%) of generated droplet sizes below 5%. As to why, several problems were identified. A few possible causes were linked to limitations in sensory data acquisition – of both optical (a, b, c) and pressure (d) data.

- a) The most significant limitation in optical data acquisition stemmed from using a non-real-time operating system (OS) running on the RPI, resulting in data acquisition rates becoming unstable. With latency in the CPU task-scheduler, occasional delays of up to several milliseconds would irregularly recur during a droplet measurement. The resulting data loss could occur anywhere along a droplet ‘waveform’, able to cause errors in both droplet size and droplet generation rate calculations. This issue was partially mitigated in software, by discarding droplet readings where the delay between data points exceeded a third of the droplet period – being updated by a moving average period.

As the cutoff delay was a static percentage, the filter was bound to be leaky. Unfiltered false readings would proceed to affect the PID controllers and cause instability spikes in the droplet generation process. The transfer of the instability spikes through the PIDs to the pumps was lessened with a set of additional moving parameter windows, set to average the outputs of the PID controllers. With optimizing the size of the moving average window and the data loss delay cutoff percentage, or making them dynamic, the impact of the erroneous droplet readings could theoretically be reduced enough to achieve a stable CV% less than 5%, however, this would come at an increasing loss of tracked/logged droplets.

- b) A secondary limitation in the optical data acquisition was using a fixed amplification on the PD-TIA signal before arriving at the ADC. In scenarios where generated droplets would need to change over a wide range of sizes, the amplification rate would be set by the largest generated droplet, to fit its absorption waveform into the available measurable window. Yet, this would also fix the lower limit to droplet sizes that are above the detection levels (safely above the noise floor). Moreover, as the droplet and its subsequent absorption waveform amplitude shrinks in the measurable window, so does the relative resolution.
- c) A tertiary limitation in the optical data acquisition was the usage of a fixed DC offset of the PD-TIA signal. Because the level of illumination was not always easily determinably, the baseline voltage of the PD-TIA during inactivity settled at different levels for different optical setups – either by use of different microscope lenses, pinhole diameters and even LEDs. To spot smaller droplets, knowing the PD-TIA baseline voltage was critical, as set lines had to be crossed for detection to be possible. To avoid having to explicitly measure the baseline voltage before each experiment, the settling level was decoupled from the PD-TIA and fixed to a known constant. However, as droplets can be generated with different liquids and illuminated by different spectrums, the resulting absorption waveforms are often non-symmetrical, non-sinusoidal, and rather made of spikes with irregular shapes and with irregular spacing. For a capacitor-decoupled level-shifted signal, such irregularities produce a weighted real average (point at equal distance of the measured minimum and maximum) that does not align with the fixed baseline. In edge case scenarios, the weighted waveform can shift one of its peaks across the limits of the measurable window, resulting in lost data and the ensuing inaccuracies in droplet size control.
- d) The main limitation in the acquisition of pressure data was related to its maximum achieved sampling rate of ~ 166 Hz. This sampling rate was not only slower than the typical droplet generation rate, but also slower than the used pumping frequencies of ~ 200 Hz and ~ 320 Hz, for water and fluorinated oil, respectively. On one hand, in a pulsatile pumping system, this slack in measurement speed could improve stability – by not sending every pumped pressure spike into the pressure control PID. Yet without the reaction to pumping pressure spikes, the pressure stabilization would be superficial.

Another possible cause for unstable droplet generation was linked to the piezoelectric pump drivers. The COTS drivers used digitally generated waveforms. In contrast to analog waveform generators at comparable scale and cost, digitally produced waveforms are more stable, predictable, and reproducible, as they are influenced less by thermal drift. But it also has a critical downside – the accompanying low resolution digitized amplitude. In the case of the used Bartels Highdriver the amplitude control resolution was split across just 32 steps. With the piezo pump driving waveform ranging up to ~255 V in amplitude, the size of each step was close to 8V. Considering a common scenario where the pumped pressure target happens to correspond to an amplitude level residing between two of amplitude steps, to stabilize at the requested pressure level, the driver must repeatedly alternate the waveform amplitude with the minimum 8V jumps.

When considering addressing the concern of point d), another bottleneck was present in the system algorithm on RPI. Namely, the cycle rate of the pump control loop on RPI averaged around 50 Hz, well below the pressure sensor sampling rate. In combination, solutions could be found in the form of faster pressure sensors and methods that reduce the computational load on the RPI such that task could be reorganized to be more equally weighted. An option to reduce the computational load on RPI could be to integrate an additional MCU to the platform. With an additional dual-core MCU, such as the ESP32, tasks most vulnerable to OS latency such as SPI communication with the ADC and its data analysis (droplet identification), could be transferred to from the RPI.

All CV% optimization problems stem from the Electronics column and require the modification of all modules besides fluidics (**Fig. 28**).

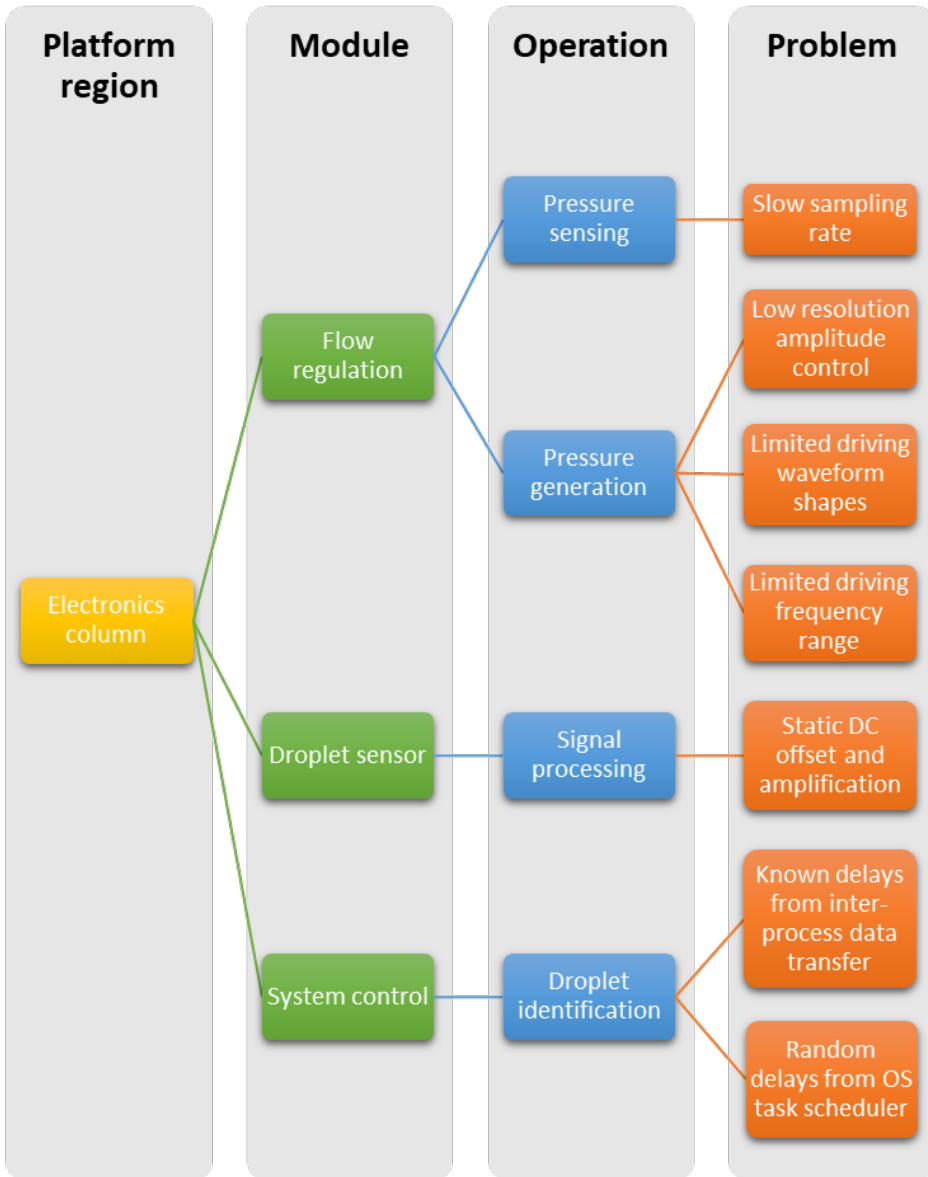


Figure 28. CogniFlow-Drop (2023) platform problems and their origin hierarchy.

4.1.2 Background of Piezoelectrically Produced Pulsations for Droplet Manipulation

A piezoelectric ceramic material such as PZT is a crystallized structure of dipolar unit cells. At the center of each unit cell lies a positive Titanium or Zirconium ion. By pulling the ions off center the unit cell becomes elongated, unsymmetrical, and forms a dipole, which is used to produce a static electric field over the material. During material synthesis, the deposition and placement of the central ions is chaotic. The resulting dipoles are randomly aligned, forming a net neutral polarization over the ceramic. When making the

material applicable as a piezoelectric transducer (PET), it's heated and poled in a strong electric field [126]. The externally applied electric field pulls on the central ions, elongating the unit cells into dipoles in alignment throughout the material body. After cooling, the ceramic stabilizes into an elongated shape with a desired directional polarity. When an electric field is re-applied across the material, the central ions are forced to move, resulting in longitudinal expansion and transverse contraction or longitudinal contraction and transverse expansion of the ceramic with a counter- or codirectional alignment with the dipole direction, respectively [126].

In microfluidics, PETs are commonly used as sound or pulsatile pressure generators as they physically deform under an alternating electric field [127]. The transfer of produced kinetic vibrations into liquid is facilitated through direct or indirect contact between the liquid and the actuator. For indirect contact, the actuation is performed near a microfluidic channel, vibrating its walls to introduce pressure waves into the flow – a field known as acoustofluidics [128], [129]. Acoustophoresis, a subset of acoustofluidics, focuses on particle and droplet manipulation with acoustics [130]. To interact with particles in a microfluidic flow, a common method entails oscillations with wavelengths small enough (e.g., $\sim 30 \mu\text{m}$ in water at $\sim 50 \text{ MHz}$) to fit in multiples across the channel width to create standing waves and pressure nodes, used to attract and influence the flow trajectory of a particle [131], [132]. This effect is often used in active droplet sorting [66], [131], [132]. In case of direct contact, actuation consists of PETs used as diaphragm pumps where the diaphragm is the ceramic itself, typically in the shape of a disk. With an alternating voltage generated across the piezo actuator, the diaphragm deforms to pull and push small volumes of liquid or gas into and out of a compartment housing the diaphragm. This motion produces pressure waves which propagate longitudinally through the tubing and microfluidic channels with the velocity of sound, specific to the pumped media.

For DIW at 20°C in atmospheric pressure ($\sim 0.1 \text{ MPa}$) soundwaves propagate at $\sim 1483 \text{ m/s}$ [133], whereas in HFE-7500 oil, the propagation speed is about 673.7 m/s [134]. At such velocities, a piezoelectric micropump (e.g., Bartels mp6-liq) operating at rates of 200 Hz for DIW or 320 Hz for HFE-7500, produces wavelengths that well exceed the length of the entire platform's fluidic pathway. However, in contrast to acoustophoresis, where waves need to be small enough to form standing waves across the channel width, in piezoelectric pumping, the periodically generated pressure waves need but to travel through the flow path to interact with droplets, more specifically droplet formation.

To illustrate an electronic equivalent of the fluidics involved in pulsatile droplet formation, a piezoelectric micropump behaves as an AC power source, its valves as a halfwave rectifier, the tubing and microfluidic channels as resistors, and the chip's outlet as ground [135]. Additionally, when tubing or channel walls are made of silicone or PDMS, the structural material exhibits compliance to deformation. As pressure rises, part of the kinetic energy is stored in the deforming structure which in essence behaves as a capacitor [136]. Due to flow channel dimensions typically shrinking from tubing to the microfluidic chip and differently sized channel segments within the chip, a significant portion of the kinetic energy from the traveling pressure wave is reflected – analogous to impedance mismatch. What can be measured across the FFD (RC equivalent) becomes a smoothed pressure level with relatively small pulsations remaining [137].

At the cross-junction of an FFD, where pulsatile flows of water and oil join to generate droplets, the crossing pressure waves, due to differing pumping frequencies and propagation speeds, interfere dynamically on top of the smoothed pressure level.

This interference appeared to have a significant impact on droplet formation. As shown in Chapter 3, the smallest average CVs were achieved with a droplet generation rate control target set to 400 Hz – a harmonic of the DIW pumping frequency. The rate control target preference was also noticeable at 200 Hz. Similar influence to generated droplet size has been observed in steady-type flows with deliberately added vibrations introduced into the dispersed phase flow [93], [138], [139]. Pulsations directed to the cross-junction of an FFD have also been shown to correlate with the droplet/bubble size [140]. Deliberate pulsations have been demonstrated to enable control of droplet size, generation rate, and spacing directly with the pulsation frequency [141].

While relying on inherently pulsatile flow generators, pumping frequencies optimized for specific liquid media, ought to remain fixed as primary pulsations. However, as PETs can be driven with practically any complex waveform, the pumping waveform could be modified to introduce additional layers of control to the droplet generation process. Based on observation, without eliminating the primary pumping frequency of 200 Hz and 320 Hz for DIW and FO respectively, a secondary pumping frequency could be introduced into the mp6-liq micropump driving waveform to move towards matched pumping pulsations with droplet formation rate. As the previously used mp-Highdriver driving waveform selection is insufficient, a different driver is required. To maintain the objectives of the droplet generation platform, the driver ought to be of similar cost and compact enough to retain the portability of the pumping module. Such commercial drivers, however, typically lack on-board custom signal generation and/or focus on driving SCPs [142]–[144]. Likewise with available commercial reference designs, waveforms are fixed and rectangular [145], [146]. Rectangular spikes carry odd-numbered harmonics which tend to produce complex pressure oscillations [147] and can be less power efficient compared to sine waves [148]. As such oscillations could interfere with the effects of a controlled superimposition of a secondary wave, purer driving signals ought to be used.

4.1.3 Design Criteria

To address the problems raised, notable changes were introduced to the electronics column, on PCBs henceforth referred to as PS-B (Pressure Sensor Board), FRC-B (Flow Regulation Control Board), PPD (Piezo Pump Driver) and DSSP-B (Droplet Sensor Signal Processing Board). Modified hardware is indicated on **Fig. 29**.

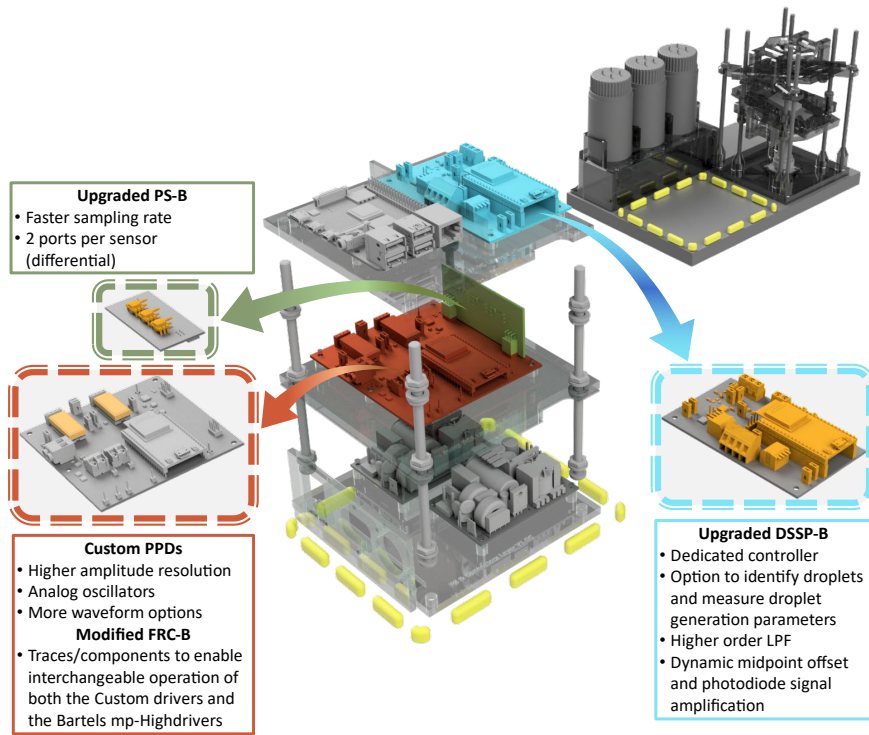


Figure 29. Exploded view of the CogniFlow-Drop platform's electronics column, highlighting PCBs affected by the required hardware modifications.

Table 15. PS-B update criteria.

Category	Value	Additional details
Sensor type	Pressure; non-reactive, liquid compatible coating; differential	Correlating to the need to calculate the differential pressure, pumping type, and liquid media.
Nr. of ports per sensor	2	Differential design.
Nr. of sensors	≥ 2	To measure differential pressure from each liquid phase inlet T-junction to the outlet T-junction. A third differential can monitor the difference between inlet pressures.
Commercial availability of components	All	To ensure design transferability.

Table 16. Criteria for custom PPD.

Category	Value	Additional details
Driver for	Piezoelectric actuators	
Targeted actuator compatibility	mp6-liq, Bartels, dual diaphragms in series	Diaphragms need equal anti-phase high voltage waveforms: Up to 400 Hz and 250 V _{PP} (from +200 V to -50 V)
Targeted driver interchangeability	mp-Highdriver, Bartels, 5V supply, DIP18	Minimized differences in overlapping input/output pins.
Design limited by	Price point of mp-Highdriver, Bartels. (72 €, excl. VAT, Q1 2024)	
On-board driving waveform source type	Analog	Potentially less noise and smoother actuation
On-board waveform generator	Wien-Bridge oscillator (sinewave)	Minimal design, relatively low distortion.
Nr. of generators	2	Primary and secondary.
Primary waveform characteristics	20 - 800 Hz 0 - 250 V _{PP}	Minimum operational requirements for different liquids.
Secondary waveform characteristics	100 - 5000 Hz 0 - 150 V _{PP}	Minimum operational requirements for different droplet generation rates.
Frequency control	Digital potentiometer (DP)	Enables digital control
Nr. of potentiometers	>= 4	At least 2 for each oscillator
DP control method	I2C	Minimum pin count scales better than SPI, and I2C pins are already required by mp-Highdriver.
Amplitude control	Voltage controlled amplifier (VCA), external control signal	High control resolution. External control broadens options to upgrade.
VCA control method	0 – 2.1 V DC	
Nr. of VCAs	2	Primary and secondary.
Output waveform amplification	High voltage (200 V) operational amplifier (OA)	4 amplifiers required for +/- pins of 2 actuators.
High voltage supply	Boost converter (BC), 4.4 – 5.5 V DC input, >= 240 V DC output	To generate enough stable voltage for the OA.
Boost converter control	On-board ~240 V limit Shutdown pin Feedback pin (max. 3.3 V)	
Commercial availability of components	All	To ensure design transferability.

Table 17. FRC-B necessary modifications to accommodate PS-B update and custom PPDs.

Category	Value	Additional details
Additional traces required from ESP32 DevKitC to Custom PPDs (2 drivers)	1x BC shutdown pin 2x BC feedback pin 2x BC PWM clock pin 2x secondary VCA control	Secondary VCA control is provided by on-board 8-bit DAC that is passed through a voltage divider and a buffer OA.
Custom PPD primary VCA control signal source	2x 14-bit DAC, SPI communication	Output passed through buffer OA.
PS-B communication	Largely unchanged SPI communication	Due to limited number of GPIOs on ESP32 DevKitC, pin connections unrelated to SPI were cut back.

Table 18. DSSP-B re-work criteria.

Category	Value	Additional details
Tasks	Signal filtering, AC coupling, Level shifting, Amplification, Signal digitization, Droplet identification*, Droplet gen, parameter measurement*, Data transfer over SPI	Added features require a dedicated controller. * Optional features
Controller	ESP32 DevKitC	2 cores, 200 MHz clock, 2x SPI, I2C, low-cost
Accommodating * Optional features	2x DIP switches (1x4) on SPI lanes	Allows to choose DSSP SPI output between the ESP32 DevKitC and the ADC
Level shifting	Dynamic (0 – 5 V), DP, I2C	
Amplification	Dynamic (1 – 20x), DP, I2C	
Commercial availability of components	All	To ensure design transferability.

4.2 Design Components

4.2.1 Upgrading Pressure Sensors in Flow Regulation Module

To detect and be able to respond to the pumping pressure pulsations, previously missed due to slow sampling rate, MPRLS0015PG0000SA sensors were replaced with ABPDRRV015PDSA3. The switched sensor has more than 10 times higher sampling rate; however, at the cost of maximum pressure sensing resolution. To reduce possible sensor-to-sensor errors and eliminate a few lines of calculation, instead of gage type sensors, differential ones were chosen. Regardless, the number of sensors on the PS-B were kept at three as shown on **Fig. 30**.

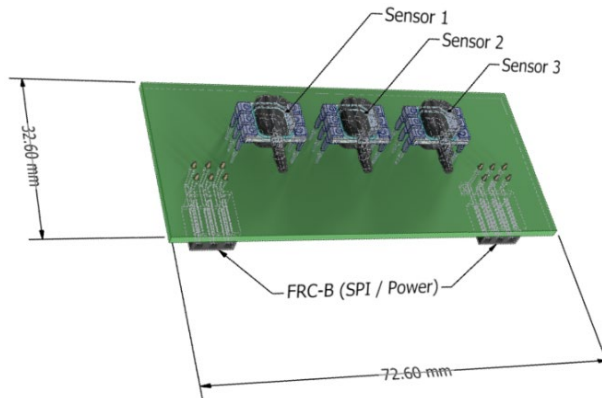


Figure 30. Updated flow regulation sensor board (PS-B) with three high speed differential piezoresistive pressure sensors.

To be able to connect all (3x2) ports of the added differential pressure sensors into the fluidics, 3D printed T-junctions were modified to enable connecting more sensor ports. Sensor 1, connected to outlet T-junction and oil input T-junction, obtained the differential pressure for oil pump feedback. Sensor 3, connected to outlet T-junction and water input T-junction, obtained differential pressure for water pump feedback. Sensor 2, however, was available to measure the pressure difference between water and oil inlet T-junctions.

The updated sensor communication differed from previous by using a 3-pin SPI, excluding MOSI, outputting its 14-bit measurement when the controller pulled low its chip select (CS) and transmitted a clock of 800 kHz. With a 0.46 ms response time, the sensors promised polling rates close to 2 kHz.

4.2.2 Developing Piezoelectric Micropump Drivers for Flow Regulation Module

To reach the required performance and extensive set of features with a custom driver on a footprint no larger than used by the previously used driver (mp-Highdriver, Bartels), at a similar or better price point, required the design to make use of the vertical space. The PPD was designed to consist of layers, connected with board-to-board pin headers, for the additional advantages of modularity and ease of disassembly. Functions were split across three layers:

- Layer 1 (L1) – Waveform generation
- Layer 2 (L2) – Waveform phase and amplitude adjustment
- Layer 3 (L3) – High voltage supply generation

L1 was designed with two analog oscillators using Wien-Bridge configurations, stabilized with a pair of diodes in the feedback loop. The bridges used fixed temperature stable X7R ceramic capacitors. To be able to adjust the frequency of the oscillators, each oscillator bridge used a quad 8-bit 100 k Ω digital potentiometer (MCP4451-104E/ML, Microchip Technology). Due to dimensional, communication, and cost restrictions, the commercial selection was limited, for which both the thermal stability and number of resistive steps suffered in consequence. With four digital potentiometers, in rheostat configuration, per Wien-Bridge oscillator, each resonant RC pair received two potentiometers. The potentiometers were set to be in parallel to significantly increase

the number of possible resistive steps (256^2). Each oscillator produces a sine wave with harmonic distortions $< 2\%$. The generated primary (WF1) and secondary (WF2) waveforms differed primarily in available frequency range, where the minimum objective range for WF1 was 0.01 – 1 kHz and 0.1 – 10 kHz for WF2. The primary waveform needed to cover frequencies available with mp-Highdriver and frequencies previously not attainable, below 50 Hz, which showed better performance with pumping mineral oil [ref RP]. WF2, however, needed to operate in a frequency band where droplet generation was aimed to be. L1 of the PPD also included a voltage-controlled amplifier (VCA) for WF2, produced from a transistor-based differential amplifier (DA). The VCA was adjustable by providing the PPD with a voltage level between ~ 0.2 to 2.2 V, from an external source. With the analog nature of the amplifier, the resolution of an external voltage level could easily be brought above the previously available 5-bit amplitude control on mp-Highdriver. After WF2 amplitude control, WF1 and WF2* were level shifted for merger without DC components. L1 operation concludes by outputting a summed WF(1+2*) signal for L2. L1 PCB can be seen on **Fig. 31**.

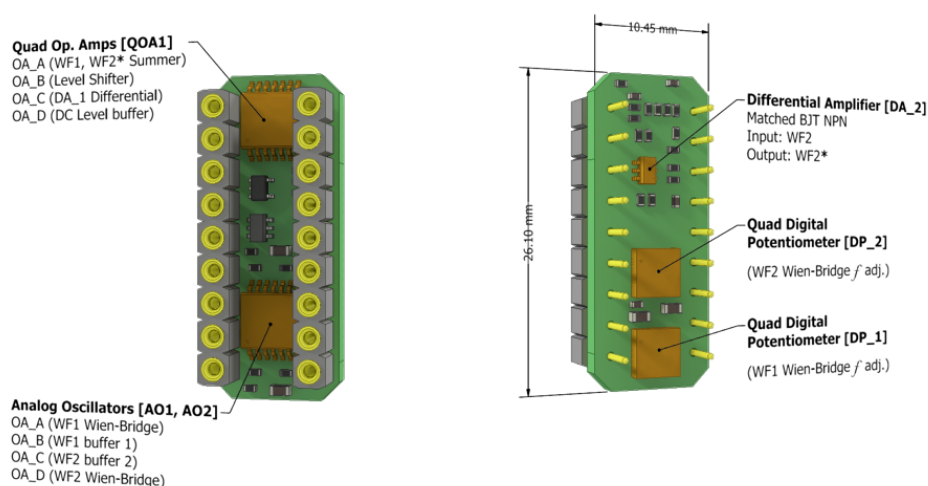


Figure 31. Top (left) and bottom (right) view of the 1st layer PCB of the custom PPD.

L2 of the PPD was designed with 3 quad operational amplifiers (QOA) to form a single WF(1+2*) into four sine waves for the dual-diaphragm piezoelectric micropumps. Considering that the mp6-liq micropumps operate with amplitudes up to 250 V_{PP}, a high voltage and high slew rate QOA was used (HV264TS-G, Microchip Technology). Because the mp6-liq piezoelectric actuators have a 50 V polarization offset (+200 V upper, -50 V lower electrode), a single anti-phase waveform generation was not sufficient. For each of the actuators a positive and negative output was required (P1+, P1-, P2+, P2-).

After WF(1+2*) generation on L1, the wave was connected to an analog switch (ASWCH). The custom PPD was given a feature to allow custom waveforms (WF_EXT) to be used as the pump driving signal. WF_EXT could be connected to a trace leading to a pin on L1 which passed it straight through to L2. On L2, WF_EXT was connected to a comparator (CMP), whose purpose was to detect the presence of WF_EXT and with it, control ASWCH's selection between WF_EXT or WF(1+2*). The selected waveform (WF_x) continued onto another externally controlled VCA with a transistor-based DA. The DA emitter junctions on L1 and L2 were offset with a resistor to operate with only a positive

rail. After the VCA, WFx^* continued through an attenuator OA, labelled as $WFxA$, to be reduced to an amplitude corresponding to $50 V_{PP}$ after final amplification. To create signals for two actuators, $WFxA$ was passed through an inverting OA, resulting in $-WFxA$. Both + and - $WFxA$ were individually through level shifter OAs, followingly labelled as WF_C and WF_B , respectively. Level shifting enabled bringing the waveform V_{min} close to $0.05 V$ which was the lowest detected input level for the high voltage QOA (HV264). At this stage, two anti-phase sine waves were ready to drive the two negative electrodes of the mp6-liq micropump (P1-, P2-). To generate waveforms for the positive electrodes, conveniently, as WF_B (P1-) and WF_C (P2-) corresponded to $50 V_{PP}$ at the output, multiplying them by 4 would produce the missing $200 V_{PP}$ the waves. To reach a combined $250 V_{PP}$ differential for the actuator, the WF_C for (P2-), amplified by 4, labelled as WF_A , was used to drive the positive electrode of the other actuator (P1+). Analogously, WF_B for (P1-), amplified by 4, labelled as WF_D , produced the wave for (P2+). L2 concludes by amplifying WF_A , WF_B , WF_C , and WF_D by a gain of ~ 67.67 and passing the produced waveforms (P1+, P1-, P2-, P2+) down, through L1 to the FRC-B. L2 PCB can be seen on **Fig. 32**.

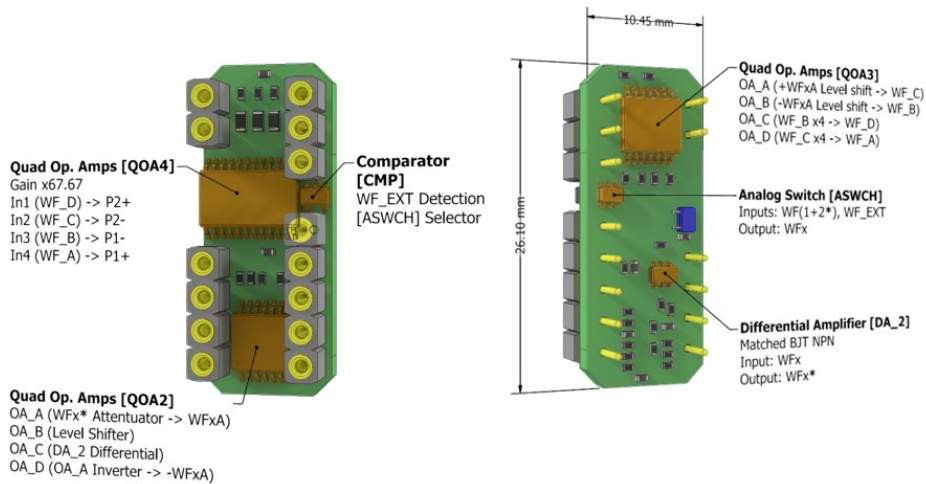


Figure 32. Top (left) and bottom (right) view of the 2nd layer PCB of the custom PPD.

To supply the high voltage QOA on L2 with a DC level above $200 V$, a boost converter was fitted onto L3. L3 contained a simple boost converter circuit, with an inductor, a diode, a smoothing capacitor, and an active switch. To generate voltages beyond $200 V$, with the source voltage of $5 V$ obtained from the FRC-B, very fast and high current switching would be required. Efficient high-speed switching could be achieved with a N-type MOSFET, typically driven with a pulse-width-modulation (PWM) signal, with a varying duty cycle. However, because most gains in efficiency come from the MOSFET's die size, limited space on L3 imposed a limit. Moreover, the larger the discrepancy of ON and OFF time of the boost controller switch (BC-SWCH), the higher the requirements are set for the N-MOS switching speeds. To balance resistive efficiency, switching efficiency, and high voltage requirement, an SMD N-type MOSFET with $100 V$ drain-source voltage (V_{DS}), $\sim 3 m\Omega$ internal resistance (R_{DS}) @ $10 V$ of gate-source voltage (V_{GS}), and $\sim 5 ns$ rise/fall times, was chosen (ISC030N10NM6ATMA1, Infineon Technologies). Switching efficiency was satisfied with a $\sim 5 nF$ input capacitance and a total gate charge of $\sim 55 nC$.

With a V_{DS} of 100 V, the boost converter output was multiplied with a voltage multiplier circuit, easily capable of reaching above 200 V DC. To drive the BC-SWCH, a gate driver (BC-SWCH-GD) was used. To drive the BC-SWCH close to optimal performance, the gate driver was supplied with ~ 9 V generated from the 5 V supply with a charge pump driver (BC-SWCH-GD-CPD). Both BC-SWCH-GD and BC-SWCH-GD-CPD were operated with a single externally supplied 48 kHz PWM. Having opted for a basic boost converter configuration, a single insulated inductor, in series with the source voltage, was used as the energy storage. To balance high magnetic capacity, at low series resistance and small form factor, the saturation current level reduced in compensation. In scenarios where the BC-SWCH would fail into a short circuit, causing current to continue pouring into and through the inductor, quickly exceeding the saturation level, an additional externally controllable switch was added to the circuit. A P-type MOSFET was placed in series before the inductor as the boost converter short circuit control switch (BC-SCC-SWCH). Additional safety features were introduced to the boost converter in the form of over voltage limiting (BC-OVL) and buffered output feedback (BC-OFB-B). BC-OVL was fixed to disable BC-SWCH-GD when the output voltage exceeded ~ 240 V, a level chosen to accommodate providing maximum supply levels for the high voltage QOA on L2, with sufficient headroom for ripple. BC-OFB was led down to FRC-B through L2 and L1, for the external PWM provider to adjust its duty cycle. L3 PCB can be seen on **Fig. 33**.

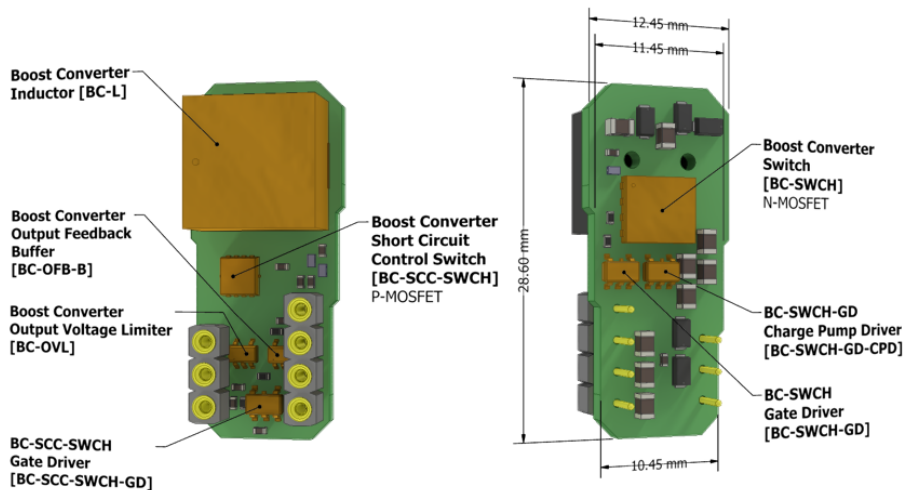


Figure 33. Top (left) and bottom (right) view of the 3rd layer PCB of the custom PPD.

To further take advantage of the layered design of the drivers, the high voltage boost converter output was not only shared from L3 to L2, but also onto FRC-B through L1. This allowed connecting an external high voltage source to FRC-B or by just relocating L3 to a different position on FRC-B. Additionally, because the nature of these drivers is to use high voltage with low current, the high voltage source from one driver could be led to other drivers with insignificant losses to resistances between, reducing the average driver cost.

For the custom PPD to be interchangeable with mp-Highdriver, the pinout of L1, making contact with FRC-B, required additional modifications. As the custom driver would sit in the same socket as an mp-Highdriver, most of the pin functionalities had to

remain the same to not introduce too many hurdles when using either driver. The layout comparison is shown on **Table 19**.

Table 19. Pinout comparison between custom PPD and mp-Highdriver.

PPD pin	mp-Highdriver pin	Driver Top view		mp-Highdriver pin	PPD pin
BC-O	NC	1	18	NC	BC-OFB
BC-SCC	NC	2	17	NC	3.3 VDC
GND	GND	3	16	VDD	5 VDC
PWM	CLK	4	15	/RESET	WF_EXT
VCA (WFx)	CLK_INT	5	14	SDA (I2C)	SDA (I2C)
VCA (WF2)	(VCA) AMP	6	13	SCL (I2C)	SCL (I2C)
WF(1+2*)	(I2C) ADDR	7	12	ADDR (I2C)	ADDR (I2C)
P1+	P1+	8	11	P2+	P2+
P1-	P1-	9	10	P2-	P2-

Functions for custom PPD, which could not find analogues in mp-Highdriver, such as 3.3 VDC supply, BC-O, BC-OFB, and BC-SCC, were placed to pins unconnected on mp-Highdriver. Other safe alterations included pin 4, 5, and 6 (**Table 19**). On pin 4, a clock signal was expected by mp-Highdriver. As it was previously provided by a PWM-capable source from the flow regulation controller (ESP32 DevKitC), changes other than in name were not necessary. CLK_INT on pin 5 of mp-Highdriver was typically not utilized, which left it open for a signal which could be driven on to 0 V when required. Thus, it became the input for the external DAC for WFx VCA without complications. On pin 6, mp-Highdriver expected an adjustable voltage level up to 1.3 V. As it was previously produced by passing an 8-bit DAC (on-board ESP32) output through a voltage divider, without additional hardware changes, it fulfilled the amplitude driving range for secondary waveform (WF2). As what is produced on pin 7 of L1 of the custom PPD is a complex alternating voltage instead of a typically fixed value suitable for an I2C address, the L1 pin 7 was mechanically cut short after assembly, to not connect with FRC-B. For pin 15, as the /RESET pin on mp-Highdriver expected to see VDD or GND, a particular design choice on FRC-B left it manually selectable with a pin header and a jumper. The open pin header offered a point of connection outside of the flow regulation module. To operate the custom PPD without WF_EXT, using the on-board oscillators, WF_EXT ought to be connected to GND.

4.2.3 Facilitative Modifications Accompanying the Changes in Flow Regulation Module

To be able to fully utilize the capabilities of the custom PPDs and the faster, differential pressure sensors, FRC-B required updates in both hardware and software.

4.2.3.1 Hardware Changes on FRC-B

As previously, the AMP and CLK pins on mp-Highdrivers were not used, being driven by I2C commands, the custom PPDs required the operation of the corresponding pins from the MCU, to adjust the amplitude of WF2 and to generate the high voltage supply with a high duty cycle switching PWM. The two custom PPDs required the connection of four

additional traces for short circuit control and boost control feedback. For droplet generation it is imperative that both pumps and thereby both pump drivers operate. If one driver is turned off through the short circuit control switch, question whether the other driver keeps operating or not, becomes moot. Therefore, the ESP32 MCU can operate BC-SCC on all drivers through one pin. Feedback pins, however, required individual traces, which were connected to 12-bit ADCs on the ESP32. To be able to rapidly adjust the amplitude of the final driving waveforms from each driver, two 14-bit DAC chips (DAC70501, Texas Instruments) were placed on the FRC-B. To match the access rates of the DACs with the upgraded pressure sensors, the DACs were addressed over SPI. All four DACs (2x DAC70501, 2x ESP32 DAC) leading to the bases of BJTs in transistor-based differential amplifiers, for additional stability, were passed through a QOA implemented as a set of buffers. Lastly for custom PPD accommodation, the high voltage boost converter outputs, led onto FRC-B through all PPD layers, from both drivers were traced to a 2x2 pin header. This enabled easy wired access from an external +200 VDC supply, or to join the high voltage rails together with jumpers. By joining the rails together, allowed one of the drivers to operate with just L1 and L2.

With significantly increased number of pins dedicated to managing two custom PPDs, all ESP32 GPIOs without a critical secondary function for boot, memory, or serial communication, were utilized. To be able to provide CS signals for the added DACs, two less critical pins were vacated. One of such was an end of conversion (EOC) pin for one of the previous model pressure sensors (MPRLS0015PG0000SA) on PS-B. The other was the shared reset pin for the previous model pressure sensors.

The updated FRC-B with custom PPDs is shown on **Fig. 34**.

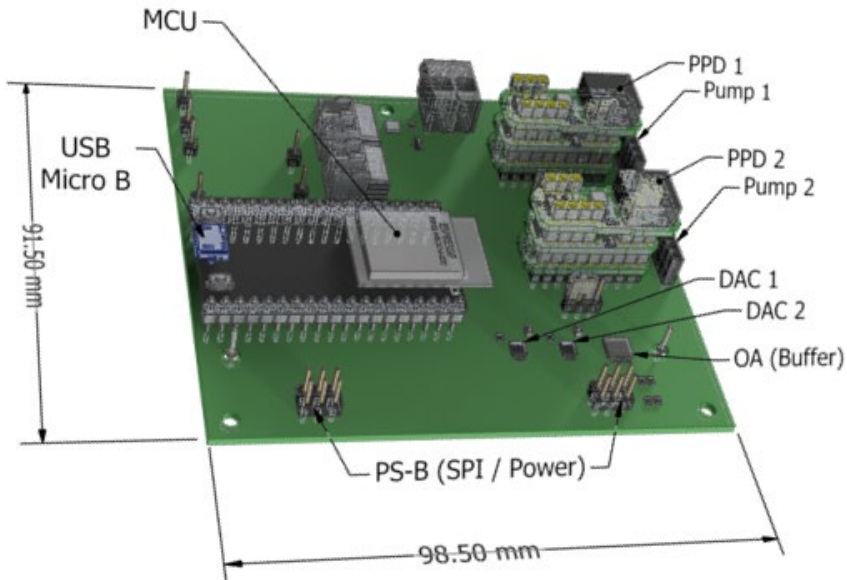


Figure 34. Updated flow regulation control board (FRC-B) with assembled custom PPDs in pump driver sockets.

4.2.3.2 Software Changes on ESP32

To continuously poll the pressure sensors every ~ 0.5 ms, the code, previously relying on FreeRTOS processing, was moved into a regular void loop, as the minimum cycle period for FreeRTOS was 1 ms. Within the ~ 0.5 ms time window, measured differential pressure data, along with step states of both external DACs, and two status bytes, were transmitted off FRC-B via serial. With serial output starting to gradually produce errors beyond 1 000 000 BAUD, to manage with 1 000 000 BAUD within ~ 0.5 ms period, the transmitted data was sent in binary, to be parsed after on the system controller. Additionally, every loop, two PID controllers were managing the custom PPD WFX VCA DACs, serial input was monitored for possible system control commands, and lastly, the boost control PWM duty cycle was operated according to the feedback value.

Code less time critical, such as the PPD frequency control of WF1 and WF2, were managed once at the setup stage over I2C communication, addressing each of the eight digital potentiometers per PPD, and again if a command and values were specified from the system controller.

4.2.4 Modified Droplet Detection

To solve the excessive random and expected delays in the droplet identification process on the system controller (RPI), the process was relocated off from the RPI. To communicate with the droplet sensor ADC and identify droplet related patterns from the PD-TIA signal, a dedicated MCU in the form of ESP32 DevKitC was added onto the DSSP-B, shown on **Fig. 35**.

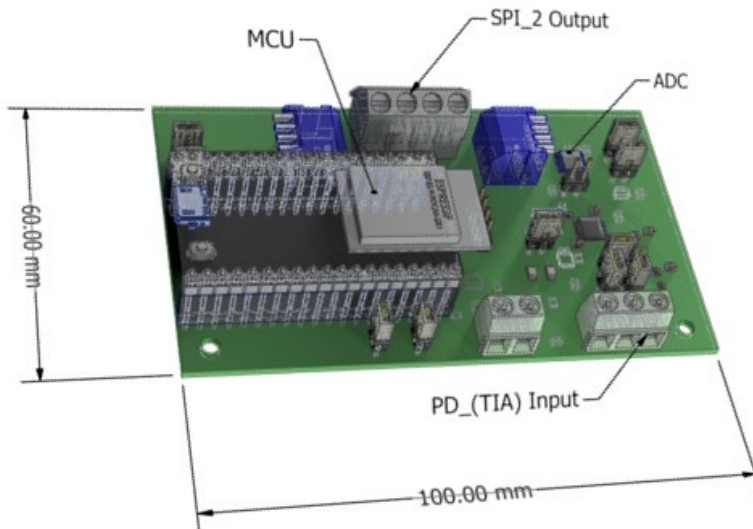


Figure 35. Updated droplet sensor signal processing board (DSSP-B) with a dedicated MCU for droplet identification.

4.2.4.1 Relocating Droplet Identification Algorithm

ESP32 being dual core, allowed one to be dedicated for droplet identification, leaving the other to communicate with the RPI. To access the second core on ESP32, a FreeRTOS task was made for RPI communication. As droplet generation rates were expected at rates close to and beyond 1 kHz, the data transmitted to RPI needed to be minimal and to be transmitted often enough to not lose droplet data. Among the communication options

offered by the ESP32, SPI was potentially the fastest. Moreover, offering two independent SPIs, communicating with two devices at random intervals further affirmed the choice of communication over SPI. However, in a master-slave configuration, the MCU on DSSP-B needed to play the role of the slave device. For RPI to properly converse with the ESP32 over SPI, the RPI required an indicator when to poll the SPI lanes. For this, after a message became ready for transmission on ESP32, as an indication a GPIO pin was raised high, to be pulled low again once the message transmission had ended. As the SPI communication with RPI was written into a FreeRTOS task, limited with the lowest cycle period of 1 ms, to be able to send data of every droplet when droplet generation rates exceeded 1 kHz, after identification, droplet data was placed into a size 4 buffer. This placed the fully capturable droplet generation rate limit at 4 kHz. While droplet-like patterns were identified on ESP32, distinction between single and double peak droplets were made on RPI with computationally lightweight classical logic.

4.2.4.2 Optical Signal Processing

Having added an MCU on DSSP-B, provided a convenient solution in solving the static design of the signal processing offset and amplifier. The OA responsible for holding the offset and signal gain, had its feedback resistor (R_f) and voltage divider in its non-inverting input replaced by digital potentiometers, DP_A and DP_B respectively (Fig. 36).

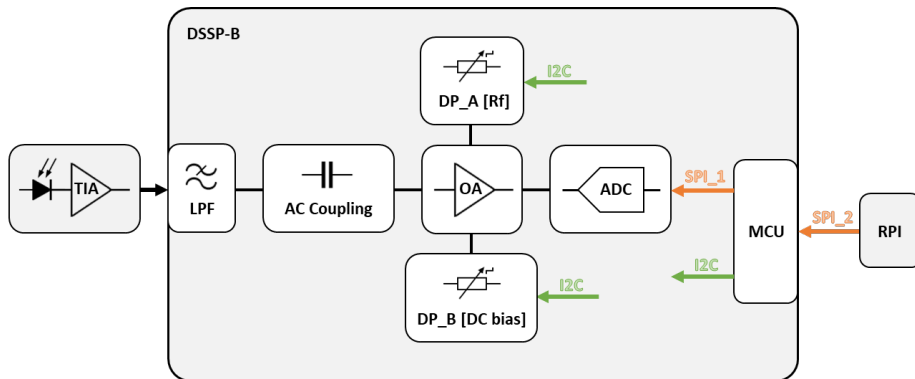


Figure 36. Modified droplet sensor signal processing board (DSSP-B) block diagram.

Using DP_B, the ESP32 was able to adjust the DC bias of the AC coupled PD-TIA signal using the droplet patterns it measured. The bias was adjusted to keep the droplet's V_{max} and V_{min} at roughly equal distances from the OA rails. Using DP_A, the ESP32 was able to control the amplitude of the droplet waveform, to maximize the utilization of the ADC resolution, spread over the $\sim 5V$ detection window. Both DP step values were continually updated and sent to RPI along with every droplet data message. This provided the RPI to calculate the original droplet waveform amplitude.

PD-TIA signal filter design was modified by excluding the HPF and extending the LPF to the 4th order, 10 kHz cutoff frequency.

4.3 Custom PPD Performance Evaluation

4.3.1 Context

To evaluate the placement of the custom PPD against the commercial driver used in Chapter 3 (mp-Highdriver, Bartels), comparisons were done of the following categories:

- Waveform shapes
- Waveform frequency and amplitude range
- Waveform frequency and amplitude control resolution (temperature drift)
- Cost

4.3.2 Results

Bartels mp-Highdriver, with digitally produced driving patterns, offers a selection of an approximated sine, square and two variants of trapezoidal waveform shapes. In contrast, the custom PPD, with its analog oscillators is primarily focused on sinusoidal waveforms. An example of its pumping waveform, at 200 Hz for water pumping, is shown on **Fig. 37**.



Figure 37. Custom PPD unloaded output waveforms at ~ 200 Hz and ~ 250 V_{pp}.

Fig. 37 shows WF1 processed into C1, C2, C3, and C4, from P1-, P1+, P2-, and P2+ driver outputs, respectively. All four waveforms were produced from one source with almost identical processing, resulting in minimal differences in amplitude from phase shifting. For comparison, an unloaded sinewave output from mp-Highdriver is shown on **Fig. 38**.

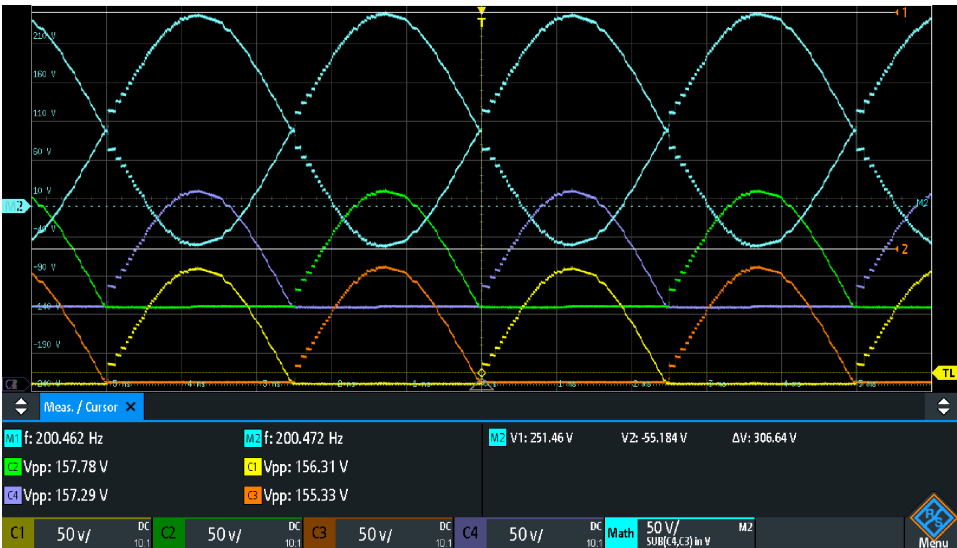


Figure 38. Mp-Highdriver unloaded output waveforms with highest amplitude at ~200 Hz.

Mp-Highdriver output, generated digitally, produced the waveform in steps. The signals were amplified through transistors and without feedback, the driver output was overcompensation for no-load condition, reaching above 300 V_{PP}. When the driver was loaded with one mp6-liq micropump, the waveform smoothed out to a degree due to the 8 nF capacitance of the piezoelectric transducer (PET). Likewise, the amplitude dropped to ~257 V_{PP}. In contrast, the custom PPD showed worsening effect when loaded. The noise of the boost converter switching at 48 kHz became noticeable, translating into a small high frequency sinewave across the PETs. The noise was significantly reduced on the custom PPD which operated without L3 on top, taking the high voltage source from the driver next to it.

By increasing the output of the DAC controlling WF2, a secondary waveform was summed over WF1, as shown in Fig. 39.



Figure 39. WF1 (~200 Hz) and WF2 (~2000 Hz) summed result.

By offsetting the Wien-Bridge notch-frequency producing resistances, brought the WF2 to clipping, resulting in a trapezoidal waveform, as shown on **Fig. 40**.

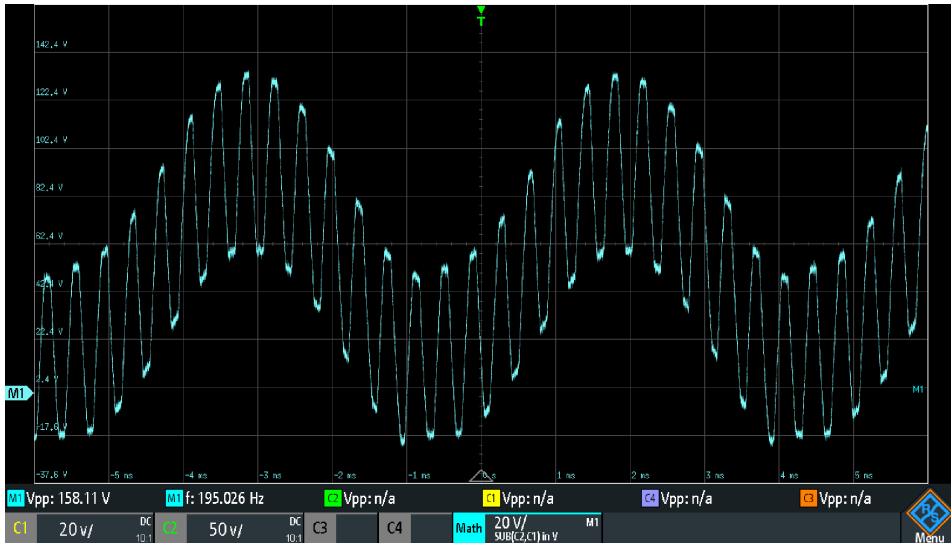


Figure 40. Custom PPD summed sine waves, with WF2 brought to clipping.

By having the ability to adjust the Wien-Bridge resistors independently, provided a secondary amplifier stage in addition to the VCA following the oscillator. Moreover, the clipping range was adjustable, providing many degrees of trapezoidal-like waveforms.

By using 100 kΩ DPs in parallel in the Wien-Bridge oscillator and capacitors of 330 nF and 33 nF for WF1 and WF2 respectively, enabled a wide range of frequencies to be produced. The oscillation frequency for a Wien-Bridge can normally be determined by the RC values (**Eq. 1**).

$$f = \frac{1}{2\pi RC} \quad (1)$$

As there were two DPs in parallel per Wien-Bridge leg, their values could be changed independently to focus in on specific frequency ranges as shown on **Fig. 41 – Left**. **Fig. 41 – Left** shows a comparison between stepping through one DP values while one is fixed (solid line) and while both change simultaneously (dotted line) – indicating that more frequencies can be accessed in the step range by having the DPs in parallel. The full frequency range for WF1 was calculated to be between 9.65 and 2469.31 Hz and for WF2 between 96.46 and 24693.13 Hz. In contrast, the mp-Highdriver provided 256 frequency options, offering 64 steps for four frequency ranges, shown on **Fig. 41 – Right**.

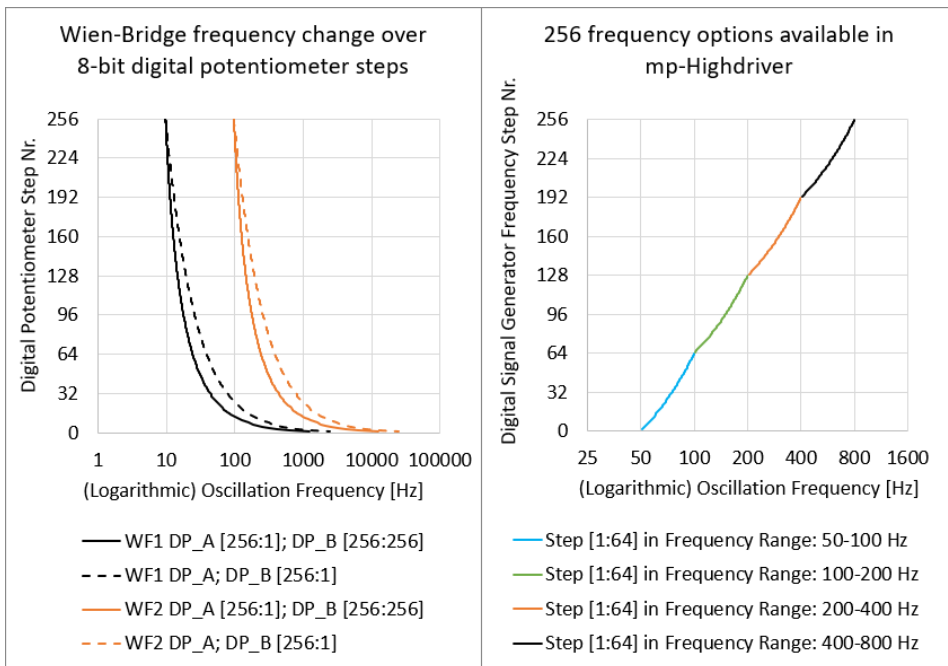


Figure 41. (Left graph) Wien-Bridge Bridge frequency graphs for RC combinations, using 8-bit digital potentiometers in parallel. (Right graph) Mp-Highdriver frequency range over 256 options.

For mp-Highdriver the frequency steps for the four ranges were as follows:

- 50 – 100 Hz range, frequency resolution 0.781215 Hz
- 100 – 200 Hz range, frequency resolution 1.5625 Hz
- 200 – 400 Hz range, frequency resolution 3.125 Hz
- 400 – 800 Hz range, frequency resolution 6.25 Hz

In comparison, the parallel DPs in Wien-Bridge provided logarithmic control, allowing to scale the resolution below 0.02 and 0.2 Hz around 256 frequencies within the full range of WF1 and WF2, respectively.

During custom PPD loaded operation, temperature increase on L2 radiated to L1, warming up the temperature sensitive diodes and capacitors, and causing the Wien-Bridge frequency and amplitude to drift until reaching a stable temperature. As the amplification stages in the waveform processing path through L1 and L2 were mostly fixed, there were two options for compensation. One was to push the VCA control input beyond 2.2 V, as the DAC could provide voltages up to 2.5 V. The other option was to offset the Wien-Bridge leg resistances and amplify WF1 before reaching the VCA.

The custom PPD with the PCBs and all components concluded with a one-off unit cost of ~67 € (~8 € for PCB; ~15.9 € for L1; ~19.7 € for L2; ~23.4 € for L3; excl. VAT) and a projected unit cost of ~35 € (from which ~3.5 € covers the PCB; excl. VAT) for a batch of 100, in contrast to mp-Highdriver's 72 € (excl. VAT, Bartels Mikrotechnik, March 2024).

4.4 Modified CogniFlow-Drop Platform Performance Evaluation

In the following preliminary tests, the processing units on FRC-B and DSSP-B were labelled simply by ESP1 and ESP2, respectively. Fluidic specifications, listed in **Table 20**, were used in all testing stages.

Table 20. Modified CogniFlow-Drop platform evaluation fluidic specifications.

Category	Value
Dispersed phase	Deionized water (DIW)
Continuous phase	HFE 7500 fluorocarbon oil (FO) + 2% w/w surfactant (perfluoropolyether (PFPE)-poly(ethylene glycol) (PEG)-PFPE triblock)
Microfluidic chip type	FFD
Cross-junction dimensions [μm]	125x100

During all tests, water and oil were connected to the FFD – because of which, when only one pump was operated during preliminary driver calibration, part of the pressure exited the chip from the liquid input which was not active, thereby being missed by the differential pressure sensor being specifically monitored. For all tests, the WF1 for DIW was at ~ 200 Hz and ~ 320 Hz for FO.

4.4.1 Context

To test if and how well the updated methods and modules worked in closed-loop droplet generation, the platform was put through the following steps:

- 1) To realize PID pressure control on FRC-B, conversion between the input of the custom PPD's VCA1 DAC was correlated with the corresponding pressure levels measured. For this step, a script was added onto ESP1 to perform a DAC stepwise ramp on command and update the RPI with new pressure readings. RPI logged pressure readings along with the VCA1 DAC step numbers. Due to the non-linearities in pressure response at the extremes, linear regression was mapped over data points starting after pressure had risen above 2000 Pa.
- 2) Pumping PID pressure control coefficients were calculated on RPI and sent back onto ESP1 to use in the PID control test ramp stage. Ramp stages were placed at [10, 35, 65, 95, 65, 35, 10] % of the maximum pressure reached during 1).
- 3) In the following step, platform fluidics, including the operation of the new sensors and pump drivers, were characterized through the setup calibration process used in Ch 3. Coefficients of the logarithmic and 3rd order polynomial were obtained and used for the closed-loop droplet generation stability tests.
- 4) The evaluation concluded with a series of droplet size [V] and generation frequency [Hz] CV% measurements. Alongside CV%, the test revealed the newly relevant RPI and ESP1 communication rate, the feasibility of the ESP32 to manage the droplet identification computational load and more importantly, the data transfer as a slave unit, while both of its cores were utilized to the fullest.

4.4.2 Results

- 1) The DAC controlling pump driver's VCA was ramped up to 88% or step 14418, to reach $\sim 250 V_{pp}$. Before applying a regression line, a largely non-linear region below 2 kPa was excluded as typical droplet generation pressure targets are not implemented below 3 kPa. The resulting pressure to DAC step relationships for both water and oil (**Fig. 42**) correlated strongly with linear regression ($R^2 > 0.99$).

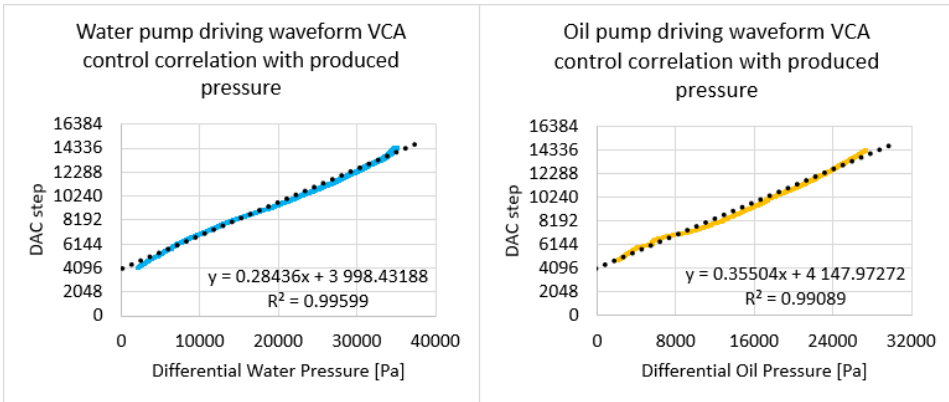


Figure 42. (Left graph) FRC-B water pump driver PID coefficient from VCA controlling DAC and resulting pressure relationship. (Right graph) FRC-B oil pump driver PID coefficient from VCA controlling DAC and resulting pressure relationship.

- 2) The coefficients a and b, from $y = bx + a$, were sent to ESP1 along with K values for the PIDs. For water, the K values were 2.0, 6.0, and 0.001 for Kp, Ki, and Kd, respectively. Calculated in percentages of the maximum measured output pressure of the water pump, water pressure targets (wPa_t) were set accordingly [3511, 12289, 22823, 33356, 22823, 12289, 3511] Pa (**Fig. 43**). The Serial data rate between RPI and ESP1 was measured around 1947 Hz.

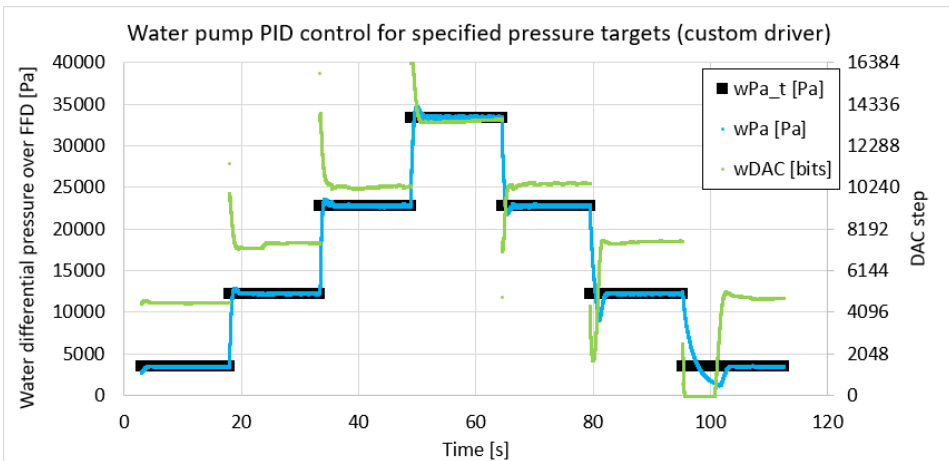


Figure 43. Water pump PID control stabilization at fixed pressure targets with a custom PPD.

The method was repeated for oil with K values set to 4.0, 6.0, and 0.01 for Kp, Ki, and Kd, respectively. Oil pressure targets (oPa_t) were set as [2738, 9583, 17796, 33356, 26010, 9583, 2738] Pa (**Fig. 44**). Serial data rate between RPI and ESP1 was measured around 1956 Hz.

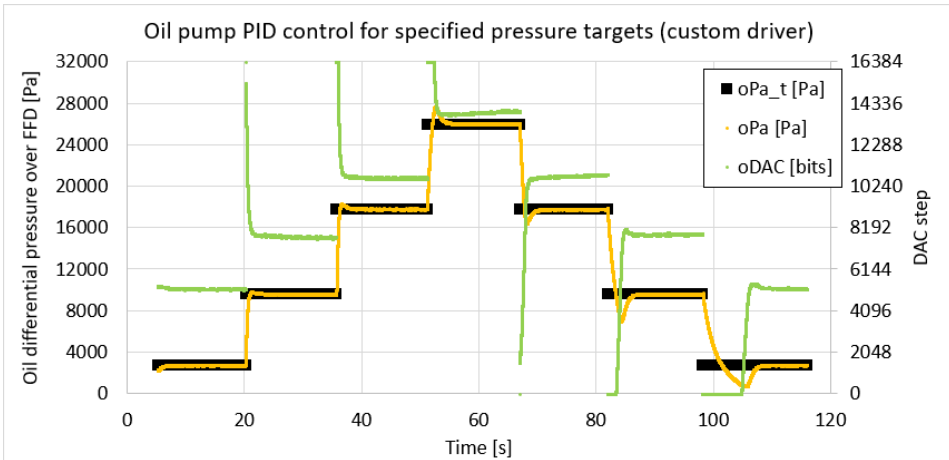


Figure 44. Oil pump PID control stabilization at fixed pressure targets with a custom PPD.

- 3) The calibration process, unchanged from Chapter 3, captured droplet and pressure data from which coefficient between droplet size and oil-water pressure ratio (**Fig. 45 - Left**) and between droplet generation frequency to droplet size ratio and oil pressure (**Fig. 45 - Right**). Measured droplet sizes (voltages) were divided by their gain (x21.25), now calculable directly from the DP status in the last stage dynamic amplifier on DSSP-B – illustrating the scale at which the PD-LED sensor detects droplets. For both relationships, the respective type correlations were > 97%.

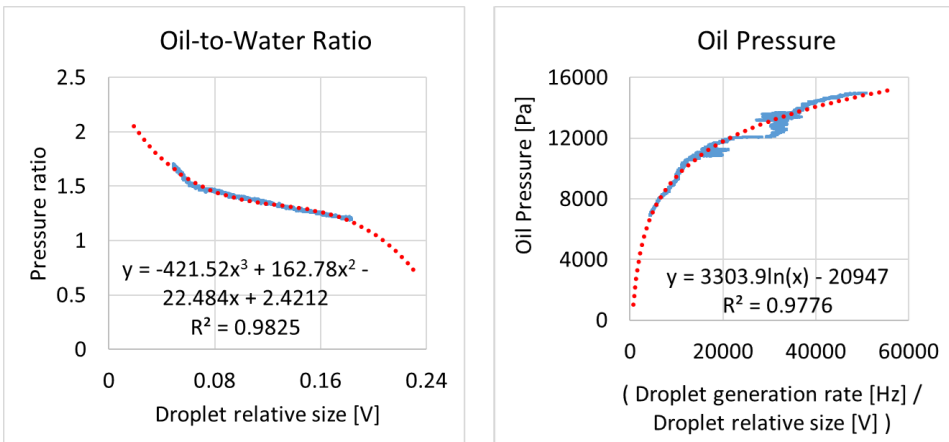


Figure 45. Characteristic 3rd order polynomial (left graph; red dotted line) and logarithmic (right graph; red dotted line) regression lines calculated using droplet size, generation rate and pressure data acquired during droplet PID calibration stages.

- 4) Comparative droplet size and generation rate target CV% obtained with the updated platform hardware can be seen on **Fig. 46**. The best result obtained was with operation frequency target at 800 Hz, reaching below 1% with both droplet generation parametric CVs.

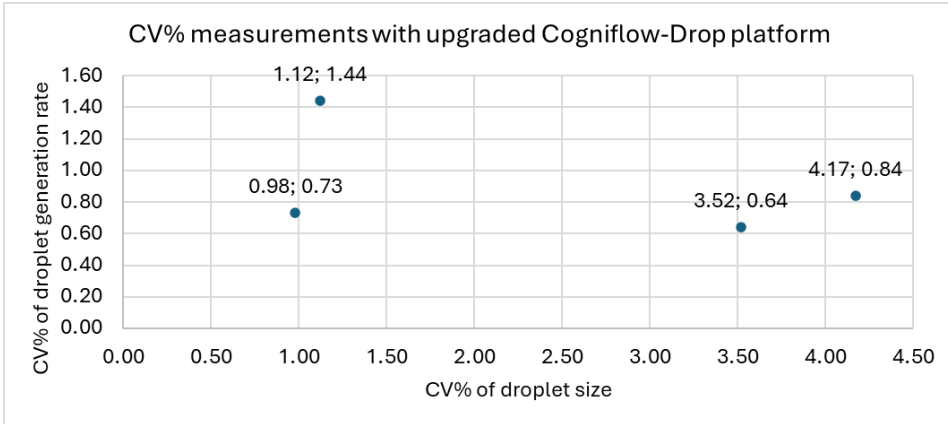


Figure 46. Droplet generation CV% results with updated CogniFlow-Drop platform.

Details of each test sample can be seen in **Table 21**. Column 1 and 3 (droplet target and average measured size respectively) show amplitudes derived from dividing the ADC-measured amplitudes with the dynamic amplifier gain (x21.25). The voltage values represent filtered droplet sensor signal amplitudes. It can be seen from Column 3 and 4, that the frequency control was significantly more accurate and stable (Columns 5 and 6). Droplet generation reached below 5% CV with > 2000 Hz generation rate.

Table 21. Modified CogniFlow-Drop CV% measurements at 500, 800, 1500 and 2000 Hz generation targets.

Size T [V]	Freq. T [Hz]	Avg Size [V]	Avg. Freq. [Hz]	Size CV [%]	Freq. CV [%]	ADC-ESP32 SPI rate [Hz]	Avg. w pressure [kPa]	Avg. o pressure [kPa]
0.25	500	0.19	500	1.12	1.44	259826	6.0	7.2
0.20	800	0.17	804	0.98	0.73	259060	7.8	9.3
0.15	1500	0.14	1502	3.52	0.64	257407	10.8	13.0
0.15	2000	0.13	2050	4.17	0.84	256071	12.0	14.4

4.5 Chapter Summary

4.5.1 Discussion

In efforts to improve the responsiveness of pressure PID control in flow regulation module, pressure sensors were upgraded with an increased sampling rate of ~2.17 kHz enabling cycling rate on the pumping module controller to be raised from ~166 Hz to ~1950 Hz. To improve the stability of the pressure PID control, piezoelectric micropumps received custom drivers with improved amplitude resolution from ~8 V to ~0.02 V. To accommodate the updated driver and pressure sensors, pump controller PCB received

updates in both hardware and firmware. As the custom drivers housed a boost converter capable of generating higher than, but hardware limited to ~ 240 V, without a clock source, the pump controller was responsible for generating the clock for the drivers with an onboard PWM and adjust its duty cycle in response to the high voltage DC output feedback from the boost converter. The developed driver was designed with three layers, connected by board-to-board pins and headers. The lowest layer housed two frequency adjustable Wien-Bridge oscillators for the primary and secondary pump driving sinewaves, with a VCA for the secondary waveform, summed before heading to the high-voltage amplification layer. The second layer housed a VCA for the summed signal before being amplified with a 200V QOA, producing two pairs of differential antiphase waveforms for the mp6-liq piezoelectric diaphragms. Additionally, the second layer was designed with the ability to switch between the driver-generated and a custom externally supplied waveform, which is yet to be investigated. The third layer housed the high voltage boost converter, using the ~ 5 VDC obtained via USB as the source. In summary, the custom driver was designed to be relatively easily interchangeable with the Bartel's mp-Highdriver, by having the same DIP18 footprint and a similar price point; to have a driver that can be easily modified to control different piezoelectric micropumps, single or dual diaphragm types; most importantly, to have a driver that can enable experimental evaluation of unusual, unique driving waveforms, locally on the CogniFlow-Drop platform.

As a solution against the OS scheduling latency and inter-process delays on the RPI, the droplet identification process and communication with the droplet sensor ADC was relocated to the updated DSSP PCB. The DSSP input filter was replaced with a ~ 10 kHz 4th order LPF. The static signal DC bias and potentiometer-adjustable amplifier were made dynamically controllable through digital potentiometers. In control of the dynamic offset and amplification; SPI communication with the ADC and RPI, was an ESP32 DevKitC. The relocated droplet identification process increased the sampling rate of the ADC from ~ 153 kHz to ~ 256 kHz. Following the modifications, droplet identification was able to keep up with droplet generation rates of up to 4 kHz – limited by the SPI between RPI and ESP32 being implemented in unoptimized custom code.

In combination, the improvements in operation frequency and higher degree of pump control, the CV% numbers were successfully brought down below 5% within the droplet generation range of 500-2000 Hz, on occasion even below 1% for both droplet size (0.98%) and generation rate (0.73%).

4.5.2 Updated Platform Specifications

Table 22. Automated, transferable droplet generation platform specifications.

Category	Value	
Module 1:	Flow regulation	
	Number of pumps	2
	Pump description	Bartels, mp6-liq, piezoelectric, dual diaphragm
	Number of drivers	2
	Driver description	Custom, DIP18, 0-250 V _{PP} , 0.01–1 kHz (Primary), 0.1–10 kHz (Secondary)
	Pumping frequency (water)	~200 Hz
	Pumping frequency (oil)	~320 Hz (HFE 7500) ~20 Hz (Mineral oil)
	Number of sensors	3
	Sensor description	Honeywell, ABPDRRV015PDSA3 pressure-based, typ. range (-103 to 103 kPa)
	Controller	ESP32 DevKitC-32U
Feedback rate	~1950 Hz	
Module 2:	Droplet sensor	
	Illumination	L128-6580CA3500001, Lumileds, 6500 K, Cool White LED, driven with ~360 mW
	Light detector	Osram SFH 2240 (photodiode)
	Detector signal amplification	x10e ⁶ (1 MV/A) (Transimpedance amplifier circuit)
	ROI focusing zoom	20x (microscope lens)
	Signal filter parameters	~10.0 kHz (generation frequency cutoff), 4 th order Butterworth LPF
	Processed signal properties	Capacitive DC decoupling (~50 Hz HPF), dynamic DC offset, inverted, dynamic amplification up to ~21.25x, within 0 – 5 V output range
	ADC	Texas Instruments, ADS8681, 1 MHz max. sampling rate, 16-bit, SPI
	Controller	ESP32 DevKitC-32U
	Max. droplet rate	4000 Hz (limited in software)
Module 3:	System Controller	
	Processing unit	Broadcom BCM2711 (Raspberry Pi 4B)
	OS	Ubuntu desktop, ver. 21.10
	Code	Python 3.9, ~117 KB (main algorithm), C++, ~42 KB (SPI and Serial com. modules)
UI	Wi-Fi, Python GUI (eCAL, v5.9.5)	
Estimated max. power consumption of the platform	~9.5 W	
Platform dimensions (footprint)	330x220 mm	
BOM Cost (Q1 2024)	~750 €	

4.5.3 Open Challenges

With stringent size, cost, and price limitations, to maintain transferability and performance of the flow regulation module, several downsides in the custom PPD design ought to be considered:

- I. Wien-Bridge frequency control through chosen diodes and capacitors introduced temperature dependent frequency drift. For WF1, the impact of it was insignificant compared to WF2, as pumping performance for different liquids was not as sensitive to pumping frequency as was droplet rate to the rate-matching pulsations.
 - o Drift mitigation could be improved using thermistors or negative-positive-zero (NPO) capacitors.
- II. Limited footprint and fully utilized 18-pin connection, did not leave room for BC output current feedback, nor could L3 fit a hardware current limiter.
- III. Switching noise from the L2 facing BC-SWCH under L3 coupled into pumping waveforms.
 - o L3 design ought to be re-worked to reduce EMI, or L3 ought to be relocated away from the drivers.
- IV. Due to the limited number of pins connecting to FRC-B and a requirement to match mp-Highdriver I2C pins, I2C addresses for four quad DPs on L1 were defined with a single pin and an on-board inverter. With just one address pin to start with, the number of I2C devices controllable was capped at four, thereby limiting the number of controllable PPDs on FRC-B to two. However, the device limit was further solidified as a consequence of the used DPs, offering just four unique addresses.
- V. Due to limited cost and space on L2, high voltage QOA could not be designed with push-pull transistors to increase potential output current and explore charge recovery options. Nor was there space for protection diodes in case of voltage spike generation from the actuators.

PPD features yet to be tested:

- I. Performance and stability evaluation of WF_EXT custom complex waveforms in encapsulation and droplet generation.
- II. PPD's summed primary and secondary waveforms could be shared among drivers through pin 7 and WF_EXT, for exact frequency matched pumping.
- III. With the output of the used high voltage QOA spanning across 400 V_{PP} (+/- 200 V), various commercial piezoelectric micropumps could be tested with the setup. Moreover, as common micropump designs are single-diaphragm types, custom dual-diaphragm designs could be explored.

Considerations with updated pressure sensors on PS-B:

- I. With the pressure sensor's differential sensitivity range of +/-103 kPa, one mp6-liq micropump barely exceeds half of its range, leaving much of the pressure resolution unused, providing an opportunity to use two mp6-liq pumps in series.
- II. The third differential pressure sensor, between water and oil inlets, gives an opportunity to investigate relationships with droplet generation for improved fluidics characterization.

Lastly, the presented method of droplet data buffering and transmission from ESP32 on DSSP-B to RPI was limited by the size of the buffer (defined in software) and the capability of the ESP32 to perform better at higher SPI clock rates. As is, droplet generation rates can exceed 4 kHz; however, not all will be seen by the RPI.

5 Conclusion

This thesis work started from an idea that was to design and construct an automated droplet generation platform for the purpose of improving accessibility to automation of experiments in biochemical laboratories. Over the course of the work, towards the obtained target platform, the perspective of it and thereby the outlook of the thesis broadened. Not only does the platform offer a portable, affordable, modular automated solution for general droplet generation purposes, the developed platform has made it feasible to start exploring microfluidic methods and components that make use of dynamic laminar flows.

The system resulting from this thesis achieved control of the generated droplet size and generation rate, both at lower variance than 1%, using pulsatile pressure-based micropumps. Using the custom-built micropump drivers, expanded the number of control vectors for dynamic flow synchronization evaluation through their product – the droplets.

Relying on lightweight and fast PID loops, the pumps could be controlled at a rate of ~ 2 kHz using a pair of MCUs like the ESP32 and an SBC like the RPI 4B. The droplet detection used an ESP32 to bring the optical sampling of droplets to a rate of ~ 256 kHz which allowed for the detectable droplet generation rate to reach 4 kHz.

With the focus on transferability, managing progress from every front, the research questions received the following answers:

RQ1: What is a highly responsive, transferable microfluidic flow regulation method, which allows for droplet generation with precise and accurate control, as well as flexible configuration for different application use cases?

→ Piezoelectric micropumps with piezoresistive pressure sensors, being both inherently highly responsive, affordable, and portable. Pressure sensing was flexible in working with both flow rate and pressure-based flow actuators. Likewise, piezoelectric micropumps, being low-power and compact, showed competitive stability in general purpose droplet generation with monodispersity reaching as low as 2%. Piezoelectric methods were flexible for generating droplets (Publication I) and bubbles (Publication II) – indicating performance metrics suitable for particle encapsulation applications and sensor development.

RQ2: Can microfluidic droplet parameters be estimated from low-cost brightfield light intensity measurements well enough for droplet generation control?

→ In Publication III, the controlled variations in oil/water pumping pressure ratios correlated to the expected increase or decrease in measured light intensity – as oil/water ratio increases, the water droplets generated become smaller, alongside it the measured light intensity decreases. The correlation noticed was not linear, but best described by third-degree polynomial. This relationship required the realization of a calibration algorithm, as without one, besides directionality, there is no knowable link between the scale of the intensity measurement and the scale of the droplet.

RQ3: How to automate droplet generation while maintaining repeatability and flexibility with pulsatile micropump actuators, pressure-based flow sensors and PD-LED droplet sensor for varying droplet generation parameters, setups, and reagents?

→ In accordance to how the problems were solved with Publication III, to automate droplet generation, control needed to be kept over both the flow and the generated droplet parameters, thereby, both values needed to be monitored in real-time. This was handled by the pressure-based flow sensors and PD-LED droplet sensor. Their data was pooled onto one controller and correlated to calculate pressure targets for the piezoelectric micropump actuators through PID controllers. Keeping the flow regulation processing unit dedicated to managing the pumps and the pressure sensors directly for stability, the workload of pressure and droplet data interpretation and response calculations could be left for the system processing unit, Raspberry Pi 4B. With an oscillating light intensity pattern observed during droplet formation, droplet generation parameters were obtained from it by establishing rules by which pattern repetition periods and amplitudes would translate to droplet generation rate and size, respectively. Collecting and combining pressure and droplet data revealed relationships, which were not continuous over different reagents (oils, surfactants) nor over changes in fluidics (FFD geometries). These differences were attributed to setup characteristics, which were recorded in a methodical manner in a custom calibration stage, before automated control of target droplet generation parameters. Characterization allowed to find a starting oil/water pressure combination to cold start droplet formation near the desired droplet generation parameters.

RQ4: How can the performance of piezoelectric micropumps in droplet generation be improved through their driving signal and what effect does it have on control stability in droplet generation with pulsatile flows?

→ With upgrades, leading to more reliable sensing of pressure and droplets, the CogniFlow-Drop platform from Publication III, was prepared for use and observation with a piezoelectric driver, capable of producing atypical driving signals; capable of faster responsiveness; capable of higher resolution driving signal amplitude control. The primary relevant upgrades for the platform came in the form of higher pressure and droplet sensing rates, complementing the driver's high responsiveness and more intricate pressure characteristics. In accordance with Publication IV, a piezoelectric driver, with an ability to produce complex piezoelectric micropump driving signals, was developed. To improve the performance of piezoelectric micropumps in droplet generation, the expected impact of the complex driving signal was analyzed around the high-level indicators of droplet generation – droplet size CV% and generation rate CV%. The custom driver was designed around improved pressure stability with higher degree of control and the effect of resonance within its driving signal. To implement the latter, a secondary frequency was added to the pump-driving waveform, adjustable in relation to the droplet generation rates. Preliminary results from driving pulsatile piezoelectric micropumps for droplet generation, using the custom dual-tone driving signal, accompanied by improved closed-loop stabilization-response features, showed indication towards a positive impact on the generated droplet monodispersity – less than 5% CV at ~2 kHz droplet generation and less than 1% at ~0.8 kHz. Improvements, while observable, the division of contribution remains yet inconclusive.

6 Future Perspectives

Much of the future work depends on the platform remaining modular. Meaning that it is expected to allow for simple integration of different types of pumps. Keeping the existing pressure feedback as flow regulation, the platform could be evaluated by replacing the piezoelectric micropumps with syringe pumps, electro-osmotic pumps, and other active pumping methods.

The automated platform could be tested with different media combinations, not only water with variations of oil, but different aqueous liquids and gases, to investigate which kinds of droplet signals could be detected under brightfield lighting, and thereby expanding the droplet identification algorithm.

In relation to the algorithms, the added control over the pumping frequency could be automated for finding the optimal pumping frequency for unfamiliar liquids. Additionally, the droplet identification (single/double peak categorization) algorithm could find improvements by implementing fuzzy instead of traditional logic.

With the higher adjustment resolution and more control vectors, the custom piezoelectric micropump driver could be used, in conjunction with additional PID controllers, for its primary and secondary waveform frequencies to allow me to explore the direct CV% control.

6.1 Addressing Limitations

Narrowing down on the existing modules on the platform. To find optimal gas pumping frequencies, even if expecting to remain below 1 kHz for the Bartels micropumps, the pressure sensors limited with 2 kHz measurement rate, may need to be upgraded further. Likewise, if different commercial piezoelectric pumps with different effective frequency ranges were to be tested.

The pulsatile nature of the piezoelectric pumps could be reduced by adding air springs and controlled pressure relief valves. Furthermore, pulsations could be reduced by using piezoelectric micropumps with different diaphragm sizes with different passive valving methods, to increase the operation frequency and bring the pumping chamber volume close to the droplet volume.

For the droplet sensing method, the tilt-bed for the microfluidic chip ought to be motorized. Motorization would increase the precision in restoring previous positions and help to automate the sensor column alignment. Furthermore, a dynamically controlled tilt can reduce time between test setups.

6.2 Created Research Interests

With the cost of high-performance surfactants being relatively high in relation to all other necessities in a droplet related research, it becomes of interest to either significantly improve the cell encapsulation rates during droplet generation or to find a method how to recover the surfactant from the empty droplets. There are mechanical methods such as centrifugation and filtration, thermal such as open-air drying and distillation, chemical methods such as mixing with salts but also electrical such as electrocoalescence. Electrocoalescence can be used to merge droplets together more easily with passing low current through the unused droplet mass. As the droplets merge into a manageable volume, it could be possible to extract the droplet content more easily and recover dry surfactant without affecting it chemically. The electric field generated is typically

alternating with an amplitude of several hundred volts per millimeter. The custom piezoelectric drivers made to control the micropumps could be employed on the platform to forcibly merge unused droplets after sorting [149]–[153]. Furthermore, integrating electrodes for electrocoalescence beneath any microfluidic chip could be explored for extending the generated droplet size range.

With the use of piezoelectric flow regulation, further investigation could be done into:

- I. Active cell encapsulation – by utilizing the piezoelectric driver’s secondary waveform to induce particle control in the disperse phase flow.
- II. Droplet formation pressure sensing from piezoelectric resistance – by analyzing deviations in the driver signal.
- III. Droplet generation control enhancement – by extending dynamic pump control with feedback leading into the driver’s waveform parameters such as the frequency and amplitude of both the primary and secondary waves; their synchronization for oil and water pumps.

List of Figures

Figure 1. A selection of widely used microfluidic droplet generation channel geometries. Reproduced from [35].	14
Figure 2. Illustration of a flow-focusing type droplet generation geometry, forming droplets from oil and water. The oil contains premixed surfactant molecules with a neutral hydrophobic tail and a polarized hydrophilic head. Polarized ends of the surfactant are attracted by the polarizable water, forming a coating layer at the oil-water interface. Surfactant coating aids in droplet formation and mitigates coalescing when coming in contact with other droplets.	15
Figure 3. Scientific database (Scopus) “ALL” fields search result counts over the past 30 years (1993 - 2023). Each queried keyword combination (1* OR a*; microfluidic*; microfluidic* AND “droplet generation”; microfluidic* AND “droplet generation” AND automation) has been plotted on a separate y-axis. Search was conducted in January of 2024.	16
Figure 4. Illustrative thesis layout showing how the supporting publications tie back to the challenges and research questions, and how they connect to each other in this thesis.	23
Figure 5. Illustrative distinction between continuous (a) and pulsatile (b) flow characteristics as pressure over time and as a gradient through a microfluidic channel.	26
Figure 6. Flow-focusing device channel design used for droplet generation. Junction dimensions are 125 μm x 100 μm (width x height), Appendix 3 [94].	27
Figure 7. Flow generation diagram in a Bartels’ dual diaphragm micropump design. Reproduced from [101].	28
Figure 8. Illustration of the droplet generation setup – including three inline pressure sensors (P1, P2, P3), an FFD, DIW as the disperse phase, MO with Span® 80 as the continuous phase, droplet/waste collector, and two inline PZT pumps.	30
Figure 9. Block diagram of the device components and communication methods, Appendix 1 [108].	31
Figure 10. a) Piezoelectrically regulated microfluidic droplet generation setup, connected to an FFD; b) Graphed water pressure readings during pump operation characterization at varying pumping frequencies; c) Sample image from a high-speed camera of water droplets flowing in mineral oil in a 625 μm wide channel. d) Graphed oil and water pressure readings of feedback-controlled pressure stabilization; e) Closeup of water pressure readings from nominal feedback control delay of ~ 5.3 ms, Appendix 1 [108].	35
Figure 11. Flow velocity sensor benchmarking setup using the dual-channel droplet generator to pump air and colored water into a 3D printed T-junction to produce a segmented flow of air and water, distinguishable by the developed flow velocity sensor, Appendix 2 [113].	36
Figure 12. Revision 1 - placement of droplet generation modules on 330 x 220 mm base platform. (“Lx” – Layer x)	44
Figure 13. Revision 2 - placement of droplet generation modules on 330 x 220 mm base platform. (“Lx” – Layer x)	45
Figure 14. Revision 2 – platform CAD model. An exploded view of the setup, Appendix 3 [94].	46
Figure 15. Cross-section of the aligned microfluidic droplet detector setup, Appendix 3 [94].	48

Figure 16. Pixel color summation application measuring the possible light intensity differences produced by a droplet passing through a photodiode viewport, narrowed with an arbitrary pinhole, Appendix 3 [94].	49
Figure 17. Illustrated acquisition of droplet's 'shadow' from a LED-PD detector with its signal processing circuit diagram.	50
Figure 18. Illustration showing how the PD signal could be captured and measured over time, resulting in quantifiable parameters of droplet size and generation frequency...	52
Figure 19. System controller diagram of its connective links and operational tasks split among its CPU cores, Appendix 3 [94].	54
Figure 20. Data exchange queues and their access relationship between Tasks 3 and 4.	57
Figure 21. Water and oil pressure characteristics in calibration phases 1 and 2, during which to collect pressure and droplet data to find the 3 rd order polynomial and logarithmic relationships, respectively – used for droplet size and generation rate control.	60
Figure 22. Photo of the assembled droplet generation platform.	62
Figure 23. ADC data of droplets generated at 500 Hz with chip variant C and liquid combination B, Appendix 3 [94].	63
Figure 24. ADC data of droplets generated at 500 Hz with chip variant B and liquid combination B, Appendix 3 [94].	63
Figure 25. Characteristic 3 rd order polynomial (left graph; red dotted line) and logarithmic (right graph; red dotted line) regression lines calculated using droplet relative size, generation rate and pressure data acquired during droplet PID calibration stages.	64
Figure 26. Droplet size and generation rate test series collective average size error graph (a), generation rate error graph (b), droplet size CV% graph (c) and droplet generation rate CV% graph (d) for different FFD cross-junction angles, Appendix 3 [94].	65
Figure 27. Droplet relative size in voltage (a) and generation rate (b) datapoints collected from a target droplet generation parameter combination of [4.4 V; 400 Hz] with chip B. Blue vertical line at the 45 s mark, indicates the point after which the generated droplets were used in the CV% calculation, Appendix 3 [94].	66
Figure 28. CogniFlow-Drop (2023) platform problems and their origin hierarchy.	74
Figure 29. Exploded view of the CogniFlow-Drop platform's electronics column, highlighting PCBs affected by the required hardware modifications.	77
Figure 30. Updated flow regulation sensor board (PS-B) with three high speed differential piezoresistive pressure sensors.	80
Figure 31. Top (left) and bottom (right) view of the 1 st layer PCB of the custom PPD.	81
Figure 32. Top (left) and bottom (right) view of the 2 nd layer PCB of the custom PPD.	82
Figure 33. Top (left) and bottom (right) view of the 3 rd layer PCB of the custom PPD.	83
Figure 34. Updated flow regulation control board (FRC-B) with assembled custom PPDs in pump driver sockets.	85
Figure 35. Updated droplet sensor signal processing board (DSSP-B) with a dedicated MCU for droplet identification.	86
Figure 36. Modified droplet sensor signal processing board (DSSP-B) block diagram.	87
Figure 37. Custom PPD unloaded output waveforms at ~200 Hz and ~250 V _{PP} .	88
Figure 38. Mp-Highdriver unloaded output waveforms with highest amplitude at ~200 Hz.	89
Figure 39. WF1 (~200 Hz) and WF2 (~2000 Hz) summed result.	89
Figure 40. Custom PPD summed sine waves, with WF2 brought to clipping.	90

Figure 41. (Left graph) Wien-Bridge Bridge frequency graphs for RC combinations, using 8-bit digital potentiometers in parallel. (Right graph) Mp-Highdriver frequency range over 256 options.	91
Figure 42. (Left graph) FRC-B water pump driver PID coefficient from VCA controlling DAC and resulting pressure relationship. (Right graph) FRC-B oil pump driver PID coefficient from VCA controlling DAC and resulting pressure relationship.	93
Figure 43. Water pump PID control stabilization at fixed pressure targets with a custom PPD.	93
Figure 44. Oil pump PID control stabilization at fixed pressure targets with a custom PPD.	94
Figure 45. Characteristic 3 rd order polynomial (left graph; red dotted line) and logarithmic (right graph; red dotted line) regression lines calculated using droplet size, generation rate and pressure data acquired during droplet PID calibration stages.	94
Figure 46. Droplet generation CV% results with updated CogniFlow-Drop platform.	95

List of Tables

Table 1. Microfluidic droplet generation platform requirements to be on par with the state-of-the-art.	18
Table 2. Overview of alignment of chapters, research questions and contributions in the thesis.	23
Table 3. Revision 1, droplet generation device, pressure sensor specifications.....	29
Table 4. Dual-channel, portable pressure pump design criteria.....	31
Table 5. Standalone, transferable pumping device specifications.....	38
Table 6. Transferable, modular, droplet generation platform design criteria.....	42
Table 7. Geometric properties of the FFD variants used for the evaluation of the droplet generation platform, Appendix 3 [94]......	59
Table 8. Liquid properties and combinations used for evaluation of the droplet generation platform, Appendix 3 [94]......	59
Table 9. Chip B – Voltage target series over fixed generation frequency targets, Appendix 3 [94].	61
Table 10. Chip B – Frequency target series over fixed voltage (size) targets, Appendix 3 [94]......	61
Table 11. Chip C – Voltage target series over fixed generation frequency targets. Target size and frequency combinations which did not result in stable droplet generation are marked with gray highlights, Appendix 3 [94]......	61
Table 12. Chip C – Frequency target series over fixed voltage (size) targets. Target size and frequency combinations which did not result in stable droplet generation are marked with gray highlights, Appendix 3 [94].	62
Table 13. System control software task loop durations, Appendix 3 [94]......	64
Table 14. CogniFlow-Drop (2023) specifications.....	68
Table 15. PS-B update criteria.....	77
Table 16. Criteria for custom PPD.....	78
Table 17. FRC-B necessary modifications to accommodate PS-B update and custom PPDs.	79
Table 18. DSSP-B re-work criteria.....	79
Table 19. Pinout comparison between custom PPD and mp-Highdriver.....	84
Table 20. Modified CogniFlow-Drop platform evaluation fluidic specifications.	92
Table 21. Modified CogniFlow-Drop CV% measurements at 500, 800, 1500 and 2000 Hz generation targets.....	95
Table 22. Automated, transferable droplet generation platform specifications.	97

References

- [1] W. L. Chou, P. Y. Lee, C. L. Yang, W. Y. Huang, and Y. S. Lin, "Recent Advances in Applications of Droplet Microfluidics," *Micromachines* 2015, Vol. 6, Pages 1249-1271, vol. 6, no. 9, pp. 1249–1271, Sep. 2015.
- [2] M. I. Hajam and M. M. Khan, "Microfluidics: a concise review of the history, principles, design, applications, and future outlook," *Biomater. Sci.*, vol. 12, no. 2, pp. 218–251, Jan. 2024.
- [3] Z. Z. Chong, S. H. Tan, A. M. Gañán-Calvo, S. B. Tor, N. H. Loh, and N. T. Nguyen, "Active droplet generation in microfluidics," *Lab Chip*, vol. 16, no. 1, pp. 35–58, Dec. 2015.
- [4] T. Glawdel, C. Elbuken, and C. L. Ren, "Droplet Generation in Microfluidics," *Encycl. Microfluid. Nanofluidics*, pp. 1–12, 2013.
- [5] H. Gu, M. H. G. Duits, and F. Mugele, "Droplets Formation and Merging in Two-Phase Flow Microfluidics," *Int. J. Mol. Sci.* 2011, Vol. 12, Pages 2572-2597, vol. 12, no. 4, pp. 2572–2597, Apr. 2011.
- [6] T. A. Duncombe, A. M. Tentori, and A. E. Herr, "Microfluidics: reframing biological enquiry," *Nat. Rev. Mol. Cell Biol.* 2015 169, vol. 16, no. 9, pp. 554–567, Aug. 2015.
- [7] A. P. Iakovlev, A. S. Erofeev, and P. V. Gorelkin, "Novel Pumping Methods for Microfluidic Devices: A Comprehensive Review," *Biosens.* 2022, Vol. 12, Page 956, vol. 12, no. 11, p. 956, Nov. 2022.
- [8] M. Zagnoni and J. M. Cooper, "Droplet Microfluidics for High-throughput Analysis of Cells and Particles," *Methods Cell Biol.*, vol. 102, pp. 23–48, Jan. 2011.
- [9] Y. Xie, L. Dai, and Y. Yang, "Microfluidic technology and its application in the point-of-care testing field," *Biosens. Bioelectron.* X, vol. 10, p. 100109, May 2022.
- [10] Z. Jiang, H. Shi, X. Tang, and J. Qin, "Recent advances in droplet microfluidics for single-cell analysis," *TrAC Trends Anal. Chem.*, vol. 159, p. 116932, Feb. 2023.
- [11] Y. Wang, Z. Chen, F. Bian, L. Shang, K. Zhu, and Y. Zhao, "Advances of droplet-based microfluidics in drug discovery," *Expert Opin. Drug Discov.*, vol. 15, no. 8, pp. 969–979, Aug. 2020.
- [12] C. Ren and A. Lee, "History and Current Status of Droplet Microfluidics," *RSC Soft Matter*, vol. 2021-January, no. 12, pp. 1–14, Nov. 2020.
- [13] O. J. Dressler, R. M. Maceiczkyk, S. I. Chang, and A. J. Demello, "Droplet-based microfluidics: Enabling impact on drug discovery," *J. Biomol. Screen.*, vol. 19, no. 4, pp. 483–496, Apr. 2014.
- [14] R. Chakraborty and S. Parvez, "Microfluidics in Drug Delivery," *Microfluid. Multi Organs Chip*, pp. 135–162, Jan. 2022.
- [15] K. Doufène, C. Tourné-Péteilh, P. Etienne, and A. Aubert-Pouëssel, "Microfluidic Systems for Droplet Generation in Aqueous Continuous Phases: A Focus Review," *Langmuir*, vol. 35, no. 39, pp. 12597–12612, Oct. 2019.
- [16] W. Su, B. Han, S. Yeboah, D. Du, and L. Wang, "Fabrication of monodisperse droplets and microcapsules using microfluidic chips: A review of methodologies and applications," *Rev. Chem. Eng.*, May 2023.
- [17] S. Da Ling, Y. Geng, A. Chen, Y. Du, and J. Xu, "Enhanced single-cell encapsulation in microfluidic devices: From droplet generation to single-cell analysis," *Biomicrofluidics*, vol. 14, no. 6, p. 61508, Nov. 2020.

- [18] P. De Stefano, E. Bianchi, and G. Dubini, "The impact of microfluidics in high-throughput drug-screening applications," *Biomicrofluidics*, vol. 16, no. 3, p. 31501, May 2022.
- [19] K. Langer and H. N. Joensson, "Rapid Production and Recovery of Cell Spheroids by Automated Droplet Microfluidics," *SLAS Technol.*, vol. 25, no. 2, pp. 111–122, Apr. 2020.
- [20] Y. Ding, P. D. Howes, and A. J. Demello, "Recent advances in droplet microfluidics," *Anal. Chem.*, vol. 92, no. 1, pp. 132–149, Jan. 2020.
- [21] L. Shang, Y. Cheng, and Y. Zhao, "Emerging Droplet Microfluidics," *Chem. Rev.*, vol. 117, no. 12, pp. 7964–8040, Jun. 2017.
- [22] L. Amirifar *et al.*, "Droplet-based microfluidics in biomedical applications," *Biofabrication*, vol. 14, no. 2, p. 022001, Jan. 2022.
- [23] S. Y. Teh, R. Lin, L. H. Hung, and A. P. Lee, "Droplet microfluidics," *Lab Chip*, vol. 8, no. 2, pp. 198–220, Jan. 2008.
- [24] T. N. D. Trinh, H. D. K. Do, N. N. Nam, T. T. Dan, K. T. L. Trinh, and N. Y. Lee, "Droplet-Based Microfluidics: Applications in Pharmaceuticals," *Pharm. 2023*, Vol. 16, Page 937, vol. 16, no. 7, p. 937, Jun. 2023.
- [25] H. Feng *et al.*, "Droplet-based microfluidics systems in biomedical applications," *Electrophoresis*, vol. 40, no. 11, pp. 1580–1590, Jun. 2019.
- [26] Y. Hou, S. Chen, Y. Zheng, X. Zheng, and J. M. Lin, "Droplet-based digital PCR (ddPCR) and its applications," *TrAC Trends Anal. Chem.*, vol. 158, p. 116897, Jan. 2023.
- [27] T. Alkayyali, T. Cameron, B. Haltli, R. G. Kerr, and A. Ahmadi, "Microfluidic and cross-linking methods for encapsulation of living cells and bacteria - A review," *Anal. Chim. Acta*, vol. 1053, pp. 1–21, Apr. 2019.
- [28] C. Regnault, D. S. Dheeman, and A. Hochstetter, "Microfluidic Devices for Drug Assays," *High-Throughput 2018*, Vol. 7, Page 18, vol. 7, no. 2, p. 18, Jun. 2018.
- [29] L. Rosenfeld, T. Lin, R. Derda, and S. K. Y. Tang, "Review and analysis of performance metrics of droplet microfluidics systems," *Microfluid. Nanofluidics*, vol. 16, no. 5, pp. 921–939, Jan. 2014.
- [30] Z. He, H. Wu, X. Yan, and W. Liu, "Recent advances in droplet microfluidics for microbiology," *Chinese Chem. Lett.*, vol. 33, no. 4, pp. 1729–1742, Apr. 2022.
- [31] K. Samlali, C. L. Alves, M. Jezernik, and S. C. C. Shih, "Droplet digital microfluidic system for screening filamentous fungi based on enzymatic activity," *Microsystems Nanoeng. 2022 81*, vol. 8, no. 1, pp. 1–16, Nov. 2022.
- [32] S. A. Byrnes, T. C. Chang, T. Huynh, A. Astashkina, B. H. Weigl, and K. P. Nichols, "Simple Polydisperse Droplet Emulsion Polymerase Chain Reaction with Statistical Volumetric Correction Compared with Microfluidic Droplet Digital Polymerase Chain Reaction," *Anal. Chem.*, vol. 90, no. 15, pp. 9374–9380, Aug. 2018.
- [33] T. Schneider, J. Kreutz, and D. T. Chiu, "The potential impact of droplet microfluidics in biology," *Anal. Chem.*, vol. 85, no. 7, pp. 3476–3482, Apr. 2013.
- [34] L. Liu *et al.*, "Step emulsification: High-throughput production of monodisperse droplets," *Biotechniques*, vol. 68, no. 3, pp. 114–116, Mar. 2020.
- [35] A. M. Pit, M. H. G. Duits, and F. Mugele, "Droplet Manipulations in Two Phase Flow Microfluidics," *Micromachines 2015*, Vol. 6, Pages 1768-1793, vol. 6, no. 11, pp. 1768–1793, Nov. 2015.
- [36] T. Deydier, G. Bolognesi, and G. T. Vladislavljević, "Scaled-up droplet generation in parallelised 3D flow focusing junctions," *Colloids Surfaces A Physicochem. Eng. Asp.*, vol. 641, p. 128439, May 2022.

- [37] A. Dewandre, J. Rivero-Rodriguez, Y. Vitry, B. Sobac, and B. Scheid, "Microfluidic droplet generation based on non-embedded co-flow-focusing using 3D printed nozzle," *Sci. Reports* 2020 101, vol. 10, no. 1, pp. 1–17, Dec. 2020.
- [38] A. L. R. Costa, A. Gomes, and R. L. Cunha, "Studies of droplets formation regime and actual flow rate of liquid-liquid flows in flow-focusing microfluidic devices," *Exp. Therm. Fluid Sci.*, vol. 85, pp. 167–175, Jul. 2017.
- [39] C. N. Baroud, F. Gallaire, and R. Dangla, "Dynamics of microfluidic droplets," *Lab Chip*, vol. 10, no. 16, pp. 2032–2045, Jul. 2010.
- [40] J. Q. Zhang *et al.*, "High diversity droplet microfluidic libraries generated with a commercial liquid spotter," *Sci. Reports* 2021 111, vol. 11, no. 1, pp. 1–7, Feb. 2021.
- [41] R. Seemann, M. Brinkmann, T. Pfohl, and S. Herminghaus, "Droplet based microfluidics," *Reports Prog. Phys.*, vol. 75, no. 1, p. 016601, Dec. 2011.
- [42] N. Dave and T. Joshi, "A Concise Review on Surfactants and Its Significance," *Int. J. Appl. Chem.*, vol. 13, no. 3, pp. 663–672, Sep. 2017.
- [43] D. J. Collins, A. Neild, A. deMello, A. Q. Liu, and Y. Ai, "The Poisson distribution and beyond: methods for microfluidic droplet production and single cell encapsulation," *Lab Chip*, vol. 15, no. 17, pp. 3439–3459, Aug. 2015.
- [44] J. F. Edd *et al.*, "Controlled encapsulation of single-cells into monodisperse picolitre drops," *Lab Chip*, vol. 8, no. 8, pp. 1262–1264, Jul. 2008.
- [45] E. W. M. Kemna, R. M. Schoeman, F. Wolbers, I. Vermes, D. A. Weitz, and A. Van Den Berg, "High-yield cell ordering and deterministic cell-in-droplet encapsulation using Dean flow in a curved microchannel," *Lab Chip*, vol. 12, no. 16, pp. 2881–2887, Jul. 2012.
- [46] S. Preetam *et al.*, "Emergence of microfluidics for next generation biomedical devices," *Biosens. Bioelectron. X*, vol. 10, p. 100106, May 2022.
- [47] N. Fu, Y. Liu, X. Ma, and Z. Chen, "EUV Lithography: State-of-the-Art Review," *J. Microelectron. Manuf.*, vol. 2, p. 19020202, 2019.
- [48] U. HIROSHI and H. TOSHIYUKI, "TARGET SUPPLY DEVICE AND EXTREME ULTRAVIOLET LIGHT GENERATION APPARATUS," 2014.
- [49] D. J. FREDERIK, A. W. H. T. MARIA, H. R. JOHANNES, V. A. N. D. E. V. E. N. B. L. W. MARINUS, and V. A. N. P. P. W. HENDRIK, "Droplet generator for lithographic apparatus, EUV source and lithographic apparatus," 2020.
- [50] M. Takken and R. Wille, "Accelerated Computational Fluid Dynamics Simulations of Microfluidic Devices by Exploiting Higher Levels of Abstraction," *Micromachines* 2024, Vol. 15, Page 129, vol. 15, no. 1, p. 129, Jan. 2024.
- [51] J. Wu, H. Fang, J. Zhang, and S. Yan, "Modular microfluidics for life sciences," *J. Nanobiotechnology* 2023 211, vol. 21, no. 1, pp. 1–30, Mar. 2023.
- [52] D. R. Reyes *et al.*, "Accelerating innovation and commercialization through standardization of microfluidic-based medical devices," *Lab Chip*, vol. 21, no. 1, pp. 9–21, Jan. 2021.
- [53] V. Ortseifen, M. Viefhues, L. Wobbe, and A. Grünberger, "Microfluidics for Biotechnology: Bridging Gaps to Foster Microfluidic Applications," *Front. Bioeng. Biotechnol.*, vol. 8, p. 589074, Nov. 2020.
- [54] S. Dekker, P. K. Isgor, T. Feijten, L. I. Segerink, and M. Odijk, "From chip-in-a-lab to lab-on-a-chip: a portable Coulter counter using a modular platform," *Microsystems Nanoeng.* 2018 41, vol. 4, no. 1, pp. 1–8, Nov. 2018.

- [55] B. Van Elburg, G. Collado-Lara, G. W. Bruggert, T. Segers, M. Versluis, and G. Lajoine, "Feedback-controlled microbubble generator producing 1×10^6 monodisperse bubbles per second," *Rev. Sci. Instrum.*, vol. 92, no. 3, p. 35110, Mar. 2021.
- [56] D. Li *et al.*, "High-throughput piezoelectric droplet dispenser driven by ultra-low voltage," *AIP Adv.*, vol. 13, no. 3, p. 35135, Mar. 2023.
- [57] L. Yobas, S. Martens, W. L. Ong, and N. Ranganathan, "High-performance flow-focusing geometry for spontaneous generation of monodispersed droplets," *Lab Chip*, vol. 6, no. 8, pp. 1073–1079, Jul. 2006.
- [58] H. H. Jeong, V. R. Yelleswarapu, S. Yadavali, D. Issadore, and D. Lee, "Kilo-scale droplet generation in three-dimensional monolithic elastomer device (3D MED)," *Lab Chip*, vol. 15, no. 23, pp. 4387–4392, Nov. 2015.
- [59] S. Zhang, K. Wang, and G. Luo, "High-throughput generation of uniform droplets from parallel microchannel droplet generators and the preparation of polystyrene microsphere material," *Particuology*, vol. 77, pp. 136–145, Jun. 2023.
- [60] J. Ryu, J. Kim, and K. H. Han, "dDrop-Chip: disposable film-chip microfluidic device for real-time droplet feedback control," *Lab Chip*, vol. 23, no. 7, pp. 1896–1904, Mar. 2023.
- [61] Z. He *et al.*, "A portable droplet generation system for ultra-wide dynamic range digital PCR based on a vibrating sharp-tip capillary," *Biosens. Bioelectron.*, vol. 191, p. 113458, Nov. 2021.
- [62] K. Mutafooulos, P. J. Lu, R. Garry, P. Spink, and D. A. Weitz, "Selective cell encapsulation, lysis, pico-injection and size-controlled droplet generation using traveling surface acoustic waves in a microfluidic device," *Lab Chip*, vol. 20, no. 21, pp. 3914–3921, Oct. 2020.
- [63] M. K. SPIRO, "Systems and methods for microfluidic particle selection, encapsulation, and injection using surface acoustic waves," 2023.
- [64] X. Yue *et al.*, "Breaking through the Poisson Distribution: A compact high-efficiency droplet microfluidic system for single-bead encapsulation and digital immunoassay detection," *Biosens. Bioelectron.*, vol. 211, p. 114384, Sep. 2022.
- [65] A. Sciambi and A. R. Abate, "Accurate microfluidic sorting of droplets at 30 kHz," *Lab Chip*, vol. 15, no. 1, pp. 47–51, Dec. 2014.
- [66] P. Li, Z. Ma, Y. Zhou, D. J. Collins, Z. Wang, and Y. Ai, "Detachable Acoustophoretic System for Fluorescence-Activated Sorting at the Single-Droplet Level," *Anal. Chem.*, vol. 91, no. 15, pp. 9970–9977, Aug. 2019.
- [67] M. Gantz, S. Neun, E. J. Medcalf, L. D. van Vliet, and F. Hollfelder, "Ultra-high-Throughput Enzyme Engineering and Discovery in In Vitro Compartments," *Chem. Rev.*, vol. 123, no. 9, pp. 5571–5611, May 2023.
- [68] "Onyx | Atrandi Biosciences." [Online]. Available: <https://atrandi.com/onyx>. [Accessed: 30-Jan-2024].
- [69] M. Bartunik, M. Fleischer, W. Haselmayr, and J. Kirchner, "Colour-specific microfluidic droplet detection for molecular communication," *Proc. 7th ACM Int. Conf. Nanoscale Comput. Commun. NanoCom 2020*, Sep. 2020.
- [70] C. ; Huang *et al.*, "Droplet Detection and Sorting System in Microfluidics: A Review," *Micromachines 2023, Vol. 14, Page 103*, vol. 14, no. 1, p. 103, Dec. 2022.
- [71] T. P. Lagus and J. F. Edd, "A review of the theory, methods and recent applications of high-throughput single-cell droplet microfluidics," *J. Phys. D. Appl. Phys.*, vol. 46, no. 11, p. 114005, Feb. 2013.

- [72] J. H. Shin and S. Choi, "Open-source and do-it-yourself microfluidics," *Sensors Actuators B Chem.*, vol. 347, p. 130624, Nov. 2021.
- [73] S. Wiedemeier *et al.*, "Parametric studies on droplet generation reproducibility for applications with biological relevant fluids," *Eng. Life Sci.*, vol. 17, no. 12, pp. 1271–1280, Dec. 2017.
- [74] Z. Chen, S. Kheiri, E. W. K. Young, and E. Kumacheva, "Trends in Droplet Microfluidics: From Droplet Generation to Biomedical Applications," *Langmuir*, 2022.
- [75] G. T. Vladislavljević *et al.*, "Industrial lab-on-a-chip: Design, applications and scale-up for drug discovery and delivery," *Adv. Drug Deliv. Rev.*, vol. 65, no. 11–12, pp. 1626–1663, Nov. 2013.
- [76] "International Carry-On Size – 1920 - The Travel Store." [Online]. Available: <https://www.worldtraveler.com/pages/international-carry-on-size>. [Accessed: 13-Mar-2024].
- [77] K. Pärnamets, "Optical Detection Methods for Droplet Microfluidic Applications," 2023.
- [78] Z. Jiao, J. Zhao, Z. Chao, Z. You, and J. Zhao, "An air-chamber-based microfluidic stabilizer for attenuating syringe-pump-induced fluctuations," *Microfluid. Nanofluidics*, vol. 23, no. 2, pp. 1–10, Feb. 2019.
- [79] C. K. Byun, K. Abi-Samra, Y. K. Cho, and S. Takayama, "Pumps for microfluidic cell culture," *Electrophoresis*, vol. 35, no. 2–3, pp. 245–257, Feb. 2014.
- [80] Y. Imura, E. Yoshimura, and K. Sato, "Microcirculation system with a dialysis part for bioassays evaluating anticancer activity and retention," *Anal. Chem.*, vol. 85, no. 3, pp. 1683–1688, Feb. 2013.
- [81] S. Schneider *et al.*, "Peristaltic on-chip pump for tunable media circulation and whole blood perfusion in PDMS-free organ-on-chip and Organ-Disc systems," *Lab Chip*, vol. 21, no. 20, pp. 3963–3978, Oct. 2021.
- [82] R. Z. Gao, M. Hébert, J. Huissoon, and C. L. Ren, "µPump: An open-source pressure pump for precision fluid handling in microfluidics," *HardwareX*, vol. 7, p. e00096, Apr. 2020.
- [83] N. A. Filatov, I. A. Denisov, A. A. Evstrapov, and A. S. Bukatin, "Open-Source Pressure Controller Based on Compact Electro-Pneumatic Regulators for Droplet Microfluidics Applications," *IEEE Trans. Instrum. Meas.*, vol. 71, 2022.
- [84] W. F. Fang and A. P. Lee, "LCAT pump optimization for an integrated microfluidic droplet generator," *Microfluid. Nanofluidics*, vol. 18, no. 5–6, pp. 1265–1275, May 2015.
- [85] H. Li, J. Liu, K. Li, and Y. Liu, "A review of recent studies on piezoelectric pumps and their applications," *Mech. Syst. Signal Process.*, vol. 151, p. 107393, Apr. 2021.
- [86] N. Okura *et al.*, "A compact and facile microfluidic droplet creation device using a piezoelectric diaphragm micropump for droplet digital PCR platforms," *Electrophoresis*, vol. 38, no. 20, pp. 2666–2672, Oct. 2017.
- [87] W. Li, W. Zhuge, Y. Jiang, K. Jiang, J. Ding, and X. Cheng, "A compact modularized power-supply system for stable flow generation in microfluidic devices," *Microfluid. Nanofluidics*, vol. 27, no. 12, pp. 1–8, Dec. 2023.
- [88] M. Trossbach, M. de Lucas Sanz, B. Seashore-Ludlow, and H. N. Joensson, "A Portable, Negative-Pressure Actuated, Dynamically Tunable Microfluidic Droplet Generator," *Micromachines*, vol. 13, no. 11, p. 1823, Nov. 2022.

- [89] A. Najmi, M. S. Saidi, and S. Kazemzadeh Hannani, "Design of the micropump and mass-transfer compartment of a microfluidic system for regular nonenzymatic glucose measurement," *Biotechnol. Reports*, vol. 34, Jun. 2022.
- [90] M. Mohammed *et al.*, "Studying the Response of Aortic Endothelial Cells under Pulsatile Flow Using a Compact Microfluidic System," *Anal. Chem.*, vol. 91, no. 18, pp. 12077–12084, Sep. 2019.
- [91] D. C. Young, J. M. Brehm, and J. Scrimgeour, "Driving complex flow waveforms with a linear voice coil actuator," *Biomicrofluidics*, vol. 13, no. 3, p. 34101, May 2019.
- [92] G. Yanfang and L. Xiang, "Analysis of Vibrational Performance of A Piezoelectric Micropump with Diffuse/Nozzle Microchannel," *Nanotechnol. Precis. Eng.*, vol. 1, no. 2, pp. 138–144, Jun. 2018.
- [93] P. Zhu, X. Tang, and L. Wang, "Droplet generation in co-flow microfluidic channels with vibration," *Microfluid. Nanofluidics*, vol. 20, no. 3, pp. 1–10, Mar. 2016.
- [94] R. Jöemaa *et al.*, "CogniFlow-Drop: Integrated Modular System for Automated Generation of Droplets in Microfluidic Applications," *IEEE Access*, vol. 11, pp. 104905–104929, 2023.
- [95] "mp6 micropumps for microfluidics." [Online]. Available: <https://bartels-mikrotechnik.shop/en/produkt/mp6-micropumps/>. [Accessed: 13-Mar-2024].
- [96] "Piezoelectric Micro Pumps - Takasago Fluidic Systems." [Online]. Available: <https://www.takasago-fluidics.com/pages/piezoelectric-micro-pumps>. [Accessed: 13-Mar-2024].
- [97] "Nitto Kohki USA - Pump Div." [Online]. Available: <http://nittokohki.com/pumps/prd/liquid-pumps.php#bimor-piezoelectric-pumps>. [Accessed: 13-Mar-2024].
- [98] "TTP Ventus Acquisition | The Lee Co." [Online]. Available: <https://www.theleeco.com/ttp-ventus-acquisition/>. [Accessed: 08-Mar-2024].
- [99] "Disc Pumps | The Lee Co." [Online]. Available: <https://www.theleeco.com/disc-pumps/>. [Accessed: 13-Mar-2024].
- [100] B. D. Iverson and S. V. Garimella, "Recent advances in microscale pumping technologies: A review and evaluation," *Microfluid. Nanofluidics*, vol. 5, no. 2, pp. 145–174, Aug. 2008.
- [101] "Animation mp6 Bartels Micropumps | Bartels Mikrotechnik - YouTube." [Online]. Available: <https://www.youtube.com/watch?v=joz1x4WV5Zw>. [Accessed: 08-Mar-2024].
- [102] V. A. N. R. R. JANSE, H. S. ANDREW, B. J. RORKE, and M. J. EDWARD, "Fluid disc pump," 2012.
- [103] B. FRANK, D. SEVERIN, U. W. E. KAMPMEYER, and R. MARKUS, "METHOD FOR SUPPLYING A FLUID AND MICROPUMP FOR SAID PURPOSE," 2012.
- [104] W. MASANORI and O. K. I. YASUMASA, "Pump using unimorph diaphragm," 2012.
- [105] TalTech-LoC, "Github - taltechloc/hw-open-pressure-pump." [Online]. Available: <https://github.com/taltechloc/hw-open-pressure-pump>. [Accessed: 15-Mar-2024].
- [106] TalTech-LoC, "Github - taltechloc/hw-open-fluidic-infra/SLA_Connectors." [Online]. Available: https://github.com/taltechloc/hw-open-fluidic-infra/tree/main/SLA_Connectors. [Accessed: 15-Mar-2024].
- [107] "GitHub - me-no-dev/ESPAsyncWebServer: Async Web Server for ESP8266 and ESP32." [Online]. Available: <https://github.com/me-no-dev/ESPAsyncWebServer>. [Accessed: 13-Mar-2024].

- [108] R. Jöemaa, M. Grosberg, T. Rang, and T. Pardy, "Low-cost, portable dual-channel pressure pump for droplet microfluidics," in *2022 45th Jubilee International Convention on Information, Communication and Electronic Technology (MIPRO)*, 2022, pp. 205–211.
- [109] "Sinno SN-50C6 MDT Syringe Infusion Pump | Automatic Syringe Identifier, Syringe indicator Status, Compatible with all brands of syringe, 8-10 hr. battery backup at best price." [Online]. Available: <https://www.hospitalstore.com/sinno-medical-syringe-pump/>. [Accessed: 30-Jan-2024].
- [110] "Digital Laboratory Syringe Pump dLSP500 - SYRINGE PUMPS - Drifton A/S." [Online]. Available: <https://www.drifton.eu/shop/24-syringe-pumps/2460-digital-laboratory-syringe-pump-dlsp500/>. [Accessed: 21-Feb-2022].
- [111] "Smith Medical Graseby 2000 Syringe Pump | Programmable infusion rates, 3 adjustable occlusion pressure settings, LCD Display at best price." [Online]. Available: <https://www.hospitalstore.com/smith-medical-syringe-pump/>. [Accessed: 30-Jan-2024].
- [112] "NE-300 InfusionONE Syringe Pump– Darwin Microfluidics." [Online]. Available: <https://darwin-microfluidics.com/products/microfluidic-just-infusion-syringe-pump>. [Accessed: 30-Jan-2024].
- [113] N. A. Prabatama, R. Jöemaa, K. Hegedus, and T. Pardy, "Low-cost open-source flow velocity sensor for droplet generators," in *2022 18th Biennial Baltic Electronics Conference (BEC)*, 2022, pp. 1–4.
- [114] D. Gawel and J. Zawala, "Automatic Single Droplet Generator with Control over Droplet Size and Detachment Frequency," *Colloids Interfaces 2019*, Vol. 3, Page 57, vol. 3, no. 3, p. 57, Aug. 2019.
- [115] P. Hadikhani, N. Borhani, S. M. H. Hashemi, and D. Psaltis, "Learning from droplet flows in microfluidic channels using deep neural networks," *Sci. Reports 2019 91*, vol. 9, no. 1, pp. 1–7, May 2019.
- [116] C. Shen, Q. Zheng, M. Shang, L. Zha, and Y. Su, "Using deep learning to recognize liquid–liquid flow patterns in microchannels," *AIChE J.*, vol. 66, no. 8, p. e16260, Aug. 2020.
- [117] S. Naji, A. Rahimi, V. Bazargan, and M. Marengo, "Numerical and artificial neural network analysis of an axisymmetric co-flow-focusing microfluidic droplet generator using active and passive control," *Phys. Fluids*, vol. 35, no. 6, p. 62008, Jun. 2023.
- [118] W. Yu, X. Liu, Y. Zhao, and Y. Chen, "Droplet generation hydrodynamics in the microfluidic cross-junction with different junction angles," *Chem. Eng. Sci.*, vol. 203, pp. 259–284, Aug. 2019.
- [119] S. Iqbal, S. Bashir, M. Ahsan, M. Bashir, and S. Shoukat, "Effect of Intersection Angle and Wettability on Droplet Generation in Microfluidic Flow-Focusing Device," *J. Fluids Eng. Trans. ASME*, vol. 142, no. 4, Apr. 2020.
- [120] L. Galluccio, A. Lombardo, G. Morabito, F. Pappalardo, and S. Quattropiani, "Droplet speed-shift keying: A modulation scheme for instantaneous microfluidic communications," *NanoCom 2023 - Proc. 10th ACM Int. Conf. Nanoscale Comput. Commun.*, pp. 110–115, Sep. 2023.
- [121] N. T. Nguyen, S. Lassemono, and F. A. Chollet, "Optical detection for droplet size control in microfluidic droplet-based analysis systems," *Sensors Actuators B Chem.*, vol. 117, no. 2, pp. 431–436, Oct. 2006.

- [122] P. Guillot and A. Colin, "Stability of parallel flows in a microchannel after a T junction," *Phys. Rev. E - Stat. Nonlinear, Soft Matter Phys.*, vol. 72, no. 6, p. 066301, Dec. 2005.
- [123] A. Venkateshwarlu and R. P. Bharti, "Effects of capillary number and flow rates on the hydrodynamics of droplet generation in two-phase cross-flow microfluidic systems," *J. Taiwan Inst. Chem. Eng.*, vol. 129, pp. 64–79, Dec. 2021.
- [124] N. Gyimah, R. Jõemaa, K. Pärnamets, O. Scheler, T. Rang, and T. Parfy, "PID Controller Tuning Optimization Using Genetic Algorithm for Droplet Size Control in Microfluidics," in *2022 18th Biennial Baltic Electronics Conference (BEC)*, 2022, vol. 2022-October, pp. 1–6.
- [125] "Welcome to Eclipse eCAL™ — Eclipse eCAL™." [Online]. Available: <https://eclipse-ecal.github.io/ecal/>. [Accessed: 13-Mar-2024].
- [126] S. Mohith, A. R. Upadhyay, K. P. Navin, S. M. Kulkarni, and M. Rao, "Recent trends in piezoelectric actuators for precision motion and their applications: a review," *Smart Mater. Struct.*, vol. 30, no. 1, p. 013002, Dec. 2020.
- [127] J. Woo, D. K. Sohn, and H. S. Ko, "Performance and flow analysis of small piezo pump," *Sensors Actuators A Phys.*, vol. 301, p. 111766, Jan. 2020.
- [128] M. Stringer *et al.*, "Methodologies, technologies, and strategies for acoustic streaming-based acoustofluidics," *Appl. Phys. Rev.*, vol. 10, no. 1, p. 11315, Mar. 2023.
- [129] Y. Q. Fu *et al.*, "Advances in piezoelectric thin films for acoustic biosensors, acoustofluidics and lab-on-chip applications," *Prog. Mater. Sci.*, vol. 89, pp. 31–91, Aug. 2017.
- [130] M. A. Sahin, M. Ali, J. Park, and G. Destgeer, "Fundamentals of Acoustic Wave Generation and Propagation," *Acoust. Technol. Biol. Med.*, pp. 1–36, Nov. 2023.
- [131] Y. Li, S. Cai, H. Shen, Y. Chen, Z. Ge, and W. Yang, "Recent advances in acoustic microfluidics and its exemplary applications," *Biomicrofluidics*, vol. 16, no. 3, p. 31502, May 2022.
- [132] H. D. Xi *et al.*, "Active droplet sorting in microfluidics: a review," *Lab Chip*, vol. 17, no. 5, pp. 751–771, Feb. 2017.
- [133] A. Kumar, P. P. Pathak, and N. Dass, "A Study of Speed of Sound in Water," *IOSR J. Appl. Phys.*, vol. 08, no. 04, pp. 21–23, Apr. 2016.
- [134] N. Muñoz-Rujas, J. P. Bazile, F. Aguilar, G. Galliero, E. Montero, and J. L. Daridon, "Speed of sound and derivative properties of hydrofluoroether fluid HFE-7500 under high pressure," *J. Chem. Thermodyn.*, vol. 112, pp. 52–58, Sep. 2017.
- [135] G. Özkayar, Z. Wang, J. Lötters, M. Tichem, and M. K. Ghatkesar, "Flow Ripple Reduction in Reciprocating Pumps by Multi-Phase Rectification," *Sensors*, vol. 23, no. 15, Aug. 2023.
- [136] A. Nakata, S. Tanaka, K. Sugano, T. Tsuchiya, and O. Tabata, "ELECTRICAL EQUIVALENT CIRCUIT MODEL OF MICROFLUIDIC SYSTEM CONTAINING PIEZOELECTRIC VALVELESS MICROPUMP AND VISCOELASTIC PDMS MICROCHANNEL."
- [137] M. Tikekar, S. G. Singh, and A. Agrawal, "Measurement and modeling of pulsatile flow in microchannel," *Microfluid. Nanofluidics*, vol. 9, no. 6, pp. 1225–1240, Dec. 2010.
- [138] B. Dincau, E. Dressaire, A. Sauret, B. Dincau, E. Dressaire, and A. Sauret, "Pulsatile Flow in Microfluidic Systems," *Small*, vol. 16, no. 9, p. 1904032, Mar. 2020.

- [139] Z. Yin, Z. Huang, X. Lin, X. Gao, and F. Bao, "Droplet Generation in a Flow-Focusing Microfluidic Device with External Mechanical Vibration," *Micromachines* 2020, Vol. 11, Page 743, vol. 11, no. 8, p. 743, Jul. 2020.
- [140] Z. Z. Chong *et al.*, "Acoustofluidic control of bubble size in microfluidic flow-focusing configuration," *Lab Chip*, vol. 15, no. 4, pp. 996–999, Feb. 2015.
- [141] Y. Y. Zhang and H. M. Xia, "PZT actuator-controlled high-frequency microdroplet generation: Reducing the restrictions of channel size, fluid viscosity, and flow rate," *Sensors Actuators B Chem.*, vol. 368, p. 132183, Oct. 2022.
- [142] "PDU100 Micro Piezo Driver | PiezoDrive." [Online]. Available: <https://www.piezodrive.com/modules/pdu100-micro-piezo-driver/>. [Accessed: 08-Mar-2024].
- [143] "BD300 - Dual Channel Driver." [Online]. Available: <https://www.piezodrive.com/modules/bd300-dual-channel-drivers/>. [Accessed: 08-Mar-2024].
- [144] "Driver Board for Piezoelectric Micro Pumps – Takasago." [Online]. Available: <https://www.takasago-fluidics.com/products/piezoelectric-micro-pump-driver-board>. [Accessed: 08-Mar-2024].
- [145] "AN2104 | Application Note | Microchip Technology." [Online]. Available: <https://www.microchip.com/en-us/application-notes/an2104>. [Accessed: 08-Mar-2024].
- [146] "TG001: PIEZOELECTRIC DISC PUMP DRIVE GUIDE." [Online]. Available: <https://www.theleeco.com/uploads/2023/06/TG001-Disc-Pump-Drive-Guide.pdf>. [Accessed: 08-Mar-2024].
- [147] B. Pečar *et al.*, "Micropump operation at various driving signals: numerical simulation and experimental verification," *Microsyst. Technol.*, vol. 21, no. 7, pp. 1379–1384, Jul. 2015.
- [148] Q. S. Pan, L. G. He, F. S. Huang, X. Y. Wang, and Z. H. Feng, "Piezoelectric micropump using dual-frequency drive," *Sensors Actuators A Phys.*, vol. 229, pp. 86–93, Jun. 2015.
- [149] K. Ahn, J. Agresti, H. Chong, M. Marquez, and D. A. Weitz, "Electrocoalescence of drops synchronized by size-dependent flow in microfluidic channels," *Appl. Phys. Lett.*, vol. 88, no. 26, p. 264105, Jun. 2006.
- [150] L. Mazutis *et al.*, "Droplet-based microfluidic systems for high-throughput single DNA molecule isothermal amplification and analysis," *Anal. Chem.*, vol. 81, no. 12, pp. 4813–4821, Jun. 2009.
- [151] M. Zagnoni, G. Le Lain, and J. M. Cooper, "Electrocoalescence mechanisms of microdroplets using localized electric fields in microfluidic channels," *Langmuir*, vol. 26, no. 18, pp. 14443–14449, Sep. 2010.
- [152] T. Leary, M. Yeganeh, and C. Maldarelli, "Microfluidic Study of the Electrocoalescence of Aqueous Droplets in Crude Oil," *ACS Omega*, vol. 5, no. 13, pp. 7348–7360, Apr. 2020.
- [153] X. Luo, H. Yin, H. Yan, X. Huang, D. Yang, and L. He, "The electrocoalescence behavior of surfactant-laden droplet pairs in oil under a DC electric field," *Chem. Eng. Sci.*, vol. 191, pp. 350–357, Dec. 2018.

Acknowledgements

First and foremost, I owe my deepest appreciation to my parents and relatives who have provided an unwavering presence of support and encouragement on my journey through the stages of higher education. Likewise, to Tallinn University of Technology and the Thomas Johann Seebeck Department of Electronics for creating these stages and providing the opportunities.

I would like to express my sincerest gratitude to my supervisor Dr. Tamás Pardy, who has always been there to offer guidance at any obstacle faced throughout my doctoral studies. Without his academic philosophy and vision, I would not have recovered from my first PhD topic, to pick up the topic of this dissertation. I highly value the thought-provoking discussions we had on many worldly and philosophical subjects.

Further, I would like to thank my co-supervisor Professor Ott Scheler, and also Professor emeritus Toomas Rang and Professor Yannick Le Moullec for their perspectives, experienced academic example, and interesting insights, valuable to me personally, to my doctoral work and academic career.

I want to express my heartfelt thanks to my close colleague Kaiser Pärnamets, PhD, whose efforts, and discussions, determined to lead to interesting ideas, have been invaluable to me and to this work.

Lastly, I want to thank my research collaborators and colleagues met along the way, for their kind support and expertise, Kanwal Ashraf, PhD, Simona Bartkova, PhD, Immanuel Sanka, PhD, Nafisat Gyimah, Fariha Afrin, Hip Kõiv, PhD, and Frederick Rang, in both the Thomas Johann Seebeck Department of Electronics and Department of Chemistry and Biotechnology.

This research was facilitated financially by projects of PRG620, PUT1435 and PSG897 granted by the Estonian Research Council (ETAG), as well as the TTU development program 2016-2022, project code 2014-2020.4.01.16-0032 and the Dora Plus programme.

Abstract

Development of a Transferable Microfluidic Droplet Generator

A two-decade old branch of microfluidics, droplet generation, popularized in research areas such as biochemistry and biomedicine, is found to be lagging in standardization and commercialization. The heavily prioritized performance metrics in generation and managing of droplets forms an ambiguous selection of cutting-edge methods.

In this thesis, to address the lack of focus on accessibility to the technology and replicability of the methods, a platform needed to be developed with modularity, affordability, and portability in mind. Accordingly, the modules from which the platform was assembled included a standalone flow regulation device, droplet detector, setup controller and interchangeable fluidics.

The flow regulation device, specifically designed for two-phase microfluidics, used an ESP32 development board to interface with two independently controlled micropumps and three pressure sensors. The pumps (mp6-liq, Bartels) used piezoelectric diaphragm oscillations to generate independent pulsatile pressure sources for two fluid phases. The performance of the flow regulation device was evaluated using a flow-focusing microfluidic chip to produce water-in-oil droplets with deionized water and mineral oil with 2% w/w Span[®] 80 surfactant. Using the sensors in a differential configuration across the chip, the pumps were managed by closed loop PID controllers at a rate of 166 Hz. Formed droplets were imaged and measured while inside the chip, yielding indirect coefficients of variability in droplet size of less than 2%. This device was able to operate continuously for ~11 h on a 14.8 Wh Li-Po battery. The adaptability of the device into a module was tested by transferring its design to a different lab for a different application (air-water segmented flow generator for an IR LED-phototransistor flow sensor).

With a similar operation principle to the flow sensor, an LED-photodiode optical sensor was used for the droplet detector module. In addition to the sensor, the detector included a multi-stage amplifier, a band-pass filter, and a 16-bit A/D converter. For the sensor to detect the droplets, it needed to be vertically aligned to the cross-junction of the droplet generation chip. To ease the alignment process, an adjustable 3D printed 3-stage sensor column was designed. The optical sensor used brightfield illumination which largely passed through the liquids and the PDMS-glass chip material, leaving mainly the phase-change interface surrounding the droplets to refract light away from the photodiode. The algorithm for interpreting the droplet size and generation rate, along with flow regulation, droplet feedback PID controllers, and wireless user access was managed by the setup controller (Raspberry Pi 4B). The fully assembled droplet generation platform (CogniFlow-Drop), costing ~650 € and consuming ~8 W of power, was sized to fit into a common carry-on luggage (55 x 36 x 23 cm). The platform demonstrated the ability to generate droplets in diameters of ~50-200 μm at generation rates between ~200 and 800 Hz with ~5-10% CV. However, < 2% CV was recorded with droplet generated from deionized water and fluorocarbon oil with 2% w/w perfluoropolyether (PFPE)-poly(ethylene glycol) (PEG)-PFPE triblock surfactant at a generation rate control target at 400 Hz (the second harmonic of the disperse phase piezoelectric pump oscillations).

The first published version of CogniFlow-Drop had left several open challenges, such as operating system (OS) task scheduler latency, inter-process data transfer delays,

inadequate pressure sensor sampling rate, and considerably limited pump driver control. As one of the solutions for the computational delays, the droplet sensor signal processing was updated by replacing the band-pass filter with an improved low pass filter, by making the second amplifier stage and the optical signal leveler adjustable from software, and an ESP32 development board to take over the sensor signal interpretation from the Raspberry Pi. As for the inadequate pressure sensors on the flow regulation module, faster sensors were introduced which brought the flow regulation PID control rate from 166 Hz up to ~1950 Hz. As a solution to the limited pump driver control, a novel piezoelectric pump driver was developed. In combination, the hardware and software modifications enabled CogniFlow-Drop to reach below 1% in coefficient of variation (CV) in both the droplet size and generation rates at a generation rate target of 800 Hz (the fourth harmonic of the disperse phase piezoelectric pump oscillations). Having relocated the droplet interpretation off of Raspberry Pi, increased the detector's A/D converter sampling rate from ~153 kHz to ~256 kHz. This also significantly reduced the impact from the latency of the OS task scheduler. The modified platform was shown to generate droplets with < 5% CVs at generation rates between ~400 and 2000 Hz. In response to the need for a generalized droplet generation solution, the upgraded CogniFlow-Drop platform fulfilled the design criteria derived from the research challenges and the state-of-the-art parameters.

Lühikokkuvõte

Ülekantava mikrovedelik-tilkade generaatori arendus

On leitud, et kahe aastakümne vanune mikrovedelikundusliku teadusala haru, tilkade genereerimine, mille kasutus on levinud valdkondades nagu biokeemia ja biomeditsiin, on standardiseerimise ja kommertsialiseerimisega ajast maha jäänud. Rangelt prioriseeritud tulemusnäitajad tilkade genereerimises ja haldamises on loonud segase valiku tiptaseme meetoditest.

Et adresseerida fookuse puudulikkust selle tehnoloogia ligipääsetavusele ja metoodika reprodutseeritavusele, on käsitletud dissertatsioonis peetud vajalikuks arendada välja vastav platvorm, sihiks pidades selle modulaarsust, taskukohasust ja transporditavust. Sellele vastavalt, koosnes koostatud seade moodulitest nagu eraldiseisev voolu reguleeriv seade, tilkade tuvastaja, süsteemi seadistamise kontrolleri ning modifitseeritav vedeliku süsteem.

Spetsiifiliselt kahefaasilise mikrovedelikundusliku süsteemi jaoks arendatud voolu reguleeriv seade, kasutas ESP32 arendusplaati, et suhelda kahe eraldi juhitava mikropumba ja kolme rõhusensoriga. Pumbad (mp6-liq, Bartels) kasutasid piezoelektrilise membraani ostsilleerimist, et genereerida eraldiseisvad pulseerivad rõhuallikad kahe vedeliku faasi jaoks. Voolu reguleeriva seadme jõudlust evalveeriti kasutades voolu fokuseerivat mikrovedelikundusliku kiipi, et toota vesi-õlis tilkasi deioniseeritud veest ja mineraalõlist koos 2% m/m Span® 80 pindaktiivse ainega. Rakendades rõhusensoreid diferentsiaalkonfiguratsioonis üle kiibi, võimaldas juhtida pumпасid PID kontrolleritega suletud ahelas 166 Hz-se sagedusega. Kiibis kujunenud tilgad talletati ning mõõdeti piltidelt, millest saadi kaudsed tilga suuruse varieeruvus koefitsendid madalamad kui 2%. Käsitletud seade suutis 14.8 Wh Li-Po aku peal töötada peatamatult ~11 tundi. Seadme kohandatavust moodulina sai testitud läbi seadme disaini ülekandmisega teise laborisse aluselise eristuva rakenduse jaoks (õhk-vesi segmenteeritud voolu generator IR LED-fototransistor voolu sensori jaoks).

Voolu sensorile sarnase tööpõhimõttega, sai tilkade tuvastus moodulis kasutatud LED-fotodiod optilist sensorit. Sensorile lisaks, hõlmas tuvastaja endas mitmeastmelist võimendit, ribafiltrit ja 16-bitist A/D muundurit. Et sensor suudaks tilkasid tuvastada, oli vajalik, et see oleks tilkade genereerimise kiibi voolude ristumiskohaga vertikaalselt joondatud. Et hõlbustada joondamist, disainiti 3D prinditav reguleeritav kolmeastmeline sensori torn. Optiline sensor kasutas helevälja valgustust, mis oli võimeline vedelikest ja PDMS-klaas kiibi materjalist suuresti läbi tungima, jättes peamiselt faasimuutva tilga pinna fotodiodist valguse eemale murdumiseks. Algoritm tilga suuruse ja genereerimise sageduse tõlgendamiseks koos voolu reguleerimise, tilga tagasiside PID kontrolleri ja juurdepääsuga juhtmevabalt kasutajale oli hallatud süsteemi kontrolleri poolt (Raspberry Pi 4B). Täielikult kokkupandud tilkade genereerimise platvorm (CogniFlow-Drop), maksumusega ligikaudu 650 € ja umbes 8 W-se energiatarbega, oli mõõdetud mahtuvat tavalisse käsipagasisse (55 x 36 x 23 cm). Platvorm näitas võimet luua tilkasid läbimõõduga umbes 50-200 µm genereerimise sagedusvahemikus umbes 200 kuni 800 Hz koos umbes 5-10% CV-ga. Siiski mõõdeti <2% CV tilkadega, mis tekitati deiooniseeritud veest ja fluoriidõlist koos 2% m/m perfluoropolüeteer (PFPE)-polü(etüleenoksiid) (PEG)-PFPE tribloki pindaktiivse ainega, 400 Hz-se genereerimise sihtsagedusega (hajutatud faasi piezoelektrilise pumba teine harmoonik).

Esmasena publitseeritud CogniFlow-Drop versioonil olid mitmed lahtised probleemid, nagu operatsiooni süsteemi (OS) ülesannete planeerija latentsus, protsessidevahelised

andmeedastuse viivitused, ebapiisav rõhu sensori mõõtmisagedus ja märkimisväärselt limiteeritud pumba juhtseadme rakendusulatus. Ühe lahendusena arvutuslikele viivitustele uuendati tilkade sensori signaalitöötlust, asendades ribaläbipääsufiltri parandatud madalpääsufiltriga, muutes teise astme võimendi ja optilise signaali tasandaja tarkvarast reguleeritavaks ning ESP32 arendusplaadi võtmaks üle optilise sensori signaali tõlgendamise Raspberry Pi-lt. Ebapiisavad rõhu sensorid voolu reguleerivas seadmes said asendatud kiirematega, mis tõid voolu reguleeriva PID kontrolleri sageduse 166 Hz-i pealt kuni ~1950 Hz-ni. Lahendusena limiteeritud pumpade juhtseadme funktsionaalsusele aretati välja uudne piezoelektriline pumba juhtseade. Kombineeritult võimaldasid riist- ja tarkvaramuudatused CogniFlow-Drop platvormil saavutada nii tilga suuruse kui ka tilkade genereerimise sageduse variatsiooni koefitsendid (CV) alla 1% genereerimise sihtsagedusel 800 Hz (hajutatud faasi piezoelektrilise pumba ostsilleerimise neljas harmoonik). Tilkade tõlgendamise algoritmi Raspberry Pi pealt ümber asetamisega, kasvas A/D muunduri mõõtesagedus ~153 kHz-i pealt ~256 kHz-ni. See vähendas oluliselt OS-i ülesannete planeerija latentsuse mõju. Modifitseeritud platvorm näitas tilkade genereerimist < 5% CV-ga genereerimise sagedustel vahemikus ~400 kuni 2000 Hz. Vastates laialdaselt kasutatava tilkade genereerimise lahenduse vajadusele, täitis täiustatud CogniFlow-Drop platvorm kõik uurimisväljakutsetest ja tipptaseme lahenduste parameetritest tulenenud disaini kriteeriumid.

Appendix 1

Publication I

R. Jõemaa, M. Grosberg, T. Rang, T. Pardy. Low-cost, portable dual-channel pressure pump for droplet microfluidics. In 2022 45th Jubilee International Convention on Information Communication and Electronic Technology (MIPRO), IEEE, 2022, doi: 10.23919/MIPRO55190.2022.9803371

Low-cost, portable dual-channel pressure pump for droplet microfluidics

R. Jõemaa*, M. Grosberg*, T. Rang* and T. Pardy*

* Tallinn University of Technology/Thomas Johann Seebeck Department of Electronics, Tallinn, Estonia

rauno.joemaa@taltech.ee
martin.grosberg@taltech.ee
toomas.rang@taltech.ee
tamas.pardy@taltech.ee

Abstract - Due to the high cost and complexity of instrumentation in droplet microfluidics, droplet generation has been limited to a small subset of the scientific community. In addition, scientific value is not in droplet generation, but rather in monodisperse microreactor environments created in droplets. To reduce the complexity of droplet generation, we designed a low-cost (~250 €), portable, dual-channel microfluidic pressure pump. In contrast with commonly used syringe pumps, our pump could control both phases in a two-phase flow simultaneously and pump continuously without refilling. Furthermore, it had wireless remote control and was battery-powered for portability. The pump was controlled through a dual core ESP32 DevKitC board, which enabled concurrent management of wireless access and flow control. Pressure setpoints could be configured remotely via Wi-Fi using a web browser based graphical user interface. Low-pulsation, continuous flows were produced by piezoelectric diaphragm pumps and regulated by closed-loop control of the pressure drop through the microfluidic chip. The pump could produce flow rates between 10-2050 $\mu\text{l}/\text{min}$ for different liquid viscosities. Powered from its internal 3.7 V, 4 Ah battery, the pump could operate for >10 h at maximum load.

Keywords – *microfluidic; piezoelectric; pressure; pump; portable; wireless; droplet generation;*

I. INTRODUCTION

Microfluidic droplets are often used in high-throughput applications with up to hundreds of millions of samples [1]. Each droplet functions as a reaction chamber with a highly consistent environment. This enables precise process control and repeatability of reactions. To produce droplets with minimal size variation, a flow generator such as a syringe pump or constant pressure source with pulseless flow characteristics is typically used [1], [2]. Droplet volumes can go down to the picolitre range, thus flow stability significantly affects droplet size variation. Since droplets are generated from immiscible liquids, such as oil and water, two stable flow sources are required. This makes the infrastructure complex and expensive. Because of this, alternative flow generators have been sought [3]–[5]. Reducing the entry barrier can greatly speed up realization of applications in blood analysis, cancer, and drug treatment research.

High flow rate resolution (~0.16 $\mu\text{l}/\text{min}$ steps) commercial laboratory syringe pumps cost several thousand Euros [6], [7] and offer a wider set of capabilities than are needed for single experiments. Medical single channel infusion pumps with a lower flow rate resolution (>>1.6 $\mu\text{l}/\text{min}$ steps) cost ~300 € - 500 € for dual-channel versions [8], [9]. However, syringe pumps need to be refilled, reset and re-stabilized, which disrupts experiments. To overcome this limitation, peristaltic pumps are often used instead, but they produce a pulsatile flow that is more difficult to control [10], [11]. Pressure pumps have no such limitations but come at a much higher cost (3000-15000€) [12]–[14]. A solution, which has no volume limit and offers a low-pulse flow profiles is using micropumps based on piezoelectric diaphragms [15].

An entrance level pump for droplet generation ought to be simple, minimally dependent on external infrastructure and enable easy operational monitoring and debugging. For better portability, it should be battery-powered and for added user comfort it should have wireless remote-control. The option to control the device wirelessly also enables use in confined spaces, for instance under fume hoods in flow chemistry applications. Furthermore, the ideal droplet generator should be able to operate as a constant pressure source without the need to refill. Software support and network communication isn't rare for higher-end pumps [16], [17]. For added portability, commercial medical syringe pumps already offer battery-powered operation, however, only at device prices up from 500 €, it's possible to see operational times (flow rate 5 ml/min) on battery power reach 8 to 10 hours [18].

In this work, we propose a compact, portable, dual-channel pressure generator that can fulfill the aforementioned needs and yet costs significantly less than previously demonstrated systems with similar performance. Compared to the closest existing work, our solution implements flow control through proportional integral derivative (PID) control development by pressure sensors configured in an arrangement that is best suited for microfluidic droplet generation chips. With the sensitive relationship between pressure and flow rate of the used piezoelectric pumps, controlling them through voltage and frequency alone over different microfluidic

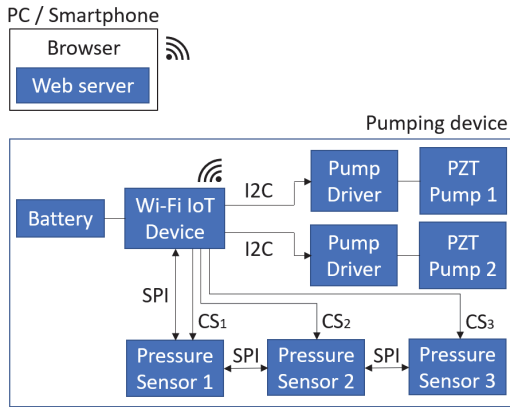


Figure 1. System overview and communication pathways

chip geometries, setup heights, or liquid densities, can be erroneous and costly to calibrate. With a PID control loop set to adjust by requested pressures over a chip, pumping rates will remain fixed within the maximum capabilities of the pump regardless of variables in the application setup. We detail the development process, design considerations and construction of the experimental device. Finally, we demonstrate the functionality of the system as a droplet generator in a proof-of-concept droplet microfluidic tests.

II. EXPERIMENTAL SETUP AND METHODOLOGY

A. System design overview

Using a commercial low-power IoT (Internet of Things) device with Wi-Fi, I2C and SPI communication options, logging sensor data, controlling multiple pumps and enabling remote GUI (Graphical User Interface) hosting, a battery powered pumping device has been designed (Fig. 1). The pumping device will host two individually drivable piezoelectric (PZT) pumps in order to control both continuous and disperse flows in droplet generation. Pumps are controlled using I2C protocol. There are three pressure sensors in total, where sensors 1 and 2 will measure the output of the PZT pumps 1 and 2 respectively. These pressures represent the inflow pressures before entering the droplet generation chip. Sensor 3 measures the pressure at the output of the microfluidic chip. Sensors are placed in series on an SPI line with individual Chip Select (CS) lines lead to each sensor PCB. The IoT device is controlled over Wi-Fi using a browser-generated web UI that can be accessed from a PC or smartphone. Aside from custom PCBs, the device ought to be made from easily available commercial components to keep the design as simple as possible. This reduces time of assembly, ensures commercial quality control, and enables easier repair or upgrading.

B. Experimental setup

1) Pump and pump control

A piezoelectric liquid pump BT-mp6-liq was selected from Bartels Mikrotechnik as it satisfies the flow rate and

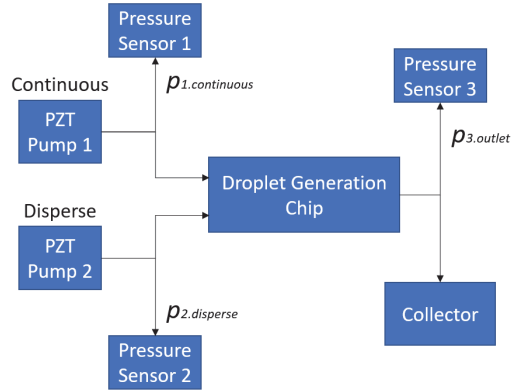


Figure 2. Pressure data collection points; PZT Pump 1 represents the continuous (water) flow source, Pump 2 represents the disperse (oil) flow source; Liquids flow from the pumps to separate inlets on the Droplet Generation Chip; Pressures $p_{1.continuous}$ and $p_{2.disperse}$ are measured from those lines; After the phases merge in the chip, the flow path continues to the Collector; Pressure value $p_{3.outlet}$ is obtained from that line.

pulsation frequency and amplitude requirements for the device. The pump driver BT-mp-Highdriver, a commercial off-the-shelf (COTS) chip, was also selected from Bartels Mikrotechnik. Together with these drivers, the pumps could operate at 50 - 800 Hz switching rate where the latter half being more suited for gases and former for liquids. Higher density liquids are moved better at lowest pumping frequencies. Additional aspects of the pump drivers were the amplitude range (10 - 250 V_{pp}) and wave form types (sine/rectangular/trapezoidal). Inside the BT-mp6-liq pumps there are two piezoelectrically actuated membranes in series, separated into volumetrically equal compartments using check valves. This design makes the pump unidirectional, offering inherent resistance to backpressure. Power consumption for a driver-pump pair at average operation is around 250 mW. BT-mp-Highdriver is controlled through I2C protocol, giving full access to changing the frequency, voltage, and wave form.

2) Sensors

Piezoresistive silicon pressure sensor from Honeywell MPRLF0006KG0000SC was selected, as it offered reasonable coverage to pressure ranges that we most often encountered in our tests, high resolution, and auto-zero calibration option. The sensor has a maximum stated differential pressure limit of 6 kPa from atmospheric pressure albeit its tested functional range was between -2 kPa to 8 kPa. While the BT-mp6-liq pump with BT-mp-Highdriver is able to build pressures up to 60 kPa, in our earlier droplet generation tests, it was rare to reach above 6 kPa, influencing our initial sensor pick. These sensors incorporate an ASIC (Application Specific Integrated Circuit) capable of 24-bit pressure values, translating into less than 0.01 Pa resolution. The settled full resolution could be polled at 5 ms intervals. However, with the autozero calibration option, the 24-bit resolution is reduced to 14-bits through an ideal transfer function which for the chosen model skims 20% off from the lower and higher ends.

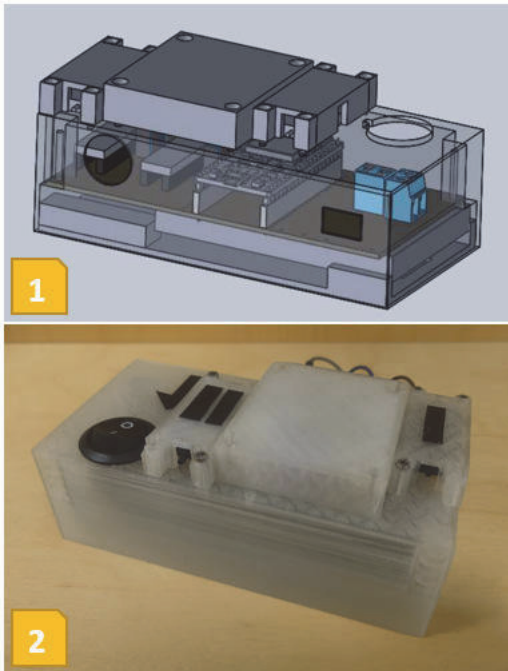


Figure 3. (1) 3D CAD view and (2) 3D printed result of the dual-channel piezoelectric pressure pump.

The pumping device used three sensors as this is a task-oriented design for droplet generation chips. Polling three sensors in parallel increased the total interval to ~ 5.3 ms on average. Droplet generation chips typically have two inlets, one for continuous and one for disperse flow, and one outlet for droplet collection. Two sensors were measuring pressures from points near the inlets of the chip while the third sensor measured the pressure near the outlet of the chip (Fig. 2). Between each of the three pressure measurement points and the chip connections, equal lengths of 0.5 mm ID PTFE tubing was used. This sensor setup enabled the measurement of differential pressures for both flow phases over the chip. MPRLF0006KG0000SC sensors operate on 3.3 V with a typical power consumption of 10 mW. The sensor can communicate using both I2C and SPI protocols. For this device, SPI was chosen for faster data transfer for a more responsive PID control.

3) Wi-Fi IoT device

The core intelligence of the device was handled by an ESP32-DevKitC-32U board by Espressif, which has a dual-core processor, allowing us to perform sensor and pump communications separately from handling readings and commands over Wi-Fi. Since the processor operates at 3.3 V, 5V supplies (external and via on-board USB) were regulated on-board to 3.3 V. Typical power consumption for this development board, with an active Wi-Fi transmission is estimated to ~ 800 mW. Since the sensors operate likewise on 3.3 V and require only around 3.3 mA of current, the sensors were supplied through ESP32-DevKitC regulated 3.3 V supply pin.

4) Power management

Battery selection was limited by the battery form factor, therefore thin lithium polymer (Li-Po) variants were searched. The pump drivers operate at 5 V, the processor and sensors operate natively at 3.3 V, whereas the processor board can also be powered with a 5 V supply, thus a 5 V external supply was needed. Since Li-Po batteries can supply a range of voltages between 3.2 and 4.2 V dependent on ambient temperature and remaining capacity, an unmarked 4.3 – 27 V step-up regulator for 3.7 - 4.2 V 18650 Li-ion batteries was ordered from eBay. An onboard potentiometer enabled setting the output voltage level to 5 V, which had to be configured while the battery was only connected to the regulator as the ordered regulators arrived with potentiometers in random positions. The regulator had a micro-USB connector for charging the battery at 4.2 V with up to 1 A.

The capacity of the battery was chosen according to the minimum operation duration requirement. With a total of 500 mW used by two driver-pump pairs, 30 mW for three sensors and 800 mW for the ESP32-DevKitC board, leaving the total power required at 1330 mW. For the average supply voltage of 3.7 V from a Li-Po battery, the current consumption would be around 360 mA. For

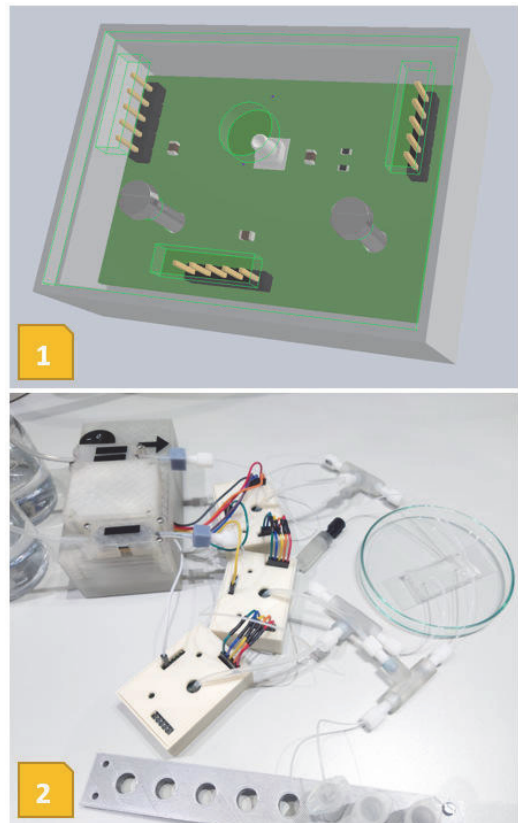


Figure 4. (1) 3D CAD view of the pressure sensor enclosure and (2) 3D printed version of the enclosures in a full droplet generation setup with wires and tubes attached to the sensor PCBs inside the enclosures.

an estimated 10 hours of continuous operation with some room for losses on the step-up regulator, a 4 Ah 3.7 V Li-Po battery (LP805080, Cellevia Batteries) was chosen.

5) PCBs

A double-layer main PCB (113.01x55.88) facilitated the processor demo board, pump drivers, pumps, stacked step-up regulator board and along with a few pull-up resistors and smoothing capacitors also the connectors for the battery and mechanical battery disconnection switch. Pull-up resistors were necessary due to the I2C pins on the ESP32 DevKitC operating in the active low mode. The sensor PCB (50.800x34.417) was designed as a standalone unit, separate from the main PCB. Its design is minimal, limited only to the sensor, decoupling capacitors and pins as the selected sensor already houses an internal amplifier and an analog-to-digital converter. The main PCB of the pumping device can be hand-soldered and easily manually assembled but the sensor PCB may benefit from a stencil or preassembly on order due to the specific surface mount package of the sensor.

6) Enclosures

With the thin Li-Po battery package, the main PCB was fitted into a 120x60x30 size 3D printed modular enclosure. Piezoelectric pumps were left outside of the main box, attached to the top (Fig. 3) to enable quick replacement and direct access to the inlet and outlet. The sensor PCBs were fitted into separate 57.8x42.417x19.5 size 3D printed enclosures (Fig. 4). 3D CAD files for the enclosures are stored online at our project Github (<https://github.com/taltechloc/hw-open-pressure-pump>). Parts were printed using Prusa 3D printers (i3 MK3S or MINI) with PLA (Polylactic Acid) filament.

7) Firmware

The firmware on the ESP32 microcontroller (MCU) is housed on a 4 MB SPI flash memory. Overview of the firmware files is given at our Github. Taking full advantage over its wireless features, over the air (OTA) programming has been implemented. For this to function, the SPI flash has been partitioned into two separate memories – one to host and operate current firmware and the other to be vacant for a new uploaded binary file. The OTA feature relies on continuous wireless communication through hosted web server. This is achieved using freely available ESPAsyncWebServer, SPIFFS and AsyncElegantOTA libraries from Github or downloaded directly through an Arduino IDE. The MCU can host a web server using ESPAsyncWebServer. The server acts as a website as it enables downloading of HTML, CSS, and JavaScript files by the user. With these options, a graphical user interface was made (Fig. 5). The web application gives options with which to adjust each pump separately and multiple settings related to PID control. Depending on whether PID pressure regulation is used, the pump can be either set to run at a fixed driving voltage or set by measured pressure differences. PID coefficients can be adjusted on the run.

As the MCU is dual-core, peripheral communications have been split using the FreeRTOS API (Application Programming Interface) function “xTaskCreatePinnedToCore”. Between cores, the tasks

were split such that polling speed sensitive pressure sensor values and PID loop were kept on one core and pump driver commands along with web server hosting was managed on the other core. Pressure sensing and PID have been set as first priority among cores. Default PID coefficients in the latest firmware have been set to K_p of 2, K_i and K_d as 0 for both pumps, which are to be configured through the web app manually as is seen best for specific application requirements.

Control of the PZT pump drivers was done over I2C lanes, through the ESP32-DevKitC board IO pins 2 (SDA) and 4 (SCL). Definitions and functions for communicating with the BT-mp-Highdriver were given as a fully applicable example code in the driver datasheet. Pump functions, mainly changing the waveform shape and frequency, were implemented in the main loop code in the lower priority core. This was because these elements of the waveform are not implemented in

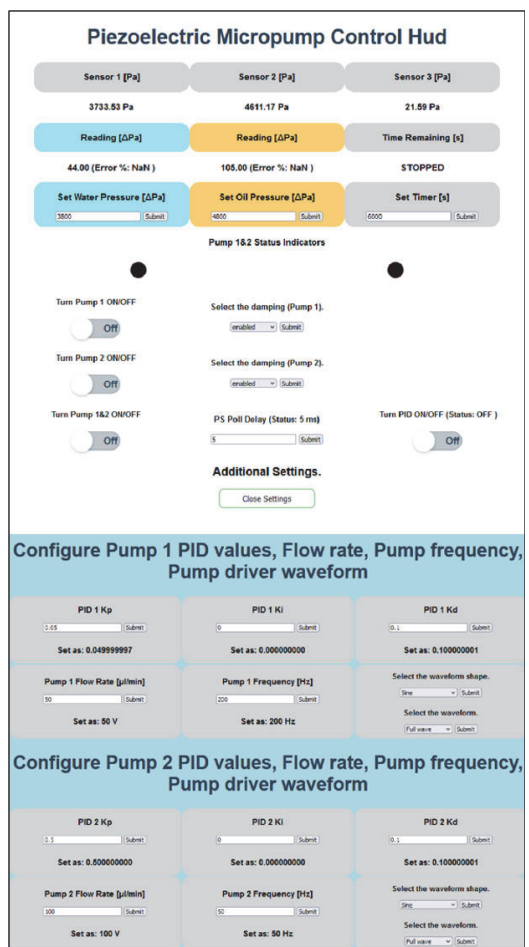


Figure 5. Web browser user interface, hosted by the MCU, for controlling the individual pump voltages, frequencies, waveforms and adjusting the PID coefficients and pressures targets. In addition to displaying current settings on the device, pressure and PID values are continuously updated and logged into the browser console.

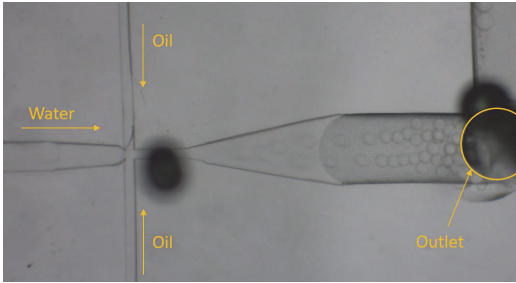


Figure 6. Droplet generation in an oil/water flow focusing microfluidic chip using the liquid flows produced by the piezoelectric pump.

automated flow control. Pump frequency is expected to be relatively fixed to density of the pumped media.

Sensor pressure values were polled using SPI lanes (MISO, MOSI, CLK) which were set to run at a clock rate of 800 kHz. Sensors were also tested to be working well at 1.2 MHz. For each of the three sensors, a chip select IO pin was defined. Since each sensor required an acquisition command and had a 5 ms saturation period,

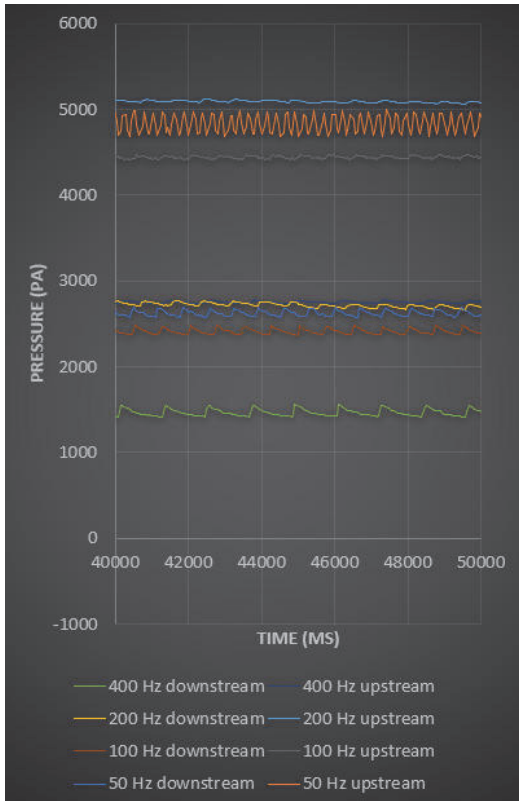


Figure 7. Transfer of pump driver frequency into secondary vibrational flow rate pulsations measured in pressure change. Flow media was water at room temperature. Pump driving waveform was sinusoidal, full wave. Two pressure sensors were placed in series after one pump with an average of 200 mm of 0.5 mm ID PTFE tubing between the pump and the upstream sensor, between the sensors and from the downstream sensor to open air.

all three pressures were handled in sequence. In this way it was possible to address pressure values obtained in the previous cycle in the PID calculations during the measurement of new values. For faster than web app data logging, pressure values were also continuously sent to the serial port of the MCU. Serial data from the micro-USB port on the MCU should only be accessed when the battery power is turned OFF as it may otherwise damage the on-board voltage regulator on the ESP32-DevKitC board.

III. PROOF OF CONCEPT TESTS

Primary test for the pump was to demonstrate droplet production. The first tests were conducted using a glass flow focusing microfluidic droplet generation chip. Stable flow of droplets could be seen (Fig. 6). During this first test, for pressure sensors, evaluation boards were used (MPRLS0001PG0000SAB, Honeywell) and the software was yet unoptimized. All following droplet generation tests were done using a custom design flow focusing PDMS-glass droplet generation chip and MPRLF0006KG0000SC pressure sensors. The setup image can be seen on Fig. 4 (2). Before next tests were ran, a varying 1 to 20 Hz pattern was noted in the pressure values measured from the water flow channel. This was considered to be from the pump vibrations travelling back and forth along the tubing. As the pump houses two PZT elements in series, actuated 180 degrees out of phase in the same axis, a rocking motion of the pump is expected. This effect was more noticeable with more flexible tubing, lower pressures in the tubes and lower pumping frequencies (for water). Preliminary PZT pump driver frequency effect on the pressure stability of water showed preference to 200 Hz region where the tested two-point deviation was the lowest, around 3.6% from the mean (Fig. 7). All continued tests were done with 200 Hz pump driving frequency for water. For oil, the vibration effect was unnoticeable in comparison.

Several droplet generation tests were conducted with and without PID implemented. In all tests, the water pump driving frequency was kept at 200 Hz and the oil pump at 50 Hz. With the PID control disabled, the driving voltage and frequency was fixed. Even if the main driving settings were kept the same, reasonable repeatability was not obtained. However, during droplet

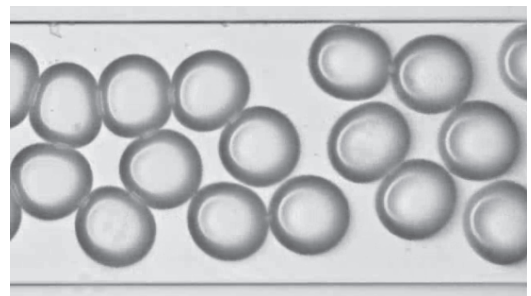


Figure 8. Frame image sample from high speed camera of droplets flowing in a channel of 625 μm width. Droplets generated with PID control disabled. Droplet generation rate ~ 30 Hz, mean droplet crosssection 28517 μm^2 .

generation, the flow remained reasonably stable. With 3 different voltage settings for both oil and water pumps, the droplets generated maintained a coefficient of variation (CV) of less than 2 %. Droplet measurements were obtained from high framerate videos taken close to the outlet of the droplet generation chip. Droplet images were taken from multiple frames of the video (Fig. 8) and analyzed using ImageJ software.

To get more reliable control over the resulting droplet size, repeatability tests were done with the PID enabled using coefficients for both oil and water pumps as K_p of 0.5, K_i as 0 and K_d as 0.1. K_i was left at zero as with minor increases, the stabilization was very difficult to reach. For the PID enabled tests, the pressure data was logged via USB to capture the PID stabilization period at high sampling rate. With the PID enabled, pressures and droplet generation parameters were repeatable, but some issues were noted as well. First repeatability test had 6 trials of fixed water pressure at 4300 Pa and at 5950 Pa for oil. The difference between the first and second half of the 6 was the PID loop delay. With an additional 50 ms added on top of the existing ~ 5.3 ms sensor polling delay, the slowest tested PID stabilization graph can be seen on

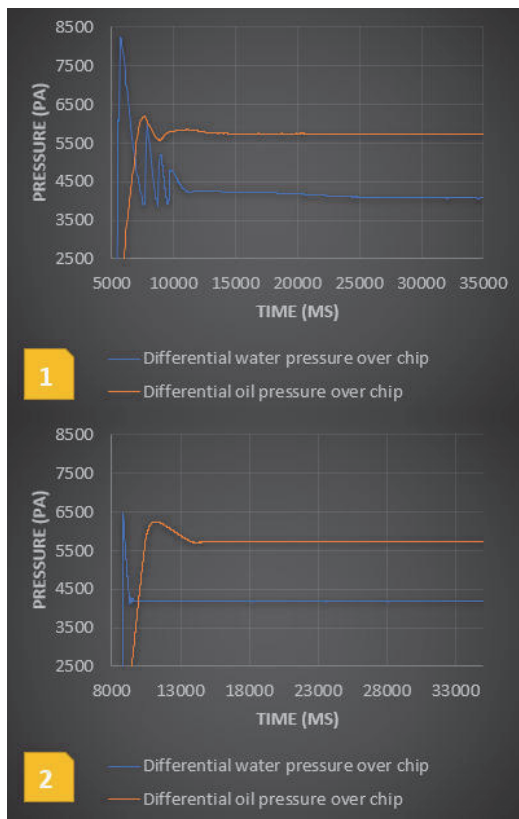


Figure 9. Differential pressure logs of a PID control enabled droplet generation startup periods. (1) 1 of 3 tests with PID loop delay ~ 55 ms, stable pressures of 4070 Pa and 5740 Pa for water and oil respectively were reached in ~ 25 s; (2) 1 of 3 tests with PID loop delay ~ 10 ms, stable pressures of 4180 Pa and 5730 Pa for water and oil respectively were reached in ~ 8 s.

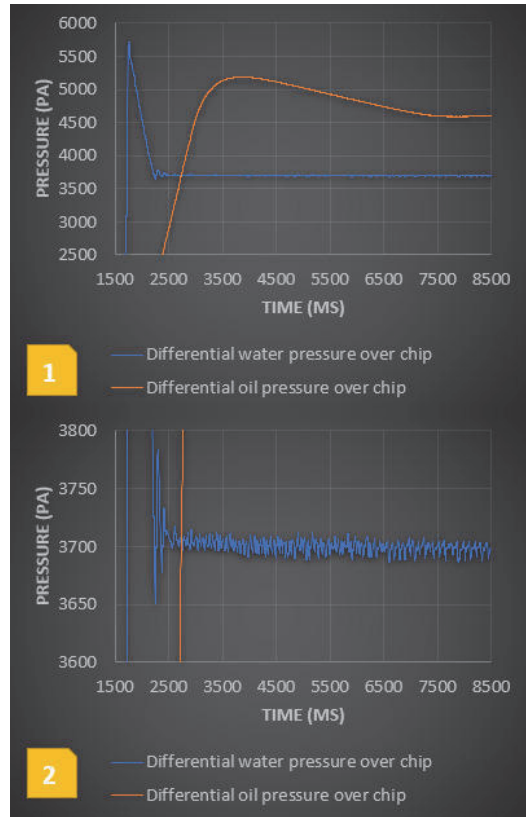


Figure 10. Differential pressure logs of a PID control enabled droplet generation startup periods. (1) 1 of 4 tests with PID loop delay ~ 5.3 ms, stable pressures of 3860 Pa and 4610 Pa for water and oil respectively were reached in ~ 7 s; (2) zoomed in graph of (1).

Fig. 9 (1). Stabilization took ~ 25 seconds to reach stable pressures. For the latter 3 tests, the PID additional delay was reduced to 5 ms instead of 50 ms. The stabilized state was reached in ~ 8 seconds as seen on Fig. 9 (2). In comparison, it was seen that with the same PID coefficients, the slower PID loop caused overshoots that reached above measurable range of 8 kPa for the water inlet side pressure sensor.

Additional repeatability tests were done with zero added PID loop delay, leaving it to the sensor delay only of ~ 5.3 ms. Pressures were fixed at 3800 Pa for water and 4800 Pa for oil. Stabilization did not improve significantly as seen from Fig. 10 (1). However, it became more noticeable that the used PID coefficients were causing a steady oscillating effect with lower PID loop delays as seen from Fig. 10 (2).

For other aspects of the pump, to test the battery powered performance, the pump was left to operate at a room temperature (25°C) with the pump voltage 250 Vpp, switching frequency 100 Hz, two channel configuration with 3 active sensors. The sensor data was updated over Wi-Fi at 1 second intervals. For the medium, deionized water was used. Test was declared finished when ESP32-DevKitC dropped its wireless

connection and pumping had stopped entirely. Our pumping device was able to operate a little less than 11 hours.

IV. CONCLUSION

In this paper, a low-cost (~250 €) pressure pump design was presented. Additional key features of the pump include wireless communication, powering from battery (> 10 h operation time with both piezoelectric pumps working at full voltage amplitude, 100 Hz pulsations and 1 Hz wireless operational data updates), controlling two pumps individually and a PID control tied to differential pressures across a microfluidic droplet generation chip. Our device demonstrated feasibly stable pumping pressures, droplet generation rates and PID enabled repeatability; however, vibrational artifacts were present in the pressure readings. One of the main targets to improve would be to add a pump fixture such as a rubber gasket, which ought to radically dampen the vibrational artifact. Oscillations caused by the used, sensitive PID coefficients would need to be addressed in follow-up experimental analysis with different flow media and finetuning to a range of droplet generation pressures. The maximum pressure sensing range of the device is -2 kPa to 8 kPa with a recommended range of 0 to 6 kPa. The pump adjusts its pumping voltage according to the difference between set and measured pressure drop over a microfluidic chip. Possible future improvements would be the choosing of pressure sensors based on the maximum pressure output of the pump. This would ensure that the possible overshoot of the PID control wouldn't reach values that could damage the sensor. This would also add headroom to the range of usable droplet generation chip's channel sizes. In case of very small microfluidic channels, or very high flow rates for droplet generation, a possible solution would be to adapt series or parallel pump configurations for one device, in order to provide boost to the pumping capabilities. Smaller improvements could be sensors with higher bit resolution for higher precision pressure readings, faster pump driver communication, pressure sensor PCB design with more robust connectors and connections, and an IPEX antenna for the improved Wi-Fi range. We hope the simple design approach of the device will encourage more researchers to explore droplet microfluidics research.

ACKNOWLEDGMENT

The authors would like to thank the Estonian Research Council for providing support under projects PUT1435, PRG620, as well as the TTÜ development program 2016-2022, project code 2014-2020.4.01.16-0032, and project colleagues S. Bartkova (Department of Chemistry and Biotechnology), K. Pärnamets (Thomas Johann Seebeck Department of Electronics), and N. Gyimah (Thomas Johann Seebeck Department of Electronics) from TalTech with their assistance with experimental droplet generation methods and tools.

AUTHOR CONTRIBUTIONS

Conceptualization, T.P.; methodology, T.P. and M.G.; design, M.G.; writing – draft preparation, R.J.; writing –

review and editing, T.P.; visualization M.G. and R.J.; supervision, T.P.; project administration, T.R.; funding acquisition, T.R. All authors have read and agreed to published version of the manuscript.

REFERENCES

- [1] T. S. Kaminski, O. Scheler, and P. Garstecki, "Droplet microfluidics for microbiology: techniques, applications and challenges," *Lab Chip*, vol. 16, no. 12, pp. 2168–2187, 2016.
- [2] T. Glawdel, C. Elbuken, and C. L. Ren, "Droplet Generation in Microfluidics," *Encycl. Microfluid. Nanofluidics*, pp. 1–12, 2013.
- [3] K. Langer and H. N. Joensuu, "Rapid Production and Recovery of Cell Spheroids by Automated Droplet Microfluidics," *SLAS Technol.*, vol. 25, no. 2, pp. 111–122, Apr. 2020.
- [4] A. Jönsson, A. Toppi, and M. Dufva, "The FAST Pump, a low-cost, easy to fabricate, SLA-3D-printed peristaltic pump for multi-channel systems in any lab," *HardwareX*, vol. 8, p. e00115, Oct. 2020.
- [5] J. J. Davis *et al.*, "Utility of low-cost, miniaturized peristaltic and Venturi pumps in droplet microfluidics," *Anal. Chim. Acta*, vol. 1151, p. 338230, Mar. 2021.
- [6] "Syringe pump - LP-LSP01-1C - Two-syringe push & puaæ syringe pump for continuous transferring." [Online]. Available: <https://www.drifton.eu/shop/24-syringe-pumps/215-push-pull-syringe-pump-lp-lsp01-1c/>. [Accessed: 21-Feb-2022].
- [7] "Mitos Quad Pump | Dolomite Microfluidics %." [Online]. Available: <https://www.dolomite-microfluidics.com/product/mitos-quad-pump/>. [Accessed: 21-Feb-2022].
- [8] "Smith Medical Graseby 2000 Syringe Pump at best price." [Online]. Available: <https://www.hospitalstore.com/smith-medical-syringe-pump/>. [Accessed: 21-Feb-2022].
- [9] "InfusionONE Syringe Pump– Darwin Microfluidics." [Online]. Available: <https://darwin-microfluidics.com/products/microfluidic-just-infusion-syringe-pump/>. [Accessed: 21-Feb-2022].
- [10] M. R. Behrens *et al.*, "Open-source, 3D-printed Peristaltic Pumps for Small Volume Point-of-Care Liquid Handling," *Sci. Rep.*, vol. 10, no. 1, pp. 1–10, Dec. 2020.
- [11] A. Gervasi, P. Cardol, and P. E. Meyer, "Open-hardware wireless controller and 3D-printed pumps for efficient liquid manipulation," *HardwareX*, vol. 9, p. e00199, Apr. 2021.
- [12] R. Z. Gao, M. Hébert, J. Huisson, and C. L. Ren, "µPump: An open-source pressure pump for precision fluid handling in microfluidics," *HardwareX*, vol. 7, p. e00096, Apr. 2020.
- [13] "Mitos P-Pump | Dolomite Microfluidics." [Online]. Available: <https://www.dolomite-microfluidics.com/product/mitos-p-pump/>. [Accessed: 21-Feb-2022].
- [14] "OB1 Microfluidic Droplet Pack– Darwin Microfluidics." [Online]. Available: <https://darwin-microfluidics.com/collections/pressure-controller/products/ob1-microfluidic-droplet-pack/>. [Accessed: 21-Feb-2022].
- [15] T. Kassis, P. M. Perez, C. J. W. Yang, L. R. Soenksen, D. L. Trumper, and L. G. Griffith, "PiFlow: A biocompatible low-cost programmable dynamic flow pumping system utilizing a Raspberry Pi Zero and commercial piezoelectric pumps," *HardwareX*, vol. 4, p. e00034, Oct. 2018.
- [16] "Digital Laboratory Syringe Pump dLSP500 - SYRINGE PUMPS - Drifton A/S." [Online]. Available: <https://www.drifton.eu/shop/24-syringe-pumps/2460-digital-laboratory-syringe-pump-dlsp500/>. [Accessed: 21-Feb-2022].
- [17] "Adagio Software/USB key | Surgical Instruments, Research Instruments, Laboratory Equipment | WPI." [Online]. Available: <https://www.wpiinc.com/504578-adagio-software-usb-key/>. [Accessed: 21-Feb-2022].
- [18] "Sinno MDT Syringe Pump, SN-50C6 at best price." [Online]. Available: <https://www.hospitalstore.com/sinno-medical-syringe-pump/>. [Accessed: 21-Feb-2022].

Appendix 2

Publication II

N. A. Prabatama, R. Jõemaa, K. Hegedus, and T. Pardy, “Low-cost open-source flow velocity sensor for droplet generators,” in *2022 18th Biennial Baltic Electronics Conference (BEC)*, 2022, pp. 1–4, doi: 10.1109/BEC56180.2022.9935606

Low-cost open-source flow velocity sensor for droplet generators

Nicky André Prabatama
Department of Electron Devices
Budapest University of Technology and
Economics
Budapest, Hungary
nickyandrepratama@edu.bmc.hu

Rauno Jõemaa
Thomas Johann Seebeck Department of
Electronics
Tallinn University of Technology
Tallinn, Estonia
rauno.joemaa@taltech.ee

Kristóf Hegedűs
Department of Electron Devices
Budapest University of Technology and
Economics
Budapest, Hungary
hegedus.kristof@vik.bmc.hu

Tamás Pardy
Department of Chemistry and
Biotechnology
Tallinn University of Technology
Tallinn, Estonia
tamas.pardy@taltech.ee

Abstract—Droplet microfluidics enables the manipulation of small sample and reagent volumes in physically discrete droplets, each acting as a separate microreactor. This opens up new analytical routes in cell analysis and chemical synthesis. Flow regulation, and in particular, flow sensing, is vital to enable controlled and automated droplet generation. However, precision flow sensing technology is typically complex and expensive, or lacking in certain performance metrics. This work targets development and demonstration of an optical flow velocity/flow rate sensor, which is compact and low-cost, communicates and functions wirelessly, and has performance metrics comparable to currently available flow sensors. The demonstrated experimental flow sensor prototype was evaluated using commercially available pressure sensors in conjunction with an in-house developed dual-channel pressure pump at various flow rates. Based on the evaluation, the sensor had a measurement resolution of 0.6 $\mu\text{l}/\text{min}$, measurement accuracy of 0.76 – 13.03 % at a total cost of $\sim\text{€}100$.

Keywords—droplets, flow velocity, sensing, pressure, open-source hardware

I. INTRODUCTION

Droplet microfluidics enables the manipulation of small sample and reagent volumes in physically discrete droplets, enabling high-throughput cell analysis, as well as applications in nanotechnology and chemical synthesis of pharmaceuticals [1]. Flow regulation technology (valves, pumps, flow sensors etc.) is essential to any microfluidics research. Flow regulation is not possible without flow sensing, be it via flow rate or pressure. However, there are several challenges remaining related to flow sensing technology, high cost and complexity being the leading issues for commercially available sensors, and technical limitations of low-cost and/or open-source alternatives [2].

In research, significant effort has gone into the development of flow sensors, starting with traditional thermocapillary, and Coriolis microflow measurement [2]. Other options include calorimetry, differential pressure measurement and impedimetric sensors [2]. Various ultra-low flow rate measurement techniques exist [3], allowing measurement down to nL, but the setups are large and complex, including expensive components, such as cameras. However, photometric sensors can be built at a low cost and complexity level [4]. High-end commercial sensors have a wide sensing range and excellent accuracy, but a single sensor can cost up to $\text{€}1600$ [5]. On the other hand, low-cost flow sensors demonstrated in scientific literature can cost as low as

$\text{€}100$, but typically cannot meet the same performance metrics. Key performance metrics are compared in Table I.

In the past we explored 3D printed microfluidics as a low-cost alternative to more commonly used materials [1]. In this work, we propose a low-cost flow sensing alternative in conjunction with a 3D printed millifluidic system. The flow velocity/rate sensor setup will be a compact, low-cost, wireless system, which can be remotely controlled and monitored via the Internet using a smartphone application. The system will be evaluated against a commercial off-the-shelf pressure sensor.

TABLE I. SUMMARY OF RESULTS AND COMPARISON WITH OTHER FLOW VELOCITY SENSORS

Parameter	Values				
	This work (preliminary results)	[6]	[7]	[8]	[5] ^b
Flow rate measurement range [$\mu\text{l}/\text{min}$]	6-73	10-200	50-1000	-	30-1000
Measurement resolution [$\mu\text{l}/\text{min}$]	0.6	-	-	4.8	-
Measurement accuracy/error	0.76 – 13.03%	-	2 – 10%	-	5%
Battery lifetime	2.5 – 3 hours	-	-	-	-
Inner diameter	1 mm	-	-	-	1 mm
Cost (€)	~ 100 ^a	-	-	-	2300

^a Not including the commercial pressure sensors and pumps used for evaluation

^b Commercial sensor, including the Mitos sensor interface

II. EXPERIMENTAL SETUP AND METHODOLOGY

A. Flow velocity sensor

Similar to [7], the sensor setup measured light intensity change along a tube at two positions 3 mm apart. Light intensity change resulted from a segmented flow of water and air (media with different absorption spectra), generated as detailed in Section II.B. Considering a flow in steady-state, distances D [mm] between droplets are uniform and can be measured through light intensity changes at the liquid-gas interfaces (Fig. 1/A). For calculating the velocity, this distance must be divided by the time between two droplets passing the two sensing junctions.

Each of the two sensing junctions (Fig. 1/B) consisted of an IR (infrared) LED (TT Electronics, OP298A) and a

phototransistor (OSRAM, SFH309) 90 degrees to each other at 3 mm distance, housed in a 3D printed enclosure with a shroud to block out ambient light. The enclosure was printed with a Prusa i3 MK3S [9] using black PLA filament. The function of the sensor's backend PCB (printed circuit board, schematics shown in Fig. 1/C, layout in Fig. 1/D) was signal acquisition and conditioning, based on a dual analog comparator IC (LM393), to compare the potentiometer reference voltage (used for manual calibration) to the output of the phototransistors.

For further details on the design (dimensions, geometry etc.), please refer to the GitHub repository [10].

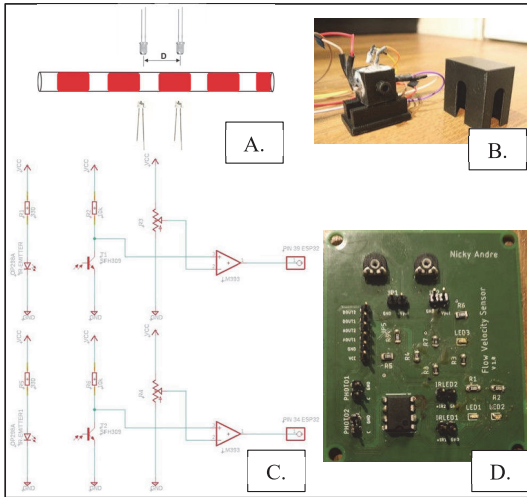


Fig. 1. Flow velocity sensor setup: A. simplified cross-sectional view, B. sensing junction, C. PCB schematics, D. PCB layout.

B. Segmented flow generation

To be able to evaluate sensor performance, distinct particles/objects/fluid phases had to be visible in flow and their relative displacement in time measured. Therefore, we generated air-liquid segmented flows using our dual-channel pressure pump (Fig. 2/A, [11]) and a 3D-printed T-junction (Fig. 2/B, [12]). The T-junction was printed on a Prusa SL1S [13] using clear resin. To generate the segmented flow, red-dyed water and air were fed into the T-junction by the pumps, and the output routed through the sensors (pressure and flow velocity). Connections were made using food-grade silicone tubing (1 mm internal diameter).

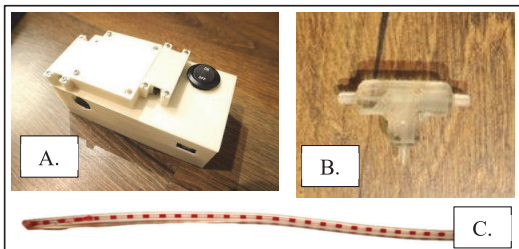


Fig. 2. Segmented flow generation setup: A. dual-channel pressure pump, B. 3D-printed T-junction, C. generated air-water segmented flow

C. Control, communication, GUI

The experimental setup was demonstrated as part of a larger IoT (Internet of Things) system consisting of the sensor boards (the object of this work, highlighted in the red box in the diagram in Fig. 3), the pump controller, as well as the applications running in the cloud and the client-side GUI (graphical user interface). The sensor boards connected to the pump controller via the ESPNOW protocol using Wi-Fi, and the pump controller connected to the Internet via a Wi-Fi access point. In the cloud, Firebase RTDB was used to store instructions (control parameters) and data from the sensor. The client-side GUI (Fig. 4) running on an Android smartphone (VIVO 1727), as well as the website GUI (Fig. 5) communicated with Firebase. Parameter I/O and data visualization were implemented via the GUIs.

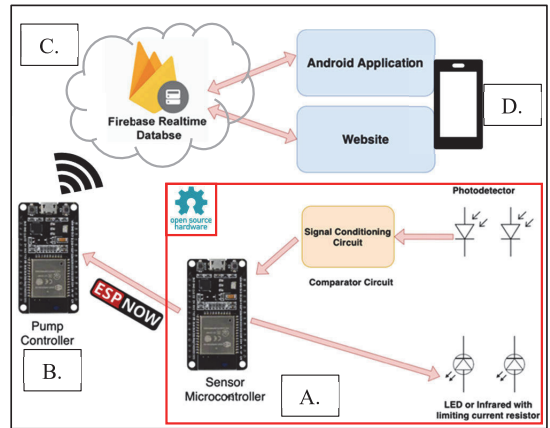


Fig. 3. IoT system architecture: (A.) Sensor data are collected and processed by the sensor boards, then (B.) transmitted to the pump controller, which connects to (C.) Firebase RTDB in the cloud, with which the client-side GUIs interface (D.).

The controller PCB of the sensor was built around an ESP32 evaluation board (Espressif, ESP32), powered by a 1.1 Ah Li-Po battery (Makerfocus), through a TP4056 charging module for battery management, and a DC-DC step-up converter (Wewooday, 2108A) for power management to provide a stable input.



Fig. 4. GUI: Smartphone application showing instrument control page where the user can configure parameters (A.) and sensor monitoring page (B.)

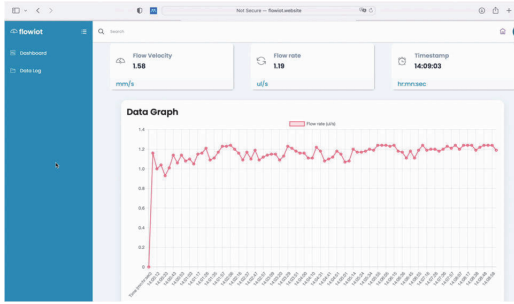


Fig. 5. GUI: Data visualization function of the webpage

D. Evaluation methodology

Flow velocity values were obtained from our internally developed flow velocity sensor ('Velocity1' in Fig. 6/A). To evaluate the accuracy of the readout, commercially available pressure sensors (Honeywell ABP2DRRT001PDAA3XX) were used. The pressure sensors were connected in series with the flow velocity sensor along the fluid flow path, and from the pressure drop, mean flow velocity ('Velocity2' in Fig. 6/A) was calculated using the Poisson equation for channels with circular cross-section [14]. The resulting flow velocities of the two measurement methods were compared to calculate the error. The complete physical experimental setup is shown in Fig. 6/B.

The analog pressure sensors were connected directly to the ADC (analog-to-digital converter) of the ESP32 microcontroller on the sensor control PCB and can be used beyond the evaluation with or without the flow velocity sensor.

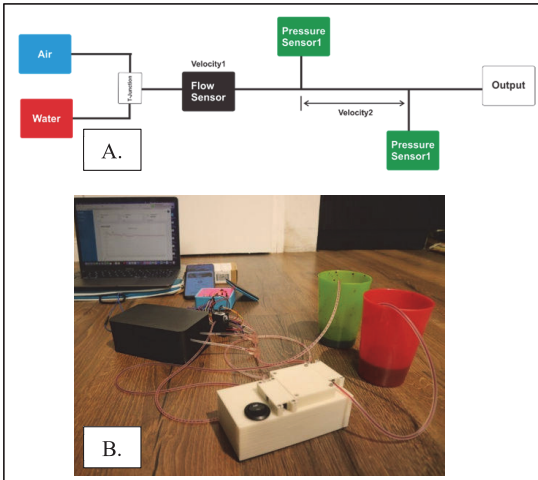


Fig. 6. Experimental setup for sensor evaluation: A. fluidic layout, B. complete experimental setup assembly

III. EVALUATION RESULTS

To evaluate the performance of the developed flow velocity sensor, commercially available (manufacturer-validated) pressure sensors were used. Three tests were conducted at decreasing flow velocities. Pump configurations

used during the tests are summarized in Table II. The system was manually tuned to obtain the desired voltage-frequency pairs.

TABLE II. PUMP CONFIGURATIONS FOR THE EVALUATION TESTS

Test no.	Property	Value	
		Pump 1 (air)	Pump 2 (water)
test 1	Voltage [V]	47	255
	Frequency [Hz]	592	203
test 2	Voltage [V]	34	255
	Frequency [Hz]	392	205
test 3	Voltage [V]	41	255
	Frequency [Hz]	461	123

Table III and Fig. 7 summarize the measured and calculated flow-velocity results for the optical (test sensor) and pressure (reference sensor) sensors. To compare the difference, the error was calculated by taking the absolute difference between measured values and dividing by the maximum of the two to get a percentage value. The error between test and reference sensor ranged from 0.76% - 13.03% and did not show linearity. The error was likely related to the mechanical constitution of the experimental setup; vibrations and/or inertial forces along the flow path. This is substantiated by the flow velocity variations, which were 4%, 7% and 10% for tests 1-3 respectively. The highest variation corresponded to the highest error and the lowest flow velocity, indicating the inherent instability of the piezoelectric pumps at low flow velocities.

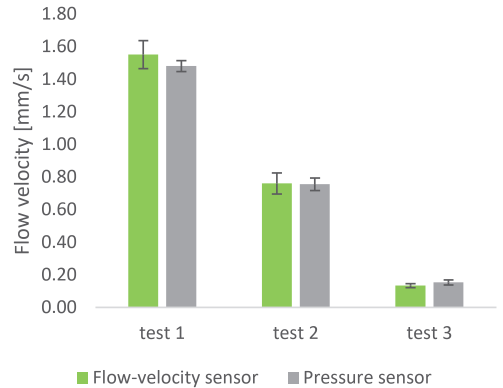


Fig. 7: Experimental evaluation results. Our flow-velocity sensor was compared to a commercially available pressure sensor at 3 distinct flow velocities.

TABLE III. SUMMARY OF EVALUATION RESULTS

Test no.	Property	Value	
		Velocity 1 (Flow-velocity sensor)	Velocity 2 (Pressure sensor)
test 1	Average [mm/s]	1.55	1.48
	STDEV [mm/s]	0.09	0.03
	Flow rate [µl/s]	1.22	1.16
	Error [%]	4.54%	

Research was funded by the Estonian Research Council under projects PUT1435, PRG620, as well as the TTU development program 2016-2022, project code 2014-2020.4.01.16-0032.

Test no.	Property	Value	
		Velocity 1 (Flow-velocity sensor)	Velocity 2 (Pressure sensor)
test 2	Average [mm/s]	0.76	0.76
	STDEV [mm/s]	0.06	0.04
	Flow rate [μ l/s]	0.60	0.59
	Error [%]	0.76%	
test 3	Average [mm/s]	0.13	0.15
	STDEV [mm/s]	0.01	0.02
	Flow rate [μ l/s]	0.10	0.12
	Error [%]	13.03%	

IV. CONCLUSIONS

In this work, we demonstrated a low-cost, open-source optical flow velocity sensor for droplet generators, constructed from widely accessible electronic components and 3D printed mechanical components (enclosure, mounting etc.). The sensor was built for portability, including an internal battery, as well as wireless communication. The instrument was demonstrated capable of work as an IoT device, reading and writing to and from a Firebase real-time database, controlled remotely from a smartphone application.

The performance of the optical flow-velocity sensor was evaluated against a commercial off-the-shelf pressure sensor by running the fluidic system at 3 different pump input voltages and frequencies and comparing flow-velocity readouts. Based on this test series, the flow rate measurement range was 6-73 μ l/min with 0.6 μ l/min resolution. The accuracy of our sensor was comparable to those demonstrated in literature. Compared to the reference sensor, the maximum error was 13% at the lowest flow rate supported by the pumps, dropping to 0-5% at higher flow rates.

This early evaluation, while promising, needs a follow-up with additional data points in the flow rate range achievable by the pump. Further investigation should also target testing with microfluidic chips instead of the current millifluidic T-junction geometry, as well as stable flow-rate driven pumps with a wide range (e.g. syringe pumps).

ACKNOWLEDGMENT

The authors would like to thank the Estonian Research Council for providing support under projects PUT1435, PRG620, as well as the TTÜ development program 2016-2022, project code 2014-2020.4.01.16-0032.

REFERENCES

[1] N. Gyimah, O. Scheler, T. Rang, and T. Pardy, "Can 3d printing bring droplet microfluidics to every lab?—a systematic review," *Micromachines (Basel)*, vol. 12, no. 3, 2021, doi: 10.3390/mi12030339.

[2] L. Huang, "Microfluidic Flow Sensing Approaches," *Advances in Microfluidics and Nanofluids*, Feb. 2021, doi: 10.5772/INTECHOPEN.96096.

[3] E. Graham *et al.*, "Ultra-low flow rate measurement techniques," *Measurement: Sensors*, vol. 18, Dec. 2021, doi: 10.1016/J.MEASEN.2021.100279.

[4] F. Cecil, R. M. Guijt, A. D. Henderson, M. Macka, and M. C. Breadmore, "One step multi-material 3D printing for the fabrication of a photometric detector flow cell," *Analytica Chimica Acta*, vol. 1097, pp. 127–134, Feb. 2020, doi: 10.1016/J.ACA.2019.10.075.

[5] "Mitos Flow Rate Sensor | Dolomite Microfluidics." <https://www.dolomite-microfluidics.com/product/mitos-flow-rate-sensor/> (accessed May 09, 2022).

[6] Z. Chen, Z. Guo, X. Mu, Q. Li, X. Wu, and H. Y. Fu, "Packaged microbubble resonator optofluidic flow rate sensor based on Bernoulli Effect," *Opt Express*, vol. 27, no. 25, p. 36932, Dec. 2019, doi: 10.1364/OE.27.036932.

[7] A. J. Harvie and J. C. deMello, "Optical determination of flow-rate and flow-uniformity in segmented flows," *Chemical Engineering Journal*, vol. 394, p. 124908, Aug. 2020, doi: 10.1016/J.CEJ.2020.124908.

[8] L. Stern *et al.*, "Doppler-based flow rate sensing in microfluidic channels," *Sensors (Switzerland)*, vol. 14, no. 9, pp. 16799–16807, Sep. 2014, doi: 10.3390/S140916799.

[9] PrusaResearch, "Original Prusa i3 MK3S+ | Original Prusa 3D printers directly from Josef Prusa." <https://www.prusa3d.com/category/original-prusa-i3-mk3s/> (accessed Jun. 13, 2022).

[10] TalTech-LoC, "Low-Cost, Wireless Flow sensor box for Lab-on-a-Chip applications," 2022. <https://github.com/taltechloc/hw-open-fluidic-flow-sensor> (accessed Jun. 13, 2022).

[11] M. Grosberg, R. Jõemaa, T. Rang, and T. Pardy, "Wireless microfluidic dual-channel pressure pump," P202200009, 2022 [Online]. Available: <https://www.etis.ee/Portal/IndustrialProperties/Display/353426b9-f02b-44b2-b581-e8f21363157a?lang=ENG>

[12] TalTech-LoC, "T-connector mini-Luer port," 2021. https://github.com/taltechloc/hw-open-fluidic-infra/blob/main/SLA_Connectors/TalTechLOC_T-con_Luer_1mmID.stl (accessed Jun. 13, 2022).

[13] PrusaResearch, "Original Prusa SL1S SPEED | Original Prusa 3D printers directly from Josef Prusa." <https://www.prusa3d.com/category/original-prusa-sl1s-speed/> (accessed Jun. 13, 2022).

[14] M. Bahrani, M. M. Yovanovich, and J. R. Culham, "ICMM2005-75109 PRESSURE DROP OF FULLY-DEVELOPED, LAMINAR FLOW IN MICROCHANNELS OF ARBITRARY CROSS-SECTION."

Appendix 3

Publication III

R. Jõemaa *et al.*, “CogniFlow-Drop: Integrated Modular System for Automated Generation of Droplets in Microfluidic Applications,” *IEEE Access*, vol. 11, pp. 104905–104929, 2023, doi: 10.1109/ACCESS.2023.3316726

Received 7 August 2023, accepted 28 August 2023, date of publication 18 September 2023, date of current version 28 September 2023.

Digital Object Identifier 10.1109/ACCESS.2023.3316726

RESEARCH ARTICLE

CogniFlow-Drop: Integrated Modular System for Automated Generation of Droplets in Microfluidic Applications

RAUNO JÕEMAA^{1,2}, NAFISAT GYIMAH¹, KANWAL ASHRAF¹, KAISER PÄRNAMETS¹, (Member, IEEE), ALEXANDER ZAFT¹, OTT SCHELER², TOOMAS RANG^{1,2}, (Senior Member, IEEE), AND TAMÁS PARDY^{1,2}, (Member, IEEE)

¹Thomas Johann Seebeck Department of Electronics, Tallinn University of Technology, 19086 Tallinn, Estonia

²Department of Chemistry and Biotechnology, Tallinn University of Technology, 19086 Tallinn, Estonia

Corresponding author: Rauno Jõemaa (rauno.joemaa@taltech.ee)

This work was supported in part by the Estonian Science Agency (ETAg) under Grant PRG620 and Grant MOBTP109, in part by the European Union's Horizon 2020 Research and Innovation Program under Grant 668995, in part by the Tallinn University of Technology (TTU) Development Program (2016–2022) under Project 2014–2020.4.01.16.0032, in part by the Estonian Research Council, in part by the European Commission, and in part by the Tallinn University of Technology.

ABSTRACT Droplet microfluidics enables studying large cell populations in chemical isolation, at a single-cell resolution. Applications include studying cellular response to drugs, cell-to-cell interaction studies. Such applications need a reliable and repeatable droplet generation with high monodispersity. Most systems used in research rely on manual tuning of flow parameters on off-the-shelf instruments. Setups are highly customized, limiting reproduction of experimental results. We propose an integrated, modular system for automated aqueous droplet generation with high monodispersity. The system provides dynamic feedback control of droplet size and input pressure. Input pressure is generated by two piezoelectric micropumps. Droplet sizes are determined via light intensity measurement in an LED-photodiode setup. The system is capable of wireless communication and has a low enough power consumption for battery-powered operation. We report on the assembly and the underlying working principle, as well as an in-depth experimental evaluation of the performance of the proof-of-concept prototype in aqueous droplet generation. Evaluation was performed on a modular as well as on a system level. During module-level evaluations, aqueous droplets were generated in a light mineral oil + Span 80 surfactant carrier medium, using 3 different flow-focusing junction geometries. The presented prototype had a significantly faster pressure stabilization time (10 s) compared to a syringe pump-based reference setup (120 s). During system-level evaluation, deionized water droplets were generated in a carrier medium of HFE7500 + PEG-PFPE triblock surfactant. Resultant droplet sizes were benchmarked with microscopy. The system was able to repeatedly generate mono- and polydisperse droplets on demand, with CVs between 5-10% in the ~50-200 μm droplet diameter range.

INDEX TERMS Lab-on-a-Chip, microfluidic, automation, pulsatile flow, droplet size control, droplet generation rate control, optical feedback, pressure feedback, closed-loop control, wireless communication.

I. INTRODUCTION

Droplet microfluidics enables studying the response of cell populations to specific chemicals, in isolation, at a very high throughput [1]. Chemical isolation is given by encapsulating

cells into aqueous droplets in an immiscible carrier medium, together with the chemicals for their treatment. For example, antibiotics and resistant bacteria, to screen for antimicrobial susceptibility, or circulating multi-drug resistant tumor cells and chemotherapy drugs to screen for drug response among other analysis targets [2], [3]. Working in droplets enables 1) higher throughput than conventional batch processing in

The associate editor coordinating the review of this manuscript and approving it for publication was Zhiwu Li¹.

2) a compact, highly integrated, automatic system as well as 3) continued work with individual droplets downstream [4]. Furthermore, it enables analysis of single-cells, or cell-to-cell interactions [5]. Droplet microfluidics has additional applications in chemical analysis and synthesis, as well as bioanalyses other than cytometry (e.g., nucleic acids) [6].

However, imaging droplet flow cytometry necessitates reliable and repeatable droplet generation with high droplet monodispersity (1-5% [4], [7]) at moderate droplet generation rates ($\sim 1-3$ kHz [7]). To date, open-loop control and/or manual tuning of flow parameters to achieve desired droplet sizes and stable droplet generation are most common [8], [9]. However, the target parameters are difficult to achieve and maintain with manual tuning. Thus, automated droplet generation with closed-loop control (or in other words, an inline quality control system of droplet generation) is necessary. Zheng et al. [10] demonstrated a reduction of steady-state error to $<2\%$ coefficient of variation (CV) across various flow conditions in droplet digital polymerase chain reaction (PCR) applications [11]. Similarly, Duan et al. [12] achieved high monodispersity (<7.6 CV%) by implementing a closed-loop control strategy, which was at least 90% lower than with open-loop control. Additionally, Zeng and Fu [13] addressed the challenge of predicting droplet size by using closed-loop control to account for the nonlinearity of flow-focusing. Moreover, a novel microfluidic system was developed to optimize cell processing conditions using deep learning algorithms for analyzing sensor data and closed-loop control to update a pressure pump and maintain optimal cell flow speed [14]. Several other works have demonstrated closed-loop control of droplet sizes by tuning flow parameters based on an image/video stream of the flowing droplets [15], [16], [17]. Most demonstrated systems (TABLE 1) used droplet imaging for control. However, overall throughput in camera-based tracking is limited by the imaging throughput of the camera (increasing throughput increases cost and heat dissipation). The price/performance ratio of imaging droplets for flow control (in contrast with cell imaging, which is a different application) is also not optimal.

A compact system with a laser-photodiode setup for bubble tracking was demonstrated in [18]. Such an integrated, compact benchtop setup enables portability between labs, which in turn enables transferring experimental workflows with excellent repeatability. It also allows replication of results, thus enabling virtual parallel labs and digital, rather than physical exchange of results and knowledge. However, at present, widely used setups are an ensemble of off-the-shelf instruments, assembled specifically for the experiment on hand, with little to no integration (TABLE 1). The lack of integration means the setup (and results created with it) cannot be easily transferred between labs. It is also notable that while in microfluidics in general, syringe pumps are the most popular choice due to their flow stability, affordability, and ease of use, in droplet microfluidics, pressure pumps are also very common, as they do not need refilling. The need to refill the syringe causes interruptions in experimental workflows,

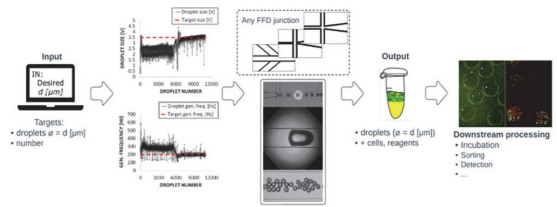


FIGURE 1. CogniFlow-Drop concept: droplets with user-defined process and dimensional parameters are generated automatically from reagents and samples needed by the user, with minimal user interaction, in a compact, standalone device. These can then be collected for further downstream processing, e.g., incubation and detection.

and possibly also the need to recalibrate flow parameters. Finally, in our earlier reviews, we found a pronounced interest towards low-cost instrumentation and the democratization of instruments for droplet microfluidics [4], [19].

As of today, compact, integrated droplet microfluidics instruments, particularly with wireless communication and low-cost hardware, are uncommon. Setups exist that meet some but not all criteria (TABLE 1) for a compact, modular, automated, wirelessly communicating droplet generator.

In this work, we describe a proof-of-concept experimental setup meeting the aforementioned criteria, its underlying methodology, and the evaluation of its performance in droplet generation experiments. The CogniFlow-Drop system concept (Fig. 1) offers the following advantages over the state of the art (TABLE 1):

1. It is integrated and modular (some modules can be swapped out for easy upgrades), improving reliability, and enabling portability. These features ensure that results and workflows are transferable between labs (enabling creation of virtual parallel labs).
2. It is low-cost ($\sim 650\text{€}$) compared to commonly used experimental setups built from off-the-shelf components. With future development, modularity will enable customization, affordability will open wider collaboration using the platform.
3. Can offer comparable performance to commonly used droplet generation setups through its dual-PID control of droplet size and generation frequency. With future optimizations, can significantly reduce carrier/sample/reagent waste. Furthermore, through automation, can ensure better repeatability without manual recalibration or in-depth knowledge of the technology.
4. Measures droplet generation in real-time via intensity change in a simple LED-photodiode setup (water droplets, passing between, causing a change compared to the carrier medium).
5. Uses tilting mounts to reliably set up chip, light source, and detector alignment, to optimize channel/droplet visibility in a given microfluidic chip. This also increases reproducibility of results.
6. Uses wireless communication, which enables remote control and monitoring of the system.

TABLE 1. Overview of the state-of-the-art feedback-controlled droplet generators compared to our novelty.

Reference	Flow actuation	Flow control algorithm	Continuous phase fluid	Discrete phase fluid	Monodispersity (CV%)	Flow sensor	Integrated & standalone?	Communication
[12]	Programmable pressure pump	PID controller	Silicone oil	Calcium chloride solution	<7.6%	N/A	No	USB
[11]	Pressure pump	PI controller	Silicone oil	Water	2%	Pressure sensor		
[16]	Pressure pump	PID controller	Fluorinated oil	Water	0.32%	N/A		
[13]	Pressure pump	PID controller	Silicone oil	Water	N/A	N/A		
[34]	Microvalves	PI controller	Silicone oil	Water	No steady state errors	N/A		
[35]	Syringe pump, and gas regulator	PI controller	BSA in NaCl	Nitrogen	N/A	N/A		
[36]	Syringe pump	PID controller	Paraffin + 10% Span80	Water	RMSE reduces from 3.4 to 0.48	N/A		
[37]	Pressure pump	Pi controller	Silicone oil	Water	N/A	Pressure sensor		
[18]	Gas-driven	Dual-PID (pressure, bubble size) control	Water + Tween80	C ₄ F ₁₀ /CO ₂ gas	N/A	Laser-photodiode		
Our work	Dual piezo pumps	Dual-PID (pressure, droplet size/gen. rate) control	HFE7500/ mineral oil + tri-block surfactant	Water	5-10%	LED-photodiode	Yes	WLAN

7. Has a sufficiently low power consumption (~ 8.0 W) that it can be powered from batteries for portable operation (based on the estimated consumption, >4.5 h battery life on a 10000 mAh Li-ion power bank).

II. COGNIFLOW-DROP SYSTEM PROTOTYPE

In this section, we present a structural overview of the complete prototype assembly (Section II-A), then in following sections (Section II-B to II-D) overview each system module in detail, including both hardware and software, from a structural as well as functional perspective (working principles).

A. OVERVIEW

The system prototype (Fig. 2/4) was constructed as a compact, modular assembly with an emphasis on ease of use and low hardware cost. In this section, we overview the assembly and subassemblies, and link to sections with further details on

each. The system consisted of three main modules (see also block diagram in Fig. 3) and the enclosure:

- 1) **Electronics module** (Section II-B and Fig. 2/1): functionally responsible for communication, instrument control and signal processing. Physically was constructed as a stack of stages onto which electronic parts were mounted:
 - a) *Power supply unit (PSU) stage* (Fig. 2/1/a): mounted the RJ45 adapter, the power switch, the mains connector, and the PSUs (ECS45US05, XP Power).
 - b) *Pump controller and pressure sensor stage* (Fig. 2/1/b): mounted the pump controller interface (with the low-level pump controller running on an ESP32 DevKitC board) and pressure regulation board. The stage was shielded from noise from above and below by copper plates attached

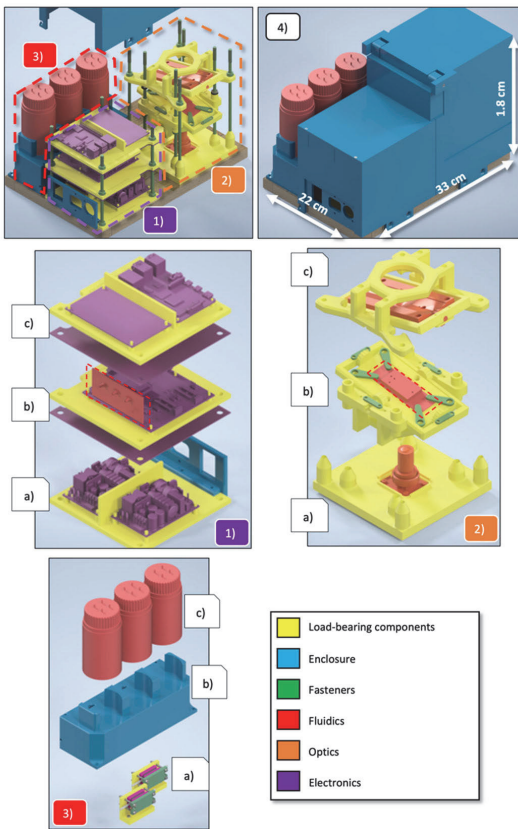


FIGURE 2. Prototype assembly, consisting of modules: (1) electronics module consisting of the power supply stage (a), the pump driver and pressure sensor stage (b) and the stage that contained the RPi4B as well as the ADC and filtering circuit for the optical sensor (c), (2) the sensorics module, consisting of the base stage with the photodiode and lens (a), the microfluidic chip mount stage (b) and the light source mount stage (c). (3) fluidics module, which included L-mounts for the pumps (a) and a foam-padded enclosure (b), as well as (c) sample, reagent, and product collection containers. (4) The enclosure with 3D printed internal and external walls, as well as a wooden base plate to which all modules were mounted for stability. The M5 bolts mounting the stages of the modules are hidden in the close-up explosion views (1)-(3).

to and grounded through structural conductive threaded rods.

- c) *Communication, control, and signal processing stage* (Fig. 2/1/c): mounted the Raspberry Pi 4B (RPI), responsible for system control and communication, and the filter-amplifier, analog-to-digital conversion (ADC) board for the optical sensor.
- 2) **Sensorics module** (Section II-C and Fig. 2/2): functionally responsible for optical flow rate measurement. Physically also holds the microfluidic droplet generator chip and consists of the following stack of stages:
 - a) *Photodetector stage* (Fig. 2/2/a): the photodetector PCB and the connecting microscope lens were mounted to the bottom plate.

- b) *Chip mount stage* (Fig. 2/2/b): included the chip mount with 3 degrees of freedom (DoF; height, roll, pitch) and a removable microfluidic chip holder.
- c) *Light source mount stage* (Fig. 2/2/c): positioned at the top of the sensorics module was an analogous 3 DoF mount stage for the light source as was for the chip mount stage. The light source was an LED, soldered to a 25 mm × 75 mm sized PCB. A diffuser/lens was attached over the LED. Aluminum or large copper area on the PCB was used for heat dissipation from the LED.

- 3) **Fluidics module** (Section II-D and Fig. 2/3, Fig. 2/1/b, Fig. 2/2/b): functionally responsible for generating droplets from the carrier medium, reagents, and sample(s). Additionally responsible for dampening secondary vibration and sound produced by piezoelectric micropumps.

- a) *Pump mount* (Fig. 2/3/a): both pumps were mounted on an L-shaped mount. The pumps were fastened to the mount with shock dampening rubber in between.
- b) *Shock- and audibility-dampening piezopump enclosure* (Fig. 2/3/b): 2-part enclosure with rubber padding fitted around the micropumps for additional sound absorption. The top of the enclosure was designed with slots for three 100 ml lab bottles.
- c) *Liquid containers* (Fig. 2/3/c): included the reagent and sample containers, as well as the product collector.
- d) *Pressure sensors* (mounted to electronics module Fig. 2/1/b)
- e) *Fluidic chip* (mounted to sensorics module Fig. 2/2/b)

- 4) **Enclosure** (Fig. 2/4): held the components together, including the interior walls between compartments, as well as the external enclosure. The base plate was a wooden board of 22 cm × 33 cm × 1.8 cm, selected to provide mechanical support to the assembly. Internal walls were used to route cables and tubing, as well as providing slots for T-junctions that bridged connections between the microfluidic chip, the pumps, and the pressure sensors. All plastic components were 3D printed. Load-bearing components were 3D printed with a Prusa i3 mk3S, the T-junctions [20] with an Any-cubic Photon Mono. Electronics and sensorics modules were fastened to the base plate with structural ISO M6 size threaded rods, whose internal components were fastened to load-bearing components with ISO M3 size bolts (metal fasteners are hidden on the explosion views for better clarity). The pump enclosure was fastened to the base plate with ISO M3 size bolts. The chip mount stage was set between spring-loaded knurled nuts (DIN 466 M6) to reduce vibrational sensitivity.

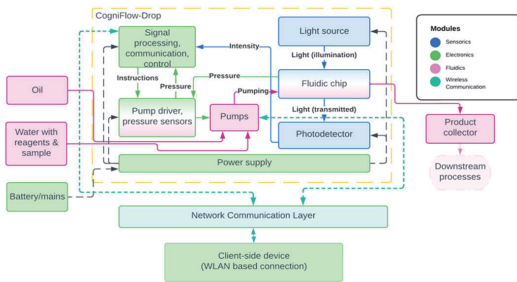


FIGURE 3. CogniFlow-Drop device: in the device, oil-water droplets of a user-defined size are generated, encapsulating cells and reagents of given kinds. The regulation of droplet sizes takes place by means of simultaneous pressure and flow rate control, resulting in a high control precision (in terms of CV% [coefficient of variation] of droplet diameter). The system implements distributed wireless control in an event-triggered manner [25].

B. ELECTRONICS MODULE

1) FLOW CONTROL STRATEGY

For the pressure-driven droplet generator, a dual-PID controller strategy with two feedback loops (inner and outer feedback loops, Fig. 4/a) was designed and implemented:

- The inner feedback loop was used to rapidly reach target pressure levels in the microfluidic chip and to reduce pressure fluctuations, inherently induced by the droplet pinch-off process, the pulsatile nature of the micropumps and the rapid target pressure level approach. The inner loop consisted of PID controllers for each micropump separately.
- The outer feedback loop was used to reach and maintain user defined droplet size and generation rates through discretized light sensor data.

The proposed design of the dual-PID control strategy (depicted on Fig. 4/a) for the CogniFlow-Drop system can be described as follows:

- 1) The inner PID closed feedback loop used pressure readings from sensors 1 (S_1) and 2 (S_2) of pumps 1 and 2, respectively, as well as pressure readings from sensor 3 (S_3) at the microfluidic chip's output.
- 2) The PID controller associated with each pump regulated the pressure drop across the chip using the differential pressures (i.e., S_1-S_2 , S_1-S_3) as feedback. The accurate and rapid control of pressures produced by the inner feedback loop action improved the stability and precision of the outer feedback loop.
- 3) The outer PID controller achieved user-defined droplet size and droplet generation frequency set points (d_{set} and f_{set}) by adjusting the pressure of pump 1 and 2 respectively (i.e., disperse and continuous phase flows). The size related pressure target was derived from using the error (e_d) between the set point (d_{set}) and the average measured droplet size (d_m). The generation frequency related pressure target was derived from using the error (e_f) between the set point (f_{set}) and the average measured droplet generation frequency (f_m). By fixing the disperse phase pressure, the

control variable relationships between “droplet size” to “disperse phase pressure” could be made as “droplet size” to “continuous phase pressure”, depending on the sensitivity of the target parameter to the fluid phase type [21].

In reference to our earlier work, the PID controller parameters (i.e., proportional gain, integral gain, and derivative gain) were derived using a Genetic Algorithm (GA). The dual-PID control strategy, adapting the framework implemented with MATLAB, Simulink in [22], was modified to include droplet generation frequency control for the presented version of the droplet microfluidics system, using Python.

2) PUMP CONTROLLER AND PRESSURE SENSOR STAGE

The pumping system embedded into CogniFlow-Drop was an updated version of the non-automated dual-channel piezoelectric pumping device demonstrated in our earlier work [23], [24]. Relevant notable modifications to our standalone pump PCBs ([24]) are mentioned in the electronic supporting information (ESI S1).

While the base design with all its features was carried over, standalone operation (wireless communication and battery power) was not. Wireless communication was not necessary as the pump controller exchanged commands and sensor data, as well as received power, over a USB cable connecting the pump controller (ESP32) to the main controller (RPI). Additional updates were required to be made to the pump controller firmware from the earlier work ([24]) with relevant notable ones mentioned in ESI S1.

3) COMMUNICATION, CONTROL, AND SIGNAL PROCESSING STAGE

RPI was selected as the main controller for the system due to its quad-core processor and extensive interfacing options. It ran Ubuntu desktop (ver. 21.10) with its tasks written in Python 3.9 and C++. With four cores, the RPI was able to dedicate one for each independent task:

- 1) Communication with the user, over local network, using the methodology described in Section II-B-IV.
- 2) Communication with the pump hardware described in Section II-B-II.
- 3) Interpretation of data obtained from the optical sensor, expanded upon in Section II-C.
- 4) Calculation of pumping pressure targets based on both the measured pressure data (obtained from task 2) and the resolved optical data (obtained from task 3), detailed in Section II-B-I.

The interpretation of links between tasks and their interactions with parts of the system, external from the Raspberry Pi, are shown in Fig. 5, and an explanation with more details about the internal mechanism of each task is described in ESI S2.

4) USER INTERFACE

Data and information flow are critical aspects when considering the design of any bioanalytical device. In our

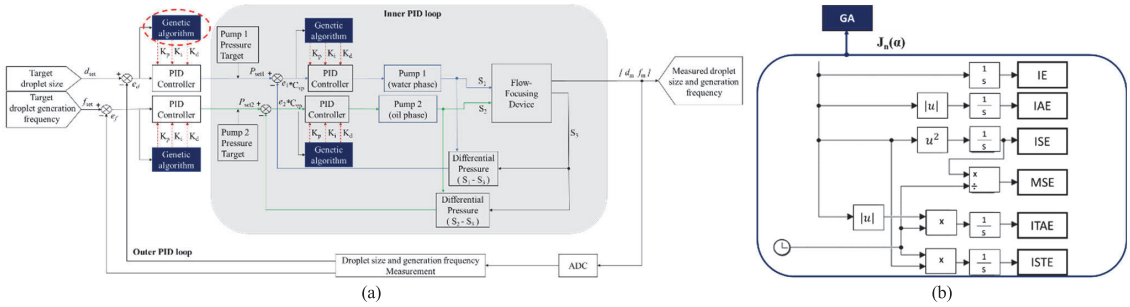


FIGURE 4. a) Structure of dual-loop PID control strategy. The inner feedback loop reduced pressure fluctuations, improved accuracy, and speed of reaching target pressure level. Outer feedback loop adjusted droplet sizes and generation rates based on optical flow rate measurement from module 2 in Fig. 2; b) Structure of PID tuning method with six objective function criteria obtained from using genetic algorithm.

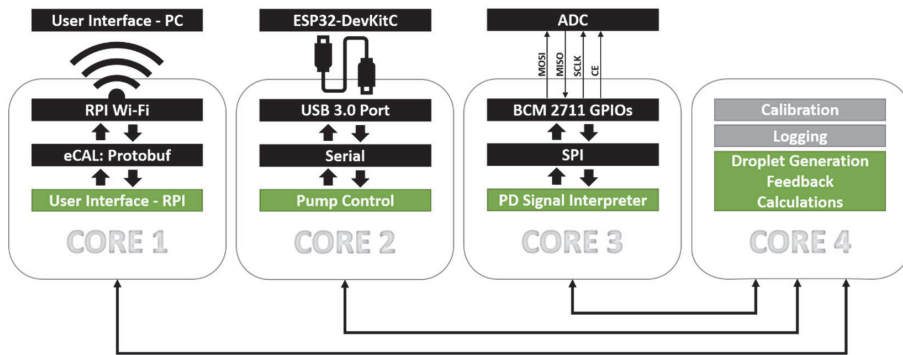


FIGURE 5. Four main tasks (in green) of the system controller were made to run concurrently on separate cores. Core 1 handled user commands received over local network using eCAL API with Protobuf format. Core 2 communicated with the pumping system’s control board ESP32-DeckItC via serial protocol. Core 3 received discretized photodiode signal from an ADC in SPI protocol format through Raspberry Pi’s BCM 2711 GPIOs and using it to measure running droplet generation parameters. Core 4 managed commands and information from the other three cores to start, stabilize and end droplet generation.

previous work we presented a framework for integrating event-triggered wireless data distribution and information flow into a bioanalytical device [24]. In this work, we focus on structured data serialization (along with metadata) using Google’s Protobuf serialization protocol [25]. With this method, the number (and type) of devices in the network could be extended with minor edits to the data structures.

Inter-host communication was performed using an enhanced Communication Abstraction Layer (eCAL, v5.9.5) middleware [27]. The data rate through eCAL was payload dependent, and the employed data-centric communication architecture offered low latency communication with fair reliability.

Data was sent between devices along with a unique device ID and name, chip name, flow rate, transmission/reception status, flag for different process activation, and droplet size (see example in Fig. 6/a) and message ID. On the publisher/sender side, a Protobuf message object (see example in Fig. 6/b), was created based on the data structure defined and serialized using the Protobuf protocol, followed by being broadcast to any listening device. For any device to catch

the broadcast data, an eCAL subscriber/receiver function was cyclically polled. Concurrently, the method was used in reverse to transfer data from the controlled device to the controller. Devices could communicate with each other in an event-triggered wireless or wired manner. The overall data transfer mechanism is shown in Fig. 7.

The CogniFlow-Drop prototype could be controlled via the graphical user interface (GUI, Fig. 8) by defining parameters for droplet generation rate and size and passing them on using the available task specific buttons. If the chosen parameters were not within acceptable limits or of the wrong type, an error was presented, asking for appropriate corrections. The entered parameters were serialized by protocol and sent to the other device in the form of messages. Unless manually halted from the GUI, tasks were halted automatically on the controlled device after completion.

5) OPTICAL FEEDBACK SIGNAL ACQUISITION

The digitization PCB before signal processing on RPI, was made with three stages.

```

1  syntax = "proto3";
2
3  package proto_message;
4
5  message spec
6  {
7      float dsize      = 1;
8      uint32 id        = 2;
9      float drate      = 3;
10     string status     = 4;
11     uint32 command    = 5;
12     string deviceName = 6;
13     string chipName   = 7;
14 }
15
16
171 #SET message command
172
173 specific.dsize = droptime
174 specific.id = message_id
175 specific.drate = input_rate
176 specific.status = status
177 specific.command = command_nr
178 specific.deviceName = device_name
179 specific.chipName = chip_name
180
181 print("Status is {}".format(specific.status))
182 if command_nr != 1:
183     print("Droplet size {} and rate {}".format(specific.dsize,specific.drate))
184     if chip_name != "None":
185         print("Chip under test: {}".format(specific.chipName))
186     else:
187         print("Chip Name is not defined")
188
189 # send message
190 while ecal_core.ok() and specific.id < repeat_msg:
191     if command_nr != 1:
192         if inputs_in_range is True:
193             pub_send(specific)
194             print("Successful transmission iteration {}".format(specific.id))

```

FIGURE 6. Communication interface implementation. (a) Data Structure for CogniFlow-Drop: droplet size (dsize), message id, droplet generation rate (drate), sender status/role, operational command, sender device name, and saved calibration parameters named with corresponding microfluidic chip. (b) instances of eCAL-based message transmissions.

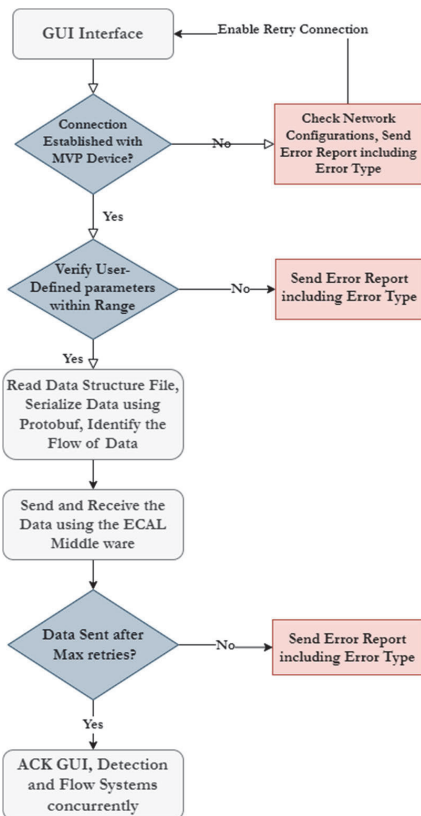


FIGURE 7. Implementation of the communication interface, data transmission, reception, verification, and a Graphical User Interface for accessibility.

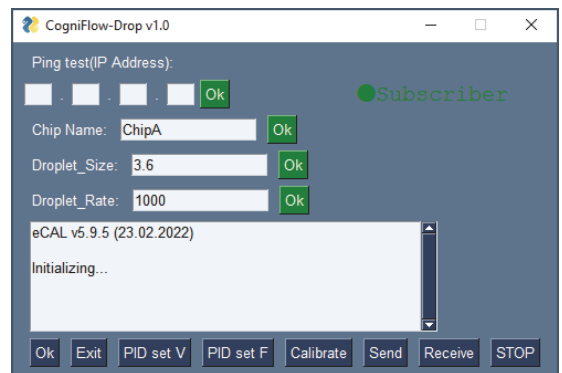


FIGURE 8. ECAL based Graphical User Interface (CogniFlow-Drop v1.0).

distortions, with a cutoff frequency at ~ 7.26 kHz and a quality factor of ~ 0.64 . Filtering was necessary to reduce noise acquired from the system (in most part from the used switch-mode PSUs).

Before discretization with an ADC, to maximize the information gained from the incoming, filtered optical signal, per bit, an adjustable inverting amplifier stage was used. This enabled scaling of captured waveform to the ADC’s analog input limits. Additionally, this filter-amplifier circuit was designed to discard any inherent DC component from the optical signal and bias it instead with 2.5 V, to position it in the middle of the 0 to 5 V ADC measurement window.

The converter used was a 16-bit ADC (ADS8681, Texas Instruments). In the presented version of the system, the PCB on which it was installed was a perforated protoboard, which introduced additional noise to the measured signal due to a non-ideal splitting of digital and analog signals.

C. SENSORICS MODULE

1) DROPLET MEASUREMENT HARDWARE

In our previous works, we demonstrated cost-effective imaging [28] and non-imaging [29] droplet flow sensor

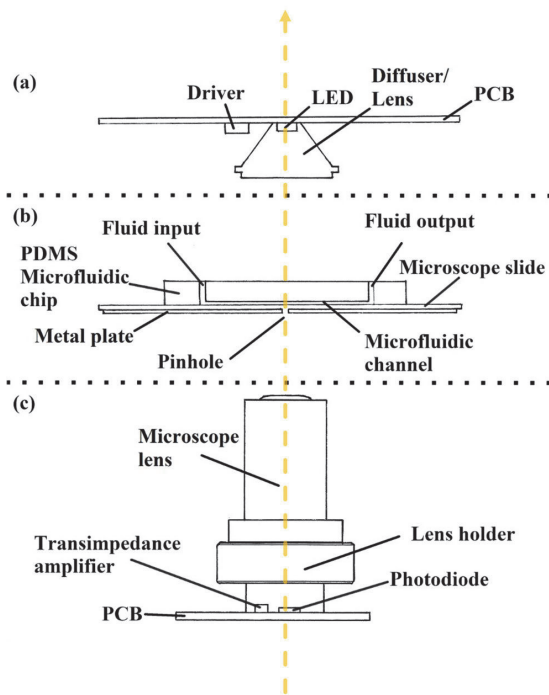


FIGURE 9. Cross-section of the microfluidic droplet measurement system with parts aligned to the axis marked with a dashed yellow line. (a) An LED with an LED driver is soldered to a printed circuit board (PCB) that is used to illuminate the microfluidic chip. In addition, a matted lens is used to diffuse and focus the light. (b) A PDMS-glass microfluidic chip is mounted to the chip holder with a metal plate with a micro-drilled pinhole positioned underneath. (c) A non-imaging photodiode collects light, while a high gain transimpedance amplifier is added nearby. On a custom PCB, components are mounted along with a lens holder and microscope lens.

prototypes with up to 750 frames per second throughput. With cost-effectiveness in mind, a more compact setup with a higher throughput for capturing droplets during generation was constructed as follows (Fig. 9):

- A light source constructed of a cold white 1 W wide-beam LED (Fig. 9/a). Soldered to a PCB with large copper areas for heat dissipation. Current-limited to ~ 150 mA using an LED driver.
- The light source was covered with a diffusing lens (Fig. 9/a) to reduce its beam angle and reduce beam intensity variations from smaller misalignments with the sensor axis.
- A PDMS-glass microfluidic chip, further detailed in Section II-D (Fig. 9/b).
- A thin metal plate, with a noise-reducing micro-drilled pinhole (sized proportionally with the chip's junction width), positioned beneath the microfluidic chip to increase the relative dimming impact of a passing droplet (Fig. 9/b).
- Based on Texas instruments application [30], using a $1\text{ M}\Omega$ as feedback resistor instead, to obtain a gain of 1 MV/A and a 1.3 pF capacitor for stability at

higher frequencies, a photodiode (PD) sensor (Osram SFH 2240, Fig. 9/c) was connected to a transimpedance amplifier (TIA). A $20\times$ microscope lens was mounted to the PCB, over the sensor, for improved focus of the droplets flowing in the microchannel.

Using the droplet flow sensor setup described above, a theoretical detection throughput was raised above 10000 droplets per second.

2) DETECTION OF DROPLET SHADOWS

The chip mount (Section II-A-II-b and Fig. 2/2/b) was positioned between the light sensing PD and the light source, all of which were vertically aligned to the pinhole under the outlet junction of the microfluidic chip (Fig. 9). As generated droplets were moving over the pinhole, a shadow was cast through it, onto the PD. The changing current through the PD was converted to voltage using a high-gain TIA, passed on to a connected filter-amplifier circuit in the electronics module (Section II-B-V and Fig. 2/1). The filtered signal moved through a DC decoupler into an inverting and level-shifting amplifier circuit. The extra amplification also provided compensation when the height of the light source was adjusted. The inversion of the photodiode voltage meant that any increase in the shadow corresponded to an increase in measured voltage. The filtered and amplified photodiode output was discretized with the ADC and sent over to the main control board using SPI. The RPI dedicated 1 of its 4 cores to communicating with the ADC, enabling photodiode voltage sampling rates of up to ~ 440 kHz (without an interpretation algorithm).

D. FLUIDICS MODULE

1) DROPLET GENERATION CHIPS

The microfluidic chip designs used in this work were adapted from the group's earlier works, notably the "Droplet counting chip" in the ESI of [31]. The principle design (Fig. 10/a) was a flow-focusing device (FFD) laid out on an SU8 mask in multiple copies with different junction widths and geometries. In TABLE 2 the chip designs used in experiments in this work are shown. The mask design is openly available on our GitHub [32]. Silanized silicon-SU8 masks were purchased from the BioMEMS group of the Hungarian Academy of Sciences [33]. PDMS-glass chips were fabricated as follows: 1) PDMS was molded off the mask (PDMS was allowed 3 days at room temperature to cure and degas), 2) the PDMS was punched to create ports using a tissue biopsy tool, 3) PDMS and glass surfaces were cleaned from dust, 4) surfaces were activated with oxygen plasma generated by a handheld corona discharge surface treater, 5) surfaces were bonded, 6) chip walls were coated with Novec™1720 Electronic Grade Coating.

2) MOUNTING OF THE DROPLET GENERATION CHIP

The removable chip holder (Section II-A-II-b) in the sensorics module (Fig. 2/2/b) had a 2 by 2 mm square hole at the

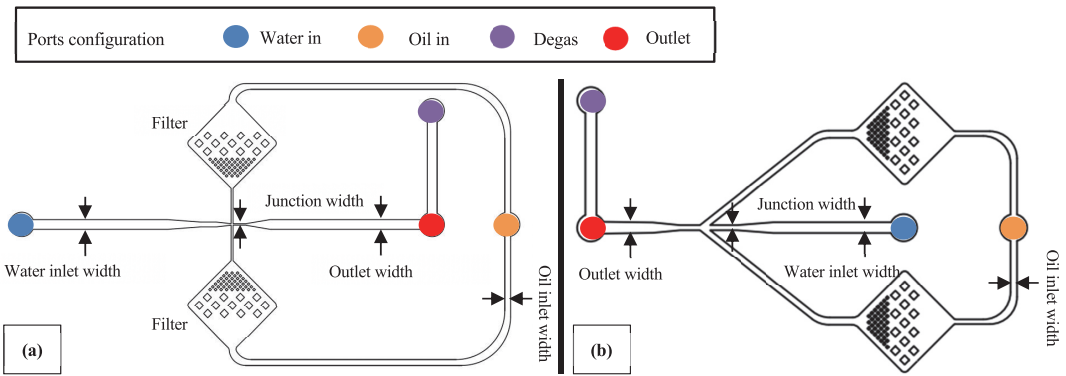


FIGURE 10. Parameterized flow-focusing device for controlled droplet generation. Oil inlet is split equally and filtered through micropillar arrays to prevent impurities on the oil line from clogging the junction. The outlet has a 1 ml gas spring attached to smoothen out flow rate fluctuations coming from the pump. Chip variant A/B (a) had a 90-degree entry in the flow-focusing junction, whereas variant C (b) had a 38.33-degree entry angle and a shorter outlet length. There was no other difference between the 3 chip variants apart from the junction width. Water inlet, outlet and oil line widths were the same.

TABLE 2. Primary/main mould design parameters for microfluidic droplet generator chips.

Chip variant	A	B	C
Junction width [mm]	90	125	280
Junction angle of entry [°]	90	38.33	
Oil inlet width [mm]	360		
Water inlet width [mm]	6		
Outlet width [mm]	0.6		
Number of filters	2		

center, over which the metal plate (Fig. 9/b) with a pinhole was placed. The pinhole was manually centrally aligned with the square hole in the chip holder. Lastly, a droplet generation chip was positioned on the pinhole plate and fastened to the holder. The chip was aligned to have the pinhole beneath the chip's outlet channel, $\sim 300 \mu\text{m}$ after the cross-junction. For the used chips, this distance mitigated capturing forming droplets and deforming droplets flowing into the wider section of the outlet where capturing distinct droplets could be jeopardized by the loss of gaps between droplets. The assembly was attached to the top of the 3 DoF chip mount (Section II-A-II-b and Fig. 2/2/b).

III. EVALUATION METHODOLOGY

In this section, we present the prototype system evaluation methodology used for characterization and benchmarking on a system as well as on a submodule level.

The first test series (Section III-A) focused on evaluation of system submodules or groups of submodules. Fine-tuning steps were also taken to prepare for the system integration. The second test series (Section III-B) focused on characterizing and benchmarking the integrated system prototype in droplet generation.

In all test setups, droplets were generated using fluids as described in TABLE 3.

In all test setups including a camera, a high-speed camera module (acA640-750uc, Basler) was used. The camera frames were captured in real time on the computer using Basler's pylon Viewer software.

A. SUBMODULE EVALUATION

The test setup used (Fig. 11/a) in this section was an early proof-of-concept implementation of the full experimental setup presented in Section II-A. The setup was derived from components demonstrated in our earlier works ([23], [24]). In the setup, DIW was used as the disperse phase, oil A or B as the continuous phase. Both phases were pumped into the droplet generation chip using our custom pumping system based on Bartels Mikrotechnik micropumps (mp6-liq). Results are presented in Section IV-A.

1) PRESSURE-BASED SYSTEM FEEDBACK MODELLING

Tests done with the following methodology gave results for: characterization of pressure control, definition of voltage to pressure transfer functions and tuned pressure feedback PID gains using the transfer functions.

TABLE 3. Fluid phases used in droplet generation experiments.

	A	B
Disperse phase	deionized water (DIW)	deionized water (DIW)
Continuous phase	Sigma-Aldrich 33079 mineral oil + 2% w/w surfactant (Span® 80, Sigma-Aldrich)	HFE 7500 fluorocarbon oil + 2% w/w surfactant (perfluoropolyether (PFPE)-poly(ethylene glycol) (PEG)-PFPE triblock)

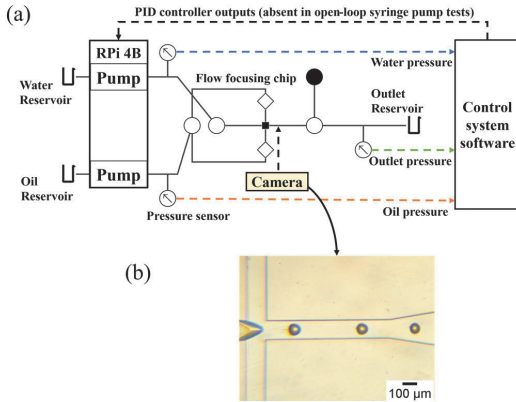


FIGURE 11. Schematic diagram for the experimental setup of droplet microfluidics system: (a) block diagram of the control system, (b) camera image of the droplet generator junction.

The pressures at the inlets and outlets of the microchannel were measured using Honeywell pressure sensors MPRLS0015PG0000SA and MPRLF0250MG0000SA, respectively, with a sampling rate of ~166 Hz. To obtain pressure to pump driving voltage relationships, driving voltage tests were conducted. For three chip variants (relevant chip dimensions in TABLE 2), the driving voltage of the piezo pumps ranged from 25 V to 250 V, with a step size of 25 V. Corresponding pressures were recorded for a duration of one minute at each step with the steady state averaged as the resulting pressure value. Measurements were done separately for DIW and oil A. Unwanted transients or spikes in the experimental data were removed using median filtering (performed in MATLAB).

To tune the PID gains, experimental data (from our earlier works [21], [22]) demonstrating the effect of inlet pressure on droplet size were used in MATLAB to derive pumping system component transfer functions. The transfer functions were implemented in Simulink in a setup-derived closed loop feedback model. PID K-values were found among six objective function criteria obtained from using genetic algorithm method: the Integral Squared Error (ISE) criterion; the Integral Time Squared Error (ITSE) criterion; the Integral of Time Absolute Error (ITAE) criteria; the Integral of Absolute Error (IAE) criterion; the Mean Squared Error (MSE) criterion; the Integral Error (IE) criterion).

2) SYRINGE PUMP VS. PRESSURE-DRIVEN PUMP

As laboratories often use syringe pumps for droplet microfluidics, the performance of our pressure-based micropump system against syringe pumps was compared here.

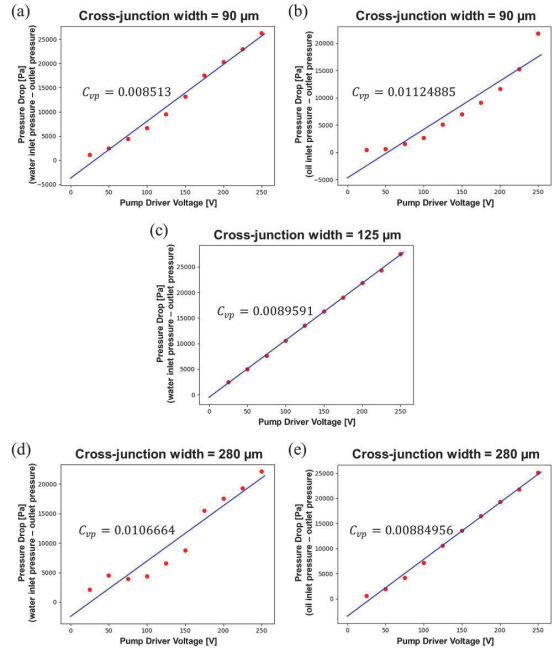


FIGURE 12. Pressure drops vs. peak-to-peak voltages of the piezoelectric micropump for the chip variants with cross-junction widths: 90 μm with DIW (a) and with oil A (b); 125 μm with DIW (c); and 280 μm with DIW (d) and with oil A (e). Driving frequency for water pump was 200 Hz sinewave. The driving voltage waveform was 200 Hz sinewave for the water pump and 50 Hz sinewave for the oil pump.

Two syringe pumps (NetPump, SpinSplit LLC, Budapest, Hungary) with plastic syringes were used to pump oil A and DIW into chip variant A. Pressure sensors were set in the established configuration (Fig. 11/a). The syringe pumps were connected to local network via Ethernet and interfaced with SpinStudio (SpinSplit LLC, Budapest, Hungary) on a desktop computer. Droplet formation was observed using a camera, placed beneath the FFD’s cross-junction. Syringe pumps were set to run for about four minutes, with fixed flow rates (Fig. 14/a), producing uniform droplets. One minute from the end of the steady state period of the measured oil and water pressure drops over the chip were averaged and used as targets for the pressure pump PIDs corresponding to the matching fluid phase. Followingly, the inlet tubes were disconnected from the syringe pumps and connected to the pressure pumps. For two minutes, pressure pumps were pumping oil and water with closed loop control, with comparable pressure (Fig. 14/b).

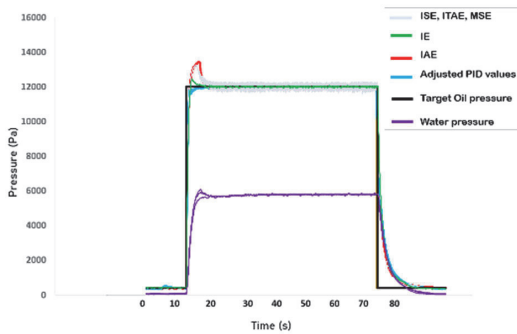


FIGURE 13. Simulation results for pressure feedback PID controller tuning with a genetic algorithm for oil pressure control.

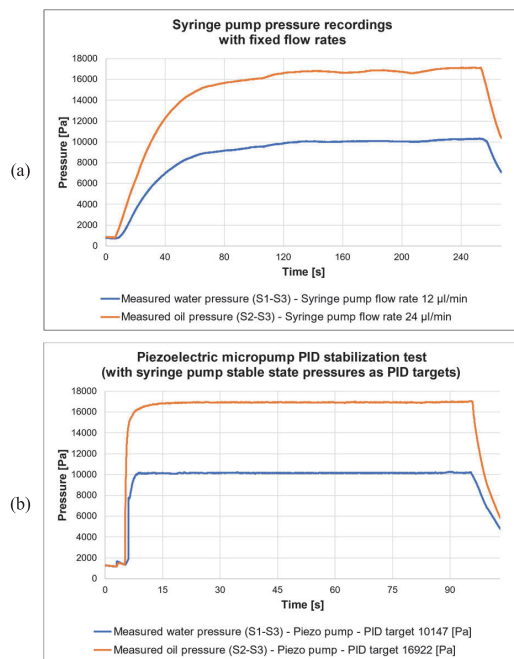


FIGURE 14. Pressure stabilization experiments performed on the setup shown in Fig. 11/a. Syringe pumps were set to pump with $12 \mu\text{l}/\text{min}$ for DIW and $24 \mu\text{l}/\text{min}$ for oil A. One minute period from the end of stable state pressures on (a) were averaged and used as pressure targets for the piezoelectric micropump PIDs. a) Responsiveness of flow-rate driven system (with third-party syringe pumps); b) Responsiveness of our pressure-driven system.

3) SENSORICS, PHOTODIODE VOLTAGE INTERPRETATION

Before droplet observations with a PD, a camera was used to analyze possible scenarios. Droplets were generated with DIW in separate combinations with oil A and B (TABLE 3). Droplets were recorded as image series to a computer and afterwards analyzed visually. Additionally, images of droplets were scanned through a custom pixel color summation program, used to estimate possible collectable wave-

forms from the PD. The custom program had an additional feature to roughly mimic a variable pinhole (determinable by the angle of the droplet generation chip in the chip mount).

4) SYSTEM CONTROLLER BENCHMARKING

The selected controller (RPI) had a quad core processor limiting concurrent tasks to four. Additionally, with RPI running a desktop OS, loop stability of each task, split using multiprocessing Python library, was measured in a one-time operation – finishing with complete termination processes. As this required all connected submodules, the test took place at the final stages of integration. All tasks running in parallel on RPI were timed over a 90 second droplet generation operation using chip variant C with oil B.

Furthermore, three additional 90 second tests were run (2 with chip variant C and 1 with chip variant B). After 45 seconds into the tests, ~ 3 seconds of ADC data (from task/core 3) was logged in more detail to analyze controller related latency and performance with a custom droplet interpretation algorithm. In the same period, a sample image was taken from the waveform entering the ADC, visualized on a connected oscilloscope (DSO5014A, Keysight).

B. SYSTEM EVALUATION

In system evaluation methodology, unless specified otherwise, oil B (TABLE 3) was used as the continuous phase.

1) DROPLET SIZE AND FREQUENCY CONTROL

For this evaluation process, two sets of target series tests (size and generation rate) were conducted for each of the two chip variants (B and C) – shown on TABLE 4–7. All samples in series were given 15 seconds for stabilization which was discarded from further calculations. The remaining 21 seconds for each sample was used for CV% and error calculations. Due to geometric differences between chip variants, target ranges of named series were limited to combinations more likely to produce droplets.

2) MEASUREMENT OF COEFFICIENT OF VARIABILITY OF GENERATED DROPLETS

To measure the stability of droplet generation with the proposed system, coefficients of variability (CV%) were calculated from “digitized” droplet data (relative droplet size over the photodiode as voltage and droplet generation rate as frequency from droplet-to-droplet period) obtained with specified droplet feedback PID targets after the setup was ran through the calibration algorithm described in ESI S3. CVs were calculated from voltage and frequency series obtained from dual-PID tests, allowing 15 seconds for stabilization at the start of each stage. This left 21 seconds of stabilized data on each target for CV calculation. CVs were also calculated from additional datasets made with longer stabilization (30 s) and stable periods (45 s). As generation frequency did not strictly apply to droplet length, CV of generation frequency was not combined with relative size CVs. However, droplet generation frequency target series were further quantitatively

TABLE 4. Chip B – voltage target series over fixed generation frequency targets.

	Fixed Generation Rate Target	Voltage / Size Target 1	Voltage / Size Target 2	Voltage / Size Target 3
1	200 Hz	2.0 V	2.8 V	3.6 V
2	400 Hz	2.0 V	2.8 V	3.6 V
3	600 Hz	2.0 V	2.8 V	3.6 V
4	800 Hz	2.0 V	2.8 V	3.6 V

TABLE 5. Chip B – frequency target series over fixed voltage (size) targets.

	Fixed Voltage / Size Target	Generation Rate Target 1	Generation Rate Target 2	Generation Rate Target 3	Generation Rate Target 4
1	2.0 V	200 Hz	400 Hz	600 Hz	800 Hz
2	2.8 V	200 Hz	400 Hz	600 Hz	800 Hz
3	3.6 V	200 Hz	400 Hz	600 Hz	800 Hz

TABLE 6. Chip C – voltage target series over fixed generation frequency targets.

	Fixed Generation Rate Target	Voltage / Size Target 1	Voltage / Size Target 2	Voltage / Size Target 3	Voltage / Size Target 4
1	200 Hz	3.2 V	3.4 V	3.6 V	3.8 V
2	300 Hz	3.2 V	3.4 V	3.6 V	3.8 V
3	400 Hz	3.2 V	3.4 V	3.6 V	3.8 V
4	500 Hz	3.2 V	3.4 V	3.6 V	3.8 V

TABLE 7. Chip C – frequency target series over fixed voltage (size) targets.

	Fixed Voltage / Size Target	Generation Rate Target 1	Generation Rate Target 2	Generation Rate Target 3	Generation Rate Target 4	Generation Rate Target 5
1	3.2 V	200 Hz	300 Hz	400 Hz	500 Hz	600 Hz
2	3.4 V	200 Hz	300 Hz	400 Hz	500 Hz	600 Hz
3	3.6 V	200 Hz	300 Hz	400 Hz	500 Hz	600 Hz
4	3.8 V	200 Hz	300 Hz	400 Hz	500 Hz	600 Hz

analyzed via standard deviations and CVs (further detailed in ESI S4). Multiple CV sets were required for observing the impact from droplet generation frequency, pumping frequency (as piezo pump driving frequency) and average pressure in the chip to droplet size CV.

In addition, to attest to the meaning and comparability of voltages obtained from the photodiode, claimed as corresponding to droplet size, visual data of droplets was needed. For visual data, droplets, generated with fixed pressure targets, were collected into an Eppendorf Tube® to be measured afterwards. Imaging for measurements was done with a trinocular microscope (BX61, Olympus) using a camera (DP70, Olympus) and a 4x/0.16 lens (UPLSAPO, Olympus). CVs and averaged cross-sectional areas and diameters were calculated using ImageJ software (further described in ESI S5). For better viewing, droplets were pushed into

Countess™ Cell Counting Chamber Slides (ThermoFisher) with a channel height of 100 μm.

IV. EVALUATION RESULTS AND DISCUSSION

In all tests, droplets were generated with liquids following the naming scheme given in Section III.

A. SUBMODULE EVALUATION

1) PRESSURE-BASED SYSTEM FEEDBACK MODELLING

With the ramping pump driving voltage (25 V to 250 V) tests, linear correlation between voltage and pressure generated in tests with all chip variants were observed (Fig. 12). The relationship of pressure drops across the chip to pumping voltages varied for the different chip variants. This was quantified with the voltage-to-pressure coefficient (C_{vp}). Furthermore, while the rising trend of the C_{vp} of water tests was rising

along with the cross-junction width, the ratio of water and oil C_{vp} was different between chips with different oil entry angles (Fig. 12/a-b vs. Fig. 12/d-e). The coefficients obtained with chip A were used in the controller design to account for differences in junction widths.

Based on our earlier works [21], [22], the system components were mathematically represented as transfer functions in eqns. 1-3, using the collected data in MATLAB software.

$$\text{t.f.}_{\text{pwat}} = \frac{-17.42s + 83.92}{s + 0.69} \quad (1)$$

$$\text{t.f.}_{\text{poil}} = \frac{-8.40s + 30.6123}{s + 0.216} \quad (2)$$

$$\text{t.f.}_{\text{chip90}} = \frac{19.04s + 0.339}{s + 0.275} \quad (3)$$

where $\text{t.f.}_{\text{pwat}}$ is the transfer function of the water pump, $\text{t.f.}_{\text{poil}}$ the transfer function of the oil pump, and $\text{t.f.}_{\text{chip90}}$ the transfer function of the chip variant A. From Simulink results the controller parameters with the lowest fitness values (error) were chosen for real-world experiments. PID's K_p , K_i , K_d values for water pump (10.5, 60.77, 1.64e5), obtained from the IE objective function, resulted in good long-term stability, albeit with an overshoot, whereas K_p , K_i , K_d values (6.69, 46.10, 5.81e-5), obtained from the IAE objective function, resulted in a response with negligible overshoot, but instead with oscillations around the target value. Based on the comparison of GA tuning results (Fig. 13), manual adjustments to K_i were made to prevent overshoot and maintain good stability, with new K_p , K_i , K_d values (10.5, 17.5, 5.81e-5) for water. Following the same process, K_p , K_i , K_d values were found for oil (40.0, 18, 4.78e-4).

2) SYRINGE PUMP VS. PRESSURE-DRIVEN PUMP

The pressure stabilization and steady states of the two test scenarios described in Section III-A-II are shown in Fig. 14. Syringe pumps took approximately 120 seconds to reach a reasonable steady state for new pressure targets, with minor oscillations persisting. Slower response time for syringe pumps was attributed to linear operation of the motors' speeds, however, the likely cause for persistent oscillations was attributed to inconsistent friction of the syringe's rubber gasket. In comparison, pressure-driven micropumps showed better responsiveness and stability between changing input pressure targets, taking about 10 seconds to reach the defined inlet and outlet pressure values.

The faster response rate helped significantly reduce experiment runtimes and reagent waste during the system evaluation tests (Section IV-B, e.g., exploring ranges of producible droplet sizes and generation rates).

3) SENSORICS, PHOTODIODE VOLTAGE INTERPRETATION

While generating droplets using oil A, the formed droplets (Fig. 15) indicated that once the droplet's diameter exceeded the larger dimension of the channel (Fig. 15/c), the shadow caused by refractions in the phase transition region would

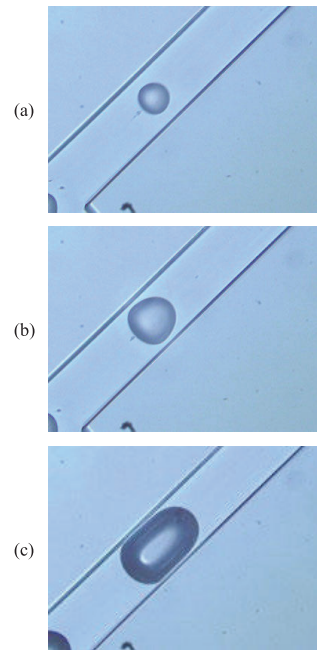


FIGURE 15. Recorded camera images of droplets generated with DIW and oil A in a 125 μm wide microfluidic channel taken at 555 frames per second under brightfield LED. a) $\sim 58.4 \mu\text{m}$ length droplet, generated with 5.2 kPa and 11.0 kPa for water and oil pressures respectively; b) $\sim 112.7 \mu\text{m}$ length droplet, generated with 5.2 kPa and 9.5 kPa for DI water and oil A pressures respectively; c) $\sim 182.0 \mu\text{m}$ length droplet, generated with 5.2 kPa and 7.5 kPa for water and oil pressures respectively.

intensify. Furthermore, a central low refraction region would emerge.

The possible impact of the low refraction region on the captured photodiode light intensity waveform was estimated from the custom pixel color summation program (Fig. 16). Given the fixed size moving window on Fig. 16/a-c, it was noted, that even with a longer than “window size” droplet, whose diameter was less than the larger dimension of the channel (Fig. 16/b), the estimated waveform gained little to no distortions. Mild distortion could be attributed to the bullet-like shape of the droplet. However, a much more noticeable distortion was noted once the low refraction region became significant relative to the window size. The non-phase transition region had the potential to invert the tip of the waveform. The impact of this effect was amplified with a less viscous continuous phase, as that reduced the surface tension of the droplet and the intensity of the droplet's shadow along with it.

Using oil B for the continuous phase, generated droplets showed inherently thinner phase transition regions and gave way for larger low refraction regions (Fig. 17). The images show a case where not only was the phase transition region very thin, but the aligned droplet acted like a lens (Fig. 17/c). To further inspect the impact of such cases, consecutive

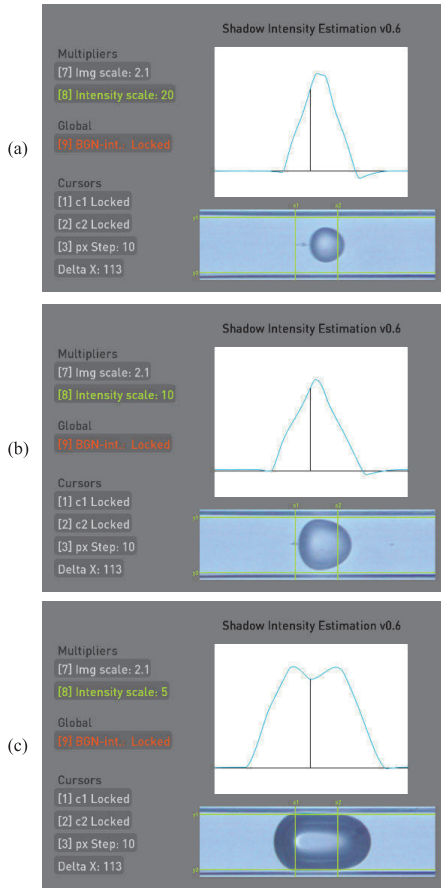


FIGURE 16. Rotated and cropped camera images shown in Fig. 15, respectively, were scanned with a fixed size moving window, indicated by green vertical lines to obtain corresponding intensity graphs (blue waveform above droplet image). a) low-distortion triangular waveform produced by the $\sim 58.4 \mu\text{m}$ length droplet with a relative intensity multiplier of 20.0; b) low-distortion triangular waveform produced by the $\sim 112.7 \mu\text{m}$ length droplet with a relative intensity multiplier of 10.0; c) high-distortion trapezoidal (double-peak) waveform produced by the $\sim 182.0 \mu\text{m}$ length droplet with a relative intensity multiplier of 5.0.

frames were viewed in the custom pixel color summation program (Fig. 18). Due to the usage of a pinhole, the extra shadows at the edges (background noise) were subtracted from further intensity calculations using the 6th additional frame (Fig. 18/f). Seen from Fig. 18 with a droplet, sized large enough to be squished in the microfluidic channel, flowing in low viscosity oil B, the possible recorded waveform for a single droplet could resemble a much more severe case of Fig. 16/c – instead of a slightly dipping peak, a waveform section representing a single droplet with a possible dip as low as to split into two discernible droplets.

4) SYSTEM CONTROLLER BENCHMARKING

Individual task duration details can be seen on TABLE 8. Maximum loop durations of the waveform interpretation and

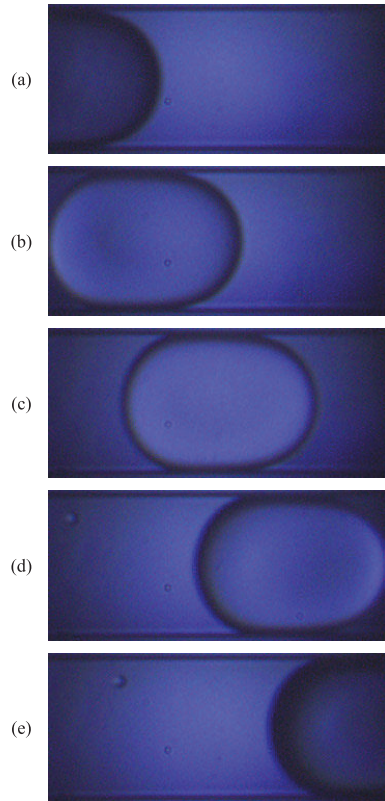


FIGURE 17. Cropped recorded frames of a passing droplet during generation with oil B. Droplet was generated at 5.0 kPa and 5.5 kPa water and oil pressures respectively. Displayed droplet measures $\sim 171.9 \mu\text{m}$ in length and was recorded at 1810 frames per second. A circular $\sim 190 \mu\text{m}$ diameter pinhole was used under the microfluidic chip below the recorded region to improve the visibility of the droplet. a) reference frame 1 in series, droplet entering the pinhole aperture; b) reference frame 2 in series, droplet approaching the center of the pinhole aperture; c) reference frame 3 in series, droplet in the middle of the pinhole aperture; d) reference frame 4 in series, droplet leaving from the center of the pinhole aperture; e) reference frame 5 in series, droplet exiting the pinhole aperture.

pumping pressure target calculation tasks (marked with * in TABLE 8) were caused by spikes in OS latency. Noticeably longer than average maximum loop durations for the remaining tasks were caused by delays from communication termination procedures included in the timing of the last loop. Total durations of tasks other than the pumping pressure target calculation task, where the main operation timer was running, were longer due to beginning their termination process after the defined 90 s time limit. Their difference was caused by sequential termination process (some extending for multiple seconds due to large log file generation). For droplet waveform interpretation task, the average loop duration extended to $\sim 6.5 \mu\text{s}$, resulting in a mean sampling rate of $\sim 153 \text{ kHz}$. The discrepancy between minimum loop duration of pump communication task ($\sim 15 \text{ ms}$) and pump

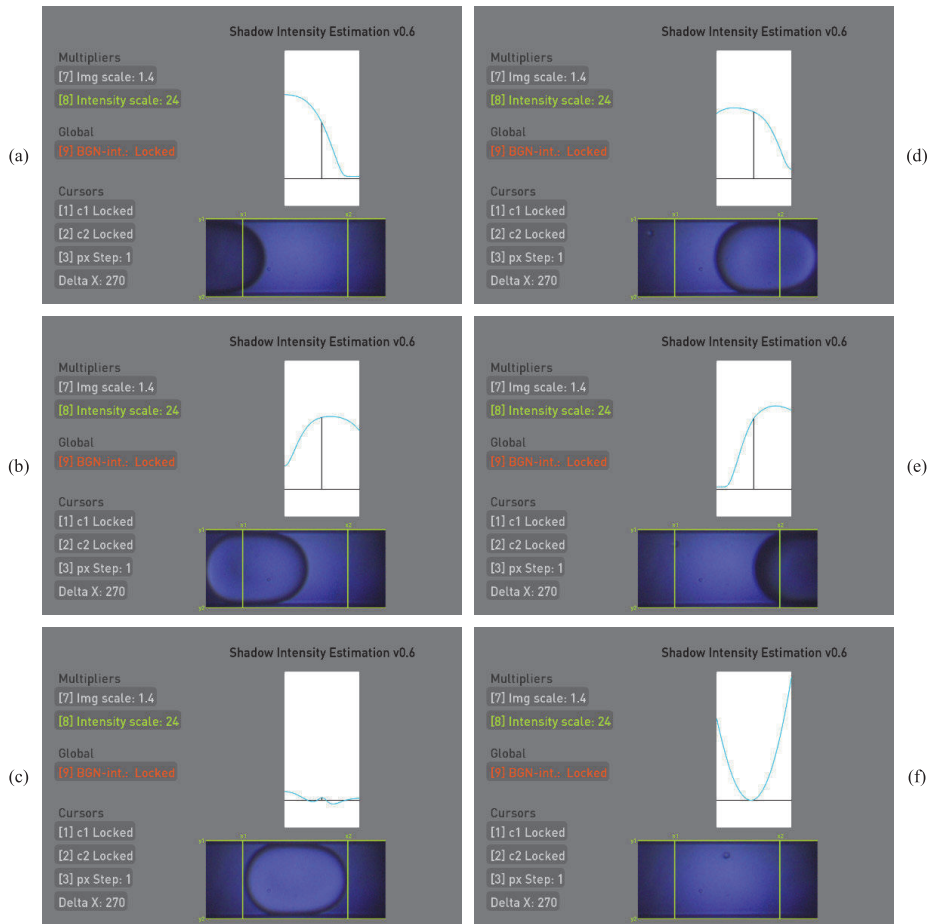


FIGURE 18. Camera images shown in Fig. 17, respectively, and an extra 6th frame were scanned with a fixed size moving window, indicated by green vertical lines to obtain corresponding intensity graphs (blue waveform above droplet image). All intensity graph scaling multipliers were kept at 245.0 for better visualization and comparability. The intensity of the 6th frame, representing the background noise, was recorded first, and locked into memory. Background intensity was subtracted from the following calculations. a) Indicating a rising shadow intensity as the darkest region of the droplet entered the pinhole aperture and the moving window; b) indicating a past-peak shadow intensity as the droplet moved closer to the center of the pinhole aperture and the moving window; c) indicating the lowest shadow intensity while the droplet was positioned at the center of the pinhole aperture; d) indicating an approaching-peak shadow intensity as the droplet was leaving the central region of the pinhole aperture and the moving window; e) indicating a falling shadow intensity as the darkest region of the droplet was exiting the pinhole aperture and the moving window; f) indicating the intensities of the shadows at the edges of the frame, caused by the pinhole.

TABLE 8. Controller software’s task loop duration.

	Core 1 – User interface coms. (Section II-B-3-1)	Core 2 – Pumping system coms. (Section II-B-3-2)	Core 3 – Droplet interpretation (Section II-B-3-3)	Core 4 – Droplet PID calculations (Section II-B-3-4)
Maximum [ms]	203.4370	215.0430	20.25914*	21.05400*
Average [ms]	102.0334	18.98948	0.006515	0.169749
Minimum [ms]	100.6310	14.74400	0.002861	0.104000
Loops counted	1005	4 758	14 640 000	530 200
Total [s]	102.54	90.35	95.38	90.00

sensor update rate of ~166 Hz (6 ms) was attributed to having used asynchronous communication method.

In the OS latency and droplet interpretation algorithm impact analysis, droplet waveform from the first additional



FIGURE 19. Oscilloscope screen capture of recorded amplified, inverted photodiode voltage during droplet generation with chip variant C, at a rate of ~ 500 Hz. Droplet alignment with the pinhole noted with blue arrows (at the “troughs”). Instability in the droplet production rate is recognizable by the varying time gaps between the „troughs“.

test with chip variant C (Fig. 19) indicated that the pinhole-aligned droplets were seen as an increase in light intensity. Meaning that the droplets functioned as lenses instead of obstacles. In this scenario, the “peak” of the alignment was measured at the “trough”. Each “trough” could be imagined as a more severe form of the dip shown in Fig. 16/c. Each “trough” was accompanied by its darker incoming and outgoing edges (Fig. 18/a, 18/e). From the logged ADC data, a sample section (Fig. 20) showed the limits of RPI running code written in Python on a non-real-time OS and specific functions circumstantially interacting poorly with the OS. As the average ADC task loop duration was measured around $\sim 6.5 \mu\text{s}$ (TABLE 8), Python’s multiprocessing Queue functions `empty()` and `get_nowait()`, called after 100 mV above the average line for every other droplet, delayed the loop duration minimally another $\sim 100 \mu\text{s}$ producing erroneous droplet size measurements. In comparison, the second test with chip variant C (Fig. 21) showed a waveform with similar sharp peaks, but each with longer duration. Long enough to preserve the peaks captured by the ADC (Fig. 22). In the third additional test, with chip variant B, OS latency was spotted causing the loss of 2-3 consecutive droplets (Fig. 23) with an unexpected delay between two ADC sampling cycles. Albeit being relatively rare, the measurement error of such events was mitigated to prevent destabilizing the flow rates. When time delay between two ADC samples exceeded 30% of the average droplet generation period, the following erroneous droplets were excluded from the logs and use in the droplet feedback PIDs. It improved fluidic stability, but in the case of random OS delays, at the cost of up to 10% of generated droplets not getting logged (losses were lower with lower generation rates). Likewise, in the case of `get_nowait()` delay, if it exceeded 30% of the average droplet generation period, the irregular droplet measurement would be excluded from the log and PID feedback.

B. SYSTEM EVALUATION

After assembly, programming, and fine-tuning through preliminary testing, connection between a laptop and the

CogniFlow-Drop device was established through a Wi-Fi hotspot to validate the communication interface. After a successful connection, the interface effectively transmitted and received message packets every ~ 100 ms, artificially delayed with eCAL message polling delay on the RPI. Other functional tests with the remote control included:

- initiating setup calibration (tied to variables: chip position/angle, chip variant, liquids used),
- initiating droplet generation with desired size and generation rate,
- initiating droplet size (V) target series test,
- initiating droplet generation rate (F) target series test.

Each feature of the GUI (Fig. 8) was proceeded to be used as remote initiator for the following system evaluation steps.

1) RESULTS OF DROPLET SIZE AND FREQUENCY CONTROL TEST SERIES

During experimentation, some target droplet size and generation frequency combinations did not yield droplets regardless of having used selective ranging – highlighted on TABLE 6-7. Overall, chip C showed lower ranges for both sizes and generation rates. Additionally, chip C behaved uniquely between voltage and frequency series, as the combination of (400 Hz; 3.4 V) in voltage series did not yield droplets, but in contrast, was unexpectedly stable in frequency series. This hinted to higher sensitivity to size target alterations during droplet production combined with how current droplet feedback PID handles high instability.

Target series over all four sets, named in Section III-B-I, resulted in averaged droplet size errors, seen on Fig. 24, which indicated higher accuracy for droplet size control with chip B, more specifically with droplet size (V) series when the marked outlier of ChipB-Fseries was taken into account. With an average error of -0.06% , ChipB-Vseries obtained averaged sizing errors between $+2.86\%$ to -1.79% . Contrast of accuracy of reaching average target size, can be seen on droplet capture graphs between ChipB-Vseries (row 4 from TABLE 4) and ChipC-Vseries (row 2 from TABLE 6) on Fig. 24/b and Fig 24/c respectively, with target sizes per sample,

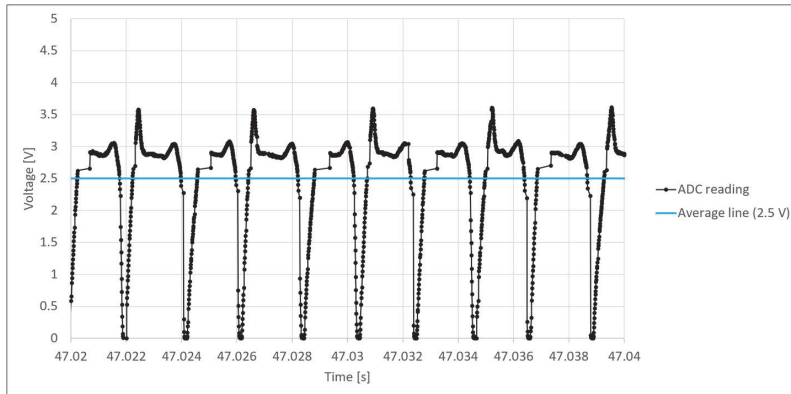


FIGURE 20. Sample frame from ADC measurement log on RPI showing ADC readings and the average line over which droplet detection was handled. Shown graph links with Fig. 19, however, with every other peak cut off due to specific cross-core communication function delays.



FIGURE 21. Oscilloscope screen capture of recorded amplified, inverted photodiode voltage during droplet generation at a rate of ~ 200 Hz. Droplet alignment with the pinhole noted with blue arrows (at the “troughs”).

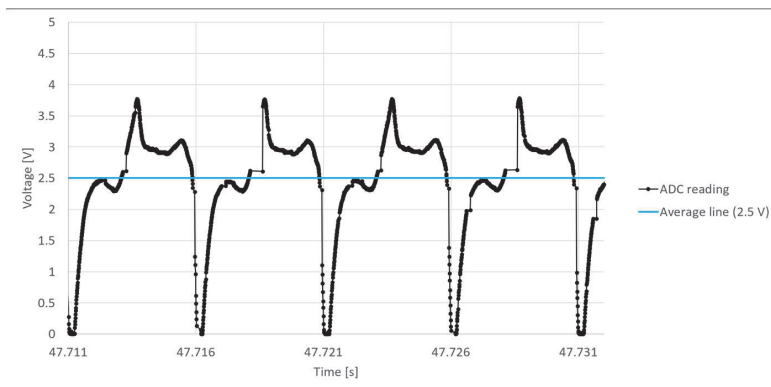


FIGURE 22. Sample frame from ADC measurement log on RPI showing ADC readings and the average line over which droplet detection was handled. Shown graph links with Fig. 21, however, in contrast to Fig. 20, cross-core function delays caused after every other detected droplet, were not long enough to cut off the relevant peaks of the droplet waveform.

segmentally overlaid as orange horizontal lines. Target size errors on Fig. 24/b were [+0.35; -1.79; -1.56] % respectively. Together with the fixed frequency (200 Hz) accompanied

with varying droplet size targets, frequency errors of [+0.88; -2.00; -5.63] %, respectively, showed a decreasing total output volume with the combined error staying further and

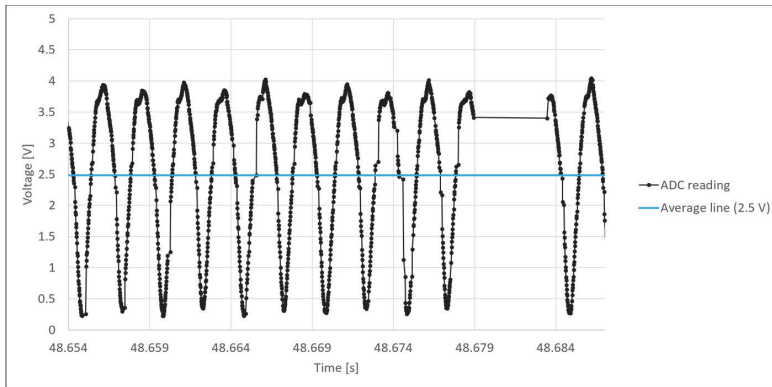


FIGURE 23. Sample frame from ADC measurement log on RPI showing ADC readings and the average line over which droplet detection is handled. In shown example, spontaneous latency delays caused by the operating system running on RPI prevented three consecutive droplets being captured and measured.

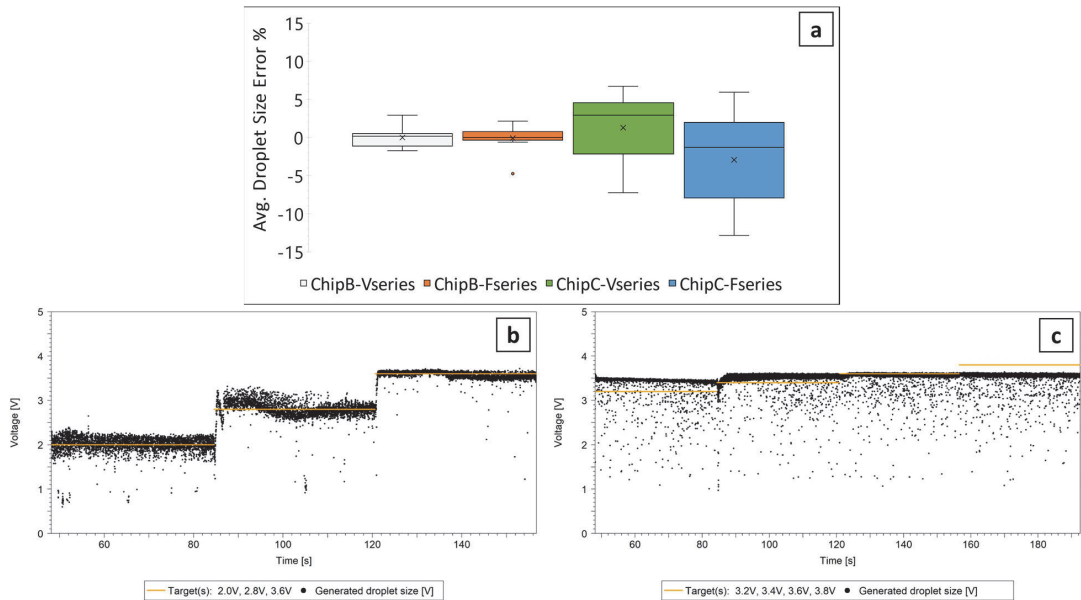


FIGURE 24. Results from Section IV-B-1. a) Averaged droplet size target errors for chips B and C, further split by size and frequency series test sets. Sample sizes for series respectively [12, 12, 9, 16]; b) Droplet size control dataset of row 1 from TABLE 4, from ChipB-Vseries test set. Graph indicating higher accuracy of stabilization around target voltage levels; c) Droplet size control dataset of row 2 from TABLE 6, from ChipC-Vseries test set. Graph indicating lower accuracy of stabilization around target voltage levels, preference to droplet size (influenced by chip geometry).

further below the targets. Target errors on Fig 24/c were [+5.62; +2.88; -2.03; -7.24] % respectively. For the comparably reduced functional size range that channel geometry of chip C offered, target size control did not yield droplets in all requested sizes. This could largely be contributed to inclinations caused by the channel geometry. This was made clear from its accompanied averaged frequency target errors of [-1.99; +2.65; -0.73; -0.30] % respectively, which did not follow the pattern of size errors. The secondary contributor was attributed to the erroneous droplet size averaging caused by what was shown on Fig. 20. Due to alterations in perception of captured droplet sizes, calibration

for chip C test series had been segmentally impacted where droplet waveforms exhibited shapes more predisposed to peak losses.

Additionally, averaged droplet generation rate errors, seen on Fig. 25/a, again indicated higher accuracy for droplet rate control with chip B, more specifically with generation rate (F) series when marked outliers of ChipC-Fseries were taken into account. With an average error of +0.94%, ChipB-Fseries obtained averaged generation rate errors between +3.62 to -1.65%. Contrast of accuracy between the best and the worst captured series of reaching average target generation rate, can be seen on droplet capture graphs between

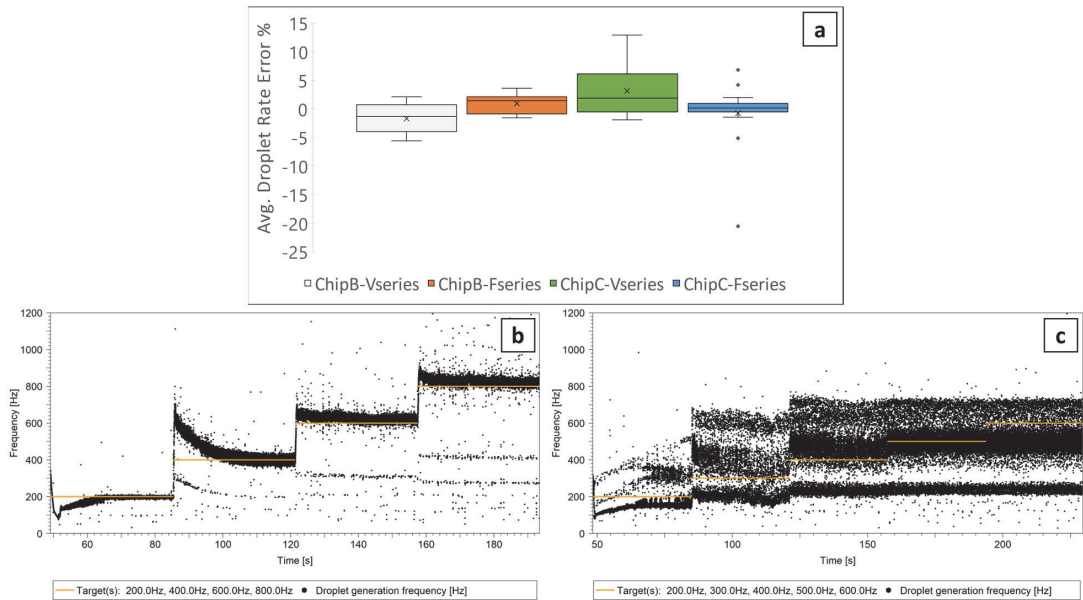


FIGURE 25. Results from Section IV-B-I. a) Averaged droplet rate target errors for chips B and C, further split by size and frequency series test sets. Sample sizes for series respectively [12, 12, 9, 16]; b) Droplet generation rate control dataset of row 2 from TABLE 5, from ChipB-Fseries test set. Graph indicating higher accuracy of stabilization around target frequency levels; c) Droplet generation rate control dataset of row 1 from TABLE 7, from ChipC-Fseries test set. Graph indicating lower accuracy of stabilization around target frequency levels and significant fluctuation in periodicity of droplet production.

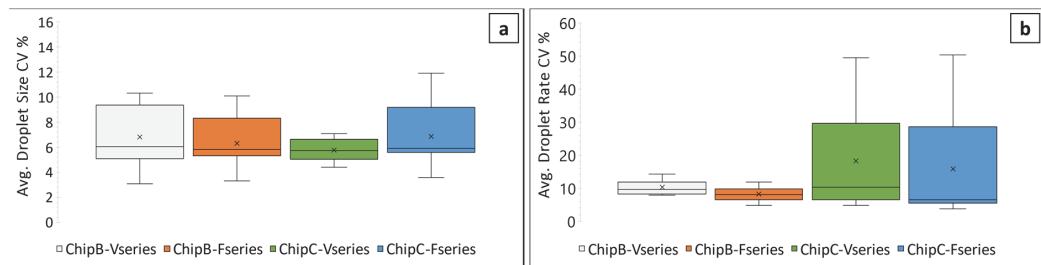


FIGURE 26. Results from Section IV-B-II. a) Averaged droplet size CVs for chips B and C, further split by size (V series) and frequency (F series) series test sets; b) Averaged droplet generation rate CVs for chips B and C, further split by size (V series) and frequency (F series) series test sets. Sample sizes for series respectively [12, 12, 9, 16].

ChipB-Fseries (row 2 from TABLE 5) and ChipC-Fseries (row 1 from TABLE 7) on Fig. 25/b and Fig. 25/c respectively, with target sizes per sample, segmentally overlaid as orange horizontal lines. Target averaged frequency errors, with chip B, on Fig. 25/b were $[-1.43; +0.86; +1.83; +1.67]$ % respectively. Together with the fixed size target (2.8 V) accompanied with the example varying frequency targets, averaged size errors of $[+0.50; -0.61; +0.61; +0.14]$ % respectively, showed no explicit relationship between size and frequency errors. This alluded to lesser impact from frequency alterations during droplet generation, in other words, lesser impact from changes in oil pressure rather than water pressure. Target averaged frequency errors, with chip C, on Fig. 25/c were $[+1.93; +4.11; +6.78; -5.11; -20.61]$ %

with accompanying size target (3.2 V) errors of $[+5.91; -0.06; -1.56; -1.09; -1.13]$ %, respectively, showing little correlation in comparison. This example showed large fluctuations in periodicity, but small droplet size variation (similar to Fig. 24/c from ChipC-Vseries).

2) MEASUREMENT RESULTS FOR COEFFICIENT OF VARIABILITY OF GENERATED DROPLETS

a: DROPLET SIZE DATA (PD VOLTAGE DISCRETIZED WITH THE ADC) FROM CONSECUTIVE DROPLET SIZE AND FREQUENCY TARGET SERIES

V and F series performed in Section IV-B-I resulted in averaged droplet size CVs represented on Fig. 26/a and averaged

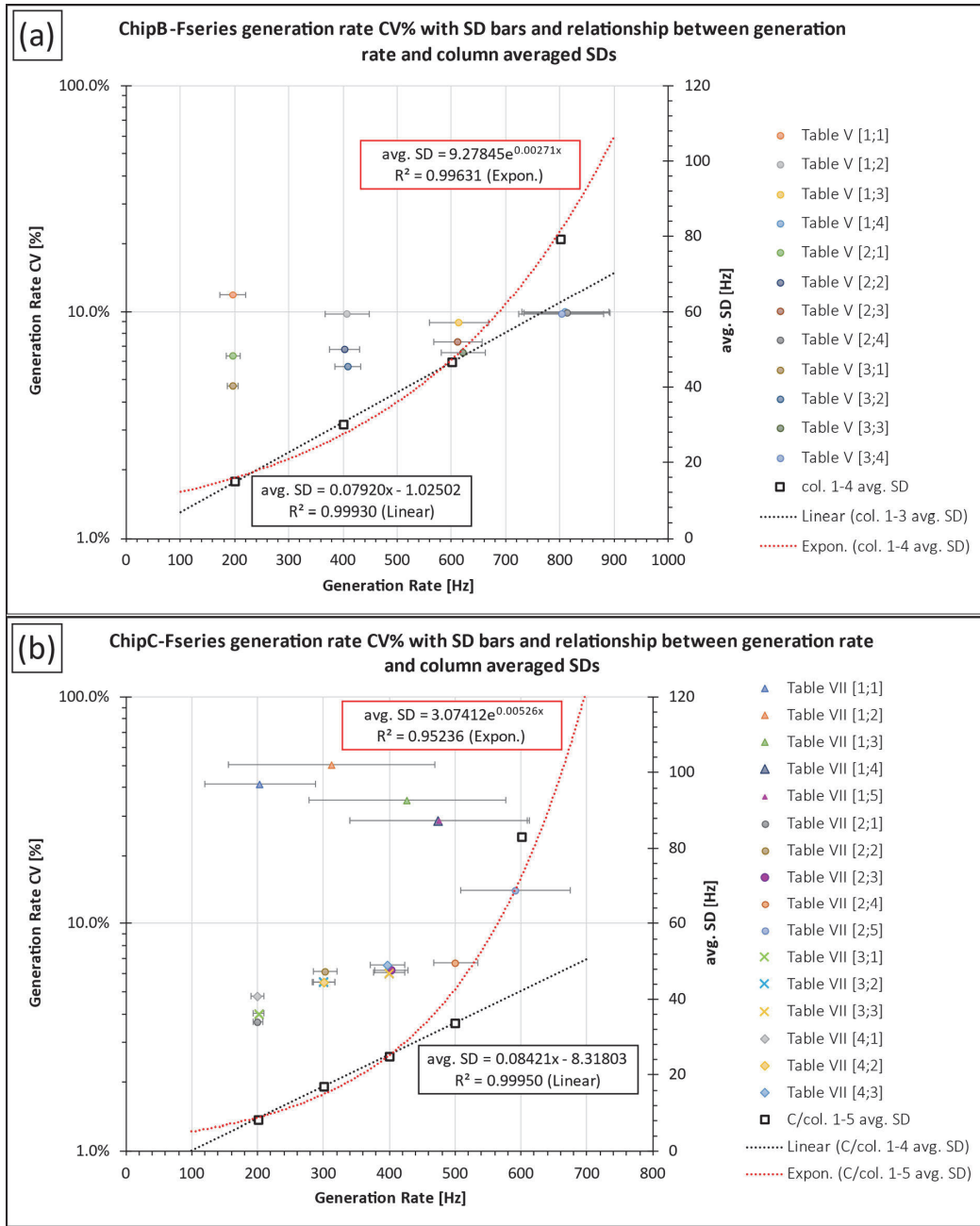


FIGURE 27. Results from Section IV-B-II. Quantitative analysis of F series data. a) Droplet generation rate CV%, from droplet size and rate combinations in TABLE 5, plotted against averaged generation rate, calculated over the stabilized generation period. TABLE 5 column (col.) averaged SDs (from target rate columns 1 to 4 and target size rows 1 to 3) plotted against column target generation rates together with a corresponding exponential regression line. Col. avg. SDs were cropped to columns 1 to 3 to highlight the highly linear correlation region; b) Droplet generation rate CV%, from droplet size and rate combinations in TABLE 7, plotted against averaged generation rate, calculated over the stabilized generation period. TABLE 7 column conditionally (C/col.) averaged SDs (from target rate columns 1 to 5 and target size rows 2 to 4 – row 1 conditionally excluded due to indicating a different mode of operation, see ESI S4 for details) plotted against column target generation rates together with a corresponding exponential regression line. C/col. avg. SDs were cropped to columns 1 to 4 to highlight the highly linear correlation region.

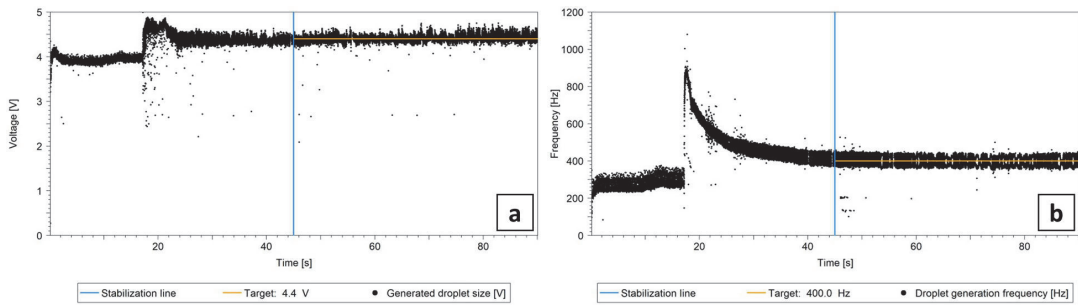


FIGURE 28. Results from Section IV-B-II. a) Droplet size target data set from a combination of [4.4 V; 400 Hz] with chip B. Stabilization period 45 seconds which includes an initial 15 seconds of default initiation period. Stabilization and stable segments are separated by blue vertical line. Target size in voltage is shown with an overlaid horizontal line; b) Droplet generation rate target data set from a combination of [4.4 V; 400 Hz] with chip B. Stabilization period 45 seconds which includes an initial 15 seconds of default initiation period. Stabilization and stable segments are separated by blue vertical line. Target size in voltage is shown with an overlaid horizontal line.

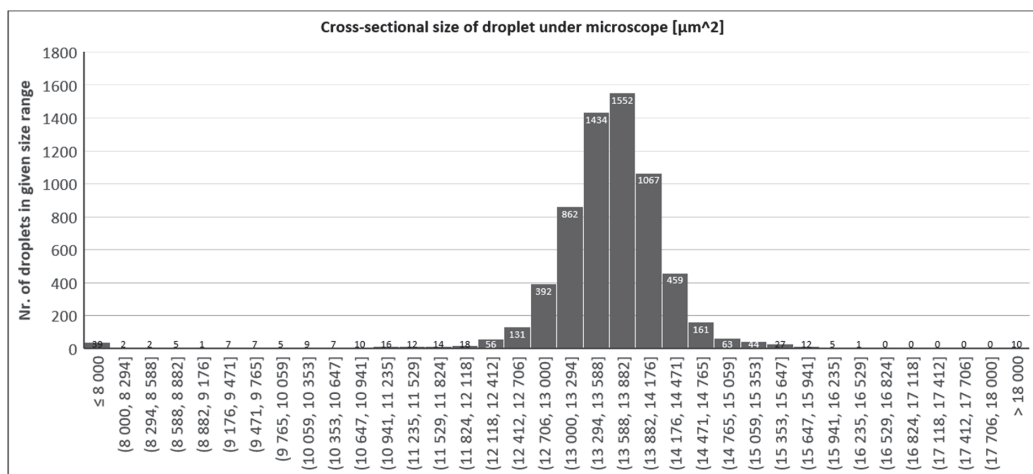


FIGURE 29. Droplet cross-sectional size spread from a droplet generation sample, generated with fixed water and oil pressure of 9 kPa and 12 kPa respectively. 6429 droplets measured over 11 images with Imagem software.

droplet generation rate CVs represented on Fig. 26/b. Medians of averaged CVs from Fig. 26/a, [6.83; 6.33; 5.78; 6.84] %, respectively, showed that while the measured droplet sizes in tests with chip C were off noticeably more than with chip B, the size stability can be better. However, minimum CVs [3.10; 3.30; 4.40; 3.60] % showed favorability towards chip B. While some maximum CVs reached over 10%, more significant reasons for the larger instabilities stemmed from the chosen pressure combinations working less favorably with chosen chip geometries. From the averaged droplet generation rate results on Fig. 26/b, the difference between chip B and C was hard to mistake. As the CVs between size and rate for chip C, have a noticeable difference in scale, it was evident that the generation frequency of droplets does not inherently link to droplet size in a pulsatile pressure-based pumping system.

Further analysis of target F series provided relationships between the generation rate to generation rate CVs at each obtained average frequency level with standard deviation

(SD) bars and between the target generation rate to column averaged SDs (SD averaging for chip C was done conditionally, further explained in ESI S4), for chips B and C respectively on Fig. 27/a and Fig. 27/b (numeric details in ESI S4, TABLE 1-4). Generation rate CVs for chip C revealed behavioral outliers with target size and rate combinations in row 1 of TABLE 7 (while producing droplets in a stable manner with size CVs < 10%, the frequency CVs were well above 25%). By omitting the TABLE 7 row 1 CVs and SDs from comparison between chip variants, the general rule of increasing SD with increasing generation rate becomes noticeable. By having excluded row 1 SDs also from averaging of SDs, chip B and C generation rate averaged SDs (SD) showed analogous trends. Both show the highest correlation to exponential relationships. Additionally, for both chip types, cropped SDs revealed high linear correlation regions up to the second highest tested respective generation rate targets (Fig. 27) which in terms of generation rates would narrow down on the stable frequency region of use for that specific

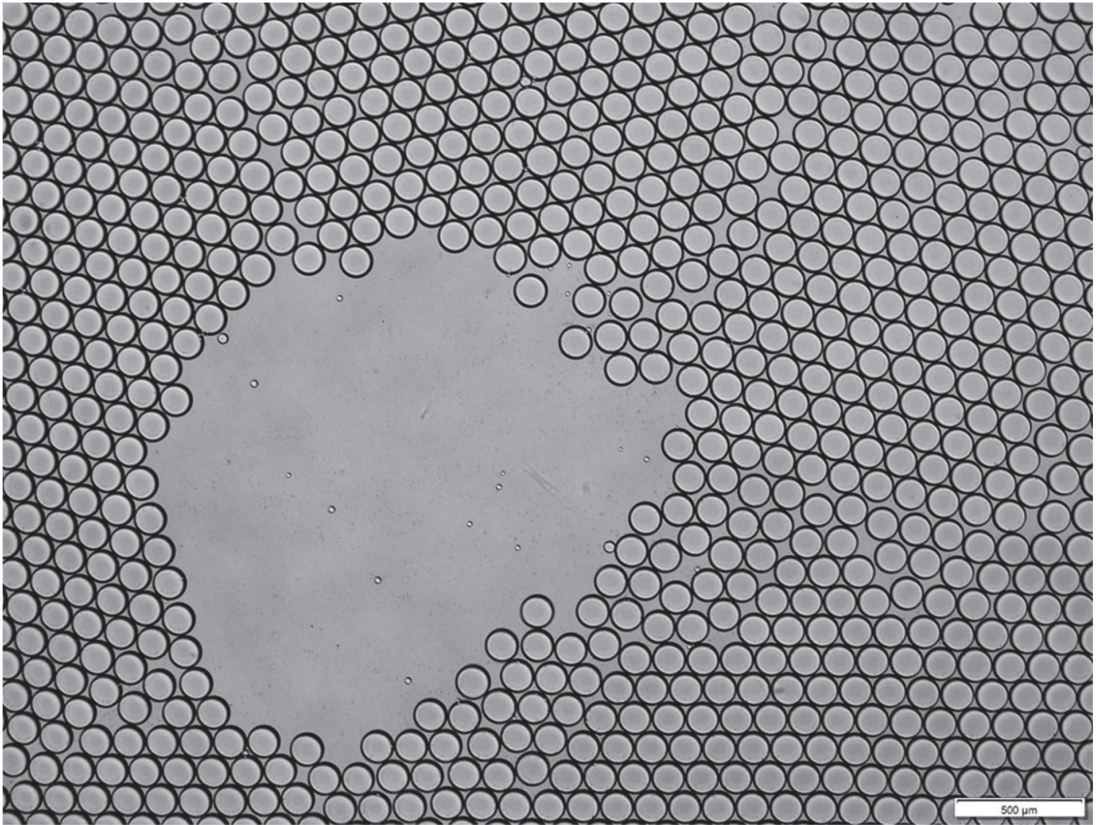


FIGURE 30. Droplets generated with chip design B with fixed water and oil pressures of 9 kPa and 12 kPa respectively, pumped using pressure-based piezoelectric micropumps, viewed under microscope (4x/0.16 lens).

chip geometry and fluidic phase combination. Between the observed initial and cropped data, beyond a certain generation rate, the behavior of frequency stability deteriorates from linear into exponential regime. The possible causes of which could be 1) stability limits, inherited from FFD channel design in combination with pulsatile flow and fluid phase properties, 2) hardware and/or software limits, RPI's droplet interpretation loop delays introducing increasing number of erroneous readings.

b: DROPLET SIZE DATA (PD VOLTAGE DISCRETIZED WITH THE ADC) FROM SINGLE SHOT DROPLET SIZE AND FREQUENCY TARGETS

Using chip B with different calibration (chip position slightly tilted in the light tower), one of the better examples with lowest target error in combination with the lowest droplet size CV (400 Hz, 4.4 V) achieved, can be seen on Fig. 28 with graphed droplet sizes and generation rates respectively. From the size dataset on Fig. 28/a, the CV% was calculated to be 1.77% with a percentage error from target droplet size of +0.27%. From frequency dataset on Fig. 28/b, the CV% was

calculated to be 6.67% with a percentage error from target droplet generation rate of +0.22%.

c: DROPLET SIZE DATA (MICROSCOPE CAMERA → IMAGE) FROM SINGLE SHOT PRESSURE TARGETS

Droplets were collected from tests with droplet feedback PIDs disabled to obtain a baseline. Tests were done with fixed water pressure at 9 kPa and several oil pressure targets in the range of 9 kPa – 12 kPa, ran over 90 seconds, where oil pressure at 12 kPa yielded the best results with 7.7% CV, with a spread of cross-sectional areas shown on Fig. 29. Average cross-sectional surface area of recorded droplets was measured $13\,558.9\ \mu\text{m}^2$, translating into an average planar diameter of $131.4\ \mu\text{m}$ when droplets were flattened in the imaging slide. A sample from a series of images taken of droplets in the droplet imaging slide can be seen on Fig. 30.

V. FUTURE PERSPECTIVE

One of the core principles of the CogniFlow-Drop system is modularity. This modularity opens the way to various future upgrades: use-cases enabled by additional modules

(Section V-A), as well as possible upgrades to the core modules (Section V-B).

A. APPLICATION USE CASES

- **Inline imaging cytometry:** The addition of a high-speed camera/detection module (and ideally a cell incubation module) could enable inline imaging cytometry.
- **Cell sorting:** The addition of a droplet sorting module, together with the aforementioned imaging cytometry modules, could enable droplet-based cell sorting for further downstream processing of select cells or cell lines. The single-cell resolution and chemical isolation provided by droplets could greatly increase the throughput, while reducing reagent and sample waste compared to current state-of-the-art flow cytometry setups.

B. POSSIBLE UPGRADES TO THE PROTOTYPE SYSTEM

- To improve the droplet capture rate and reliability, an additional ESP32, or a similar low-cost device with an SPI bus and two cores, could be placed between the RPI and ADC to take over task 3 from the RPI. Additionally, the added computational power could enable more complex waveform analysis (e.g., waveform slope measurement and droplet lensing effect detection).
- To improve the droplet size and generation frequency control accuracy and fault tolerance, machine learning models could be implemented on the RPI.
- To improve automation, the following features could contribute: self-priming, self-cleaning, auto-chip-positioner, auto-pinhole-positioner, self-analyzing (e.g., detection of blockages or leaks in the fluidics module), auto-focusing, and auto-calibration-ranging.
- To improve the user interface, the GUI, after calibration, could offer feasible droplet size and generation frequency ranges, with highlighted combinations yielding the best CV% for that specific chip and position. Furthermore, by user request, the GUI could poll captured waveform samples during operation.
- To correlate relatively inexpensively and rapidly measured droplet sizes from their shadows to real droplet volume, a secondary in-line camera setup could be joined in the communication line over eCAL. To image droplets, as proposed in Section V-A, during cytometry.

VI. CONCLUSION

A proof-of-concept prototype of an integrated, modular system for automated aqueous droplet generation with high monodispersity was presented. The system measured droplet sizes and generation rates using a visible spectrum LED-photodiode setup aligned with the cross-junction of the FFD, converting the droplet's shadow to voltage. Resulting peak-to-peak voltages were correlated with relative size of the droplet whereas the time between the beginnings of droplets were used to obtain the generation rate. We reported on the assembly and the underlying working principle, as well as the experimental evaluation of the performance of the prototype,

both on a module level and system level. Module-level evaluation and comparison to reference syringe pumps indicated a 12 times reduction in pressure stabilization times. The system-level evaluation proved that the system was capable of repeatedly generating droplets with stability comparable to other state-of-the-art droplet generation systems. Droplet generation stability was proven over 2 different carrier media and 3 different junction geometries in total. The lowest relative droplet size CV% recorded was 1.77% (~0.00031 PDI) using Chip B with fluid phase combination B. With droplets controllably generated in tested relative size targets between 2.0 to 4.4 V, polydisperse (PDI > 0.1) droplets with a stable size distribution can also be generated. Unique characteristics from relationships between droplet size/generation rate and chip geometry were made observable through automated calibration and parameter target test series with different chips. Conditional droplet generation rate analysis also revealed high linear correlation regions for the “SD of the generation rate” with the “target rate” for chips B and C, from 200 Hz up to 600 Hz and 500 Hz respectively. In conclusion, the presented prototype system has comparable droplet generation performance metrics to other state-of-the-art droplet generation setups, but offers several advantages: 1) modularity, integration, wireless communication and the option to run from battery power, enabling portability; 2) affordability; 3) automation and ease of use, increasing repeatability of results and allowing transfer of protocols between labs, as well as reducing manual workloads; 4) user-friendly (re-)calibration of chip alignment.

ACKNOWLEDGMENT

The authors would like to thank researcher Simona Bartkova (Department of Chemistry and Biotechnology) from the Tallinn University of Technology with their assistance with droplet imaging and droplet generation chip fabrication methods and tools. The perfluoropolyether (PFPE)-poly(ethylene glycol) (PEG)-PFPE triblock surfactant, used with fluorinated oil, was a kind gift from Prof. Piotr Garstecki from the Institute of Physical Chemistry, Polish Academy of Sciences.

REFERENCES

- [1] T. S. Kaminski, O. Scheler, and P. Garstecki, “Droplet microfluidics for microbiology: Techniques, applications and challenges,” *Lab Chip*, vol. 16, no. 12, pp. 2168–2187, 2016, doi: [10.1039/C6LC00367B](https://doi.org/10.1039/C6LC00367B).
- [2] W. Postek, P. Gargulinski, O. Scheler, T. S. Kaminski, and P. Garstecki, “Microfluidic screening of antibiotic susceptibility at a single-cell level shows the inoculum effect of cefotaxime on *E. coli*,” *Lab Chip*, vol. 18, no. 23, pp. 3668–3677, 2018, doi: [10.1039/C8LC00916C](https://doi.org/10.1039/C8LC00916C).
- [3] O. Scheler, K. Makuch, P. R. Debski, M. Horka, A. Ruszczak, N. Pacocha, K. Sozański, O.-P. Smolander, W. Postek, and P. Garstecki, “Droplet-based digital antibiotic susceptibility screen reveals single-cell clonal heteroresistance in an isogenic bacterial population,” *Sci. Rep.*, vol. 10, no. 1, p. 3282, Feb. 2020, doi: [10.1038/s41598-020-60381-z](https://doi.org/10.1038/s41598-020-60381-z).
- [4] K. Pärnamets, T. Pardy, A. Koel, T. Rang, O. Scheler, Y. Le Moullec, and F. Afrin, “Optical detection methods for high-throughput fluorescent droplet microflow cytometry,” *Micromachines*, vol. 12, no. 3, p. 345, Mar. 2021, doi: [10.3390/mi12030345](https://doi.org/10.3390/mi12030345).
- [5] M. Li, H. Liu, S. Zhuang, and K. Goda, “Droplet flow cytometry for single-cell analysis,” *RSC Adv.*, vol. 11, no. 34, pp. 20944–20960, Jun. 2021, doi: [10.1039/D1RA02636D](https://doi.org/10.1039/D1RA02636D).

- [6] Y. Ding, P. D. Howes, and A. J. Demello, "Recent advances in droplet microfluidics," *Anal. Chem.*, vol. 92, no. 1, pp. 132–149, Jan. 2020, doi: 10.1021/acs.analchem.9b05047.
- [7] S. Stavarakis, G. Holzner, J. Choo, and A. de Mello, "High-throughput microfluidic imaging flow cytometry," *Current Opinion Biotechnol.*, vol. 55, pp. 36–43, Feb. 2019, doi: 10.1016/j.copbio.2018.08.002.
- [8] C. Cha, J. Oh, K. Kim, Y. Qiu, M. Joh, S. R. Shin, X. Wang, G. Camci-Unal, K.-T. Wan, R. Liao, and A. Khademhosseini, "Microfluidics-assisted fabrication of gelatin-silica core-shell microgels for injectable tissue constructs," *Biomacromolecules*, vol. 15, no. 1, pp. 283–290, Jan. 2014, doi: 10.1021/BM401533Y.
- [9] R. Samanipour, Z. Wang, A. Ahmadi, and K. Kim, "Experimental and computational study of microfluidic flow-focusing generation of gelatin methacrylate hydrogel droplets," *J. Appl. Polym. Sci.*, vol. 133, no. 29, pp. 1–10, Aug. 2016, doi: 10.1002/APP.43701.
- [10] W. Zeng, H. Fu, and S. Li, "Characterization of the pressure-driven flows for droplet microfluidics," in *Proc. CSAA/IET Int. Conf. Aircr. Utility Syst. (AUS)*, Jun. 2018, pp. 309–313, doi: 10.1049/cp.2018.0090.
- [11] W. Zeng, S. Yang, Y. Liu, T. Yang, Z. Tong, X. Shan, and H. Fu, "Precise monodisperse droplet generation by pressure-driven microfluidic flows," *Chem. Eng. Sci.*, vol. 248, Feb. 2022, Art. no. 117206, doi: 10.1016/j.ces.2021.117206.
- [12] X. Duan, Z. Zheng, Y. Luo, and C. Song, "Closed-loop feedback control for droplet-based microfluidics: A characteristic investigation on passive and on-demand droplet generation," *Proc. SPIE*, vol. 12550, pp. 183–188, Jan. 2023, doi: 10.1117/12.2666602.
- [13] W. Zeng and H. Fu, "Precise monodisperse droplet production in a flow-focusing microdroplet generator," *Chem. Eng. Res. Des.*, vol. 160, pp. 321–325, Aug. 2020, doi: 10.1016/j.cherd.2020.06.002.
- [14] N. Wang, R. Liu, N. Asmare, C.-H. Chu, O. Civelekoglu, and A. F. Sarioglu, "Closed-loop feedback control of microfluidic cell manipulation via deep-learning integrated sensor networks," *Lab Chip*, vol. 21, no. 10, pp. 1916–1928, 2021, doi: 10.1039/d1lc00076d.
- [15] E.-C. Yeh, C.-C. Fu, L. Hu, R. Thakur, J. Feng, and L. P. Lee, "Self-powered integrated microfluidic point-of-care low-cost enabling (SIMPLE) chip," *Sci. Adv.*, vol. 3, no. 3, Mar. 2017, Art. no. e1501645, doi: 10.1126/sciadv.1501645.
- [16] D. F. Crawford, C. A. Smith, and G. Whyte, "Image-based closed-loop feedback for highly mono-dispersed microdroplet production," *Sci. Rep.*, vol. 7, no. 1, pp. 1–9, Sep. 2017, doi: 10.1038/s41598-017-11254-5.
- [17] B. Miller, "Manipulation of microfluidic droplets," U.S. Patent EP2411148 B1, Mar. 23, 2010.
- [18] B. van Elburg, G. Collado-Lara, G.-W. Bruggert, T. Segers, M. Versluis, and G. Lajoie, "Feedback-controlled microbubble generator producing one million monodisperse bubbles per second," *Rev. Sci. Instrum.*, vol. 92, no. 3, Mar. 2021, Art. no. 035110, doi: 10.1063/5.0032140.
- [19] N. Gyimah, O. Scheler, T. Rang, and T. Pardy, "Can 3D printing bring droplet microfluidics to every lab?—A systematic review," *Micromachines*, vol. 12, no. 3, p. 339, Mar. 2021, doi: 10.3390/mi12030339.
- [20] TalTech-LoC. *HW-Open-Fluidic-Infra*. Accessed: May 16, 2023. [Online]. Available: <https://github.com/taltechloc/hw-open-fluidic-infra>
- [21] N. Gyimah, O. Scheler, T. Rang, and T. Pardy, "Digital twin for controlled generation of water-in-oil microdroplets with required size," in *Proc. 23rd Int. Conf. Thermal, Mech. Multi-Phys. Simul. Experiments Microelectron. Microsystems (EuroSimE)*, Apr. 2022, pp. 1–7, doi: 10.1109/EuroSimE54907.2022.9758876.
- [22] N. Gyimah, R. Joemaa, K. Parnamets, O. Scheler, T. Rang, and T. Pardy, "PID controller tuning optimization using genetic algorithm for droplet size control in microfluidics," in *Proc. 18th Biennial Baltic Electron. Conf. (BEC)*, Oct. 2022, pp. 1–6, doi: 10.1109/BEC56180.2022.9935596.
- [23] R. Joemaa, M. Grosberg, T. Rang, and T. Pardy, "Low-cost, portable dual-channel pressure pump for droplet microfluidics," in *Proc. 45th Jubilee Int. Conv. Inf., Commun. Electron. Technol. (MIPRO)*, May 2022, pp. 205–211, doi: 10.23919/MIPRO55190.2022.9803371.
- [24] M. Grosberg, R. Jõemaa, P. Tamas, and T. Rang. (2022). *Wireless Microfluidic Dual-Channel Pressure Pump*. [Online]. Available: <https://www.etis.ee/Portal/IndustrialProperties/Display/353426b9-f02b-44b2-b581-e8f21363157a>
- [25] K. Ashraf, Y. L. Moullec, T. Pardy, and T. Rang, "Model-based system architecture for event-triggered wireless control of bio-analytical devices," in *Proc. 24th Euromicro Conf. Digit. Syst. Design (DSD)*, Sep. 2021, pp. 465–471, doi: 10.1109/DSD53832.2021.00076.
- [26] Alphabet. (2022). *Protocol Buffers* | Google Developers. Accessed: Oct. 31, 2022. [Online]. Available: <https://developers.google.com/protocol-buffers/docs/reference/overview>
- [27] Eclipse. (2022). *Welcome to Eclipse eCALTM—Eclipse eCALTM Documentation*. Accessed: Oct. 31, 2022. [Online]. Available: <https://eclipse-ecal.github.io/ecal/>
- [28] K. Parnamets, A. Koel, T. Pardy, and T. Rang, "Open source hardware cost-effective imaging sensors for high-throughput droplet microfluidic systems," in *Proc. 26th Int. Conf. Electron.*, Jun. 2022, pp. 1–6, doi: 10.1109/IEECONF55059.2022.9810383.
- [29] N. A. Prabatama, R. Joemaa, K. Hegedus, and T. Pardy, "Low-cost open-source flow velocity sensor for droplet generators," in *Proc. 18th Biennial Baltic Electron. Conf. (BEC)*, Oct. 2022, pp. 1–4, doi: 10.1109/BEC56180.2022.9935606.
- [30] J. Caldwell. (2014). *An IMPORTANT NOTICE at the End of This TI Reference Design Addresses Authorized Use, Intellectual Property Matters and Other Important Disclaimers and Information*. Accessed: May 12, 2023. [Online]. Available: www.ti.com
- [31] O. Scheler, T. S. Kaminski, A. Ruzczak, and P. Garstecki, "Dodecylresorufin (C12R) outperforms resorufin in microdroplet bacterial assays," *ACS Appl. Mater. Interfaces*, vol. 8, no. 18, pp. 11318–11325, May 2016, doi: 10.1021/acsmi.6b02360.
- [32] TalTech-LoC. (2020). *HW-MVP-Chip*. Accessed: Sep. 21, 2022. [Online]. Available: <https://github.com/taltechloc/hw-mvp-chip>
- [33] (2022). *BioMEMS Group*. Accessed: Oct. 31, 2022. [Online]. Available: <https://biomems.hu/>
- [34] W. Zeng, S. Li, and Z. Wang, "Closed-loop feedback control of droplet formation in a T-junction microdroplet generator," *Sens. Actuators A, Phys.*, vol. 233, pp. 542–547, Sep. 2015, doi: 10.1016/j.sna.2015.08.002.
- [35] Y. Xie, A. J. Dixon, J. M. R. Rickel, A. L. Klibanov, and J. A. Hossack, "Closed-loop feedback control of microbubble diameter from a flow-focusing microfluidic device," *Biomicrofluidics*, vol. 14, no. 3, May 2020, Art. no. 034101, doi: 10.1063/5.0005205.
- [36] S. Motaghi, M. Nazari, N. Sephiri, and A. Mahdavi, "Control of droplet size in a two-phase microchannel using PID controller: A novel experimental study," *Amirkabir J. Mech. Eng. Amirkabir J. Mech. Eng.*, vol. 53, no. 7, pp. 1013–1016, 2021, doi: 10.22060/mej.2020.18250.6783.
- [37] H. Fu, W. Zeng, S. Li, and S. Yuan, "Electrical-detection droplet microfluidic closed-loop control system for precise droplet production," *Sens. Actuators A, Phys.*, vol. 267, pp. 142–149, Nov. 2017, doi: 10.1016/j.sna.2017.09.043.



RAUNO JÕEMAA was born in Estonia, in 1991. He received the bachelor's degree in electronics and bionics and the master's degree in communicative electronics from the Tallinn University of Technology, where he is currently pursuing the Ph.D. degree with the Thomas Johann Seebeck Department of Electronics. He is a Junior Researcher with the Department of Chemistry and Biotechnologies, Tallinn University of Technology. His current research interests include electronics and microfluidics.



NAFISAT GYIMAH received the B.S. degree in electrical and electronic engineering from the Kwame Nkrumah University of Technology, Kumasi, Ghana, in 2013, and the M.S. degree in communicative electronics from the Tallinn University of Technology, Tallinn, Estonia, in 2020, where she is currently pursuing the Ph.D. degree in high-speed droplet microfluidics sorting and encapsulation. From November 2021 to January 2022, she was with SelfDiagnostics Deutschland GmbH, where she focused on the thermal and electrical characterization of SARS-CoV2 microfluidic multitest kits. She was a Cognitronics Engineer with the Tallinn University of Technology, from June 2020 to December 2020. Her current research interests include lab-on-a-chip, droplet microfluidic system control, and flow control simulations using computational fluid dynamics (CFD).



KANWAL ASHRAF received the bachelor's degree in electrical engineering from the University of the Punjab, Pakistan, and the joint-international master's degree in smart system integration from Heriot-Watt University, U.K., the University of South-Eastern Norway (USN), Norway, and the Budapest University of Technology and Economics (BME), Hungary, in 2020. She is currently pursuing the Ph.D. degree with the Tallinn University of Technology, Estonia. Her current research interests include the application of wireless communication in CPSs and the co-design of wireless networked control systems for bioanalytical applications.



KAISER PÄRNAMETS (Member, IEEE) was born in Tallinn, Estonia, in January 1989. He received the B.Sc. and M.Sc. degrees in engineering from the Tallinn University of Technology, in 2013 and 2016, respectively, where he is currently pursuing the Ph.D. degree. From 2014 to 2017, he was a hardware engineer in the electronics industry and has been an electronics lecturer for bachelor's and master's students, since 2018. His current research interests include lab-on-a-chip and microfluidics.



ALEXANDER ZAFT was born in 1997. He received the bachelor's and master's degrees in computer science from the University of Würzburg, Germany, in 2019 and 2022, respectively. In Summer 2022, he joined the Lab-on-a-Chip Group, Tallinn University of Technology, as an Intern. Since November 2022, he has been a Software Engineer with Heinz-Maier-Leibnitz Zentrum, Garching, Germany.



OTT SCHELER received the Ph.D. degree in biotechnology from the University of Tartu, Estonia, in 2012. He was a Postdoctoral Researcher of microfluidics with the Institute of Physical Chemistry, Polish Academy of Sciences, from 2014 to 2018. After that, he joined the Tallinn University of Technology, where he is currently an Associate Professor of microfluidics with the Department of Chemistry and Biotechnology. His current research interests include microfluidics, microbiology, and biotechnology.



TOOMAS RANG (Senior Member, IEEE) received the Ph.D. degree in semiconductor electronics from the Hungarian Academy of Sciences, in 1981. He is currently a Professor Emeritus with the Thomas Johann Seebeck Department of Electronics and a Senior Research Fellow with the Department of Chemistry and Biotechnologies, Tallinn University of Technology, Estonia. He has supervised 15 Ph.D. students and has fulfilled the PI position in several European and domestic research and industrial projects. His current research interest includes applied microfluidics approaches for lab-on-chip applications. He is the Initiator and today the honor Chairperson of the Baltic Electronics Conference (BEC) Series, in 1987, supported by IEEE, since 1996.



TAMÁS PARDY (Member, IEEE) received the M.Sc. degree in info-bionics engineering from Peter Pazmany Catholic University, Budapest, Hungary, in 2014, and the Ph.D. degree in electronics and telecommunication from the Tallinn University of Technology, Tallinn, Estonia, in 2018. He is currently a Senior Researcher with the Tallinn University of Technology. He has supervised one Ph.D. thesis and five M.Sc. thesis and has authored or coauthored over 20 scientific publications. His current research interest includes flow- and temperature control of lab-on-a-chip devices.

...

Curriculum vitae

Personal data

Name: Rauno Jõemaa
Date of birth: December 30, 1991
Place of birth: Estonia, Haapsalu
Citizenship: Estonia

Contact data

E-mail: rauno.joemaa@taltech.ee

Education

2018–2024 Tallinn University of Technology
Information and Communication Technology, PhD
2016–2018 Tallinn University of Technology
Communicative Electronics, MSc
2011–2016 Tallinn University of Technology
Electronics and Bionics, BSc
1998–2011 Haapsalu Gymnasium

Language competence

Estonian Native
English Fluent
German Conversational

Professional employment

2020–... Tallinn University of Technology, Junior Researcher
2016–2019 Skeleton Technologies OÜ, Electronics Engineer

Elulookirjeldus

Isikuandmed

Nimi: Rauno Jõemaa
Sünniaeg: 30 detsember 1991
Sünnikoht: Eesti, Haapsalu
Kodakondsus: Eesti

Kontaktandmed

E-post: rauno.joemaa@taltech.ee

Hariduskäik

2018–2024 Tallinna Tehnikaülikool
Info- ja kommunikatsioonitehnoloogia, doktoriõpe
2016–2018 Tallinna Tehnikaülikool
Elektroonika ja kommunikatsioonitehnoloogiad, magistriõpe
2011–2016 Tallinna Tehnikaülikool
Elektroonika ja bioonika, bakalaureuseõpe
1998–2011 Haapsalu Gümnaasium, Keskkharidus

Keelteoskus

Eesti keel Emakeel
Inglise keel Kõrgtase
Saksa keel Kesktase

Teenistuskäik

2020–... Tallinn University of Technology, doktorant-nooremteadur
2016–2019 Skeleton Technologies OÜ, elektroonikainsener

ISSN 2585-6901 (PDF)
ISBN 978-9916-80-191-8 (PDF)